Colloid Vibration Potential for Imaging in Engineering and Medicine

Fria Hossein

Submitted in accordance with the requirements for the degree of
Doctor of Philosophy

The University of Leeds
School of Chemical and Process Engineering

August 2019

ACKNOWLEDGEMENTS

At the end of this journey towards my PhD degree it is time to give thanks to the many individuals who made my journey successful.

First, and mostly, I would like to thank my amazing and best supervisor Professor Mi Wang for his huge support and encouragement during my study. His advice has helped me every step along the way in completing my project successfully. I also want to thank my co-supervisor Dr Xiaodong Jia for his great advice during my research work.

This thesis is dedicated to my lovely parents, my dad Hossein, and my mum Halaw, my brothers, Farman and Hiwa, and my sisters, Kazhall, Allwan, Darya, and Darun. I would like to thank Miss Rachanekorn Meaw.

A huge thanks also goes to the technician Mr Robert Harris for his help during my experimental work. I want to thank all my colleagues, Dr Qiang Wang, Mr Bishali Karki, Mr Philip Nwufoh, Mr Kun Li and Dr Jabbar Gardy for all their support during my PhD study. I gratefully acknowledge Dr Girish Kale for his valuable feedbacks and suggestions during my 1st year and 2nd year exam.

I would like to take this opportunity to thank Professor Daryl Williams (external examiner) and Dr Timothy Hunter (internal examiner) for their very helpful feedbacks, suggestions and comments.

ABSTRACT

Ultrasound Vibration Potential (UVP) is an electric signal generated when ultrasound pulses travel through a colloidal suspension or ionic electrolyte. The electric potential can be measured, providing information useful to characterize the nanoparticles and ionic electrolytes in engineering and particularly, complimentary information to conventional ultrasound imaging in medicine. The main advantage of this method over current conventional ultrasound imaging is that it can measure and further, image differences in ion recipe or physiochemical properties of particles in colloids. The simple approach is to apply external ultrasound pressure wave propagating through a nanoparticle suspension or ionic electrolytes. The nanoparticles begin to vibrate due to the ultrasound pressure, and this results in the generation of electric potential which can be detected by an electrode sensor attached to the body.

This thesis reviews the fundamental physical theory of ultrasound and UVP imaging techniques. The ultrasound vibration potential distribution (UVPD) model based on a static charge dipole field is established and analysed in a numerical method. A new UVP testing phantom made from agar, called the Leeds standard III UVP device for UVP imaging, has been designed, in which electrodes are non-intrusively attached to the body. The measurements using the mock body phantom, containing either ionic or nanoparticle species, are in good quality comparing those measurements obtained from colloidal suspension and consistence with results from the numerical simulation. A method of frequency domain analyse with a number of segmented chirp signal ranges is proposed, which reveals both frequency and phase angle responses are function of particle size. The research also demonstrates how UVP can reveal specific physiochemical structures of colloids or tissue which the conventional ultrasound technique cannot see, with samples of ionic species, silica and titanium dioxide nanoparticles and further the animal (pork) tissue.

The results, along with previous findings, further support the potential of UVP for application in engineering for nanoparticle and ionic electrolyte characterisation and providing new and/or complementary knowledge for medical diagnosis and research.

TABLE OF CONTENTS

LIST OF TABLES

LIST OF FIGURES

NOMENCLATURE

Symbols	Abbreviations	Unit
CVP	colloid vibration potential	mV
CVI	colloid vibration current	mA
IVP	ionic vibration potential	mV
UVP	ultrasound vibration potential	mV
ESA	electro-sonic amplitude	mV
k	wave number	$1/\mathrm{m}$
ω	angular frequency	$\mathrm{radians/s}$
f	frequency	Hz
λ	wavelength	m
A	amplitude	mV
Z	acoustic impedance	$\mathrm{N.S/m^3}$
c	sound speed	$\mathrm{m/s}$
φ	The volume fraction of particle	1
α	attenuation coefficient	$1/m$
∇P	pressure gradient	p
a	particle radius	nm
D_i	diffusion coefficient of ion species	cm^2/s
d	particle diameter	nm
e	elementary electric charge	coulomb
E	electric field strength	coloumb
$\mathrm{F_{hook}}$	Hookean force	$\mathrm{Kg.m/s^2}$
$\mathrm{N_A}$	Avogadro's number	$\mathrm{mol^{-1}}$
$\mathrm{N_p}$	number of particles	
P	pressure	$\mathrm{N/m^2}$

t	time	sec
T	absolute temperature	kelvin
u	speed of the motion	$\mathrm{m/s}$
γ	hydrodynamic friction coefficient	
ɳ	dynamic viscosity	$\mathrm{kgm^{-1}s^{-1}}$
μ	electrophoretic mobility	$\mathrm{m^2(V-s)}$
c_i	concentration of the ith ion	
c_e	electrolyte concentration	
Du	Dukhin number	
f	Frequency of ultrasound	Hz
F	Faraday constant	C/mol
F^h	hydrodynamic friction force	
k	Boltzmann constant	
I	intensity of sound	Watt/$\mathrm{m^2}$
j	complex unit	
m_i	mass of solvated ions	
$v^{\pm}$	volume of solvated ions	
$z^{\pm}$	valences of the cation and anions	
β_r	colloid spatial distribution	
ε	dielectric permittivity	F/m
εo	dielectric permittivity of vacuum	F/m
κ	Debye length	$1/\mathrm{K}$
ρ_p	Particle density	$\mathrm{g/cm^3}$
ρ_u	Liquid density	g/ml
σ	surface charge density	coloumb/$\mathrm{m^2}$
ξ	electrokinetic potential	mV
ψ^d	diffuse layer potential	mV

ψ_s	stern potential	mV
Ω	drag coefficient	
v	particle displacement velocity	m/s
n	bulk density of ions	
F_{DL}	double layer force	
X_e	electric sustainability	
Q	parameter of relaxation force	
K^*	complex conductivity	S/m
D	dielectric displacement	C/m^2
C	capacitance	Farad
P_a	electrical polarization	coloumb/m^2
Q	charge on the particle	coulomb

CHAPTER 1: INTRODUCTION

1.1 Background

UVP is an electroacoustic phenomenon applied to colloid particles and ionic electrolytes. It consists of two categories: colloid vibration potential (CVP), and ion vibration potential (IVP). CVP is produced by applying ultrasound energy to a nanoparticle suspension, for example, titanium oxide. IVP is produced by applying ultrasound energy to an electrolyte solution, for example, barium chloride.

The concept of IVP for ionic electrolytes dates back to Debye (1933). He realized that an electric signal (IVP) is generated in electrolytes upon the introduction of ultrasound pressure. Different anionic and cationic masses result in different displacement amplitudes, and this difference creates an electric potential between any two points in the solution Dukhin and Goetz, (2002). The experimental results for IVP were first reported by Zana and Yeager, (1967), while the theory of IVP was given by, John et al., (1947). In early 1945 and 1960, there was much interest in this effect because it was a promising tool to characterise ionic electrolytes, but today the main interest is directed towards colloids and medicine.

The first report on CVP was made by Hermans, (1938) followed by other researchers Rutgers and .Rigole.,(1957). The theory of CVP of dilute solutions was first presented by, Booth and Enderby, (1952) while early experimental work on colloidal suspensions was conducted by Zana and Yeager (1967). O'Brien (1987) then developed a model which explained the electric potential generated by the sound wave in colloidal suspensions. The analytical expressions for both IVP and CVP derived by Ohshima and Dukhin, (1999). There has also been speculative and experimental work carried out in this field by both Brown University Vitalyi and Diebold, (2005) and the University of Leeds Guang et al.,(2011). The analogue model of ultrasound vibration potential distribution presented between two parallel grounded electrodes calculated for an infinitive colloidal layer by Cuong et al., (2008). In this model the relationship of the measured voltage via integrations is not revealed and the results not evaluated experimentally. However, a numerical, and experimental solution required to present the potential distribution for the device optimizations. In the past, two standard devices

have been established for UVP measurements. The first device established by the Brown University (thereafter called UVP standard 1) Andrew et al., (2004) the lack of repeatability with this device and changing the sample is not easy. It is not capable of non-intrusive measurement. The amount of ultrasound energy traveling into the sample of interest is reduced because the cling film creates an interface between the sample and the delay line. The second UVP device established by the University of Leeds (UVP standard II) Khan, (2010), this device was introduced based on the UVP standard I device. Its advantages over (standard I) are its repeatability as it is easier to change the sample and it also enhances the signal quality. However, again, the UVP standard II device is not capable of non-intrusive measurement and the use of cling film to cover the sample creates an interface and decreases the sound energy traveling into the medium. In both devices, the delay lines are water-based, and electrodes set near the sample (e.g. in mm or cm) which is far from the volumetric size either in engineering and medicine, and the optimized electrode locations remained unknown.

1.2 Objectives

The overall aim of this research is to develop the ultrasound vibration potential (UVP) imaging of colloidal suspensions, ionic electrolytes, and tissue for engineering and medicine. The ultrasound vibration potential distribution (UVPD) is a challenging phenomenon for future device optimization. The previous UVP measurement devices are not capable of nonintrusive measurements, and the use of cling film for sealing the samples causes the reduction of the amount of energy to be transfered through the sample. The sensing system and the measurement method requires further improvements to enhance the signal quality and the capability of this method for nonintrusive tissue imaging. The additional signatures of CVP may reveal specific physiochemical structures of tissue, and this may compare to the current conventional ultrasound imaging. The UVP measurement method uses to detect the physiochemical feature characterization of nanoparticles further to measure the particle size distribution.

There are six significant objectives:

A. Engineering Applications:

1. The modelling of ultrasound vibration potential distribution (UVPD) using the static charge dipole field in a finite boundary conditions and evaluate the

measurement and the potential distribution along the ultrasound propagation direction.

2. To progress on the sensing system using electrodes non-intrusively placed outside a body, containing either ionic or nanoparticular species to show the potential to provide physiochemical properties of the sample.
3. To characterize the physicochemical feature properties of nanoparticles and ionic species in colloids.

B. Medical Applications:

1. To establish a new testing phantom which is capable of non-intrusive ultrasound vibration potential measurement, and enhance the UVP signal strength.
2. To investigate whether CVP signal can be measurable from animal tissue and the feasibility to be developed as a new functional imaging for medical diagnosis and research.
3. To review a method of imaging colloidal/ionic objects, using low power source of excitation, to report a unique feature of UVP, and additional signatures of UVP to reveal specific physiochemical structures of the sample.

1.3 Organization of the Thesis

The organization of this thesis is as follows:

Chapter 2: The literature review will discuss the important concept of ultrasound characteristics, which applies to the ultrasound vibration potential theory. The principles of the conventional ultrasound imaging technique and the general method analysis of colloidal suspensions are presented. The principles of the double layer in colloidal suspensions demonstrated. It describes the previous and current status of the ion and colloidal vibration potential models presented by both Brown University and the University of Leeds. It reviews the theoretical and experimental work done by previous researchers e.g. Debye, Ohshima, and O'Brien etc. The ultrasound vibration potential distribution introduced for colloidal infinitive layers by Brown University is presented.

Chapter 3: This Chapter provides a fundamental principles of ultrasound vibration potential excitation signal, polarizations, and measured UVP electrical signal. The theoretical and numerical solutions presented for ultrasound vibration potential

distribution. The voltage generation via the integration over the finite region of a colloidal layer is demonstrated.

Chapter 4: Here, the physicochemical characterization of the nanoparticles in colloidal suspensions and ionic electrolytes is presented. As part of the experiment, the frequency response as the particle diameter changes is also investigated. The phase shift as a function of particle size for a specific sample such as, for example, TiO_2, SiO_2 is presented in this chapter.

Chapter 5: This Chapter describes a new test phantom including the apparatus design, construction, instrumentation, and sensor design. It will give details of the signal detection and the equivalent circuit diagram of the measured signal. It will describe the chemical property of agar, the history, and uses in biomedicine research. It will demonstrate the uniqueness of this method in comparison to the earlier model. IVP signal strength and CVP signal strength are both measured with non-intrusive electrodes placed outside a mock body made from agar. In this Chapter the effect of pH and salt on UVP signal is also analysed.

Chapter 6: In this Chapter, the difference between conventional ultrasound imaging and UVP imaging is highlighted. The sequence and methods in the use of the Leeds standard III UVP phantom are also presented in this section. Another important section in this Chapter is the investigation of whether the CVP signal can be measured and the feasibility of this being developed as a new functional imaging method for medical diagnosis and research. To simplify the approach, pork meat was selected and examined with our current CVP instrumentation and also the conventional ultrasound reflection detection (URD) device (a Mindray DP-6600 ultrasound machine) to explore the difference between CVP and URD signals.

Chapter 7: This Chapter summarizes all experimental results and reviews the achievements and problems in this study. Ways to improve the measurement technique in this field are explained and recommendations on possible future work given.

CHAPTER 2: LITERATURE REVIEW

Summary: *This chapter explains the basic principles of the ultrasound wave, ultrasound imaging, and ultrasonic transducers. It expresses the theory of ultrasound vibration potential (UVP) imaging and reports the correlated basic theories of colloids, surface science, double layer (DL), and dispersion forces associated with UVP. The theoretical and experimental status of both IVP and CVP are addressed. The ultrasound vibration potential distribution is presented.*

2.1 Introduction

This chapter gives a comprehensive literature review includes the principles of ultrasound vibration potential and conventional ultrasound imaging. This reviews the most recent background related to the research area. The first section will discuss the basic principle of traditional sonography, the ultrasound wave, and its characterizations. A review of ultrasound transducers and its wave characterizations are presented.

The second section will discuss the colloidal science, dispersion forces, surface charge density, and the double layer (DL) in colloidal suspensions. This section will present the colloid dispersion characterizations that are related to the research area.

The third section will explain the literature conducted in UVP imaging. Previous research in the area of UVP, the theoretical and experimental status of UVP is also presented.

General methods for the possible measurement of the ultrasound vibration signal include the slab model and the 3D dipole model and these are explained. The ultrasound vibration potential distribution introduced by Brown University for the infinitive colloidal layers between two parallel grounding electrodes are presented.

2.2Ultrasound Imaging

The science behind ultrasound can be traced back to Lazzaro Spallanzani Kane et al., (2004) who demonstrated that bats can navigate by inaudible sound. Diagnostic ultrasound within the field of medicine was first used by Karl Dussik in 1942, and later, George Ludwig used ultrasound to study gallstones Beaker, (2005). Ultrasound wave can travel through air, liquid, and solids, but cannot go through a vacuum. The ultrasound technique is used in various fields, e.g. to detects objects, to measure

distance, and ultrasound imaging, or sonography, and is also used in medicine. Ultrasound can also be applied to the physicochemical characterization of nanoparticles, such as particle size distribution, Dukhin and Goetz (2001).

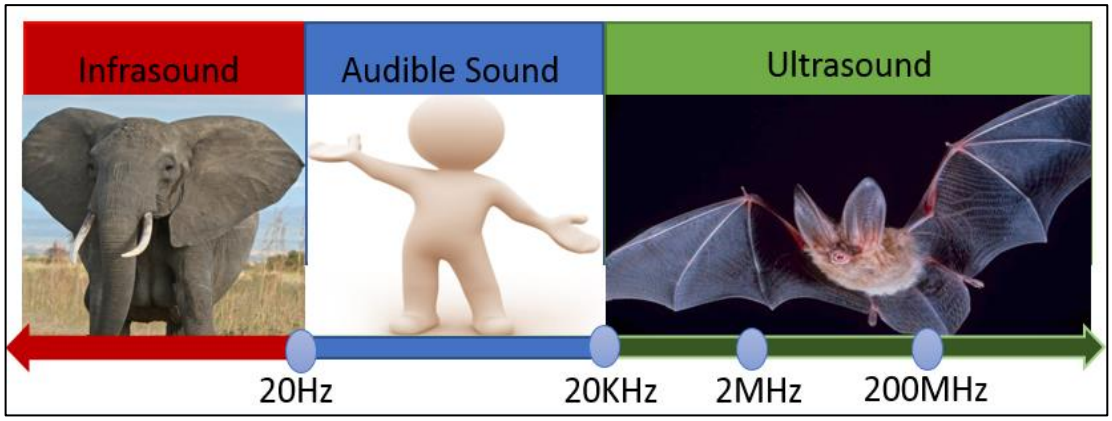

Figure 2.1: The spectrum of sound frequency.

Ultrasound diagnostic imaging is an imaging technique that can be used to visualize the size and structure of the internal organs of the human body. The principle is that a high-frequency sound wave (typically, 1–6 MHz) is sent through the body by using a probe (transducer). The distances and sizes of the organs can be calculated by the speed of the sound wave through the body, and by the arrival time of the signal. The choice of frequency used can be for high-resolution imaging of for deeper, penetrative imaging. For example, a lower frequency signal gives a lower quality image but can penetrate deeper into the body, Craig (2007).

In ultrasound imaging the main concern is attenuation because it causes a reduction in signal amplitude. The intensity and the amplitude of the ultrasonic waves decrease when the ultrasound travels from one medium into another medium.

The reduction in amplitude (attenuation) is caused by several factors such as absorption, scattering, reflection, divergence, and diffraction. Absorption is the reduction of intensity, this happens when the ultrasound propagates through the tissue some of its energy loss in the form of heat. The scattering occurs when the ultrasound wave strikes a structure with a different medium. The reflection of ultrasound wave occurs when the ultrasound wave travels through a different medium having different impedances. The divergence is related to the sensor property, e.g. the divergence increase with lower transducer frequency and small sensor diameters. Diffraction happens when the wave paths around the barrier, or when the wavelength of the propagated ultrasound is smaller

than the obstacle, Pascal and Guillaume (2017). The primary concern in ultrasound imaging is that the ultrasound energy develops heat within the tissue which results in an increase in temperature locally, causing bubbles to form when the dissolved gases are released. However, ultrasound is safe and painless and less expensive than an X-ray. The patient is not exposed to radiation in order to capture images of the soft tissue, which does not show up well on X-ray, Dukhin and Philip (2001).

2.2.1 Characterization of a Sound Wave

A sound wave is a mechanical disturbance that transfers energy through a medium. An ultrasound wave is a mechanical disturbance that is transmitted as a longitudinal wave or a transverse wave. Longitudinal wave can travel through a gas, fluids, and solids, whereas, a transverse wave can travel through solids only, Assadi (2011).

The frequency $\boldsymbol{f}$ is measured in hertz (Hz), and it is the number of waves per unit of time, given in seconds (s):

$$\boldsymbol{f = \frac{1}{T}\ (Hz)} \qquad (2.1)$$

Where C is the speed of ultrasonic wave propagation in the medium and is measured in $(\boldsymbol{m/s})$:

$$\boldsymbol{C = \frac{2\pi f}{k}\ (m/s)} \qquad (2.2)$$

The sound speed depends on the property and temperature of the medium – the wavelength λ is measured in $(\boldsymbol{m})$:

$$\boldsymbol{\lambda = \frac{2\pi}{k}\ (m)} \qquad (2.3)$$

Where $\boldsymbol{\omega}$ is the angular frequency, and measures the angular displacement per unit of time, and is a scalar measure of rotation rate:

$$\boldsymbol{\omega = 2\pi f\ (Hz)} \qquad (2.4)$$

In this research, a longitudinal wave can travel through liquid and tissue. In a longitudinal wave, the displacement of the medium is parallel to the propagation of the wave, but in a transverse wave, the displacement of the medium is perpendicular to the direction of the wave propagation. An ultrasound wave can be described as a harmonic wave at position **x** and time $\boldsymbol{t}$ with the frequency $\boldsymbol{f}$ and wavelength λ, and can be given by Equation 2.5, (Mortimer (1982):

$$\mathbf{y(x,t) = Asin(\omega t - kx)} \tag{2.5}$$

Where $\boldsymbol{A}$ denotes the wave amplitude, $\boldsymbol{k}$ is the wave number, $\boldsymbol{\omega}$ is the angular frequency, and $\boldsymbol{\lambda}$ is the wavelength.

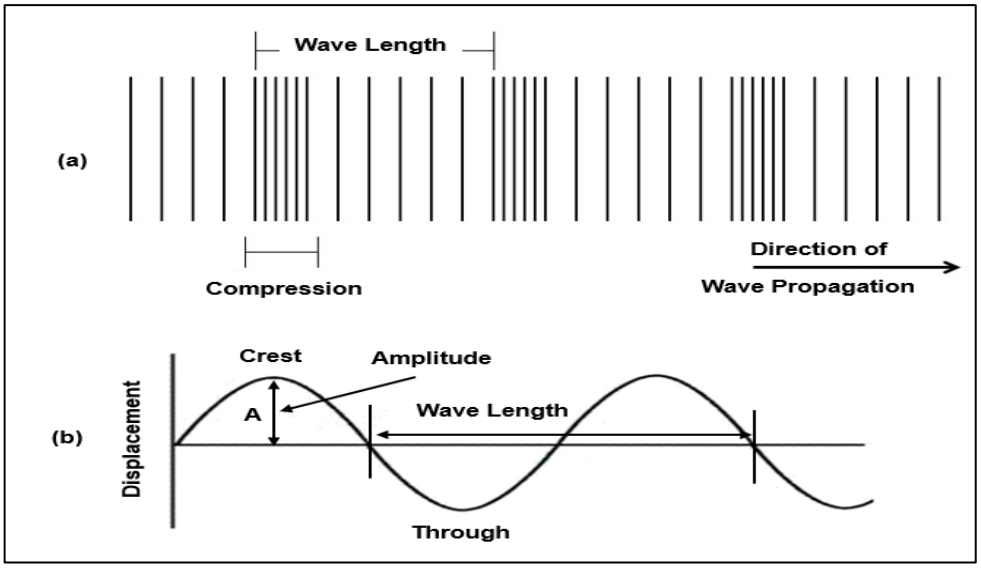

Figure 2.2: (a) The longitudinal wave, (b) The transverse wave (Ben, 2013).

The ultrasound pressure can be given by the first derivative of Equation 2.5:

$$\boldsymbol{P = \frac{dy(x,t)}{dt} = A\omega cos(\omega t - kx)} \tag{2.6}$$

When the sound wave is incident on an interface between any different media, some of the energy is reflected, and some is transmitted. The amount of energy reflected depends on the impedance of the material. The more significant the difference in impedance between the two media, the higher the amount of energy reflected. The acoustic impedance (Z) can be given by:

$$\boldsymbol{Z = \frac{P}{v}} \tag{2.7}$$

Where $\boldsymbol{P}$ denotes the sound pressure, and $\boldsymbol{v}$ is the particle displacement velocity. The higher the impedance, the higher the sound energy reflected. When the wave travels through a medium the wave amplitude changes, given by Equation 2.8 below.

$$\boldsymbol{A = A_o e^{(-\alpha x)}} \tag{2.8}$$

Where $\boldsymbol{A}$ is the wave amplitude and $\boldsymbol{A_o}$ is the reduced amplitude of a medium, and $\boldsymbol{\alpha}$ denotes the attenuation coefficient, which is measured in (Nepers per second). Table 2.1 shows the attenuation coefficient for different materials (Liu et al., (2017)).

Table 2.1: Attenuation coefficient for different materials (Hariharan and Paul (2011)).

Body Tissue	Ultrasound Velocity (m/s)	Attenuation Coefficient $(\mathrm{db/cm.\,mhz})$
Water	1480	0.002
Blood	1570	0.18
Fat	1450	0.63
Liver	1550	0.5–0.94
Kidney	1560	1.0
Muscle	1580	1.3–3.3
Agar	1610	0.194

The decibel is a logarithmic value and can be given by Equation 2.9:

$$\boldsymbol{dB = 20log_{10}\left(\frac{A}{A_o}\right)} \qquad (2.9)$$

Where $\boldsymbol{A}$ and$\boldsymbol{A_o}$, are the amplitude of signal 1 and 2 respectively. In Table 2.2 useful relationships between two signals (measured in dB) are presented.

Table 2.2: Conversion ratio of two amplitudes to dB (Vimal and Krishnan, (1996))

Ratio A/A_o	dB
1.2589	2
1.6	4
4	12
10	20
100	40
1000	60

Attenuation is the loss of ultrasound signal amplitude while the wave travels through different media due to absorption, and scattering. In some cases, some sound energy is converted to heat, and this causes attenuation in the sound amplitude. The attenuation is a function of frequency and is proportional to the square of the sound frequency, NTD, (2017).

2.2.2 Ultrasonic Transducer

The ultrasound transducer is an acoustic sensor and is divided into three different categories, for e.g. transmitter which converts the electrical signal into a mechanical signal, receiver which converts the mechanical signal into an electrical signal, and trans-receiver which can transmit and receive the signal at the same time, Roberts (2001).

The ultrasonic transducer consists of three different parts; an active element, a backing, and a wear plate, Beranek and Tim, (2012).

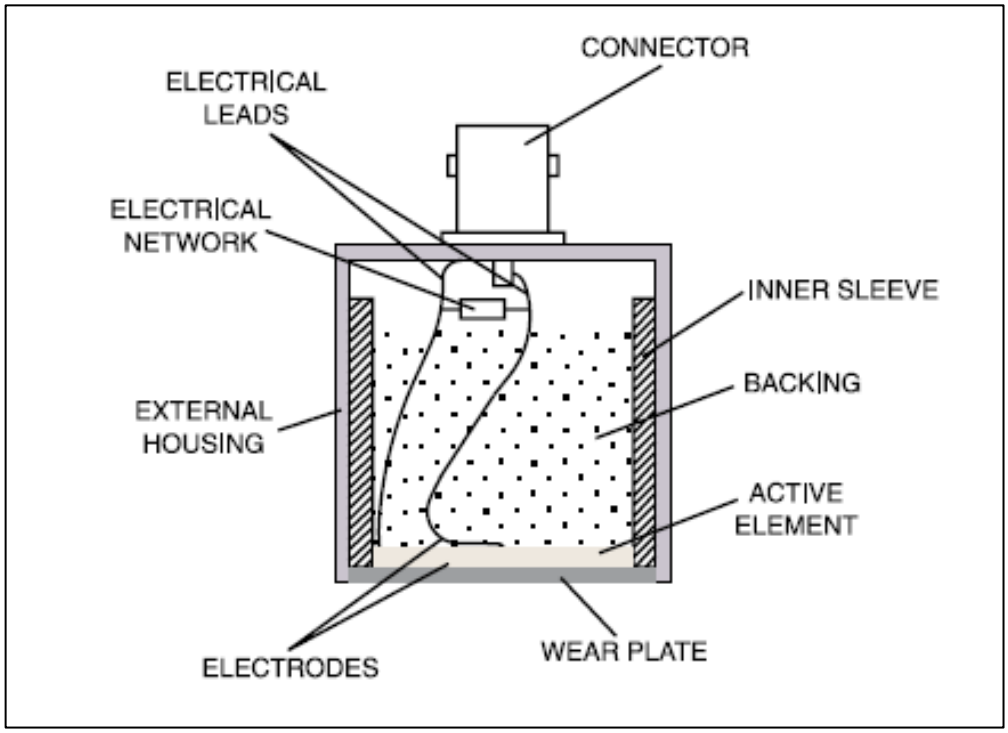

Figure 2.3: Transducer design (NTD, 2019).

The transducer has two zones; the near field, and the far field. From the front of the transducer, the beam's amplitude goes through at a distance of N from the transducer. The far field is the area beyond the near field area where the beam starts to diverge. The near field distance can be measured and is given by Equation 2.10:

$$N = \frac{D^2}{4\lambda} \tag{2.10}$$

Where **D** is the element diameter, **λ** is the wavelength.

The ultrasound probes are used to apply sound energy to agitate particles in a wide range of lab applications.

When the voltage is applied to the sensor, the piezoelectric crystals change shape and size and makes them oscillate at the same frequency and produce an ultrasound wave. The curvilinear transducer (model Mindray 35C50EA) allows a full field of vision and has a central frequency of 3.5 MHz and a frequency range of 2–6 MHz.

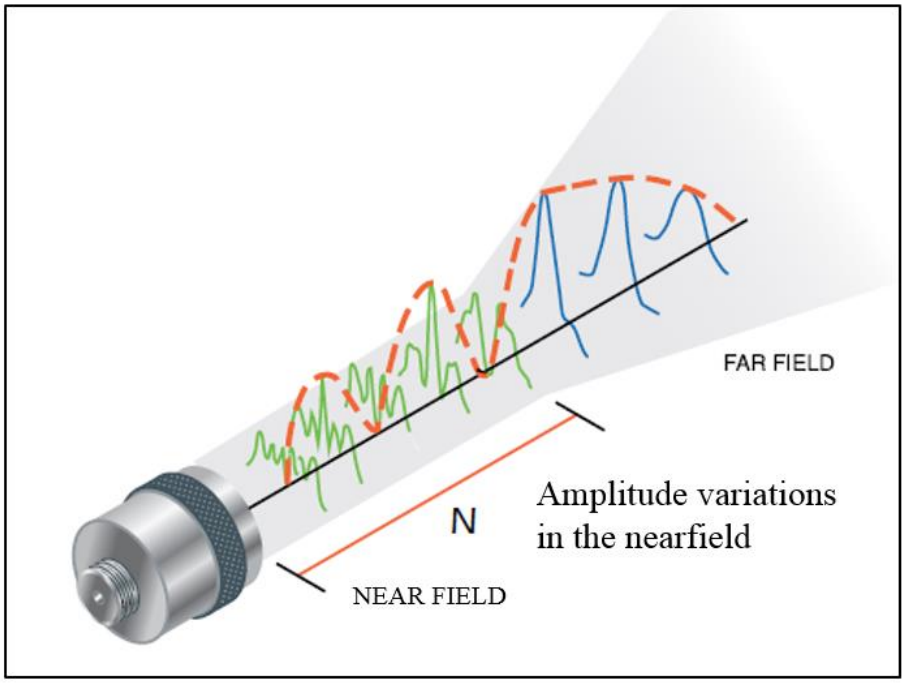

Figure 2.4: Transducer sound field zones (NTD, 2018).

A wide range of pulses from a large number of elements was used for each scan. At each line, a pulsed delay sequence of the whole array of features creates a unique interference pattern. This transducer has a wide scanning angle of 66° and emits 66 beams. It is commercially used in abdominal sonography.

The transducer connected to the conventional ultrasonic diagnostic machine (the Mindray DP-6600) for imaging the object. As noted above, this curvilinear transducer has a primary frequency of 3.5 MHz and can scan 20 frames per second.

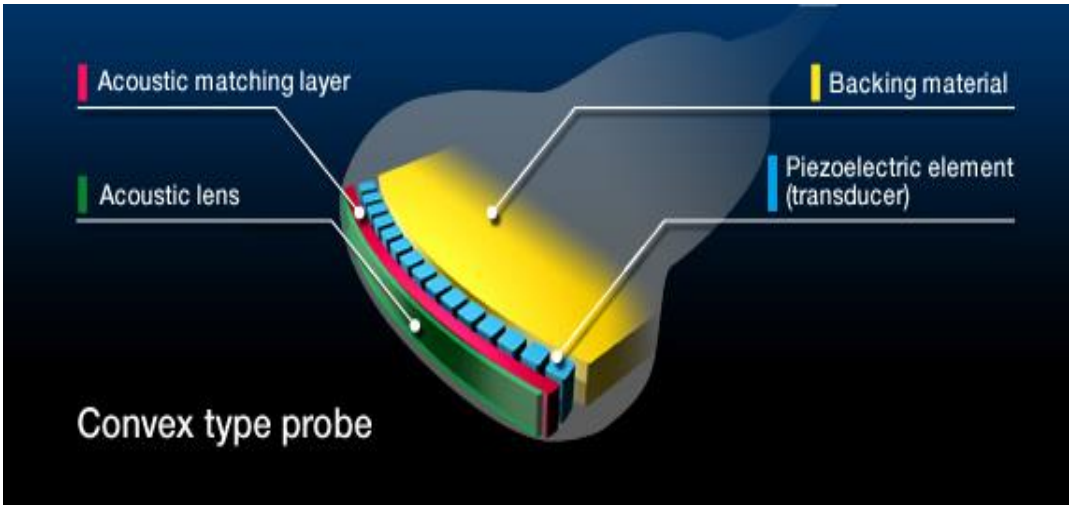

Figure 2.5: Curvilinear transducer (NDK, 2019).

This type of transducer can scan at different angles and is designed for deeper imaging in the human body, such as the abdominal area. A convex probe uses a lower frequency in order to penetrate, and thus view, deeper within the body, Demer and Renfree, (2008). The ultrasonic array consists of many individual single elements and is controlled in groups. The array elements are incrementally switched on and off to generate pulse-echo signals.

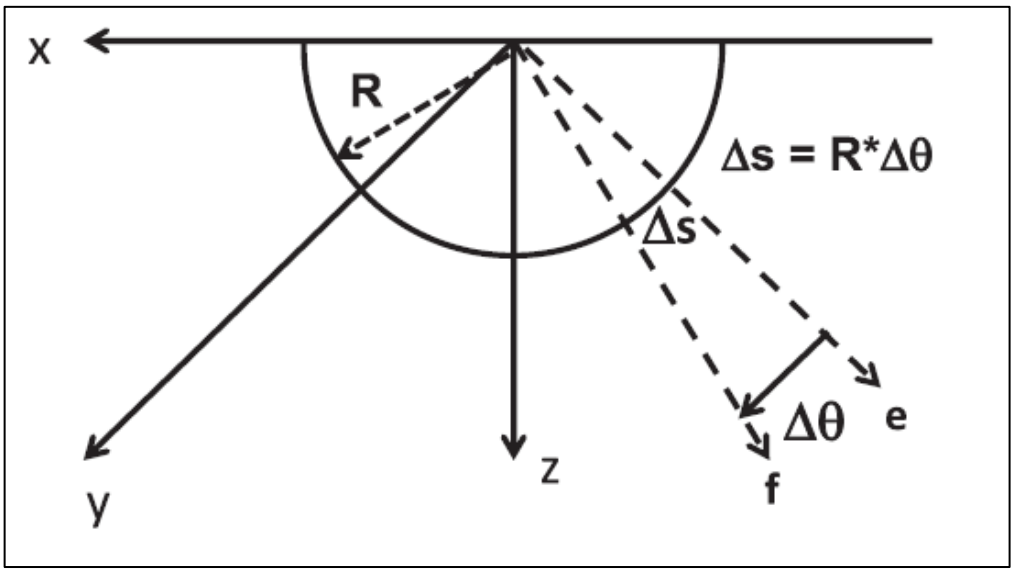

Figure 2.6: Scanning of the curvilinear transducer (Tomas, et al., 2013).

Figure 2.6 shows a simple system to demonstrate and understand the scanning method of the curvilinear transducer. The transducer scans in the $\boldsymbol{xz}$ plane. The acoustic beams

move incrementally by Δ**x** distance along the x-axis each time or at each position that the pulse-echo beam is created. An alternatively elements shift the beam angle by Δ**θ** and image in the $\boldsymbol{xz}$ plane. The array is situated on a curve with radius **R**, and line increments Δ**S**, along the curved surface:

$$\Delta \boldsymbol{S} = \boldsymbol{R} \times \Delta \boldsymbol{\theta} \tag{2.11}$$

The transducer scans from point $\boldsymbol{e}$ to point $\boldsymbol{f}$ as shown in Figure 2.6. At any time one element sends a beam and receives the reflected beam, the next element with an angle difference of $\Delta \boldsymbol{\theta}$ send a beam and receives echoes. Different types of transducer are used for various clinical imaging applications.

2.2.3 How Ultrasound Imaging Works

In the previous section, a brief explanation of the ultrasound wave and its characterization was given by Jens et al., (2013). The ultrasound wave propagates through the body and is partially reflected when it hits the interface, such as tissue or muscle, due to the difference in acoustic impedance given by Hamilton et al., (2004). The reflected wave spreads back to the tissue interface and is detected by the same transducer. The transducer records the time taken for the transmitted wave to arrive and be reflected back, Tomas, (2004). The time of flight (TOF) is given by Equation 2.12:

$$\mathbf{2d} = \mathbf{t} \times \mathbf{C} \tag{2.12}$$

Where **d** is the distance in metres (m), C is the ultrasound velocity in the medium, $\boldsymbol{t}$ is the time of flight (TOF) in seconds (s) through the medium, and the factor number **2** is the number of flights through medium since the signal travels back to the transducer. In some cases, the reflection of sound is minimal due to the similarity in tissue impedances. In medical imaging, a specific transducer with a particular frequency is used to image different organs. A lower frequency is used to penetrate deeper organs and vice versa.

$$\boldsymbol{dB_{loss}} = \mathbf{10}\boldsymbol{Log_{10}}[\mathbf{4}\frac{\boldsymbol{Z_2 Z_1}}{(\boldsymbol{Z_2} + \boldsymbol{Z_1})^2}] \tag{2.13}$$

Where $\boldsymbol{Z_2}$ and $\boldsymbol{Z_1}$ are the acoustic impedance of material two and material one respectively.

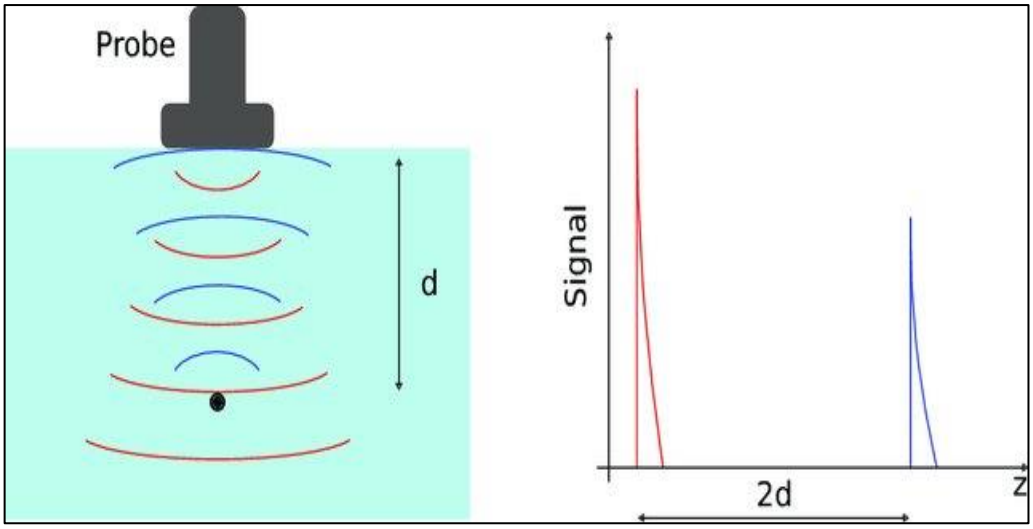

Figure 2.7: Principle of ultrasound imaging, (Stephane, 2016).

Figure 2.7 shows how ultrasound imaging works – the ultrasound beam is transmitted through the body by the transducer (probe). The sound wave is reflected from the interface of the object. The sensor records the time when the signal was transmitted and is also able to record the time when the signal is received back when it is reflected by the object.

Doppler ultrasound imaging measures the blood flow direction and speed of blood cells. When the blood cell moves the pitch of the reflected sound wave changes, ultrasound imaging is generally safe and painless, but if used for a long time, it may heat the tissue. The larger the tissue the more difficult it is to take an ultrasound image due to the attenuation issue. Ultrasound has difficulty in penetrating bone; therefore, is only able to see outside the bone not inside. Ultrasound is also not able to examine lungs, and currently, is not able to tell whether a tumour is cancerous or not, Wells, P et al., (1988).

2.3 Colloids

The colloid is an entity of the system and having the length scale between (1–1000) nm e.g. milk, muddy water. It is a mixture in which one substance, such as nanoparticles, is dispersed through a second substance, Booth and Enderby, (1952). The positive and negative ions form a charge cloud and the ions tend to approach the particle surface for neutralization, Dukhin and Goetz (2002). In a colloid, the surface property of the particle

is fundamental. The ratio of surface area to the volume of the particles increases as the particle diameter is reduced, Albert et a., (1980).

$$\frac{\boldsymbol{A}}{\boldsymbol{V}} = \frac{\mathbf{1}}{\boldsymbol{R}} \tag{2.14}$$

Where $\frac{\boldsymbol{A}}{\boldsymbol{V}}$ is the ratio of surface area to volume, and $\boldsymbol{R}$ is the particle radius.

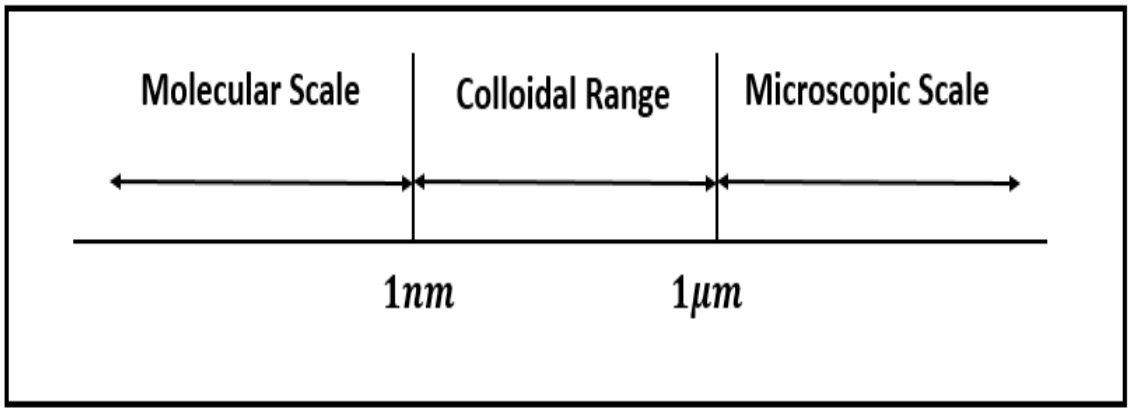

Figure 2.8: Range of colloidal phenomena (Cosgrove, 2010).

This section only demonstrates the most relevant in relation to the research area. The most relevant here are: double layer (DL), particle diameter, zeta potential and surface area of the particles, along with all the external forces in the colloid, such as drag force, pressure force, attractive and repulsive force. All these properties are related to CVP imaging in colloids.

2.3.1 Double Layer (DL)

Particles In a colloidal suspension carry charges and the cloud of charged ions tends to surround the particle surface for neutralization. These charges create two layers surrounding the particles and this is called the *double layer* (DL).

In a colloid, when two particles approach each other, their electrical DL will start to overlap, and this results in a repulsive force. The expression for this repulsive force was given by Derjagum et al., (2007) and is noted below:

$$\boldsymbol{V_R} = \frac{\mathbf{128}\boldsymbol{\pi a_1 a_2 nkT}}{(\boldsymbol{a_1} + \boldsymbol{a_2})^2 \boldsymbol{K^2}} \boldsymbol{\gamma_1 \gamma_2 e^{(-Kh)}} \tag{2.15}$$

Where $\boldsymbol{h}$ is the surface separation, $\boldsymbol{a}$ is the particles radius, $\boldsymbol{K}$ is the Debye-Huckel length, $\boldsymbol{n}$ is the bulk density of ions, and $\boldsymbol{\gamma}$ and is the surface potential.

Where:

$$\gamma = tanh\left(\frac{ze\psi}{4kT}\right)$$

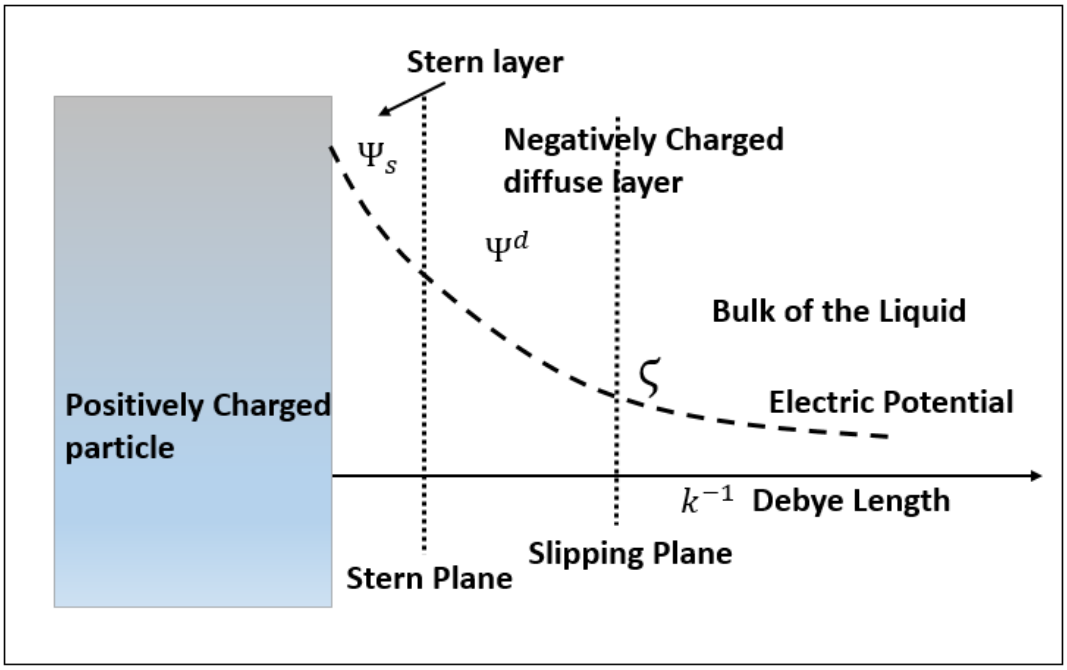

Figure 2.9: The structure of the electrical double layer (Dukhin and Goetz, 2002).

These equations are only valid when $\boldsymbol{h << a}$. Deryaguin expression gives a better result for larger particles. The vibration of particles in the colloid causes the distortion of the DL and the expression for this DL force was presented by Bowen and Jenner, (1996):

$$\boldsymbol{F_{DL} = -\frac{1}{3}S_{\beta}(D)n^{o}KT\left(cosh\left(\frac{ze\psi_{\beta}(D)}{KT}\right) - 1\right)} \qquad (2.16)$$

Where $\boldsymbol{S_{\beta}(D)}$ is the surface area of the spherical cell around the particle, $\boldsymbol{n^o}$ is the ion number concentration, $\boldsymbol{K}$ is Boltzmann's constant, $\boldsymbol{T}$ is the absolute temperature $\boldsymbol{z}$ is the valence of the ions, $\boldsymbol{e}$ is the elementary charge, and $\boldsymbol{\psi_{\beta}(D)}$ is the potential of the surface of the spherical cell.

2.3.2 Zeta Potential (z-potential)

The electrical potential between the diffuse layer and the Stern layer in a colloid dispersion is called the *zeta potential*. It has a vital role in controlling the stability of the

solution, Robert et al., (1981). It is the boundary between the moving particle and the suspending fluid and is crucial because it is related to particle mobility. The significant values to determine if the dispersion is either stable or unstable are +30 mV or –30 mV with respect to human body fluid, Hus et al., (2000). The system is deemed to be stable if the value of the zeta potential exceeds these values, i.e. if it is more positive than +30 mV or more negative than –30 mV , Ohshima, (2009).

$$\Delta\boldsymbol{\psi}(\boldsymbol{r}) = -\frac{\boldsymbol{\rho}(\boldsymbol{r})}{\in_{\boldsymbol{r}}\in_{\boldsymbol{0}}} \tag{2.17}$$

Where Δ is a Laplacian operator, $\boldsymbol{\rho}(\boldsymbol{r})$ is the density of the free charge at position **r** in the electrolyte, $\in_{\boldsymbol{r}}\in_{\boldsymbol{0}}$ are the relative permittivity of the electrolyte and a vacuum. Boltzmann's Law for the distribution of electrolyte ions is given by, Sven and Michal, (1999):

$$\boldsymbol{\rho}(\boldsymbol{r}) = \boldsymbol{ze}\{\boldsymbol{n}(\boldsymbol{r})\} = \boldsymbol{2zen\ sinh}\left\{\frac{\boldsymbol{ze\psi}(\boldsymbol{r})}{\boldsymbol{KT}}\right\} \tag{2.18}$$

Where $\boldsymbol{n}$ the bulk concentration is $\boldsymbol{k}$ is the Debye–Hückel parameter. The potential distributions are explained by, Dukhin and Goetz (2002) for flat surfaces, spherical surfaces and soft particles.

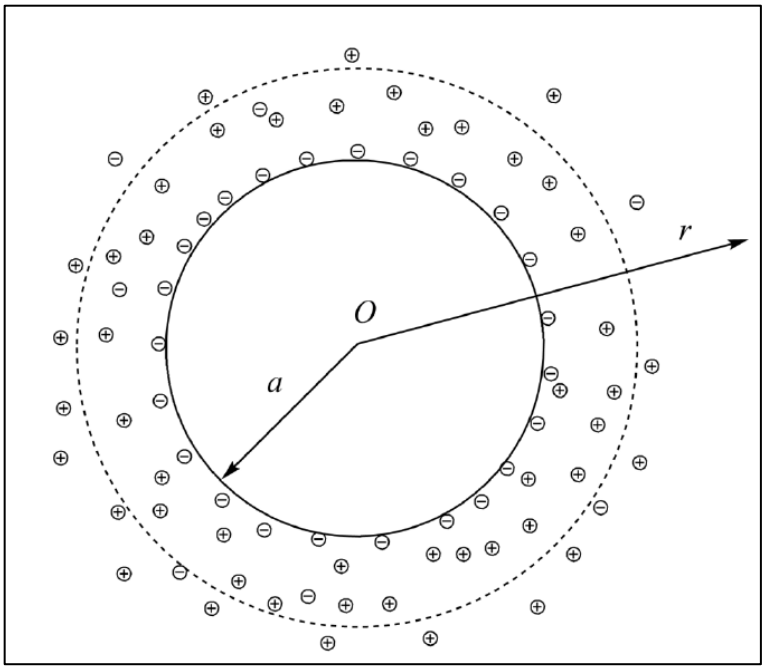

Figure 2.10: Particles spherical surface with a radius **r** (Ohshima, 2005).

The general analytical solution for potential is $\boldsymbol{\psi \ll \frac{RT}{F} = 25.8mv}$ and is called the Debye–Hückel approximation. This is valid for any value of $\boldsymbol{ka}$ and yields the following approximations:

$$\boldsymbol{\psi(r) = \frac{\psi^d a}{r} e^{(-k(r-a)}} \tag{2.19}$$

The relationship between the diffuse and the stern potential becomes:

$$\boldsymbol{\sigma^d - \varepsilon_o \varepsilon_m k \psi^d (1 + \frac{1}{ka})} \tag{2.20}$$

For a thin layer, $\boldsymbol{ka > 1}$ and for a thick layer, $\boldsymbol{ka < 1}$.

Let us now calculate the surface charge density as a function of surface potential.

The surface charge density $\boldsymbol{\sigma}$ given by:

$$\boldsymbol{\sigma = \frac{q}{A}} \tag{2.21}$$

Where, **A** denotes the surface area of the particle, and $\boldsymbol{q}$ is the charge on the particle. From Poisson's equation:

$$\boldsymbol{\frac{d^2\psi}{dx^2} = -\frac{\rho}{\varepsilon}} \tag{2.22}$$

The net charge per unit area is $\boldsymbol{\int_0^\infty \rho dx}$

$$\boldsymbol{\sigma + \int_0^\infty \rho dx = 0} \tag{2.23}$$

From Equation 2.22 and Equation 2.23 we get:

$$\boldsymbol{\sigma = -\int_0^\infty \rho dx \leftrightarrow \sigma = -\int_0^\infty -\varepsilon \frac{d^2\psi}{dx^2} dx} \tag{2.24}$$

$$\boldsymbol{\sigma = \varepsilon \int_0^\infty \frac{d^2\psi}{dx^2} dx}$$

The potential decays exponentially as a function of particle diameter, Yanlin (2012). The electric potential arises due to the polarization of cations and anions, and in the case of stability, the summation of these potentials is zero. The surface charge density is a function of surface area. The effect of surface area and the volume on the UVP signal will be discussed later in Chapter 5 section 5.7.

2.3.3 A measurement principles of zeta potential and particle size using dynamic light scattering

*Particle size measurement

Dynamic light scattering (DLS) is a technique in engineering used to determine the particle size distribution in a suspension. This method is based on the Brownian motion. When particles suspended in liquid, they move randomly in all directions. Dynamic light scattering measures the Brownian motion and this related to the size of particle, small particles diffuse rapidly and large particles diffuse slowly. The velocity of Brownian motion is defined by the translational diffusion coefficient (D). A laser with a single frequency is directed into the suspension, the incident laser is scattered in all directions due to the presence of particles in the suspension. The scattered light detect with a certain angle over a time. The translational diffusion coefficient can be converted into a particle size using the Stokes-Einstein equation. According to the Stokes-Einstein theory of Brownian motion, the diffusion coefficient can be used to determine the particle size, Setefield et al., (2016).

$$D = \frac{KT}{6\pi\eta a} \tag{2.25}$$

Where, K is the Boltzmann's constant, T is the absolute temperature, η is the viscosity, and D is the diffusion coefficient.

*Zeta potential measurement

When charged nanoparticles suspended in the liquid, the cloud ions surrounding the particles with opposite charge. In principle, of zeta potential measurements, an electric field is applied into the suspension, charged particles move due to the interactions between the charged particle and the electric field. The velocity of the motion is a function of electric field strength, and the suspending medium. The particle velocity is measured by the scattering light. Since the particles are moving the scattering light measured at certain angle θ and particle velocity is measured from the frequency shift. The mobility is measured which is the ratio of velocity to the electric field.

$$\mu = \frac{\lambda f_d}{E.\sin(\theta/2)} \tag{2.26}$$

Zeta potential is then measured using Smoluchwski model.

$$\zeta = \frac{\eta\mu}{\varepsilon f(ka)}$$

Where ζ -zeta potential, μ -Electrical mobility, E -Electric field strength, ε-solvent dielectric constant, η-solvent viscosity, $f(ka)$-Henry coefficient.

Colloidal Dynamics introduces a ZetaProbe and AcousticSizer to allow the direct measurement of particle size and zeta potential in concentrated suspensions. The advantage of these devices over the dynamic light scattering is that they can measure the size and zeta without dilution. The dilution takes time and can lead to an error in the zeta potential measurement due to changes in concentration of the electrolyte background. In this method the high electric field is applied to the suspension and the ultrasound signal generated by the motion of charged particles in the alternated electric field. The electroacoustic technique combined with the measurement of ultrasound attenuation to determine the zeta potential and the particle size, Colloid Dynamics., (2019).

Ultrasound vibration potential (UVP) is an electric signal generated from the vibration of particles or ions along the trajectory of the ultrasound pulses travelling through a colloidal suspension or ionic electrolyte. When the ultrasound pulses travel through colloidal suspensions, particles and cloud ions vibrate in different rate due to the difference in their masses, and this polarization of charges create a number of dipoles, summing these dipoles measured as a colloid vibration potential. Therefore, CVP may be used to characterize or image the physiochemical property of particles or ions. This method dilution not required and particle size and zeta potential can be measured with the highest concentration of 50%.

2.3.4 Particles in a Colloidal Suspension

When an ultrasound wave is applied to a colloidal suspension signal attenuation arises due to the effects of absorption and scattering. This absorption and scattering effect is explained in Section 2.2.1. In ultrasound, both methods can be analysed using the frequency explained by Dukhin and Goetz, (2002). In this research, the nanoparticles are suspended in a colloidal system and the absorption and scattering process is discussed briefly. The force acting on this volume of a particle is proportional to the gradient pressure of the sound wave, ∇P. The balance of these forces is represented in the following equations introduced by Dukhin and Goetz (2002):

$$-\boldsymbol{\varphi}\boldsymbol{\nabla P} = \boldsymbol{\varphi}\boldsymbol{\rho_P}\frac{\boldsymbol{\partial u_p}}{\boldsymbol{\partial t}} + \boldsymbol{\gamma}(\boldsymbol{u_p} - \boldsymbol{u_m}) \tag{2.28}$$

$$-(\mathbf{1}-\boldsymbol{\varphi})\boldsymbol{\nabla P} = (\mathbf{1}-\boldsymbol{\varphi})\boldsymbol{\rho_o}\frac{\boldsymbol{\partial u_o}}{\boldsymbol{\partial t}} + \boldsymbol{\gamma}(\boldsymbol{u_p} - \boldsymbol{u_o}) \tag{2.29}$$

$$\boldsymbol{\gamma} = \frac{\mathbf{9}\eta\boldsymbol{\varphi}'\Omega}{\mathbf{2}\boldsymbol{a^2}} \tag{2.30}$$

$$\boldsymbol{F_d} = \mathbf{6}\boldsymbol{\pi}\eta\boldsymbol{a}'\Omega(\boldsymbol{u_p} - \boldsymbol{u_m}) \tag{2.31}$$

Where $\boldsymbol{\eta}$ is the dynamic viscosity, and $\boldsymbol{a}$ is the particle radius, $\mathbf{u_p}$ **and** $\mathbf{u_m}$ are the velocity of the particle and the medium, and $\boldsymbol{\gamma}$ is the friction coefficient and is proportional to the volume fraction and particle hydrodynamic coefficient $\boldsymbol{\Omega}$.

Both Equation 2.30 and Equation 2.31 refer to the coupled phase model. The equation can be solved for the speed of a particle relative to the fluid/liquid and is given by presenting a monochromatic wave:

$$\Psi(\boldsymbol{x},\boldsymbol{t}) = \boldsymbol{A}\boldsymbol{e}^{\boldsymbol{j}(\boldsymbol{\omega t}-\boldsymbol{kx})}$$

Where $\mathbf{j}$ is a complex number and $\boldsymbol{k}$ is the compression complex number, and $\boldsymbol{A}$ is the amplitude.

$$\boldsymbol{\gamma}\left(\boldsymbol{u_p} - \boldsymbol{u_m}\right) = \frac{(\boldsymbol{\rho_p} - \boldsymbol{\rho_s})}{\boldsymbol{\rho_s} + \boldsymbol{j\omega\varphi}(\mathbf{1}-\boldsymbol{\varphi})\dfrac{\boldsymbol{\rho_p}\boldsymbol{\rho_m}}{\boldsymbol{\gamma}}}\boldsymbol{\nabla P} \tag{2.32}$$

Where $\boldsymbol{\rho_s} = \boldsymbol{\varphi}\boldsymbol{\rho_p} + (\mathbf{1}-\boldsymbol{\varphi})\boldsymbol{\rho_m}$ and $\boldsymbol{\varphi}$ is the volume fraction of the particles.

Ultrasound propagation corresponds to the second case due to the movement of the particles. The relative speed of the particles and the liquid are considered. The balance of forces acting on the colloidal suspension consist of drag force, gravity force, pressure force and an attractive force. In the case of small particles < 100 nm, the lift force and the gravity force cancel each other out.

The interaction between particles can make the force one of attraction or of repulsion. Colloid interaction becomes less critical as particle size increases, Nguyen, (2009). The forces acting on the nanoparticle suspension are: $\boldsymbol{F_A}$ – an attractive force (lift force) holding the particle together; $\boldsymbol{F_D}$ – fluid drag caused by flow parallel to the surface; and $\boldsymbol{F_g}$ – gravitational attraction acting in opposition to the lift force, Tharwat, (2013).

$$\sum \boldsymbol{F} = \boldsymbol{m}\frac{\boldsymbol{dV}}{\boldsymbol{dt}} \tag{2.33}$$

Where $\boldsymbol{m}$ is the mass, $\boldsymbol{V}$ (velocity) is the derivative of diplacement, and $\boldsymbol{t}$ is the time. The total forces in colloidal dispersion given by :

$$\sum \boldsymbol{F} = \boldsymbol{F_A} + \boldsymbol{F_P} + (-\boldsymbol{F_d}) + \boldsymbol{F_g} \tag{2.34}$$

Where the density $\boldsymbol{\rho}$ is the mass per unit volume If we have a cubic area $\boldsymbol{dA}$ and height $\boldsymbol{dZ}$, then:

$$\boldsymbol{a} = -\frac{\mathbf{1}}{\boldsymbol{\rho}}\frac{\boldsymbol{dP}}{\boldsymbol{dZ}} = -\frac{\mathbf{1}}{\boldsymbol{\rho}}\boldsymbol{\nabla P} \tag{2.35}$$

In a harmonic oscillation:

$$\boldsymbol{y(x,t)} = \boldsymbol{Asin(\omega t - kx)} \tag{2.36}$$

Amplitude as a particle displacement: $\boldsymbol{A} = \frac{\boldsymbol{P}}{\boldsymbol{2\pi\rho c}}$

$$\boldsymbol{P} = \boldsymbol{2\pi A\rho c} \tag{2.37}$$

Where $\boldsymbol{\rho}$ is the density of the particle and **C** is the speed of the acceleration**.** Different forces is affect the motion of the particle within the medium. The most important forces are the pressure force and the drag force, Arup (2019). The force on a small sphere moving through a viscous liquid can be given by:

$$\boldsymbol{F_d} = \boldsymbol{3\pi\gamma vr} \tag{2.38}$$

Where $\boldsymbol{v}$ is the particle velocity, $\boldsymbol{u}$ is the fluid velocity, **r** is the particle radius, and $\boldsymbol{\gamma}$ is the fluid viscosity.

$$\frac{\boldsymbol{mdv}}{\boldsymbol{dt}} = \frac{\boldsymbol{6\pi\gamma r}}{\boldsymbol{C_D}}(\boldsymbol{u} - \boldsymbol{v}) + \sum_{\boldsymbol{i}} \boldsymbol{F_i} \tag{2.39}$$

$\sum_{\boldsymbol{i}} \boldsymbol{F_i}$ is the external forces.

Several main forces come into play to maintain the colloidal stability. The force is induced from the dipole moment of the neighbouring dipoles called *Van der Waals force*. The dispersion forces acting between the colloid objects, and the attractive force between two colloid objects can be given by:

$$\boldsymbol{F_A} = \frac{\boldsymbol{A}}{\boldsymbol{12D^2}} \tag{2.40}$$

$\boldsymbol{A}$ is the Hamaker constant = $\boldsymbol{8.3 \times 10^{-21}}$ **joules** and $\boldsymbol{D}$ is the separation of the two surfaces.

The electric force exerting between two electrical points can be given by Coulomb's law, Kovacs, (2001):

$$F = \frac{q_1 q_2}{4\pi r^2 \varepsilon} \tag{2.41}$$

Where r is the distance between two charges. The drag force by the liquid on a moving particle is given by:

$$F_D = \frac{1}{2}\rho v^2 A\alpha \tag{2.42}$$

Where ρ is the density of the fluid, A is the surface area, v is the velocity of the particle and, $\propto$ is the drag coefficient. For this research, we assume that we have a colloid containing spherical nanoparticles with a low concentration of 1wt%, and the distance between particles are much greater than the particle size, and particles can be treated as isolated from one another, hence, for simple understanding we assume that, the particle-particle interaction can be ignored.

2.4 Sound Wave in a Colloidal System

In general, when a sound wave propagates through a colloidal system, the interaction of the sound wave with the colloids can be explained by six different mechanisms, Clarke, (1981).

1. Viscous mechanism: when ultrasound wave travels through a colloid the particles vibrate and a shear wave is produced. The difference in volume fraction, charge, and the densities of these particles plays an important role in understanding the movement of the particles within the medium. The shear stress resulted in energy loss due to the friction effect, and it influences the electro-kinetic effects.

2. A temperature gradient occurs near the particle surface and it may cause dissipation and dominate the attenuation, however, the attenuation is too small.

3. The wave can be redirected e.g. scattered, and this mechanism is similar to the behaviour of light. There would be no dissipation of acoustic energy.

4. Another mechanism for loss of acoustic energy is the interaction of the wave with the particles and other materials within the medium. This is called the intrinsic mechanism.

5. The primary mechanism is that the particles combine together in network formations. This results in a loss of sound energy and wave oscillation under the sound pressure.

6. The electro-kinetic effect is the most significant feature, and this is the interaction between a sound wave and the DL of the particles in the colloid. This mechanism is essential for describing the physicochemical feature characterization of nanoparticle and ionic electrolyte in colloids. This mechanism is to create the so-called ultrasound vibration potential (UVP), Barisik et al., (2014).

The term ‘scattered’ is meaning the separation or going in different directions. The term ‘absorption’ is means taking in but not reflecting back. The above mechanisms happen during ultrasound propagation in colloidal suspensions, Carbo and Molero, (2002).

2.5 Ultrasound Vibration Potential Theory and Experiment

UVP is an electrical signal generated when a powerful sound wave is applied to a colloidal suspension or to ionic electrolytes. When a high-pressure ultrasound is applied to an ionic electrolyte the motion of anions and cations are different due to the difference in their masses and this generates an electric potential called IVP, (Beveridge et al., (2004). A similar phenomenon happens in colloidal suspensions, but the colloidal particles are much larger and carry higher charges than electrolyte ions so the CVP signal is much larger than the IVP signal. This method can be used for tissue imaging, Gusev and Diebold, (2004). In the following sections, I will try to present some of the theoretical and experimental literature around UVP.

2.5.1 Ion Vibration Potential (IVP)

The concept of IVP for electrolytes originally dates back to Debye (1933). His method introduced an ultrasound wave into an ionic solution and then measured the potential difference created within the solution. Hermans (1938) demonstrated that Debye’s equation had a disadvantage when the density of the ions and the solution are the same, and the expression for the potential is not zero, Marlow and Fairhurst, (1987).

$$\boldsymbol{e_j X - j(v_j - v_o) = m_j \frac{dv_k}{dt}} \tag{2.43}$$

Equation 2.44 is the equation of motion presented by Hermans (1938). Where the electric field $\mathbf{X}$ confirms Poisson’s expression, $\mathbf{X = 4\pi S/D.}$ Where, $\mathbf{S}$ is the charge density, $\boldsymbol{e_j}$ is the charge, $\boldsymbol{m_j}$ is the mass and $\boldsymbol{v_j}$ is the velocity of the ion in the ultrasonic field and $\boldsymbol{v_o}$ is the solvent velocity. Later, Bugosh et al., (1947) modified Debye’s equation which states that the sum of the forces acting on particles within solutions must be equal to the mass and its acceleration.

$$\boldsymbol{e_j X - \rho_j(v_j - v_o) - e_j \left\{ \frac{|e_1 e_2| q_K X}{(3DkT)\left[1 + \sqrt{q(1 + i\omega\theta)^{\frac{1}{2}}}\right]} \right\}} \\ \boldsymbol{- \frac{e_j X \rho_j}{6\pi\eta_o} - \frac{kT}{n_j}\frac{\partial n_j}{\partial x} + V_j s_o \frac{dv_o}{dt} = m_j \frac{dv_k}{dt}} \tag{2.44}$$

The first term in Equation 2.44 represents the force associated with an electrical ion, **j**, with a charge of $\boldsymbol{e_j}$, the second term is the frictional force with a coefficient of $\boldsymbol{\rho_j}$ multiplied by the velocity difference between the ions and the solvent $(\boldsymbol{v_j - v_o})$. The relaxation force is represented in the third term, with angular frequency $\boldsymbol{\omega}$ of the oscillation field, $\boldsymbol{k}$ is Boltzmann's constant, $\boldsymbol{D}$ is the dielectric constant of the solvent, and $\boldsymbol{T}$ is the absolute temperature. The fourth term represents the electrophoretic force.

In 1967 Zana and Yeager presented their experimental work on ionic electrolytes. In this work they found that the IVP signal increases as a function of molecular weight by Zana and Yeager, (1967). They presented the solution for two types of ions, ion 1 and ion 2:

$$\boldsymbol{q} = \left(\frac{\boldsymbol{e_1}}{\boldsymbol{\rho_1}} - \frac{\boldsymbol{e_2}}{\boldsymbol{\rho_2}}\right)\left[(\boldsymbol{e_1} - \boldsymbol{e_2})\left(\frac{\mathbf{1}}{\boldsymbol{\rho_1}} + \frac{\mathbf{1}}{\boldsymbol{\rho_2}}\right)\right]^{-\mathbf{1}} \tag{2.45}$$

The final equation for alternating potential $\boldsymbol{\varphi}$ at any point given by:

$$\boldsymbol{\varphi = \varphi_o e^{[i(\omega\tau - \sigma x - \Delta)]}} \tag{2.46}$$

Where

$$\boldsymbol{\varphi_o} = \left[\frac{\sum \boldsymbol{n_j e_j(\omega_i - d)/\rho_j}}{\sum \boldsymbol{n_j e_j\, e_j/\rho_j}}\right]\sqrt{\left[\frac{(\mathbf{4\pi L_\infty})^2}{(\mathbf{4\pi L_\infty})^2 + (\boldsymbol{\omega D_\omega})^2}\right]}$$

$$\Delta = \boldsymbol{arc}\,\mathbf{tan}\,\frac{\boldsymbol{\omega D_\omega}}{\mathbf{4\pi L_\infty}}$$

$$\boldsymbol{\omega_j = m_j - v_j s_o}$$

$$\boldsymbol{d = kT/C^2}$$

The IVP was detected for a number of 1:1 ionic electrolytes (**e.g.** $\boldsymbol{LiOH, NaOH, KOH}$), and 1:2 ionic electrolytes (**e.g.** $\boldsymbol{Li_2SO_4, Na_2SO_4, K_2SO_4}$) and 2:1 ionic electrolytes (**e.g.** $\boldsymbol{MgCl_2, CaCl_2, SrCl_2, BaCl_2}$). The full explanation of their experimental procedure is given in their article.

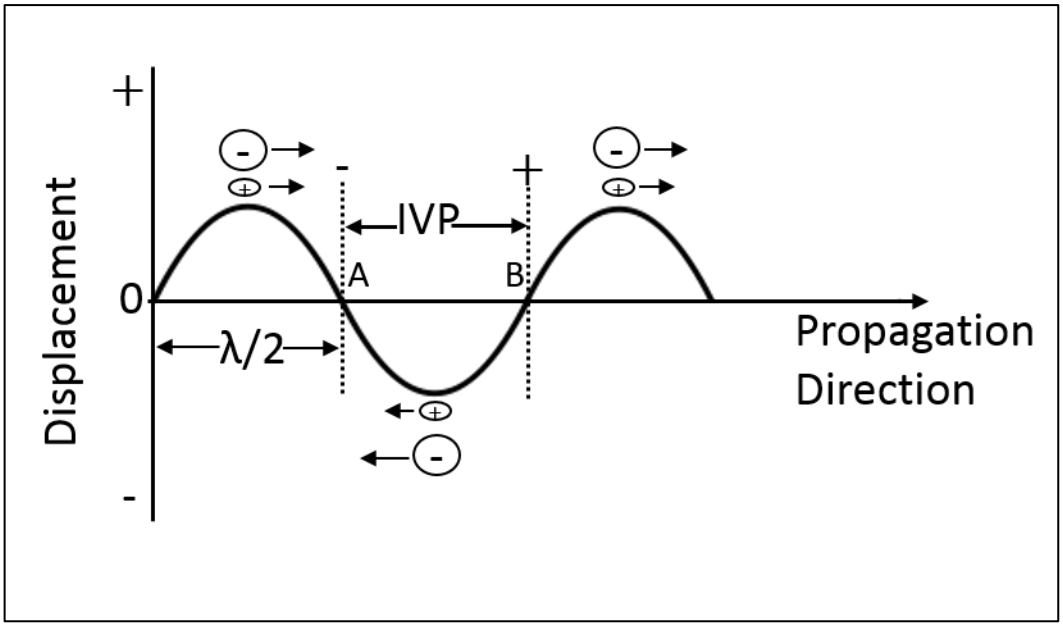

Figure 2.11: The relative movement of the anions and cations (Marlow and Fairhurst, 1988).

Figure 2.11 shows the principle of IVP signal generation. Dukhin and Goetz (2002) developed the original ion vibration current (IVI) theory. The system contains N electrolyte species, and for the ultrasound propagate in x-direction defined as a 2N+1 system by Dukhin and Goetz (2002), and this explained in equation 2.47.

The basis of their theory is that a system of $(\boldsymbol{2N+1})$ equations, can be used to characterize the electro-diffusion effects that occur when the longitudinal wave is travelling along the x-axis, and can be given by Booth and Enderby, (1952):

$$\boldsymbol{ez_jE-\gamma_j(u_j-u_m)-\frac{qkEez_j}{3\varepsilon_mKT\left[1+\sqrt{\frac{j\omega}{\omega_{MW}}}\right]}-\frac{ez_jkE}{6\pi^{\eta}}-v_j\rho_m\frac{d\rho_m}{dt}=m_j\frac{dv_j}{dt}} \quad (2.47)$$

Equation 2.47:

$\boldsymbol{ez_jE}$ is electroacoustic term, $\boldsymbol{\gamma_j(u_j-u_m)}$ is friction term, $\frac{qkEez_j}{3\varepsilon_mKT\left[1+\sqrt{\frac{j\omega}{\omega_{MW}}}\right]}$

Is relaxation term, $\frac{ez_jkE}{6\pi^{\eta}}$ is electrophoretic term, $\boldsymbol{v_j\rho_m}\ \frac{d\rho_m}{dt}$ is pressure term, and

$\boldsymbol{m_j}\frac{dv_j}{dt}$ Is reaction term.

Where **e** is the electric charge of an electron $-\boldsymbol{k}$ is Boltzmann constant, $\boldsymbol{n}$-is ion concentration, the index $\boldsymbol{i}$ is species the ion species $\boldsymbol{z}$ is the ion valance, $\boldsymbol{u}$ is the ion

velocity, $\boldsymbol{E}$ electric field strength, $\boldsymbol{v}$ and $\boldsymbol{m}$ are the volume and mass respectively of the solvent ion and $\boldsymbol{q}$ is the parameter of the relaxation force.

IVI depends on the concentration of the electrolyte because of changes in the Maxwell-Wagner frequency, Hosseini et al., (2015), and this could be a potential to the conductivity of the media $\boldsymbol{K_m}$. The IVI is the linear function of frequencies that exceed the Maxwell-Wagner frequency, and the IVP becomes independent on the electrolyte concentration.

2.5.2 Colloid Vibration Potential (CVP)

The first report on CVP was made by Hermans (1938). Hermans stated that when an ultrasonic wave travels through a suspension of spherical particles, the particles lag behind the solvent and a dipole moment is created. Summing these dipoles for all dipoles gives a potential between nodes and antinodes. In 1952 a theory was developed for CVP by. There have been many theories and experimental work conducted in the past explaining the generation of electrical potential in colloidal suspensions, but here I would like to present the well-known argument made by, O'Brien, (2006).

$$\boldsymbol{\mu_d = \frac{ESA(\omega)\rho_m}{A(\omega)F(z_t - z_s)\varphi(\rho_p - \rho_m)}} \tag{2.50}$$

ESA is the electro-sonic amplitude.

$\boldsymbol{A(\omega)}$ is the instrument constant founded by calibration.

$\boldsymbol{F(z_t - z_s)}$ Is the function of the acoustic impedance of the transducer.

A similar expression can be used for colloid vibration current (CVI):

$$\boldsymbol{\mu_d = \frac{CVI(\omega)\rho_m}{A(\omega)F(z_t - z_s)\varphi(\rho_p - \rho_m)}} \tag{2.51}$$

$$\boldsymbol{\omega = k^2 D_{eff} = \frac{k_m}{\varepsilon_0 \varepsilon_m}} \tag{2.52}$$

Where $\boldsymbol{\varepsilon_0 \varepsilon_m}$ are the dielectric permittivity of the vacuum and medium respectively.

$\boldsymbol{K_m}$ is the conductivity of the medium.

And, the molar mass is given by:

$$\boldsymbol{W = N_A(m - \rho_m v)} \tag{2.53}$$

$$\boldsymbol{-\varphi \nabla P = \varphi \rho_p \frac{du_p}{dt} + \gamma(u_p - u_m)} \quad \text{[for particles]} \tag{2.54}$$

$$-(\mathbf{1}-\boldsymbol{\varphi})\boldsymbol{\nabla P}=(\mathbf{1}-\boldsymbol{\varphi})\boldsymbol{\rho_0}\frac{\boldsymbol{du_0}}{\boldsymbol{dt}}+\boldsymbol{\gamma}(\boldsymbol{u_p}-\boldsymbol{u_0})\quad\text{[for liquids]}$$

The above two equations together are generally referred to as the coupled phase model.

Where $\boldsymbol{\rho_s}=\boldsymbol{\varphi\rho_p}+\boldsymbol{\rho_m}-\boldsymbol{\varphi\rho_m}$

$$-\boldsymbol{\gamma}(\boldsymbol{u_p}-\boldsymbol{u_m})=\boldsymbol{\varphi\rho_p}\frac{\boldsymbol{du_p}}{\boldsymbol{dt}}+\boldsymbol{\varphi\nabla P} \tag{2.55}$$

$$\boldsymbol{\gamma}(\boldsymbol{u_p}-\boldsymbol{u_m})=\frac{\boldsymbol{\varphi}(\boldsymbol{\rho_p}-\boldsymbol{\rho_s})}{\boldsymbol{\rho_s}+\boldsymbol{i\omega\varphi}(\mathbf{1}-\boldsymbol{\varphi})\frac{\boldsymbol{\rho_p\rho_m}}{\boldsymbol{\gamma}}}\boldsymbol{\nabla P} \tag{2.56}$$

Where $\boldsymbol{\gamma}=\frac{\mathbf{9}\boldsymbol{\varphi}^{\eta}\Omega}{\mathbf{2}\boldsymbol{a^2}}$

If $\boldsymbol{\omega}\rightarrow\mathbf{0}$, then:

$$\boldsymbol{\nabla P_{rel}}=\frac{\boldsymbol{\varphi}(\boldsymbol{\rho_p}-\boldsymbol{\rho_s})}{\boldsymbol{\rho_s}}\boldsymbol{\nabla P} \tag{2.57}$$

The conductivity of the system $\boldsymbol{K_s}$ is given by:

$$\boldsymbol{K_s}=\frac{\boldsymbol{CVI}}{\boldsymbol{CVP}}$$

$$\boldsymbol{CVI_{\omega\rightarrow 0}}=\boldsymbol{CVP}*\boldsymbol{K_s}=\boldsymbol{\mu}\frac{\boldsymbol{\varphi}(\boldsymbol{\rho_p}-\boldsymbol{\rho_s})}{\boldsymbol{\rho_s}}\boldsymbol{\nabla P} \tag{2.58}$$

$$\boldsymbol{\mu}=\frac{\boldsymbol{\varepsilon_0\varepsilon_m c K_s}}{\boldsymbol{K_m}^{\eta}}$$

$$\frac{\boldsymbol{CVI_{\omega\rightarrow 0}}}{\boldsymbol{\nabla P}}=\boldsymbol{\mu}\frac{\boldsymbol{\varphi}(\boldsymbol{\rho_p}-\boldsymbol{\rho_s})}{\boldsymbol{\rho_s}}=\frac{\boldsymbol{\varepsilon_0\varepsilon_m c K_s}}{\boldsymbol{K_m}^{\eta}}\frac{\boldsymbol{\varphi}(\boldsymbol{\rho_p}-\boldsymbol{\rho_s})}{\boldsymbol{\rho_s}} \tag{2.59}$$

$$\boldsymbol{\mu_d}=\frac{\boldsymbol{\varepsilon_0\varepsilon_m c K_s}}{\boldsymbol{K_m}^{\eta}}\frac{(\boldsymbol{\rho_p}-\boldsymbol{\rho_s})\boldsymbol{\rho_m}}{(\boldsymbol{\rho_p}-\boldsymbol{\rho_m})\boldsymbol{\rho_s}} \tag{2.60}$$

$$\boldsymbol{\mu_d}=\frac{\boldsymbol{CVI}(\boldsymbol{\omega})\boldsymbol{\rho_m}}{\boldsymbol{A}(\boldsymbol{\omega})\boldsymbol{F}(\boldsymbol{z_t}-\boldsymbol{z_s})\boldsymbol{\varphi}(\boldsymbol{\rho_p}-\boldsymbol{\rho_m})} \tag{2.61}$$

$$\boldsymbol{CVP}=\boldsymbol{K_s}\frac{\boldsymbol{\varphi}(\boldsymbol{\rho_p}-\boldsymbol{\rho_s})}{\boldsymbol{K_s\rho_s}}\boldsymbol{\Delta P} \tag{2.62}$$

Where $\boldsymbol{K_s}$ is the conductivity, $\boldsymbol{\Delta P}$ is the pressure gradient, $\boldsymbol{\varphi}$ is the volume fraction and $(\boldsymbol{\rho_p}-\boldsymbol{\rho_s})$ is the difference between the particle and fluid densities. O'Brien's theory cannot account for concentrated systems or inter-particle interactions. O'Brien's

approaches applies the suspension principle for calculating the electro-acoustic signal of polydispersed colloids, Ohshimaa and Dukhin, (1999).

2.5.3 Methods of UVP Imaging

This section will present two models, the 2D Slab model, and the 3D Dipole model.

2D SLAB Model:

The first model (Slab Model) was presented by Brown University, Vitalyi and Diebold, (2005), and Wang et al., (2005). Nanoparticles in a colloid suspensions carry a charges and cloud ions with the opposite charge surround the particles. When the ultrasound pressure is applied to the solution the positive and negative charges are separated and create a dipole. The integration of these dipoles is measured as a UVP. This electric signal is given by:

$$\boldsymbol{E} = \frac{\emptyset \Delta \boldsymbol{\rho} \boldsymbol{\mu_E}}{\boldsymbol{\rho K^*}} \boldsymbol{\nabla P}(\boldsymbol{x}, \boldsymbol{y}, \boldsymbol{z}) \qquad (2.63)$$

where $\boldsymbol{E}$ represents the electric field produced by an ultrasound wave, $\emptyset$ is the volume fraction, $\boldsymbol{\rho}$ is the suspension density, $\Delta\boldsymbol{\rho}$ is the density difference between the liquid and the particles, $\boldsymbol{\mu_E}$ is the electrophoretic mobility, $\boldsymbol{K^*}$ is the complex conductivity, and $\boldsymbol{\nabla P}$ is the ultrasonic pressure gradient.

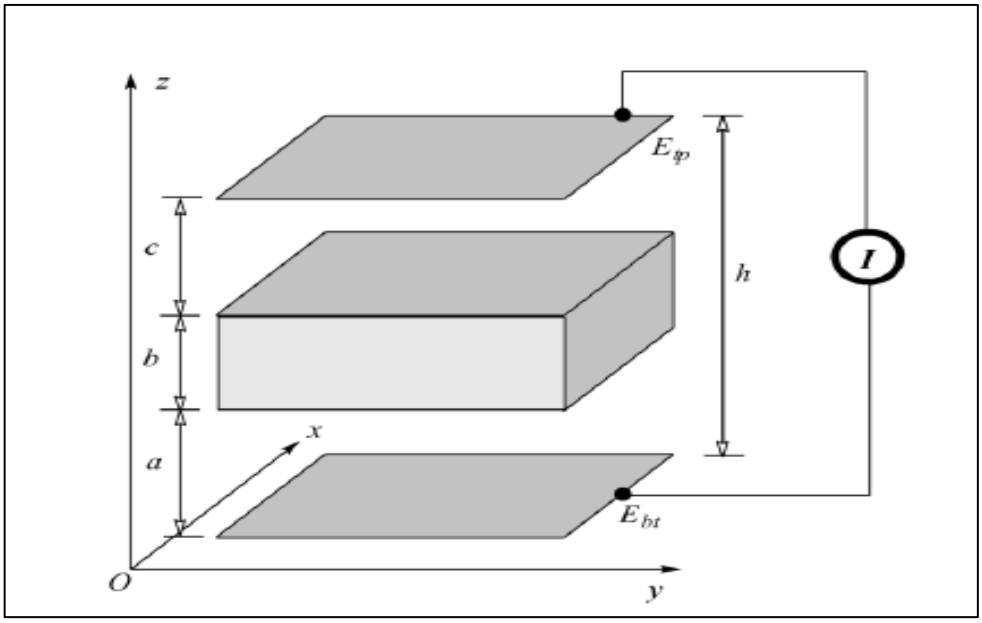

Figure 2.12: 2D Slab model (Wang et al., 2013).

Figure 2.12 shows the diagram of 2D slab model arrangements. This model is assumed that the plane ultrasound wave propagate through a domain **b** in **z**-direction. The domain composed with two layer of water. The two electrodes, $\boldsymbol{E_{bt}}$ bottom electrode and $\boldsymbol{E_{tp}}$ top electrode and a zero impedance current meter is used to measure the current flow produced by the medium **b** due to the presence of ultrasonic pressure gradient. The general form of the solution for the current density at any time given by:

$$\boldsymbol{J = -i\omega D = -\frac{i\omega}{h}\int_{z_1}^{z_2} \alpha \Delta \hat{P} dz} \qquad (2.64)$$

Where $\boldsymbol{D}$ is the electric field displacement, $\boldsymbol{J}$ is the current density, $\boldsymbol{\omega}$ is the angular frequency, $\boldsymbol{z}$ is the propagation direction and $\boldsymbol{h}$ is the separation distance between bottom and the top electrode, $\boldsymbol{\alpha}$ is the special distribution of the colloidal object, and $\boldsymbol{\Delta P}$ is the pressure gradient. In order for us to understand the effect of the number of ultrasonic wave periods that go through the medium, four different cases have been presented.

Case 1: It assumed that all wave periods are located inside the homogenous medium $\boldsymbol{b}$ (see Figure 2.13). The particular function of $\boldsymbol{\alpha}$ is treated as a constant.

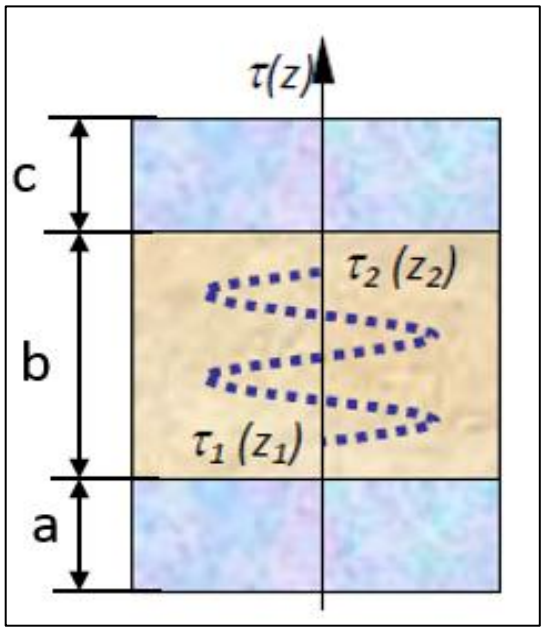

Figure 2. 13: 2D Slab model (Case 1) (Wang et al., 2013).

The UVP is zero when all periods are located inside the medium $\boldsymbol{b}$. The positive and negative charges cancel each other if the attenuation is ignored.

Case 2: It assumed that all pulse periods are across each boundary such as ***a*** and ***b*** or ***b*** and ***c*** the UVP signal is not zero.

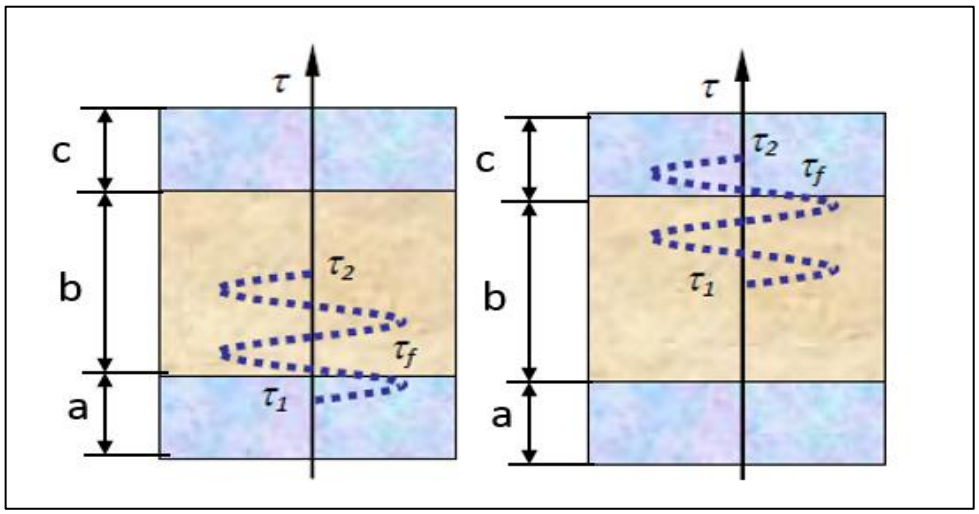

Figure 2.14: 2D Slab model (Case 2) (Wang et al., 2013).

In this case the UVP signal is not zero, and the current measured has a sinusoidal wave form, and has the opposite sign at the entrance and the exit to medium ***b***. The maximum values can be measured at $\boldsymbol{2n\pi + \pi/2}$.

Case 3: When the length of the ultrasound pulses are longer than the length of medium ***b***, the current is maximized or minimized.

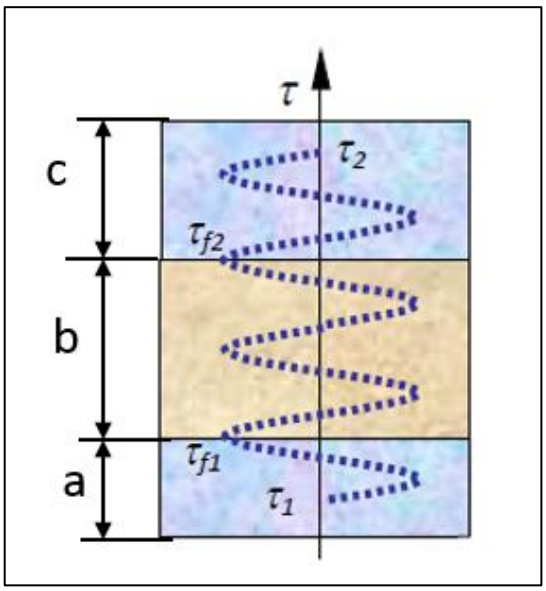

Figure 2.15: 2D Slab model (Case 3) (Wang et al., 2013).

Case 4: When the medium ***b*** is not homogenous, the output signal is never zero.

Electric Dipole Model:

When the ultrasound pulses travel through the colloidal suspension the signal can be detected outside the medium and this measurement depends on the electrode locations for the detection of the signal amplitude. The dipole model was first introduced by, Wang et al., (2013). and it considers the potential distribution in space. This model assumed that the ultrasonic pulses travel in the **z**-direction through a homogenous medium.

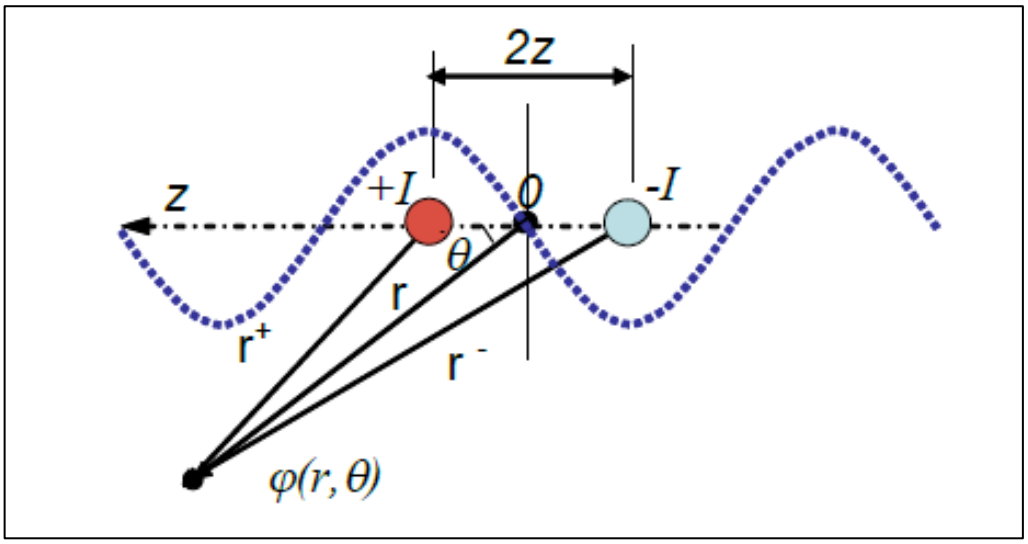

Figure 2.16: Electric dipole model (Wang et al., 2013).

Figure 2.16 is an assumption made by Wang et al., (2013) for the electrical potential distribution. It assumed the ultrasound propagated in **z**-direction through a homogenous medium as shown in figure 2.16. The generated current due to the vibration of nanoparticles described as a number of dipoles along the **z**-direction. The centre between two dipoles assumed that the current is zero, and the general form of the potential given by:

$$\boldsymbol{\varphi_{sum}} = \frac{\boldsymbol{\beta^{+} cos\theta}}{\boldsymbol{r^2}} . \int_{\mathbf{0}}^{\boldsymbol{kz}} \boldsymbol{z sinkz\, dz} \qquad (2.91)$$

Where $\boldsymbol{\beta^{+}}$ is the specific property of colloidal region, $\boldsymbol{r}$ is the distance between the point where the potential measured and the centre between the two charges. $\boldsymbol{\varphi_{sum}}$ has non-zero value anywhere except when $\boldsymbol{\theta = \pi/2}$. $\boldsymbol{\varphi_{sum}}$ has maximum values with the opposite sign at $\boldsymbol{\theta = 0 \text{ and } \theta = \pi}$. The dipole model aims to explain the potential

measured at any point far from the centre of the two charges, at a time where these two charges are separated.

2.5.4 UVP Test Devices and Circuit Model

In the past, two standard devices had been established for UVP measurements. The first device was established by Brown University (UVP standard 1) and the second device was by the University of Leeds (UVP standard II). In this Section, I will present both UVP standard devices, and the circuit model in detail.

UVP Standard I Device

Brown University introduced this standard device. This device was built based on O'Brien's theory and was made from an aluminium housing. The apparatus of this device consists of a cell containing an object of interest, which is equipped with a delay line made of water at the top and at the bottom. The transducer is mechanically fixed at the top of the device. The sample of interest is sealed with cling film and placed inside the aluminium housing, Schlaberg et al., (2011).

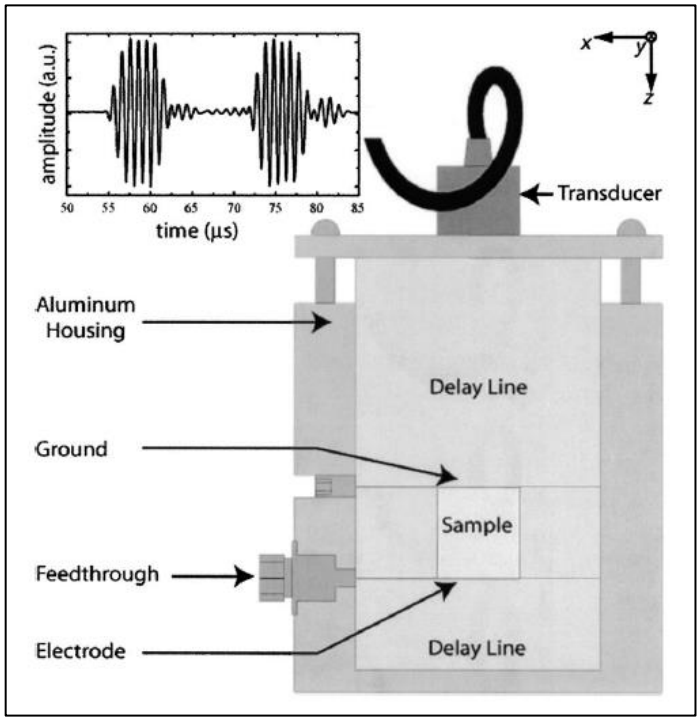

Figure 2.17 UVP standard I device (Andrew et al., 2004).

The sensing method is made with two wire electrodes attached two both sides of the sample. One of these electrodes is connected to the aluminium housing to earth the device, and the other electrode is connected to the feedthrough to form the UVP signal.

The lack of repeatability with this device is that the phantom do not allow for repositioning of the sensor, the sample, and changing the sample is not easy. The delay lines made with water and this make more difficult to relocate the sample. It is not capable of non-intrusive measurement. The amount of ultrasound energy travelling into the sample of interest is reduced because the cling film creates an interface between the sample and the delay line.

For the experimental procedure, the same UVP standard device was used (see Figure 2.17). A number of colloidal and ionic solutions were tested, including colloidal gold (15 μV), India ink (44 μV), colloidal silver (13 μV), LiCl (69 μV), NaCl (23 μV), Kill (39 μV), RbCl (85 μV), and CaCl (132 μV). Muscle tissue from chicken breast, beef, and pork, produces a UVP of less than 0.02 μV.

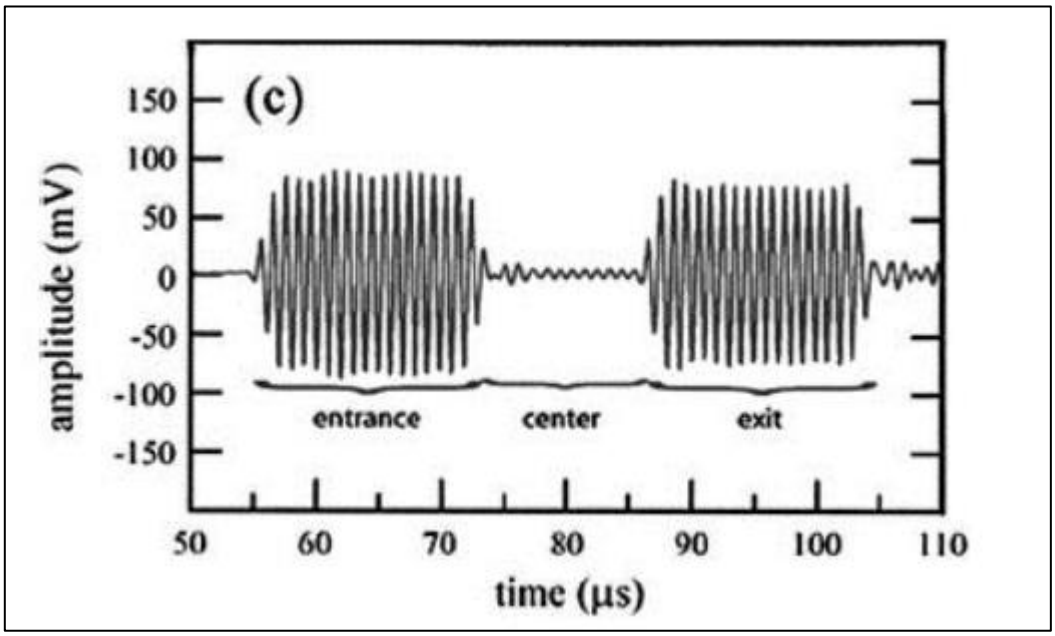

Figure 2.18: Ultrasound vibration potential signal generated by 32 cycles and 0.9865MHz, and amplification of 100.

Figure 2.18 shows the ultrasound vibration potential signal, recorded at the interfaces of 2.5cm thick layer of colloidal gold nanoparticles with a frequency of 0.9865MHz, and amplitude of $150m$ with and amplification factor of 100.

UVP Standard II Device

This device was introduced by the University of Leeds by Khan et al., (2010). This device is made with polypropylene material and lies horizontally. The dimensions of the device are: 33 cm in length, 7.5 cm in width, 13.5 cm in height, and with a wall thickness of 1.7 cm, as shown in Figure 2.19.

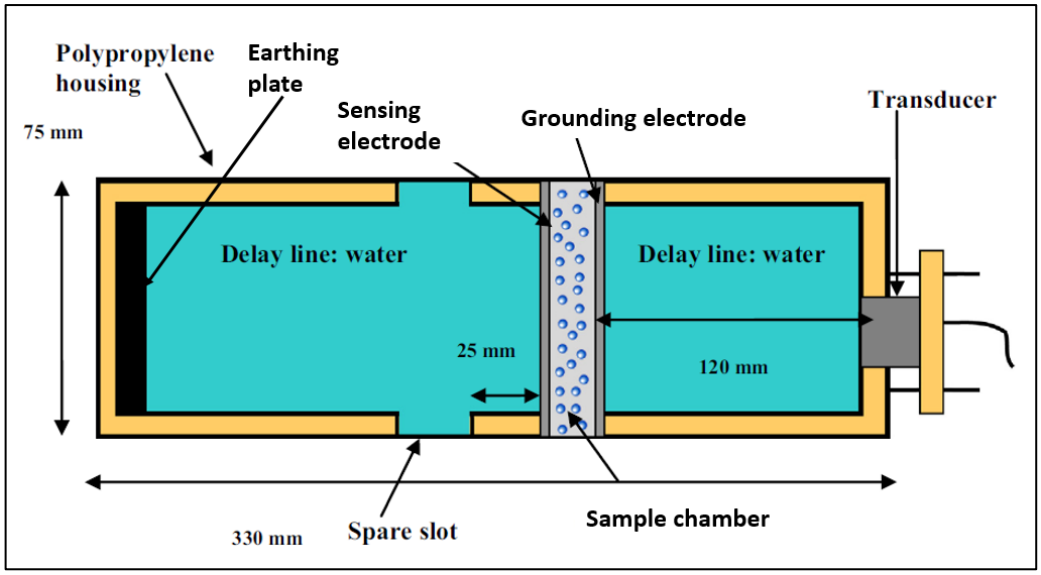

Figure 2.19: Leeds standard II device (Khan, 2010).

At the far end of the device a tin coated copper disk (earthing plate) installed to serve grounding of the measurement system and a piece of sponge was inserted in front of it to absorb the ultrasound.

The transducer is mechanically fixed at the side of the device. The placement of the transducer was 15mm from the bottom of the device. . Two slots are made to insert a sample chamber containing the materials. The distances to the slots are 12 cm and 14 cm. At the far end of the device there is a tin-coated copper plate to earth it.

The two delay lines are made with water at both sides of the sample in order to separate the signals. An electromagnetic (EM) shield box is introduced to enhance the signal quality. The EM shield box is large enough to place the whole standard II device inside.

The source chamber is made with PVC and sealed with cling film with a hole at the top in order to add the samples. The dimensions of the chamber are: 12.5 cm in height, 2 cm in length and 62 mm in width. The cling film is glued to each side of this chamber.

The delay lines made with water to separate the signals (Excitation and UVP). The excitation ultrasonic signal with 6 cycles and wavelength of 9mm used to generate the UVP within the sample. The mesh sensor was designed for detecting the ultrasound vibration potential; it's comprised of a frame with wire and both made with stainless steel material. The frame has 123mm in length, 63mm in width, and the detection sensor consists of two frames (one grounding and one sensing the signal). The mesh wire has a thickness of 0.14mm this to avoid the reflection of ultrasound signal from its surface.

The equivalent circuit diagram for the IVP measurement is presented in Figure 2.19. The cling film was used for sealing the sample introduced as a capacitors of $\boldsymbol{C_1}$ **and** $\boldsymbol{C_2}$, and the impedance of $\boldsymbol{Z_1}$**and** $\boldsymbol{Z_2}$.

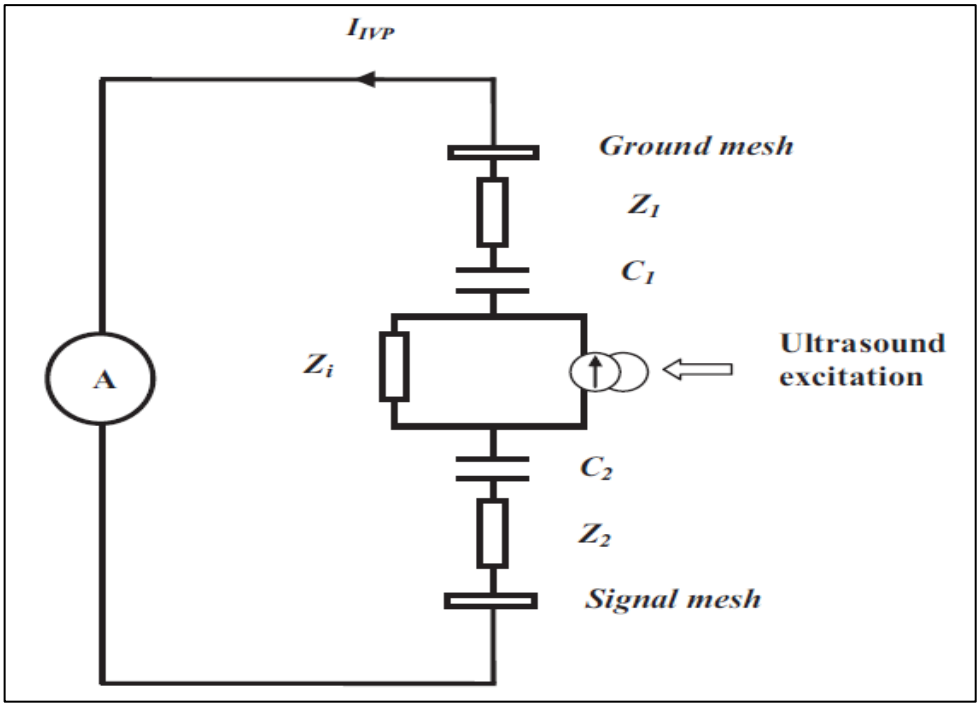

Figure 2.20: The equivalent circuit diagram of the Leeds standard II (Khan et al., 2013.

This device was introduced based on the UVP standard I device. Its advantages are its repeatability as it is easier to change the sample and it also enhances the signal quality. However, again, the UVP standard II device is not capable of non-intrusive measurement and the use of cling film to cover the sample creates an interface and decreases the sound energy travelling into the medium.

The IVP signal measured for ionic electrolytes [NaCI, KCI, RbCI, CsCI], as a function of concentration. The largest signal measured for a concentration of 3M for all four electrolytes. The IVP signal measurement reported by Yeager and Zana (1967) for all ionic electrolytes with the same concentration, but the signal amplitude was relatively larger, thus because the Yeager and Zana inserted the electrode directly into the ionic solution while University of Leeds placed the electrodes outside the sample.

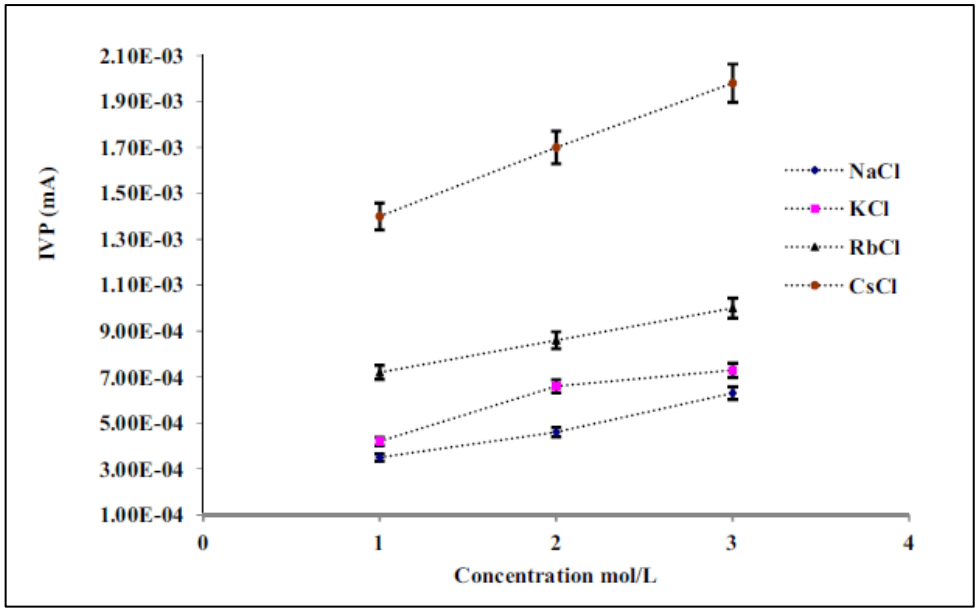

Figure 2.21: IVP signal measured with 1MHz transducers as a function of concentration of ionic electrolytes with an amplification factor of 500KV/A.

2.5.5 UVP Imaging Technique

Brown University conducted a few experiments in the field of UVP, Andrew et al., (2004). Through these experiments they were able to show an image of a colloidal region within a body.

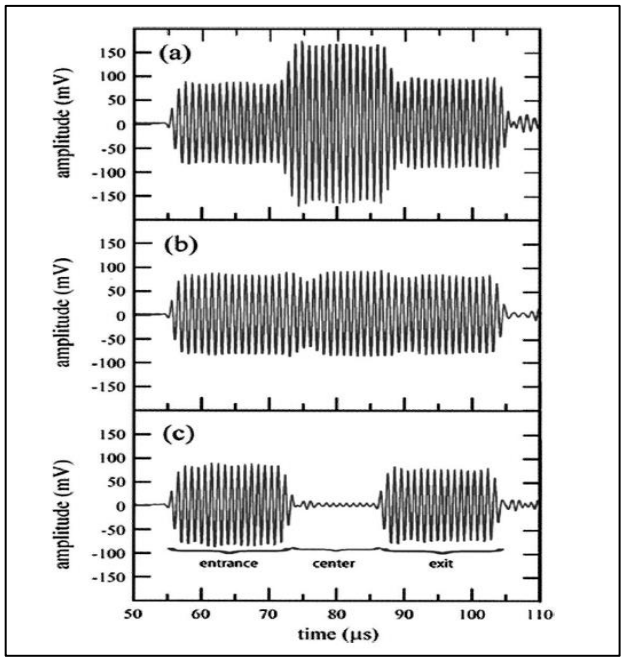

Figure 2.22: UVP trace signals generated by 32 pulses of a) 1.0165 MHz b) 1.0069 MHz and c) 0.9865 MHz, (Andrew et al., 2004).

In Figure 2.22 the signal appeared at the entrance of the colloidal object with the initial time of ($\mathbf{55 - 75\ \mu s}$) and exist time of ($\mathbf{85 - 105\ \mu s}$) respectively. The apparatus used in these experiments is shown in Figure 2.19, and the bottom electrode connected to an RF amplifier with a voltage amplification of 100 V. The ultrasound is generated by a 2.54 cm diameter LiNbO3 transducer driven by a programmable function generator. The ultrasonic signal pulses with six cycles with a frequency of 1 MHz applied to the cell

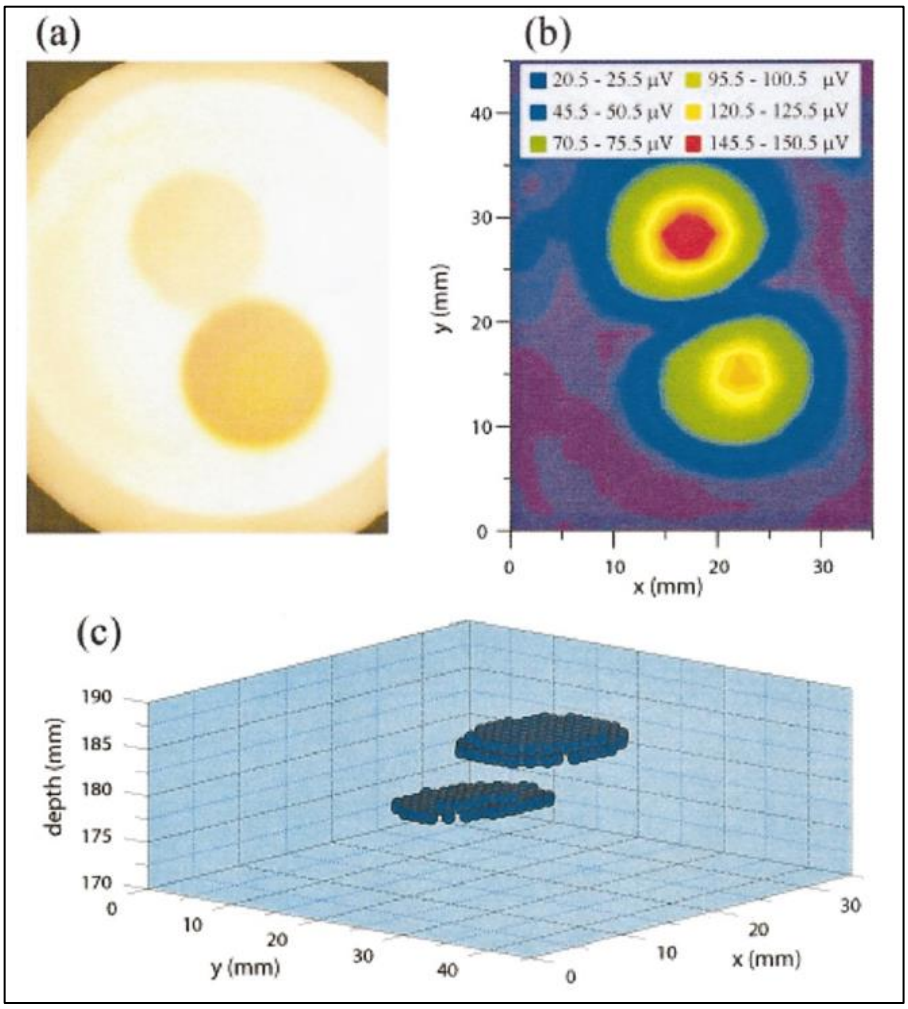

Figure 2.23: The photograph, amplitude and arrival time imaging of agar block (Andrew et al., 2004).

The data is collected from a frequency range of 0.8984 MHz to 1.0765 MHz and the length of the colloidal object is $\mathbf{2.553 \pm 0.025\ cm}$.

In their experimental results, they have shown that the imaging method requires the timely arrival and the relative phase and amplitude for the image processing. Focused transducer with a high frequency used to increase the image resolution — the results are

presented in Figure 2.21. The ultrasound beam width was 3 mm in diameter over the length of the sample. The burst drove in range of 28 μs — the scanning procedure was controlled by the computer. At the University Leeds, several experimental works were undertaken including the use of the standard II UVP device. The first early work was presented by Guang (2010) to detect the UVP signal. The diagram for system is shown in Figure 2.24. The sample was sealed with cling film and placed inside the water tank. Two delay lines were made from the top and the bottom of the cell to separate the signals. The earthing electrode and the sensor electrode were attached to the sample inside the water tank.

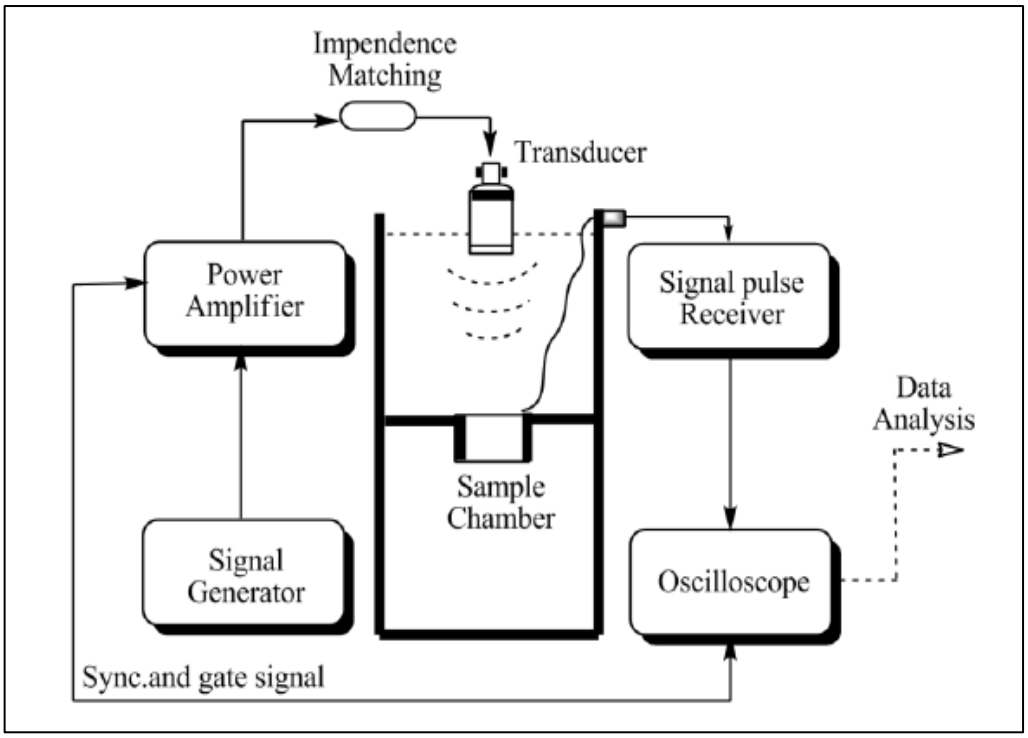

Figure 2.24: A diagram of the test system (Guang et al., 2011).

The ultrasound wave is generated by the function generator and is then amplified by an RF amplifier before being introduced to the piezoelectric transducer. The sound wave travels through the sample and the UVP is generated due to the polarization of the particles.

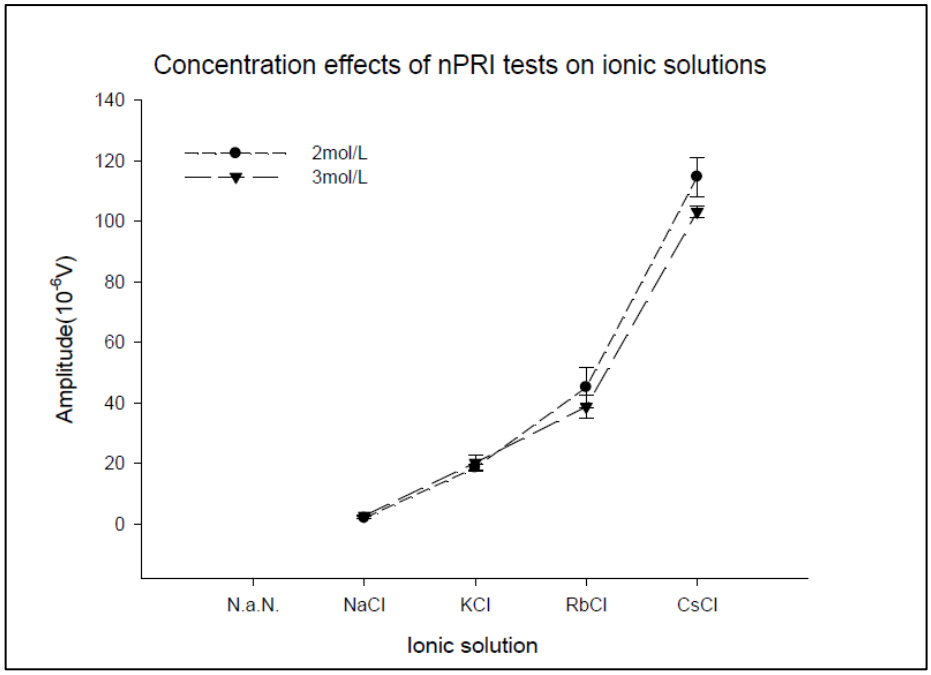

Figure 2.25: IVP signal for ionic electrolytes (Khan et al., 2013).

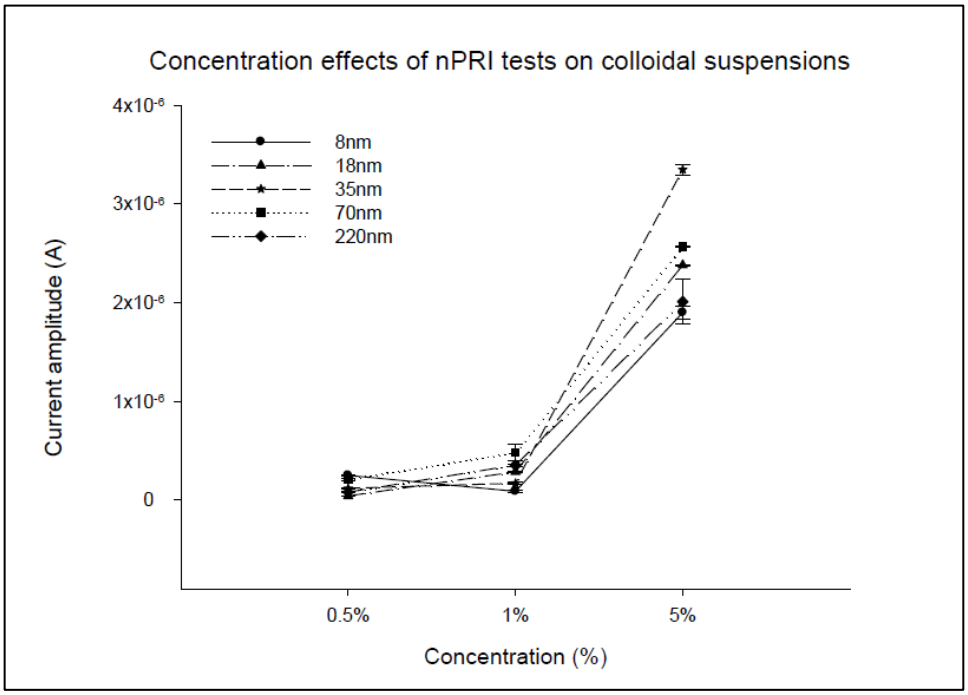

Figure 2.26: CVP signal measured for silica dioxide nanoparticles (Guang, et al., 2013).

The experimental results for the IVP of both are shown in Figure 2.25, and for the CVP in Figure 2.26. The IVP results are shown for [$NaCl, KCl, RbCl, CsCl$], with two different concentrations of 2 mol/L, and 3 mol/L.

The CVP signal measurements by the University of Leeds for silica nanoparticles with different particle sizes and various concentrations are presented in Figure 2.24. The results show that the CVP signal is increased with small particle sizes and with increasing concentrations.

Another experimental was carried out by, Guang, et al., (2013) to image three different layers of colloidal suspension. The material consists of four interfaces and three layers — the thickness of the testing material is made with agar, silica. The interfaces include water-agar, agar-silica, silica-agar, and agar-water. The sensing method is shown in Figure 2.24. The electrode sensor is placed at both sides of the sample.

The four signal bursts appeared with different amplitude. The signals detected corresponded to the property of the different media. The IVP signal increases with increasing atomic weight and concentration. Further discussion relating to IVP changes with respect to the effect of frequency, concentration, and atomic mass can be found in Khan's work. The imaging of a multilayer sample was first introduced by Guang, et al., (2011). They used two layers of colloidal objects with a layer of agar in between as shown in Figure 2.24. The first layer is made up of a colloidal sample of silica dioxide, the middle layer is made with agar gel and the third layer with a colloidal suspension of silica.

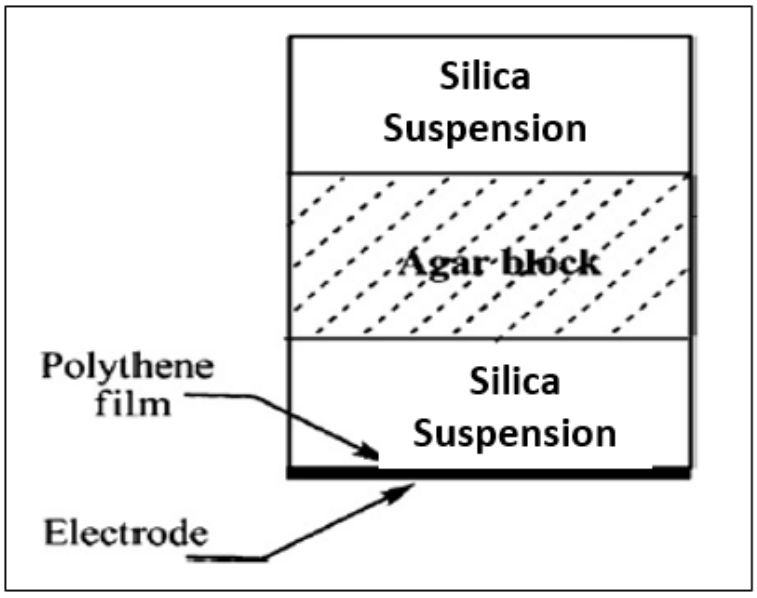

Figure 2.27: A non-homogeneous sample layer (Guang et al., 2011).

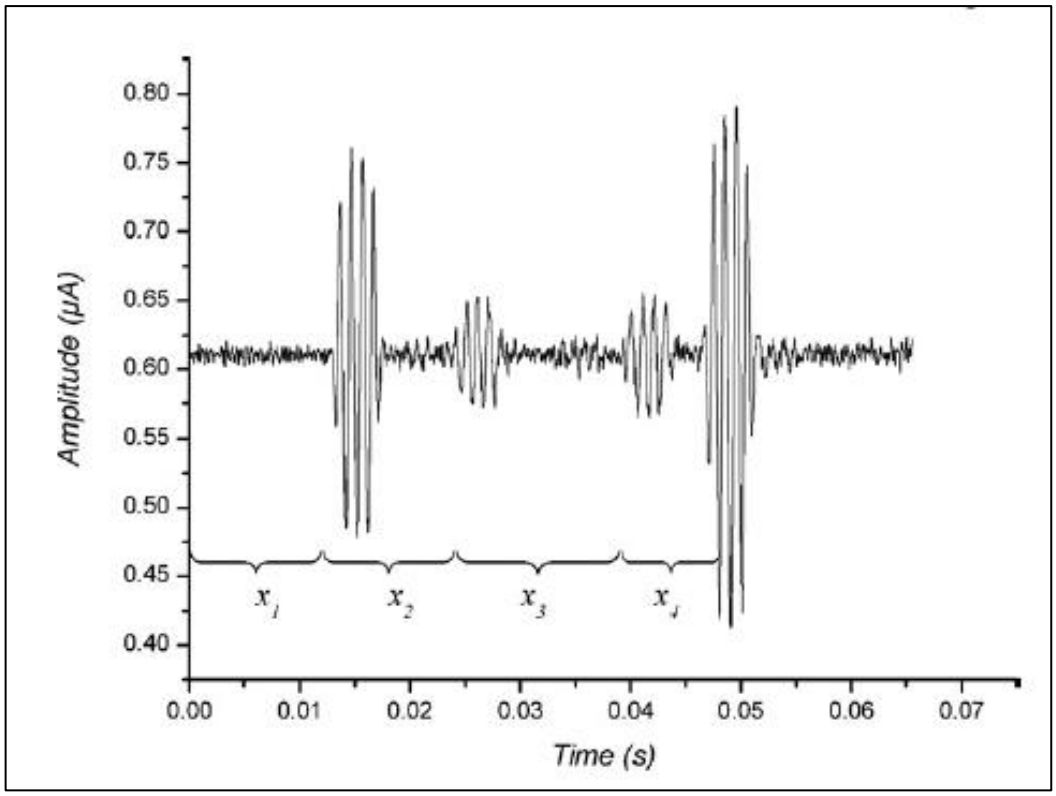

Figure 2.28: CVP signal for two layers of silica and one layer of agar (Guang et al., 2011).

The measured CVP signals are shown in Figure 2.28. The signals appeared with different amplitudes due to the different properties between the layers. The distances between the two generated signals measured by counting the ultrasound arrival time of the signal and ignoring the electrical signal transmission times.

2.5.6 Ultrasound Vibration Potential Distribution

The analogue calculation for the potential distribution of a colloidal layer in an infinitive rectangular shape was given by Brown University by, Nguyen et al., (2009). The potential distribution between two parallel plates was calculated for infinitive colloidal layers of cylinders and spheres. They describe the potential distribution for a weak material between two parallel plates that generate an electrical signal when the ultrasonic wave is applied. The arrangements for recording the acoustically generated current is shown in Figure 2.27.

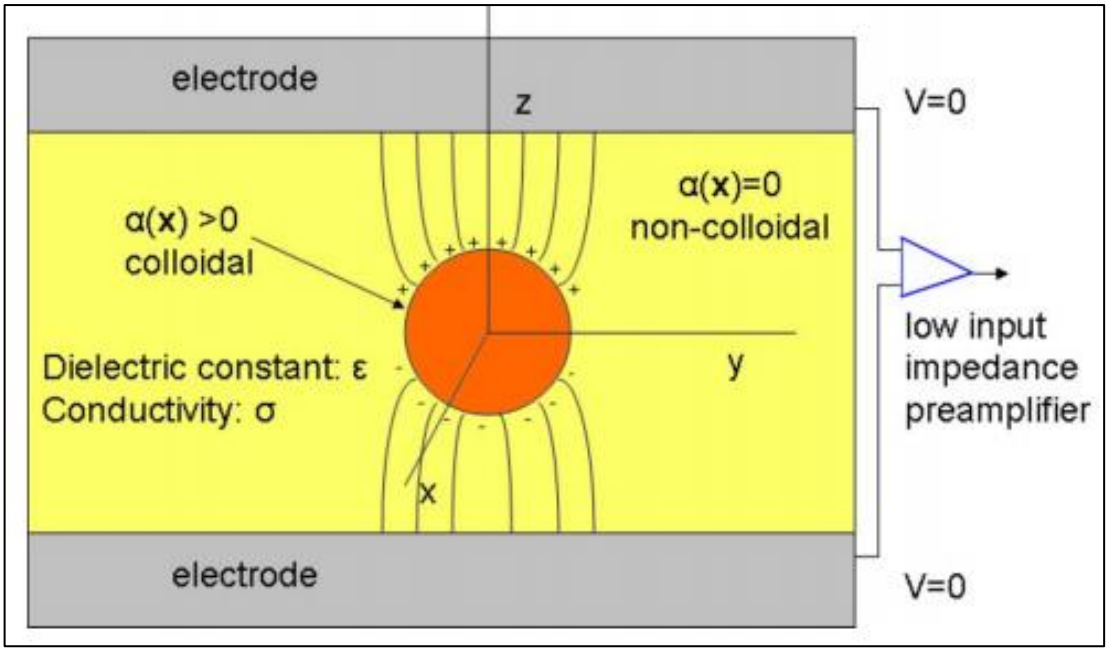

Figure 2.299: Diagram of the electrodes, dielectric, and colloidal object ((Cuong et al., 2008).

The potential distribution in the region between two parallel infinitive plates given by:

$$\boldsymbol{\nabla^2 \varphi(r) = \nabla.(\alpha^{\text{I}} \nabla P)} \qquad (2.95)$$

The potential $\boldsymbol{\varphi(r)}$ in a medium with a dielectric constant of $\in$, conductivity $\boldsymbol{\sigma}$ containing a colloidal sample whose spatial dependence given by $\boldsymbol{\alpha(r,\omega)}$ can be presented as a volume integral over a Dirichlet Green function $\boldsymbol{G_D(r,r^-)}$.

$$\boldsymbol{\varphi(r) = \frac{i\omega}{\sigma + i\omega\epsilon} \int G_D(r,r^-) \nabla^-.[\alpha(r^-,\omega) \nabla^- P(r^-)] dV^-} \qquad (2.96)$$

$$\boldsymbol{G_D(r,r^-) = \frac{2h}{\pi^2} \sum_{n=1}^{\infty} \frac{\sin(n\pi z h) \sin(n\pi z^- h)}{n^2}} \qquad (2.97)$$

Where $\boldsymbol{h}$ is the distance between the two plates, and the ultrasound wave is propagated along the z-axis. It has been considered at $\mathbf{z = 0}$ and $\mathbf{z = h}$ for a wave with wave number k and forms pressure of $\boldsymbol{p = p_o \exp(-ikz)}$.

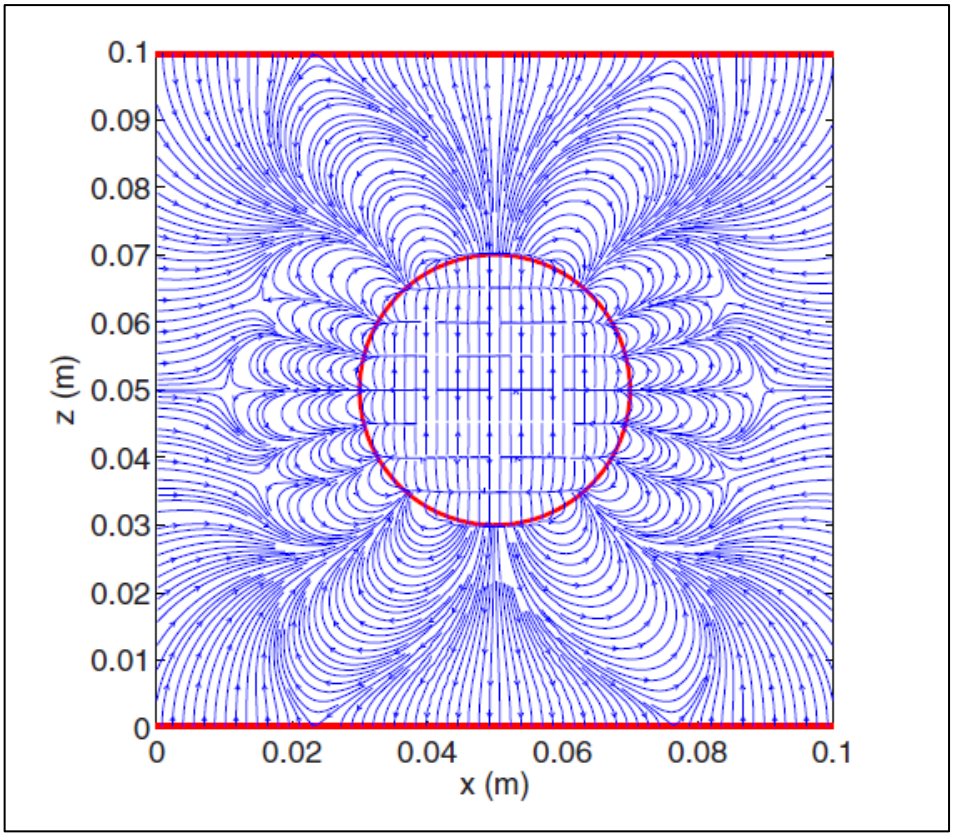

Figure 2.30: Electric field distribution for a colloidal sphere (Nguyen, 2009).

Figure 2.30 shows the electric field that is present for an active colloidal region. On the outside of the layer, the electric field (and the current), is not generated. In the case of a sphere, the current was found by integration of the current density over one plate, and it is proportional to $[\boldsymbol{sin}(\boldsymbol{ka}) - (\boldsymbol{ka})\boldsymbol{cos}(\boldsymbol{ka})]/\boldsymbol{ka^2}$. In this case, polarization was made by the ultrasound wave and it is time dependent. This leads to the production of a current, or voltage, and it is dependent on the boundary conditions at the electrodes. These results are similar to a classical electrostatic event in which the magnitude of the charges are inversely proportional to the square of the distance between the end two points, Cuong et al., (2013). With this model the generated voltage via the integration over a region is not discussed and not evaluated.

2.6 Summary

In summary, the basic principles of an ultrasound wave and its characterizations have been presented. The conventional ultrasound imaging methodology, and how ultrasound imaging works, including the transducer operations, was demonstrated. This research

focuses more on nanoparticles in colloidal suspensions and ionic electrolytes, including medical imaging; therefore, I have included a background and theoretical explanation of colloids, and ultrasound imaging. Further understanding on the generation of UVP in colloidal suspensions and previous work in this field are also given in detail. I have presented the essential theoretical and experimental background for both ion IVP and CVP. The current UVP measurement devices are not capable of nonintrusive measurements, and the UVP distribution model is required for feature device optimizations. A measurement method of using chirp signal for nanoparticle characterization is required to further develop the feature of this research in engineering for nanoparticle characterizations. The sensing system and the measurement method require further improvements to enhance the signal quality and the capability of this method for tissue imaging. This works aims to further support the scientific understanding of UVP for application in engineering for nanoparticle characterization in colloid and providing a new knowledge for medical diagnosis and research, this by introducing, ultrasound vibration potential distribution (UVPD) model to evaluate the measurement and the potential distribution along the ultrasound propagation direction. Further progressing on the sensing system using electrodes, non-intrusively placed outside a body, to provide physiochemical properties of the sample. Initiating a measurement method to analyse the physicochemical feature properties of nanoparticles and ionic species in colloids. Establishing a new testing phantom which is capable of non-intrusive ultrasound vibration potential measurement, and enhance the UVP signal strength. To review a method of imaging colloidal/ionic objects, using a low power source of excitation, to report a unique feature of UVP, and additional signatures of UVP to reveal specific physiochemical structures of the sample. Investigating whether CVP signal can be measured from animal tissue and the feasibility to be developed as a new functional imaging for medical diagnosis and research.

CHAPTER THREE: MODELLING OF ULTRASOUND VIBRATION POTENTIAL DISTRIBUTION

Summary: *This Chapter will give an explanation to understand the principles of an ultrasound vibration potential (UVP) signal. It explains the, excitation signal, UVP signal and the polarization phenomena in colloidal suspension. An electrical ultrasonic vibration potential distribution (UVPD), for device optimization, will be also demonstrated.*

3.1Introduction

This Chapter presents further explanation in order to understand ultrasound excitation, along with a model to explain UVP signal generation. The generation of UVP, due to the vibration of nanoparticles in the colloidal suspension, and double layer (DL) polarization due to the presence of ultrasound pressure, creates dipoles.

An electrical ultrasonic vibration potential distribution (UVPD), for device optimization, will be also demonstrated. A new vibration model is introduced to explain the vibration of the particles in colloidal suspensions for electric signal generation. The first section of this Chapter, will give a brief explanation of the excitation signal uses for the generation of ultrasound vibration potential signal.

The second section will explain the electrical signal generation and measurements. This explains the polarization of charges in colloidal suspension due to the presence of ultrasound pressure. In the third section a new disc dipole model will be given to explain the ultrasound vibration potential distribution (UVPD).

3.2Excitation Signal

A piezoelectric quartz crystal can be specially cut and if compressed, then the compressed crystal becomes electrically charged and an electric current is generated, Minding (1971). The direction of the current can be reversed by stretching the crystal rather than compressing it. If we apply a current to the crystal with a matching frequency, the crystal will expand and contract with an alternating current (AC). The wave propagation depends on the way the crystal is cut, Jrank (2019). In our method,

we have used longitudinal waves, because they can propagate through both liquids and solids. We used an immersed transducer which has an impedance matching layer to help more energy to be transmitted through the material. We use a pulsed wave in order to separate the signals for ease of measurement. The ultrasound burst pulses generated with the number of cycles is presented in Figure 3.1.

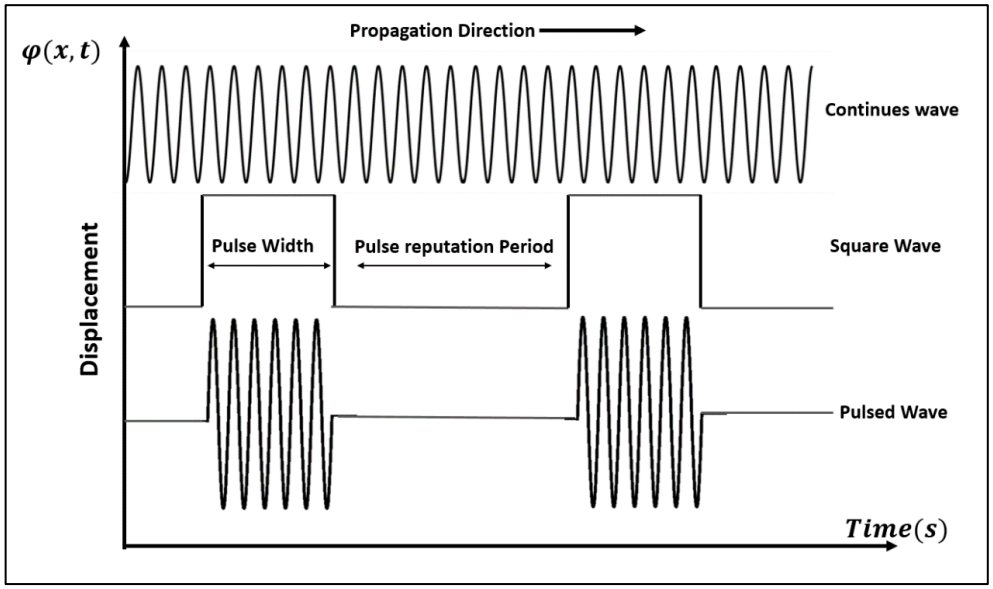

Figure 3.1: Continuous, square, and pulse ultrasound waves.

The signal is set in a function generator with frequency $\boldsymbol{f}$, amplitude $\boldsymbol{A}$, and time periods $\boldsymbol{t}$. In UVP methods we use a pulsed wave, therefore, we apply a square wave to synchronize the required signal with a certain number of cycles. The pulsed wave can be generated with frequency $\boldsymbol{f}$, time periods $\boldsymbol{t}$, and pulse repetition periods $\boldsymbol{T}$. The electric signal, with a certain number of cycles, is generated from the function generator, and the electrical signal is converted to a mechanical signal by the piezoelectric transducer before being applied to the sample of interest. The mechanical ultrasound pressure wave can be given from Equation 3.1:

$$P = Asin(\omega t - kx + \theta) \tag{3.1}$$

Where, $\boldsymbol{k} = \frac{2\pi}{\lambda}$ is the wave number, $\boldsymbol{\omega}$ is the angular frequency, $\boldsymbol{\theta}$ is the phase angle, and $\boldsymbol{x}$ is the propagation direction positions. The duty cycle can be calculated using Equation 3.2:

$$Duty\ cycle\ \% = \frac{t}{T} \times 100\% \tag{3.2}$$

The pulse repetition period is important to set a duty cycle because many amplifiers have a limited duty cycle in order to amplify the applied signal. The number of pulses of the excitation signal is important in UVP signal detection as it will affect the generated signal. This was briefly explained in Section 2.5.3.

3.3Electrical Polarization

A UVP signal is produced by applying ultrasound pressure into a colloidal suspension containing nanoparticles, O'Brien, (1988). This potential can be measured by using two electrodes attached to the body in a parallel sequence. A similar process happens in ionic electrolytes, and these two phenomena are explained in Sections 2.5.1 and 2.5.2. If we have a colloidal suspension containing many nanoparticles, these particles carry a positive or negative charge and cloud ions, with the opposite charge, surround them. In the time periods where no ultrasound pressure is applied to the suspension, the system is balanced. When cloud ions with the opposite charge surround the nanoparticles they create a DL. The only static electric E presented at this time. When ultrasound pressure is applied to the suspension, the particles and ions accelerate at different rates. Due to the difference in motion between the cloud ions and the particles the polarization in the DL creates, this generates dipoles. Summing these dipoles can be measured as an electrical potential. It is very important to know that the signal is measured by the integration over the region where the signal is generated. The theory to explain the integration effect on the measured signal is explained in Section 2.5.3.

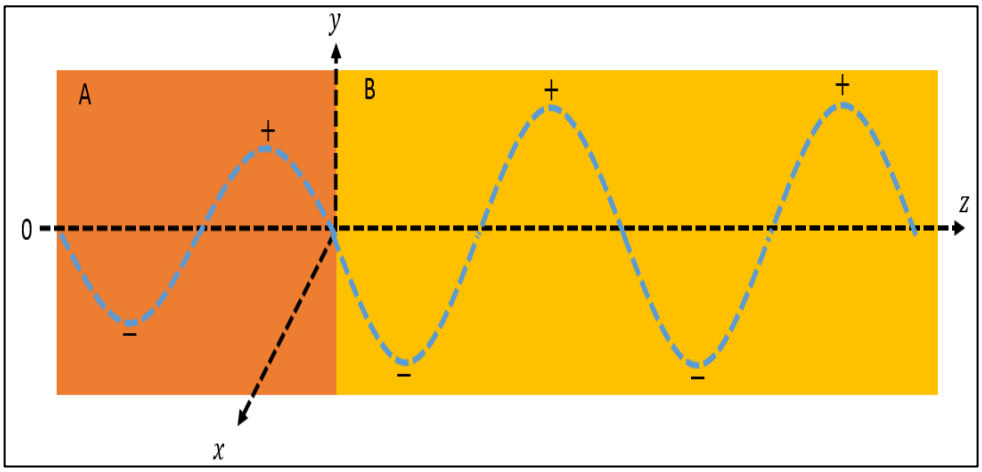

Figure 3. 2: polarized charges in two colloidal layers.

Figure 3.2 shows the two colloidal layers (A) and (B) having different colloidal properties. The charges in this two medium are polarized due to the presence of external pressure.

The integration of these polarized charges is measured as an electrical signal. The integration value is zero if these two colloidal layers have given similar signal amplitude, and it's not zero if they have given different signal amplitude. The signal shows different amplitude in Figure 3.2 because the two colloidal layers A and B having different colloidal properties, and this present materials' physiochemical features. When ultrasound pressure is applied to a colloidal suspension or ionic electrolytes the system is polarized. For example, in colloids the particles are heavier than the ions, therefore they vibrate at different rates. The ions try to relocate to their previous positions, but due to the vibration, not all ions are able to relocate to their stable positions, therefore polarization $(\boldsymbol{P_a})$ is created. When ions with the opposite charge are polarized, dipoles are created, and summing these dipoles by integration over the region gives us an electric potential signal we call *ultrasound vibration potential*.

In the colloidal region the relationship between the displacement vector and the electric field is given by, Dluzhnevskii, (1970):

$$\vec{\boldsymbol{D}} = \boldsymbol{\varepsilon}\vec{\boldsymbol{E}} \tag{3.3}$$

$$\boldsymbol{\varepsilon} = \boldsymbol{\varepsilon_o}\boldsymbol{\varepsilon_r} = \boldsymbol{\varepsilon_o}(\mathbf{1} + \boldsymbol{x_e}) = \boldsymbol{\varepsilon_o} + \boldsymbol{x_e}\boldsymbol{\varepsilon_o}$$

$\boldsymbol{x_e} = (\boldsymbol{\varepsilon_r} - \mathbf{1})$ in material

$\boldsymbol{x_e} = \mathbf{0}$ in a vacuum

$$\vec{\boldsymbol{D}} = \boldsymbol{\varepsilon_o}\vec{\boldsymbol{E}} + \boldsymbol{x_e}\boldsymbol{\varepsilon_o}\vec{\boldsymbol{E}}$$

$$\boldsymbol{x_e}\boldsymbol{\varepsilon_o}\vec{\boldsymbol{E}} = \overrightarrow{\boldsymbol{P_a}}$$

$$\vec{\boldsymbol{D}} = \boldsymbol{\varepsilon_o}\vec{\boldsymbol{E}} + \overrightarrow{\boldsymbol{P_a}} \tag{3.4}$$

Where **D** is the dielectric displacement, $\boldsymbol{\varepsilon_o}$ is a free space permittivity, $\boldsymbol{\varepsilon_r}$ is the relative permittivity, $\overrightarrow{\boldsymbol{P_a}}$ is the polarization density, and $\boldsymbol{x_e}$ is the electric sustainability. The electric sustainability is a constant and indicates the degree of polarization within the material and is proportional to the number of polarizations. The general function of polarization given by:

$$\boldsymbol{P_a}(\boldsymbol{t}) = \boldsymbol{\varepsilon_o}\boldsymbol{x_e}\boldsymbol{E} \tag{3.5}$$

Combining Equation 3.3 and Equation 3.6 we obtain:

$$\boldsymbol{P_a = \acute{\varepsilon}\frac{\emptyset\Delta\rho\mu_E}{\rho K^*}\nabla P = \beta(r)\nabla P} \quad (3.6)$$

Where $\boldsymbol{\beta(r)}$ is the special distribution properties of the medium, $\boldsymbol{E}$ represents the local electric field, $\emptyset$ is the volume fraction, $\boldsymbol{\rho}$ is the suspension density, $\Delta\boldsymbol{\rho}$ is the density difference between the liquid and the particles, $\boldsymbol{\mu_E}$ is the electrophoretic mobility, $\boldsymbol{K^*}$ is the complex conductivity, and $\boldsymbol{\nabla P}$ is the ultrasonic pressure gradient.

For the homogenous colloidal layer the integration of these dipoles inside the colloidal layer is zero (UVP=0), but this integration is not zero if we have a non-homogenous colloidal layer or between two colloidal layers (UVP≠ 0).

3.4Ultrasound Vibration Potential Distribution (UVPD)

In this section we aim to investigate the relative change in the potential distribution due to the electrode position relative to the charge source. The UVPD between two parallel electrodes attached to an agar region, having dielectric constant $\boldsymbol{\varepsilon}$, and conductivity $\boldsymbol{\sigma}$ and contains a colloidal layer whose special distribution is given by a function $\boldsymbol{\beta(r)}$ that generates a voltage due to the passage of ultrasonic pressure are presented.

The ultrasound wave is propagated along the y-direction only, the beam pathway is uniform everywhere within the region, and the colloidal object has infinitive volume. We consider the frequency of the ultrasound wave which is associated with the vibration and generates the electric field to be around MHz, while the electric field emission outside the finite body is ignored. The arrangement for recording the potential difference within the region is shown in Figure 3.3.

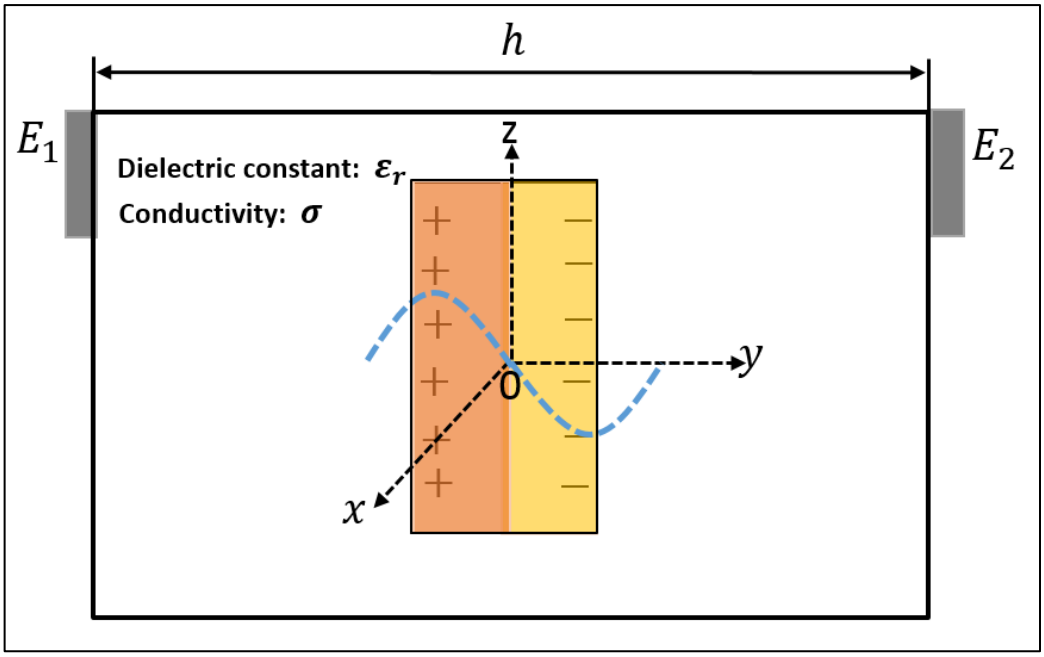

Figure 3.3: Infinitive rectangular colloidal layer lying along the y-axis between two electrodes $E_1$and E_2 having the separation distance, h.

We assume that the current outside the region is zero, so there is no current source outside the region. The only voltage generated in the colloidal region is due to the vibration of particles. In the presence of ultrasound pressure, the polarization (P_a) produces an electric field within the medium, given in Equation 3.6.

The electrophoretic mobility $\boldsymbol{\mu_E}$ is a method for calculating the property of a surface charged with colloidal particles in an electrolyte. For a particle carrying a charge $\boldsymbol{Q}$ in a medium containing counter ions with valence $\mathbf{z}$, the electrophoretic mobility was defined by, Makino and Ohshima, (2010) and is given in Equation 3.7:

$$\boldsymbol{\mu_E = \frac{Q}{4\pi\varepsilon_o\varepsilon_r}\frac{ze}{KT}} \tag{3.7}$$

Where $\boldsymbol{Q}$, is the total is charge on the particle, $\boldsymbol{\varepsilon_r}$, $\boldsymbol{\varepsilon_o}$, and $\boldsymbol{\eta}$ are relative permittivity, free space permittivity and electrolyte viscosity respectively, and $\boldsymbol{e}$ is the elementary charge. The special distribution of the colloidal region $\boldsymbol{\beta(r)}$ is given by:

$$\boldsymbol{\beta(r) = \frac{\varepsilon' \emptyset \Delta \rho}{\rho_m \sigma^*} \frac{Q}{4\pi \varepsilon_o \varepsilon_r} \frac{ze}{KT}} \tag{3.8}$$

From Equation 3.6 and Equation 3.7 we can obtain:

$$\boldsymbol{D = \varepsilon_o \mathbf{E} + \beta(r) \nabla P} \tag{3.9}$$

Where, $\boldsymbol{E}$, is the electric field, **D** is the dielectric displacement, and $\boldsymbol{\nabla P}$ is the pressure gradient. From Ohm's law $\boldsymbol{J = \sigma E}$ and $\boldsymbol{\nabla . \sigma E = -\frac{\partial \rho}{\partial t}}$ and from Gauss's law:

$$\boldsymbol{\rho = \nabla . D} \tag{3.10}$$

Where **j** is the current density and $\boldsymbol{\rho}$ is the charge density.

$$\boldsymbol{-(\nabla . D) = \nabla . (\varepsilon E)} \tag{3.11}$$

$$\boldsymbol{\nabla . (\sigma E) = -\frac{\partial}{\partial t} (\nabla . D)} \tag{3.12}$$

$$\boldsymbol{\nabla . \left[\sigma E + \varepsilon \frac{\partial}{\partial t} E\right] = -\frac{\partial}{\partial t} (\nabla . P_a)} \tag{3.13}$$

Taking the permittivity of a weak conductor such as water, $\boldsymbol{\varepsilon}$ **= 80,** $\boldsymbol{\omega = 1}$ **MHz**, and conductivity $\boldsymbol{\sigma = \frac{0.3 mS}{cm}}$. The imaginary part in Equation 3.13 i.e. $\boldsymbol{\varepsilon \frac{\partial}{\partial t} E = i\omega \varepsilon \nabla E}$, is too small and can be ignored, hence Equation 3.13 becomes:

$$\boldsymbol{\sigma \nabla E = -\frac{\partial}{\partial t} (\nabla . P_a)} \tag{3.14}$$

If $\boldsymbol{\varphi = \varphi_o e^{i\omega t} \ and \ P_a = P_a e^{i\omega t}}$, **then** $\boldsymbol{\frac{\partial}{\partial t} = i\omega}$

$$\boldsymbol{\sigma \nabla E = -i\omega (\nabla . P_a)} \tag{3.15}$$

$$\boldsymbol{\nabla . E = -\frac{i\omega}{\sigma} (\nabla . P_a)} \tag{3.16}$$

From Equation 3.15 and Equation 3.16 we get:

$$\boldsymbol{\beta^{\dagger}(r) = \frac{\varepsilon' \emptyset \Delta \rho}{\rho_m \sigma^*} \frac{Q}{4\pi \varepsilon_o \varepsilon_r} \frac{ze}{KT} \nabla \mathbf{P}} \tag{3.17}$$

$$\boldsymbol{\beta}^{\dagger}(\boldsymbol{r}) = -\frac{\boldsymbol{i\omega}}{\boldsymbol{\sigma}}.\boldsymbol{\beta}(\mathbf{r})$$

Equation 3.17 has the form of Poisson's equation

Boundary conditions:

Neumann conditions: We assume that no current goes through the boundary, and on the current line orthogonal to the boundary.

$I_n = 0$ and $\frac{\partial \varphi}{\partial n} = 0$

There is no current passing through the region: $i_n = 0$

Dirichlet boundary condition: The voltage on the electrodes are constant and sufficient small, and the modification to the boundary the potential distribution is ignorable. The voltage on the electrode V= constant and sufficient small.

The pressure of the ultrasound propagation is given by:

$$\boldsymbol{\nabla P = -A\omega sin(\omega t - kx)} \tag{3.18}$$

$$\boldsymbol{\Delta\varphi(r) = -A\omega\,\nabla.(\beta^{\dagger}(r)sin((\omega t - kx)))} \tag{3.19}$$

Based on the above assumptions and the dipole model given by (Wang et al. 2013) arguments about the effect of ultrasound focusing disc and boundary condition in the simple dipole model, as well as the complex in approach the solution with the analogous model. With an assumption of the temporal steady state of ultrasound propagation and the effect of integration, as well as a uniform and planar ultrasound on its beam propagation and ignoring the other effects (e.g. reflection, deflection etc.), a disc dipole model is developed.

To solve the potential distribution, we use a numerical model. In our static model we assume that a plane wave of ultrasound pressure travels through a medium containing a colloidal object (represented as a two-disc dipole) centred between two electrodes. The medium has finite dimensions $[\text{width} = 82\text{ mm}, \text{depth} = 56\text{ mm}, \text{height} = 66\text{ mm}]$ and is constructed using COMSOL Multiphysics software. The two-disc dipoles are made with silica properties and are adjusted to be parallel to each other inside an agar block with a diameter of 25 mm placed at the centre of the cube/block.

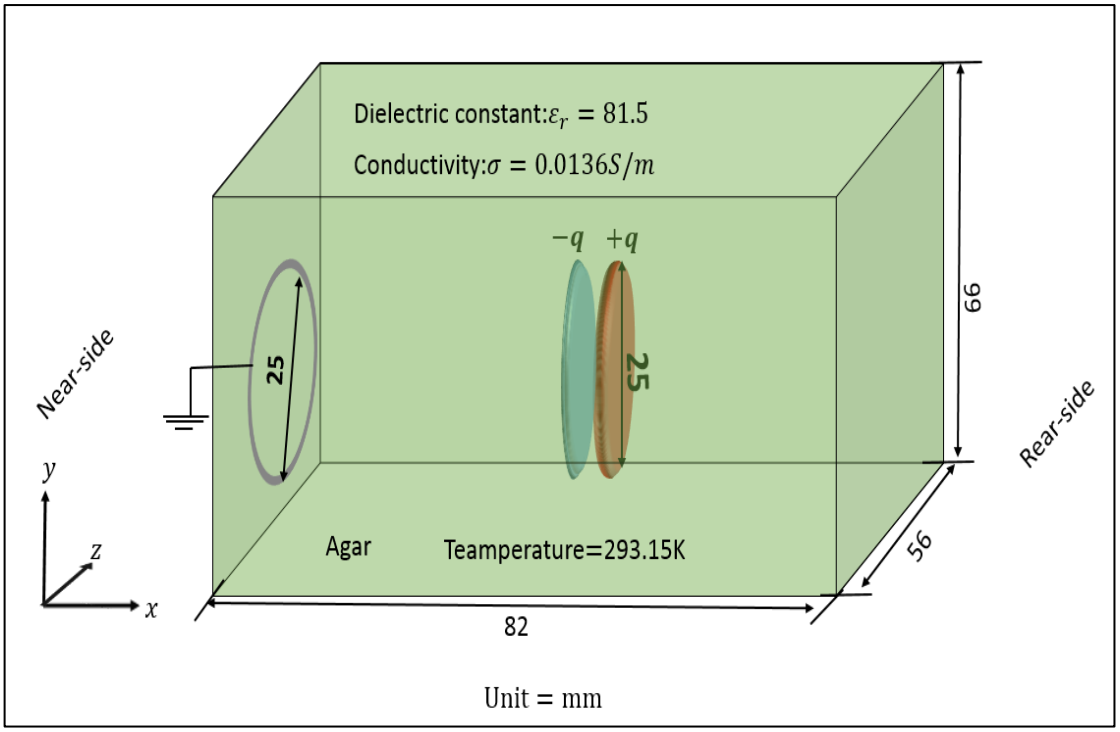

Figure 3.4: Disc dipole model diagram.

Figure 3.4 shows the arrangement of disc dipole model used to solve the UVPD. The distance between the centres of the two-disc dipole ($\boldsymbol{d(\lambda)}$) is 1.8 mm, and the ring attached to the nearside of the agar block represents the earthing point for the transducer. The separation distance between the centres of these two-disc dipoles are $\boldsymbol{\lambda}$=1.6 mm, and the thickness of each disc is 0.2 mm.

Both discs have similar properties with a silica coating with zero electrical conductivity. The charge applied to both discs is $\boldsymbol{\pm 1\,C}$. The agar mock body is set with physical properties of: conductivity $\boldsymbol{\sigma = 0.0136\,S/m}$, relative permittivity of $\boldsymbol{\varepsilon_r}$ = 81.5 and temperature $\boldsymbol{T = 293.15K}$. The speed of the ultrasound is measured at $\boldsymbol{C = 1600\ m/s}$. and the frequency is set at $\boldsymbol{f = 1\,MHz}$, with a wavelength of $\boldsymbol{\lambda}$ =1.6 mm. In our static model, we assume that the centre between both dipoles is zero. One dipole is at position $\boldsymbol{x = x_o}$ at time $\boldsymbol{t = 0}$, as described in Figure 3.4.

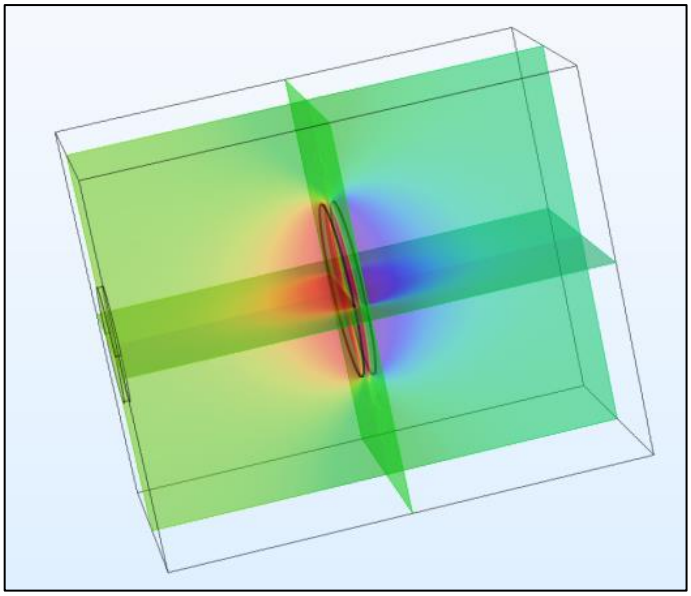

Figure 3.5: UVPD in 3D, the disc dipole placed at the centre of the cube.

Figure 3.5 shows the potential distribution for a colloidal region representing disc dipoles inside a block of agar. The potential is measured by two electrodes attached to the body in parallel. It assumes there is no current outside the source and that no current passes from the inside to the outside.

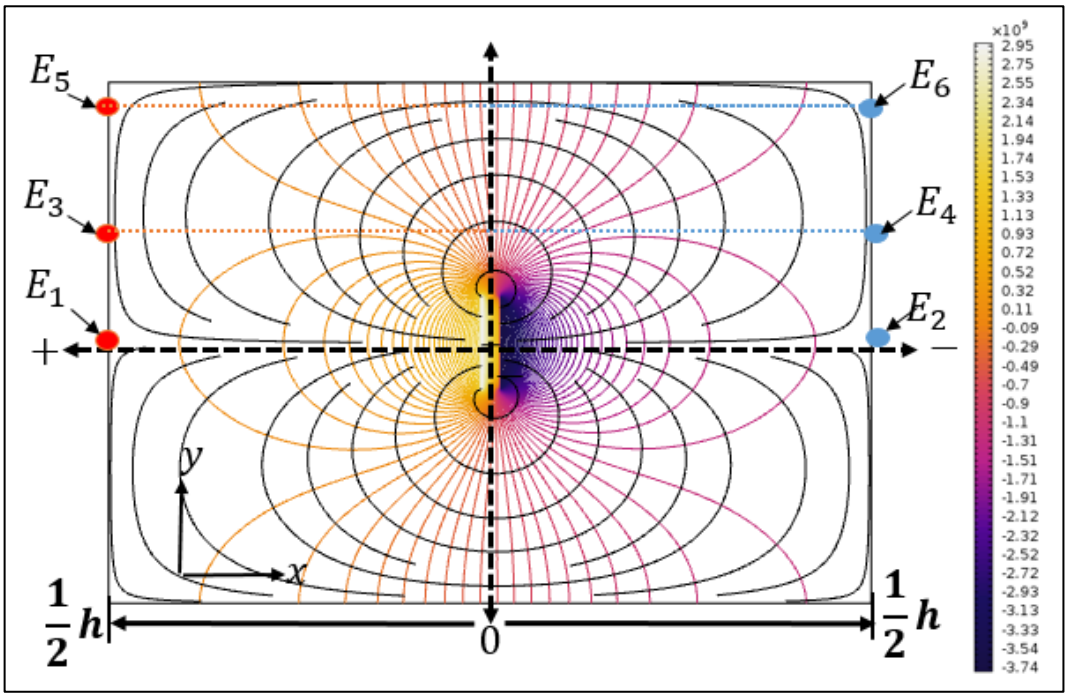

Figure 3.6: Potential distribution for colloidal silica – Equi-log-potential lines are coloured, and current streamlines are black.

Figure 3.6 shows the potential distribution represented for our disc dipole model. The coloured lines represent the equipotential lines, and the black lines represent the streamlines of the current. In the figure, point zero is the centre between the two charge points and the potential is zero. The distance between the two electrodes is $\boldsymbol{h}$ and the distance between each electrode from the centre of the disc dipole is $\frac{1}{2}\boldsymbol{h}$. The electric potential is largest for the electrodes placed along with the ultrasound propagation direction.

UVP refers to the potential difference between any two points in the field (or electrical field integrated between two points). The electrical potential can be measured at maximum value across the propagation direction.

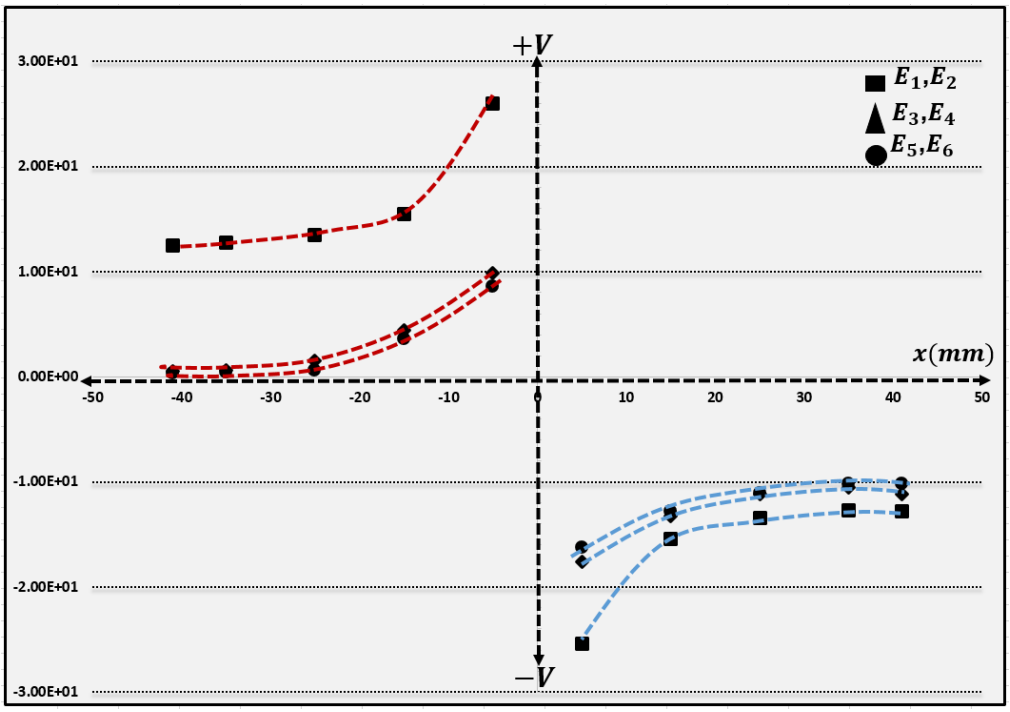

Figure 3. 7: UPVD along E1 (0.1, 28); E2 (81.9, 28), E3 (0.1, 38), E4 (81.9, 38), E5 (0.1, 48), E6 (81.9, 48).

Figure 3.7 shows the potential distribution across the infinitive agar region which contains a two disc dipole. The UVPD is measured across the infinitive agar region with electrodes placed at different locations. The potential measured by E1 and E2, is

larger than the potential measured by E3 and E5, and also is smallest when measured by E4 and E6. E1-E6 are points in the model.

The electric potential increases when the electrode located closer to the source of charge and it's inversely proportional to the distance between the electrodes and the source of charge. The maximum potential can be measured when the electrodes placed parallel across the propagation direction.

The ultrasound beam diameter has a significant effect on the signal generation, the strong vibration of nanoparticles and ions, generate larger signals, this effect analysis by presented the different disc dipole size effect on electric potential measured across the body is presented in figure 3.8.

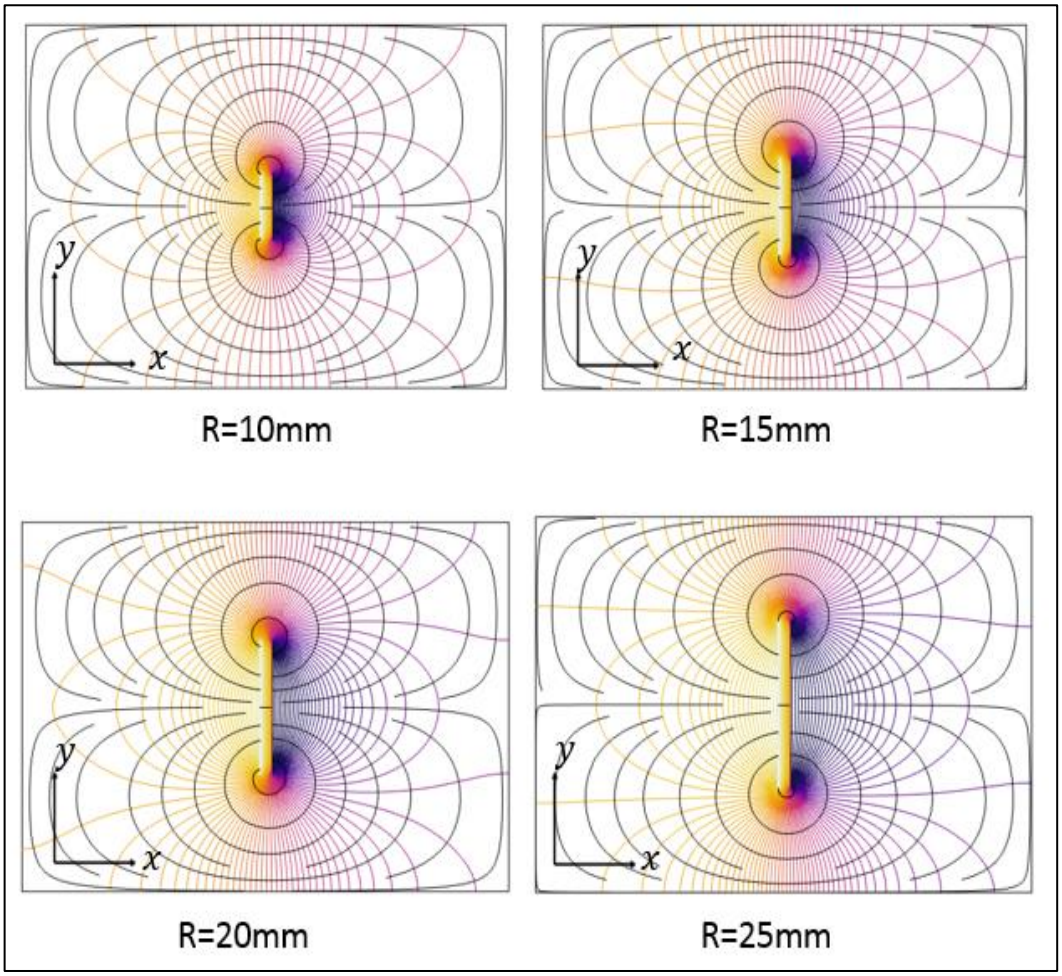

Figure 3.8: Equipotential and current streamlines for different disc dipole diameters (R).

Figure 3.8 shows the relative change in the electric field inside the agar body generated by the disc dipole as a function of disc diameter. It was noted that the potential increases with increased disc dipole diameter, and that the potential becomes more uniform inside the body by increasing the disc dipole diameter.

In order to fully demonstrate the potential distribution in the mock body of agar, we relocated the position of the disc dipoles inside the body and the potential differences were measured by the two electrodes attached to the agar block. This tells us the ultrasound propagation beam has a significant effect on the UVP signal amplitude. According to this result the UVP signal is decrease when the ultrasound beam diameter reduced, this cause a less amount of energy travels through the colloidal region.

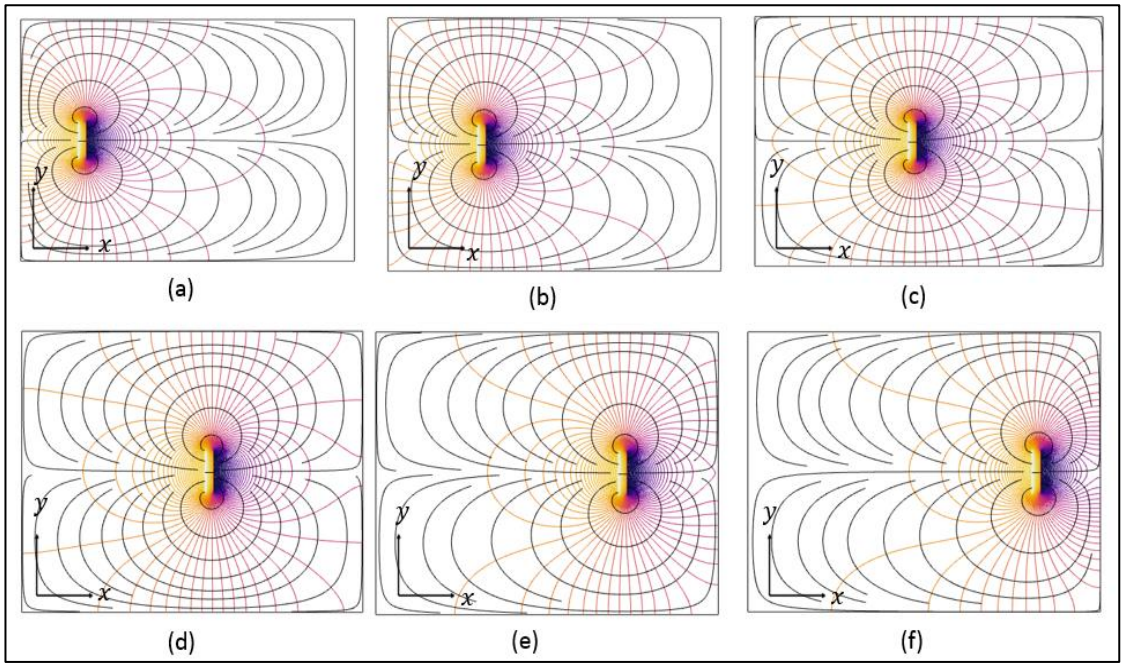

Figure 3.9: UVPD for disc dipoles at different positions relative to the electrodes.

Figure 3.9 each time the disc dipoles location inside the agar block changed in the x-direction from left to right and represent in (x, y) plane. In Figure 3.9a, the disc dipoles are positioned at (14, 16) mm, in Figure 3.9bb they are positioned at (22, 24) mm, in Figure 3.9cc they are positioned at (36, 38) mm, in Figure 3.9dd they are positioned at (44, 46) mm, in Figure 3.9e they are positioned at (58, 60) mm, and in Figure 3.9f they are positioned at (66, 68) mm.

The UVPD measurements for Figure 3.9 are represented in Table 3.1. The relative change in potential difference is larger for disc dipoles with smaller diameters compared to larger disc dipoles with larger diameters. The UVPD is measured by two electrodes attached to the body and increases when the distance between the electrodes and the source of the charge are smaller and vice versa.

According to Figure 3.9, the electric potential has a high value when the distance, $\boldsymbol{h}$, between the dipole and the electrode is small. The potential is more negative when the disc dipole moves closer to electrode E_1, and it is more positive when the disc dipole moves closer to electrode E_2.

Table 3. 1 : UVPD measurements from disc dipole model

$\boldsymbol{Disc_1}$ $\frac{1}{2}h_1(mm)$	$\boldsymbol{Disc_2}$ $\frac{1}{2}h_2(mm)$	ΔV_1 (Disc diameter 10mm)	ΔV_2 (Disc diameter 15mm)	ΔV_3 (Disc diameter 20mm)	ΔV_4 (Disc diameter 25mm)
14	16	15.0536	12.233	10.0084	8.4304
22	24	10.025	9.7479	8.3184	7.6637
36	38	7.6656	7.5656	7.3826	7.136
44	46	7.7912	7.6555	7.3983	7.1647
58	60	10.2090	9.3168	8.4381	7.8287
66	68	15.8516	13.9184	10.8016	8.7422

Table 3.1 shows the potential difference measured by both electrodes across the region. Where $\frac{1}{2}\boldsymbol{h_1}$ is the distance between the negative point of charge and E_1, and $\frac{1}{2}\boldsymbol{h_2}$ is the distance between the positive point charge and E_2. From the table, we can see the change in potential difference relative to the distance between the electrode and the point of charge is larger for a smaller charge source.

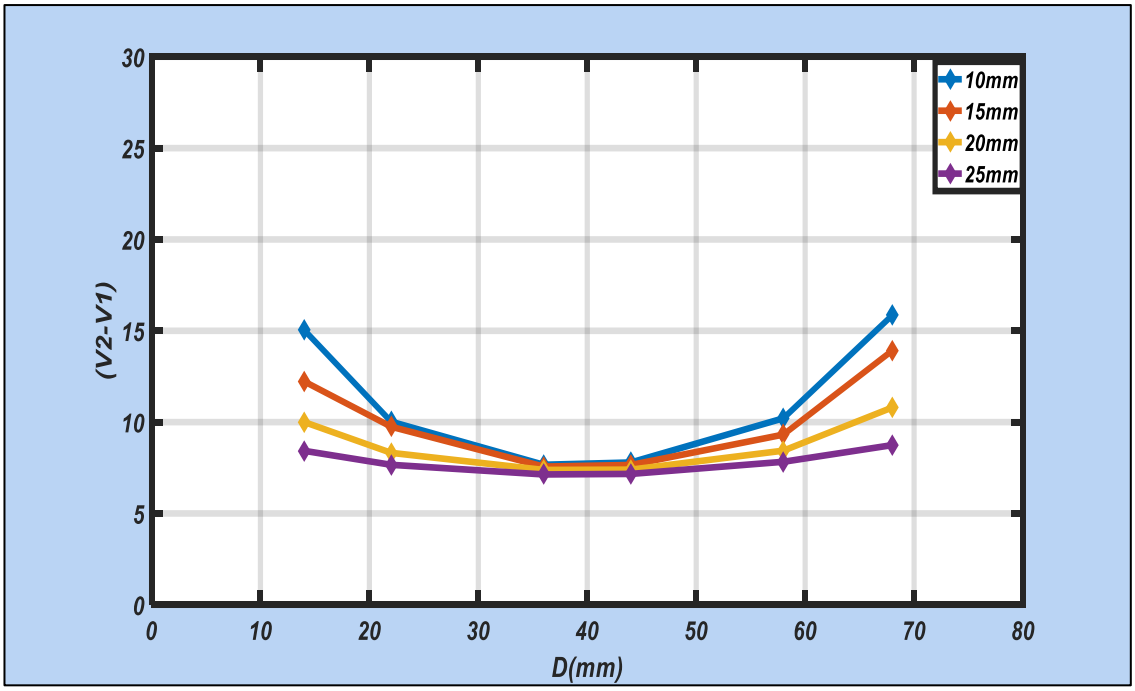

Figure 3.10: UVP measurement across the length (D) of agar body from the disc dipole model for a disc charger with diameter of (R=10, R=15, R=20, R=25) mm.

Figure 3.10 shows the potential difference measured by both electrodes, E_1 and E_2. The result shows the signal attenuated when the electrodes are far away from the source of the charge. The effect of the disc dipoles on signal attenuation is not the same for discs with different diameters. This is because larger discs give a larger charge, and a larger charge inside the body has less attenuation as compared to a smaller charge within the same body.

3.5Summary

In this Chapter, the setup for the excitation signal of the UVP imaging system was explained. The polarization of ions in a colloidal solution arises due to the presence of ultrasound pressure. This creates multiple dipoles, and the summing of these dipoles is measured as an electric signal, called the UVP. The pulsed excitation signal required for the UVP method of measurement is explained. The description of this polarization as it arises in the colloidal solution or ionic electrolyte was demonstrated.

A new static charged disc dipole model with its equivalent circuit model are presented which provides a simple method to review the ultrasound vibration potential distribution

(UVPD) inside a finite region and an agar mock body, respectively. This (UVPD) model based on a static charged disc dipole field is proposed. Set-ups with single and multiple sample cell are numerically simulated. The effect of the disc dipole diameter on UVP signal strength is simulated. The simulation also indicates the optimized locations of electrodes should be at the nearside and rear-side of the body, although UVP can be measured between anywhere around the body except the locations in orthogonal to the direction of ultrasound propagation, in the principle. The experimental data for UVPD 0evaluation not presented in literature, therefore to evaluate our model, With an assumption of the ultrasound beam width being the same as the diameter of the ultrasound transducer (in 25 mm), signals from a setup with multiple sample cells are measured as given in (Chapter 5 section 5.8,Figure 5.18).

CHAPTER FOUR: FREQUENCY RESPONSE AND PHASE ANGLE AS A FUNCTION OF PARTICLE SIZE

Summary: *This chapter presents two primary objectives. The first objective is to report the frequency response as a function of particle size. This was carried out by measuring the colloid vibration potential (CVP) signal from selected silica dioxide particles. The second objective is to demonstrate the particle size as a function of the phase shift. It explains how large and small particles vibrate when a high ultrasound pressure is applied into a colloidal region – these tests were conducted by detecting the ultrasound vibration potential (UVP) signal from both silica and titanium dioxide.*

4.1Introduction

This Chapter details the experimental work explaining the spectroscopic frequency response measurement for silica dioxide, SiO_2. We tried to set the chirp signal to measure the CVP signal, but due to the facility limitation, it was not possible to use the chirp signal. Our facility provides a chirp signal with a minimum period of 1 ms, and this requires at least a 1.5 m width of sample in order to detect the UVP signal. Therefore, we have had to use a different method to measure the frequency response as a function of particle size.

An impedance/gain phased analyser was used under the control of SMART software to send a series of consecutive frequency pulses. To measure an accurate frequency response from the particles, we calibrated our data with the transducer's performance in the water. We used silica dioxide, with different particle diameters to measure the frequency response – the frequency range used was from 500 kHz to 2 MHz with increments of 100 kHz.

The second part of this Chapter explains the experimental method used to demonstrate the particle size as a function of phase shift in colloidal suspensions. This innovative work was carried out for the two different materials, titanium dioxide and silica dioxide. The objective of this work was to characterize the particle size in terms of frequency response and phase shift.

4.2Materials and Methods

4.2.1 Ionic Electrolyte

Potassium chloride, magnesium chloride, calcium chloride, rubidium chloride, strontium chloride, and barium chloride were purchased from Sigma Aldrich (UK). We used molar solutions which are the most useful in chemical reaction calculations because they directly relate to the mole of the solute to the volume of solution. The sample were prepared at a 1 M concentration. The table below (Table 4.1) shows the preparation of the electrolytes. We prepared a 50 ml solution for each electrolyte by mixing their anhydrous chloride with 50 ml of deionized water.

Table 4. 1 : Ionic electrolytes

Solution	**Formula**	**Mw (gram/mol)**	**Weight (gram)**	**Solubility in Water**
Potassium chloride	KCl	74.55	3.7275	Soluble
Magnesium chloride	$MgCl_2$	95.211	4.760	Soluble
Calcium chloride	$CaCl_2$	110.98	5.549	Soluble
Strontium chloride	$SrCl_2$	158.53	7.9265	Soluble
Barium chloride	$BaCl_2$	208.23	10.4115	Soluble
Rabidium chloride	$RbCl_2$	296.094	14.8047	Soluble

We used hydrogen chloride (HCl) and sodium hydroxide (NaOH) to adjust the pH value to 7. The ionic species $(\text{i.e. } N = 4), H^+, OH^- \; Na^+, Cl^-$ were dissolved in the solution.

4.2.2 Colloid Suspensions

Colloidal suspension of titanium dioxide (TiO_2) were purchased from Ionic Liquid Technologies [Iolitec, Salzstrasse 184, D-74076 Heilbronn]. The sample size provided by the manufacturer was 5, 15, 20, 35, 70, 100, 200 nm. The sample was first weighed using a balance accurate to 2 decimal places and the original sample was deionized using ion exchange resin beads (from Bio-Rad) and diluted to 1 wt% concentration. The commercial samples had to go through a pre-treatment process in order to remove unknown ions. The samples were filtered using a Büchner funnel and flask. The ultrasound probe used for sonication had an amplitude control of 38% (controlled amplitude by the sonicator) which enables control of the probe intensity. The particle size distribution was measured by a Malvern Zetasizer and gave measurements of 12, 21, 33, 45, 55, 85, 113, and 201 nm respectively. The particle size changes due to the aggregation and pretreatment process.

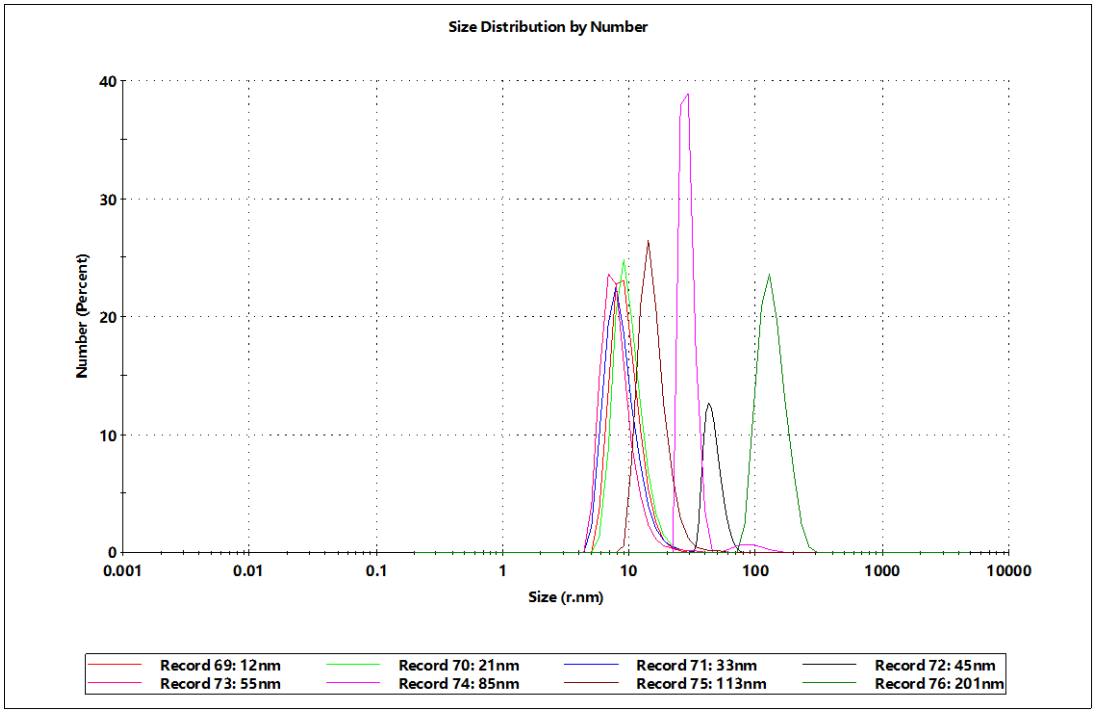

Figure 4.1 Particle size distribution for titanium dioxide nanoparticles suspended in deionized water with a concentration of 1 wt%.

Figure 4.1 shows the average particle size distribution as measured by the Mastersizer. The particles become charged through protonation and deprotonation processes, (Murat, (2014). The ionic mass transportation within the electrolyte is governed by the Poisson-Boltzmann equation:

$$\nabla^2\varphi = -\frac{\mathrm{F}}{\varepsilon\epsilon}\sum \mathrm{z_i C_{io}} \exp[\mathrm{z_i F}\varphi/\mathrm{RT}] \tag{4.1}$$

Where $\boldsymbol{\varphi}$ is the electric potential of the fluid, $\boldsymbol{F}$ is Faraday's constant, and $\boldsymbol{C_{io}}$ is the bulk molar concentration. The ionic species valences are $i = 1H^+$, $i = 3Cl^-$, $i = 4$, for OH^-, $\boldsymbol{R}$ is the gas constant, and $\boldsymbol{T}$ is the fluid temperature. The charge regulation can be accounted for by two single protonation reactions, T_i, with equilibrium constant K_A and K_B:

$$T_iOH \leftrightarrow T_iO^- + H^+ \tag{4.2}$$

$$T_iOH + H^+ \leftrightarrow T_iOH_2^+ \tag{4.3}$$

$$K_A = \frac{N_{T_iOH} - [H^+]}{N_{T_iOH}} \tag{4.4}$$

$$K_B = \frac{N_{T_iOH_2^+}}{N_{T_iOH_2^+} - [H^+]} \tag{4.5}$$

The total number of site densities are:

$$N_{total} = N_{T_iOH} + N_{T_iO} - N_{T_iOH_2^+} \tag{4.6}$$

$$\sigma = FN_{total}\left[\frac{K_A - K_B[H^+]^2}{K_A + [H^+] + K_B[H^+]^2}\right] \tag{4.7}$$

Where, σ is the surface charge density for the titanium nanoparticles.

The colloidal suspension of silica nanoparticles (SiO_2) was purchased from Fuso Chemical Co. Ltd, Japan [Quartron PL Series]. The sample preparation was similar to the titanium dioxide process. The sample size provided by the manufacturer was 12 nm. The particle size distribution was measured at 21 nm using the Malvern Zetasizer. The particle size changes due to the aggregation and pre-treatment process.

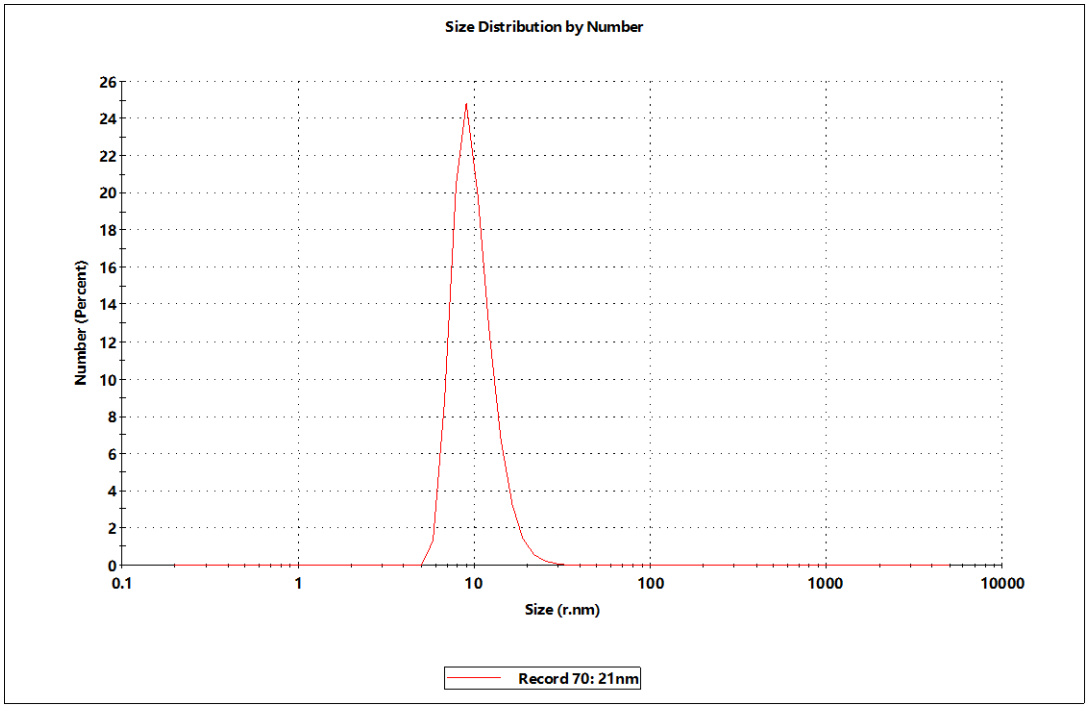

Figure 4.2: Particle size distribution (SiO_2, 21 nm.1 wt %).

4.3 Frequency Response Measurement

This experimental work consisted of an electro-acoustic spectroscopic measurement of a selected silica dioxide sample in deionized water. The CVP measurement was conducted using the Leeds standard II device and the signal transferred from a time domain to a frequency domain. The procedure for this work is explained in the following sections.

4.3.1 Sample Preparation

In this experiment we used silica dioxide purchased from [Sigma-Aldrich, UK, Pcode 1001046586]. The particle sizes provided by the manufacturer were 12, 20, 80, and 200 nm. The process involved in making the colloidal suspension is explained briefly in Section 4.2.2. The nanoparticles were suspended in deionized water with a concentration of 1 %wt. The particle size distribution (PSD) was measured by a Malvern Zetasizer and the results are shown in Figure 4.3.

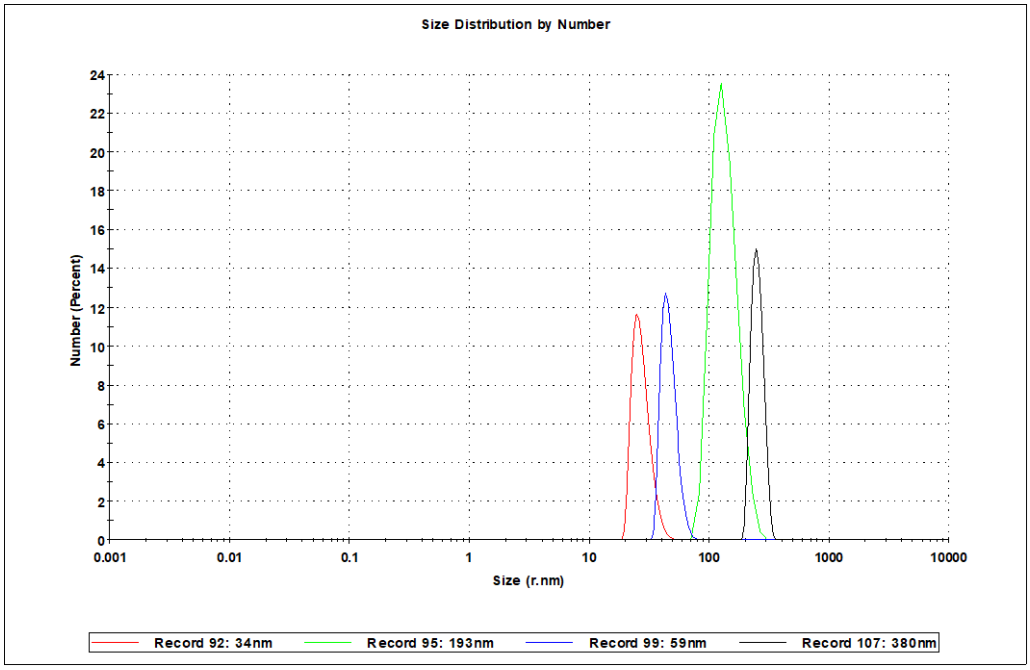

Figure 4.3: Particle size distribution for SiO_2 nanoparticles suspended in deionized water with a concentration of 1 wt%.

The actual measured particle size is different from the measurements provided by the manufacturer. The sample was prepared in three days and the PSD measured by the Zetasizer, Malvern, (2017). The change in particle measurement was to be expected due to the aggregation and sample preparation process. If you leave a sample for a while, the nanoparticles in a colloidal suspension stick together and the measured particle size can, therefore, be altered.

The measured particle size is the average size – the suspension could, of course, contain smaller and larger particles. The pre-processing method of sample preparation affects the measurements and also the number of ions in the suspension.

4.3.2 Transducer Calibration

We examined the transducer performance in water which is related to the central transducer frequency maximizing related signal. The aim of calibrating the data is to remove the transducer performance measurement from the material measurements as they responded to the frequency. The set up for the transducer calibrations is given in Table 4.2.

Table 4. 2 : Transducer calibration test setup

Instrumentation	Specification
Function Generator Frequency (start-stop) Amplitude Sweep Time	 (500 kHz – 2 MHz) 2 $V_{(pk-pk)}$ 1 ms
Ultrasound Pulser/Receiver	Gain 39 dB
Transducer1	1 MHz
Transducer 2	1 MHz
Oscilloscope	Channel 2 synchronized Channel 3 signal

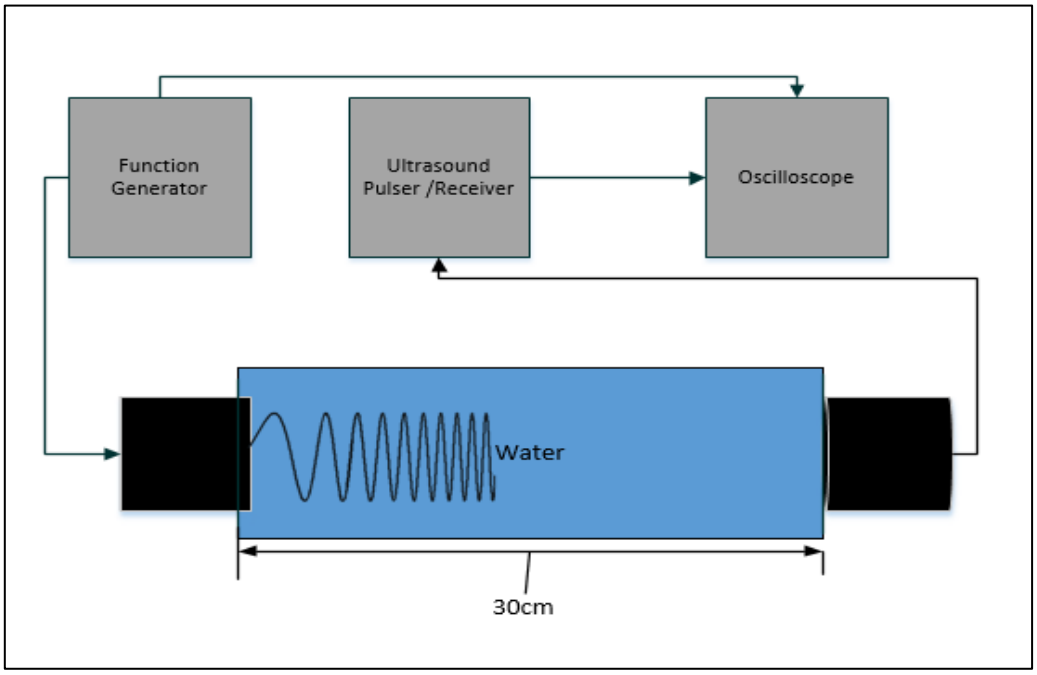

Figure 4.4: Diagramm for detecting the transducer performance in the water.

Figure 4.4 shows the connection diagram for the transducer signal detection. Both transducers were placed in parallel and facing each other. We used two transducers: one as a transmitter which was directly connected to the function generator and the second as a receiver which related to the ultrasound pulser/receiver. Both sensors had the same

frequency of 1 MHz and the ultrasound pulser/receiver was used to amplify the detected signal and pass it to the oscilloscope for calibration. The calibration test was carried out to find the transducer's performance in the water. The experiment setup diagram and connections is shown in Figure 4.4.

Both transducers were placed face down in the water and both have similar properties. The tank was filled with deionized water. In order to fully calibrate the data, we need to normalize the data first. The normalization procedure was carried out first by normalizing the transducer performance in the water; the calculation is to subtract the minimum amount from each value and then divide this by the difference between the maximum and minimum values.

The equation below explains this calculation:

$$\boldsymbol{N_i(A_i) = \frac{A_i - A_{min}}{A_{max} - A_{min}}} \tag{4.1}$$

Where, $i = 1,\ 2\ , 3, \ldots n,\ A_i$ is a signal amplitude, A_{min} is the signal with minimum amplitude, A_{max} is the signal with maximum amplitude, and $N_i(A_i)$ is the normalized signal amplitude. The normalized data for the transducer's performance in water is shown in Figure 4.5.

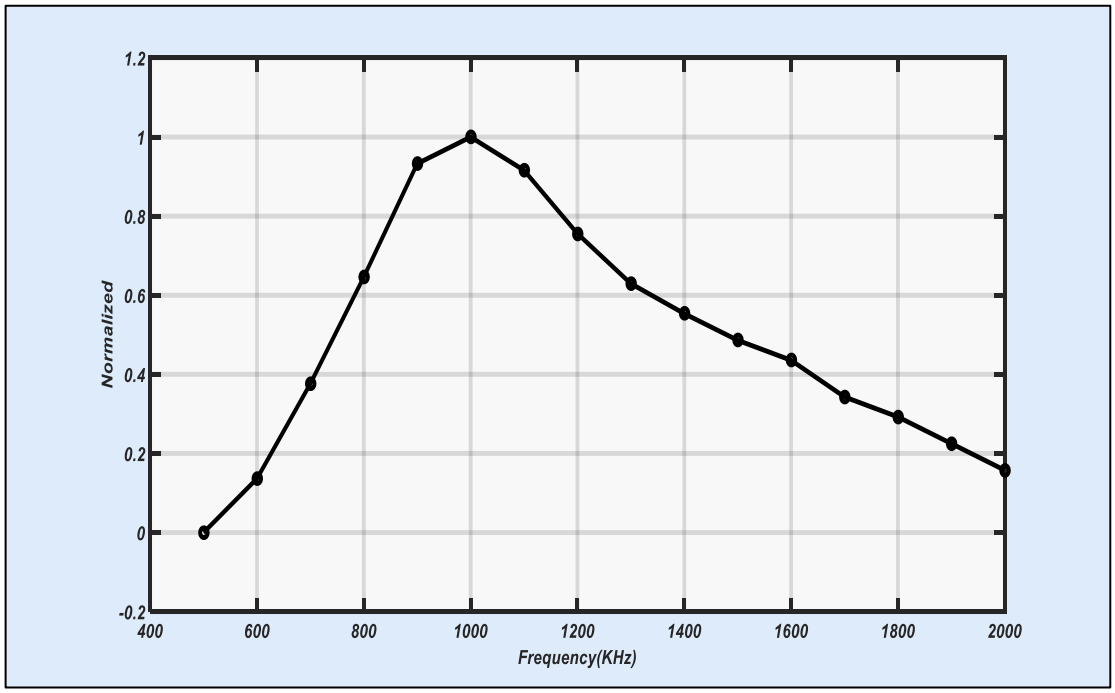

Figure 4.5: 1 MHz transducer performance in the water.

4.3.3 The CVP Measurement Setup and Procedure

The experimental procedure for the CVP measurement and the diagram of connections are shown in Figure 4.6. This experiment has both inputs and outputs. The input consists of an impedance/gain phased analyser, Ametek., (2019) to generate the signal controlled by a computer with SMART^{i} impedance measurement software to set the value of sweep frequency at 500 kHz–2 MHz, with 10,000 repeatable loops, and an amplitude of 1 $V_{(pk–pk)}$. The generated signal was sent to an RF gated amplifier to amplify the signal. The RF amplifier has a duty cycle of 0.3% and is able to amplify the signal up to 1000 $V_{(pk–pk)}$, but it has a potentiometer to control the output so we amplified our signal up to 600 $V_{(pk–pk)}$ only. The signal was synchronized by a signal generator. The amplified signal was sent through the sample via a piezoelectric transducer having a frequency range 1–5 MHz, and a crystal diameter of 25 mm. The CVP electrical signal was generated by the sample and detected by the two mesh sensors placed at both sides of the sample. The output signal was collected by the mesh sensor and sent to the voltage amplifier with an amplification factor of 39 dB. The amplified signal was then sent to the oscilloscope for calibration and collection of the data. The CVP signal was detected in the time domain and we used a fast Fourier transform (FFT) to convert the time domain to the frequency domain.

FFT is an algorithm which converts a signal, for example, over a period of time and divides it into its frequency components. It converts a signal in its original domain to a frequency domain, Paul, (1998) and vice versa. The time domain is how the signal changes over time, but the frequency domain is how much signal lies within each frequency band over a range of frequencies. The Leeds standard II device was used in this experiment rather than the Leeds standard III device only because of the time the experiments were carried out.

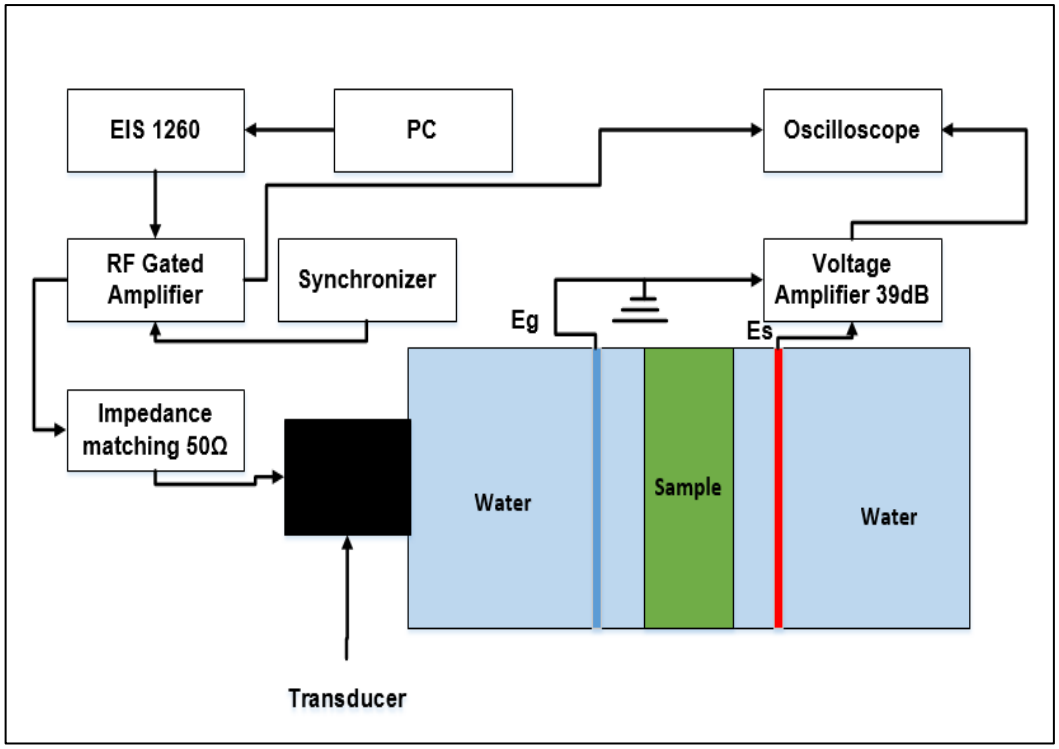

Figure 4.6: Diagram of experiment setup and connections.

Figure 4.6 shows the diagram of our experimental setup and connections for CVP measurement using different frequency ranges between 500 kHz–2000 kHz.

4.3.4 Results and Discussion

The CVP signal was generated by the silica dioxide suspension and measured by both mesh sensors placed at each side of the sample. This signal was amplified by the voltage amplifier with an amplification factor of 39 dB and then displayed on the oscilloscope. The data collected from the oscilloscope and the CVP signal processed by using the MATLAB. All samples have similar concentrations of 1 wt%. The particle size is presented in the graphs below in the form of $(\boldsymbol{m})\boldsymbol{n}$, where $\boldsymbol{n}$ is the measured PSD by the ZetaSizer and $\boldsymbol{m}$ is the size provided by the manufacture.

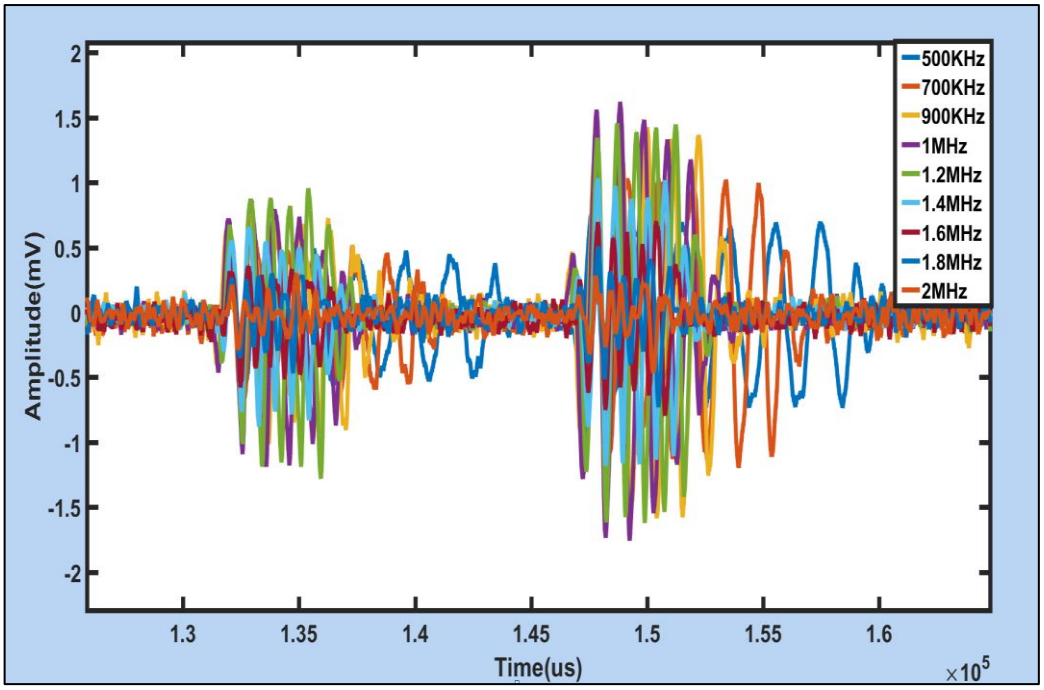

Figure 4.7: CVP signal for silica nanoparticles (12)34 nm, a concentration 1 wt %, and frequency ranges from 500 kHz to 2 MHz).

Figure 4.7 shows the CVP signal for silica dioxide suspensions having a concentration of 1 wt%, with different frequencies ranging from (500–2000) kHz in increments of 200 kHz. The measured CVP signals are presented in different colours for each frequency. The CVP signal for the same silica sample shows a different amplitude and this is due to the transducer performance for different frequency ranges. The CVP signal presented in Figure 4.7 is in the time domain, and in order to change it into a frequency domain we must use the FFT method, Hans (2015). The signal was transferred to the frequency domain using the FFT method and the data normalized, as explained in Section 4.3.1, using Equation 4.1. The transformation process of the signal from the frequency domain to the time domain carried out by using the MATLAB (see the MATLAB code in Appendix A2).

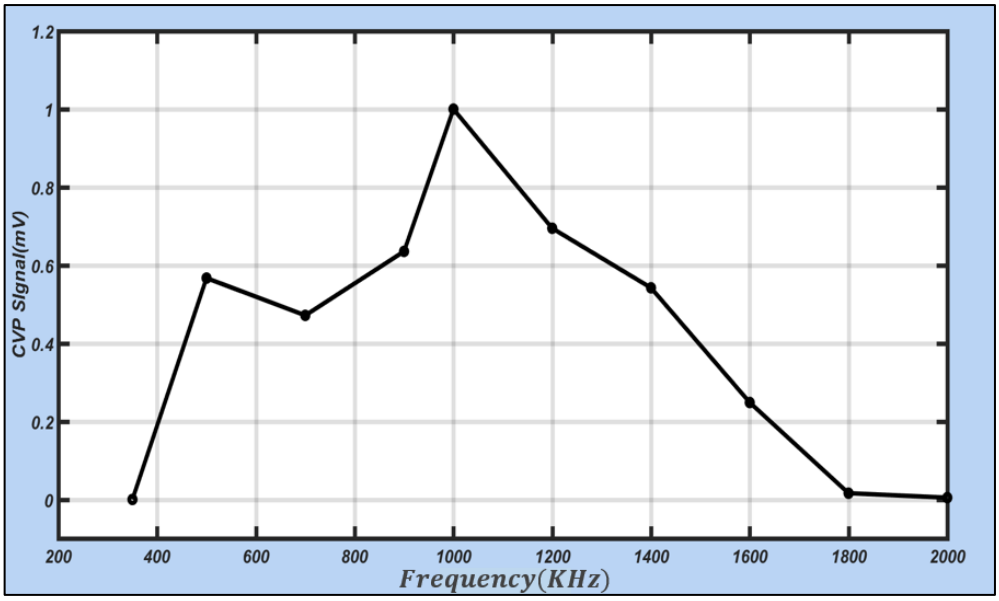

Figure 4.8: The frequency response measurement for the silica nanoparticles ((12)34 nm diameter and concentration of 1 wt %).

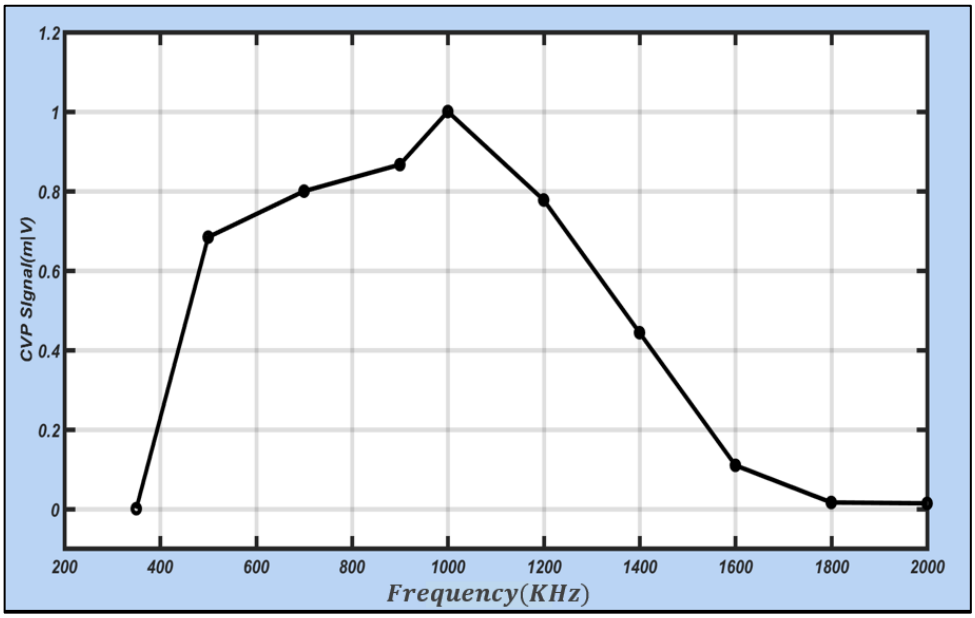

Figure 4.9: The frequency response measurement for the silica nanoparticles ((20)59 nm diameter and a concentration 1 wt%).

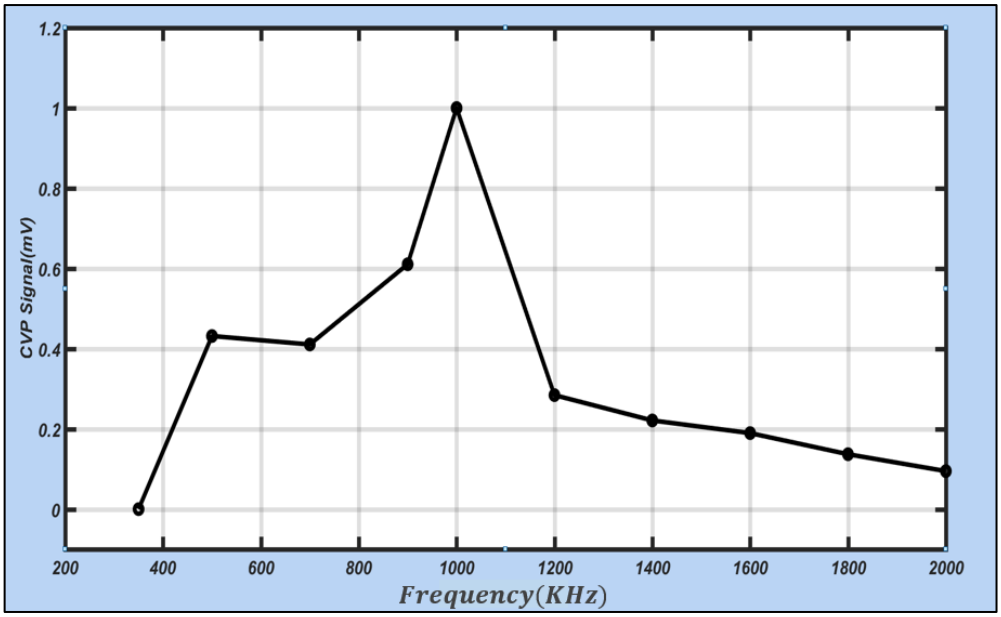

Figure 4.10: The frequency response measurement for the silica nanoparticles ((80)193 nm diameter and a concentration 1 wt%).

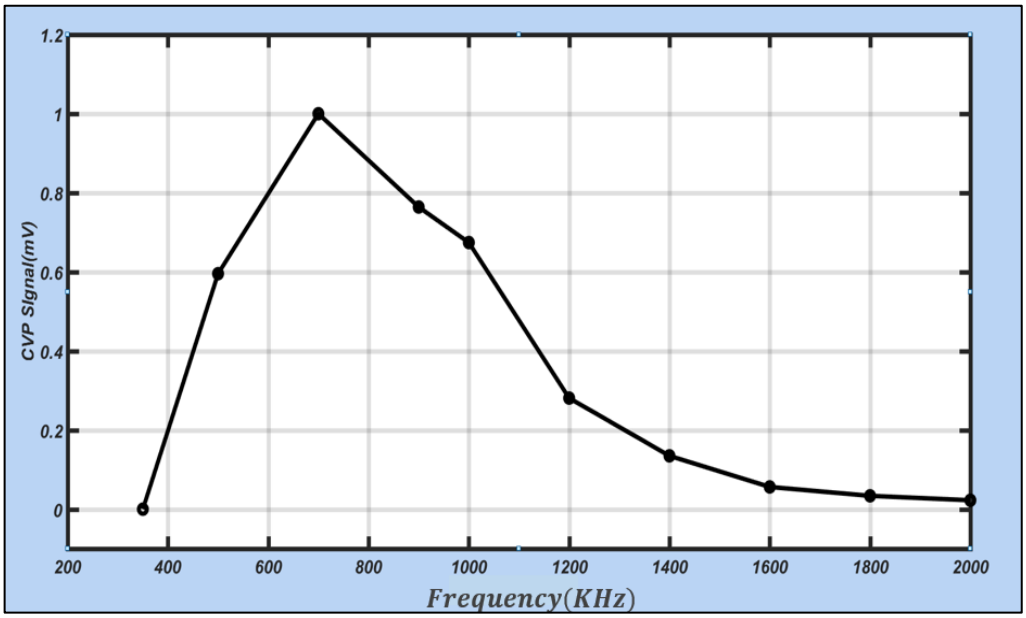

Figure 4.11: The frequency response measurement for the silica nanoparticles ((200)380 nm diameter and a concentration 1 wt%).

The detected data are expected with the resonance frequency of the transducer, the amplitude decreases at both sides and is shifted at 1MHz. A similar process was carried out for all silica nanoparticles with different particle diameters.

The transducer performance is related to a central frequency, this maximizes the signal amplitude. We need to present the true frequency response from the nanoparticles vibration, and in order to do that, we remove the transducer performance through the calibration process. So, in order to remove this effect on our data we calibrated our data. The information on how to calibrate the data and the transducer performance can be seen in, Khan, et al (2010).

The transducer's performance in water is presented in Section 4.3.1. All data are normalized in Figures 4.7, 4.8, 4.9, 4.10, and 4.11. The normalization process was carried out using Equation 4.1. The normalization procedure for the CVP signal in colloidal suspensions is explained by Equation 4.2:

$$\frac{\boldsymbol{A_j - A_{min}}}{\boldsymbol{A_{max} - A_{min}}} = \boldsymbol{N_j(A_j)} \tag{4.2}$$

Where, $j = 1, 2, 3, \ldots n,$ A_j is a signal amplitude, A_{min} is the signal with minimum amplitude, A_{max} is the signal with maximum amplitude, and $N_j(A_j)$ is the normalized signal amplitude. The same procedure was used for both transducers' performance in water and the CVP signal amplitude measured for each sample. To calibrate our CVP data with the transducer performance we used Equation 4.3:

$$\boldsymbol{N(A)} = \frac{\boldsymbol{N_i(A_i)}}{\boldsymbol{N_j(A_j)}} \tag{4.3}$$

Finally, the data using Equation 4.3 is presented in Figure 4.12. The graph shows all the previous figures combined into one for ease of comparison – it is the frequency response measurement for silica nanoparticles with diameters of 34^{12}, 59^{20}, 193^{80}, and 380^{200} nm.

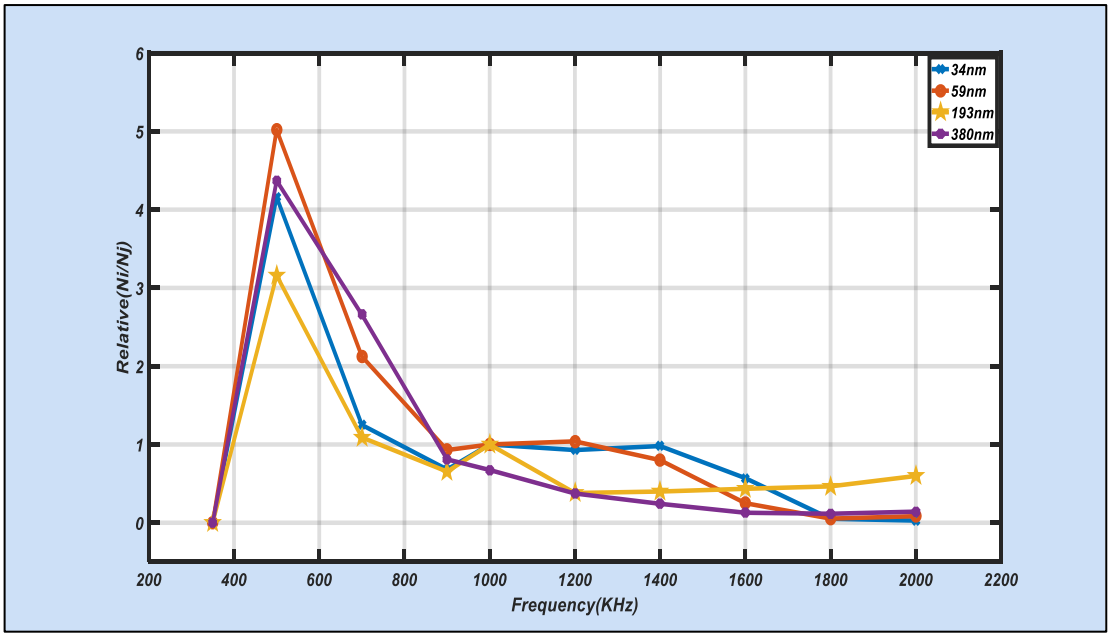

Figure 4.12: The frequency response measurement from all the silica nanoparticles suspended in deionized water with diameters of $[(12)34, (20)59, (80)193, and (200)380]$ nm, with concentration 1wt%.

From Figure 4.12, we can see the frequency shifted for all the different sized particles around a frequency of 700 kHz and shows the highest peak for all at 500 kHz, due to domenance of concentration effect. This method is a good method for PSD measurement because it can characterize particle size at high concentrations of up to 50%. This method can also characterize a suspension with more than one dispersed phase. These two unique features make this method very attractive for PSD in many different samples. However, light technique methods are not suitable for these applications because most optical methods require the sample to be diluted prior to measurement, and most light-based systems cannot measure PSD for multi-dispersed systems. According to O'Brien (1987), the excitation frequency is indirect proportion with the electrophoretic mobility constant. Detecting the effect by frequency response measurements is possible. Further work can be done using a chirp signal and high concentrations of multi-dispersed systems.

4.4The Particle Diameter as a Function of Phase Angle

The CVP signal measurement is explained in Chapter 5, Section 5.3.3. The overall aim is to investigate how small and large particles vibrate in colloidal suspensions under

ultrasound pressure. This method can be used for characterizing nanoparticles in colloids, such as the particle size measurement. In order to study how larger particles and smaller particles vibrate, we need to measure the phase difference as a function of particle diameter. Different particle diameters have different phase angles and different vibration accelerations due to the different forces acting on them e.g. pressure and drag force. This experimental investigation was carried out using silica dioxide with particle diameters of 34, 59, 193, and 380 nm (PSD shown in Figure 4.3) and titanium dioxide with particle diameters of 51, 185, 285, and 384 nm (PSD shown in Figure 4.1). The samples were suspended in deionized water with a concentraion of 1 wt%. The CVP signal was measured using the UVP Leeds standard II methodology, and the samples fixed at the exact same position for all measurements.

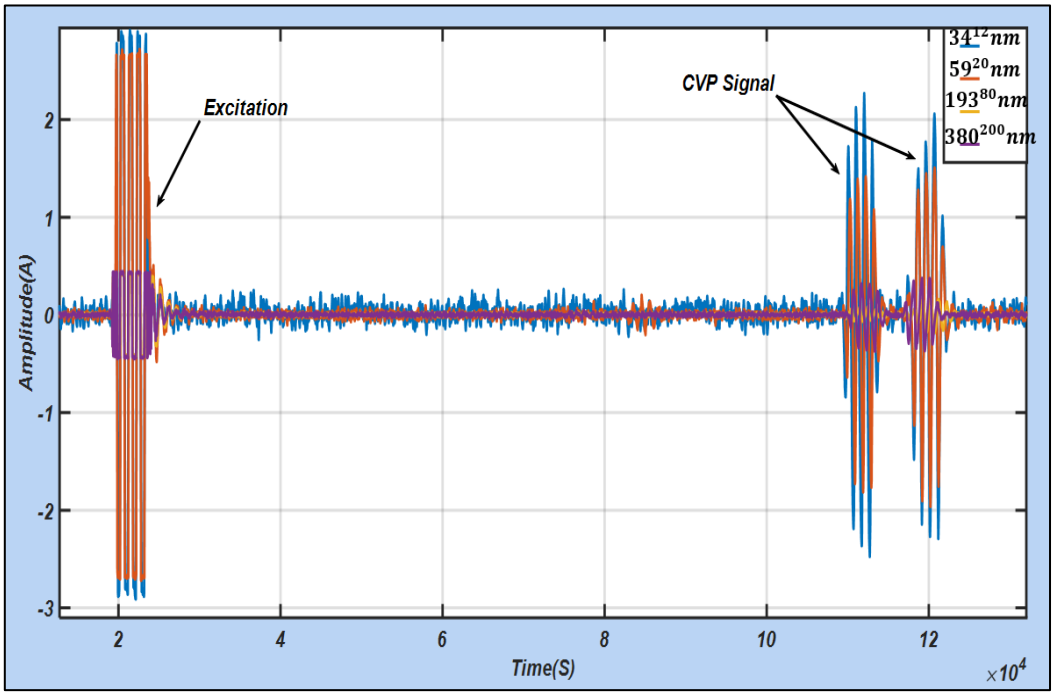

Figure 4.13: CVP signal measurement for silica nanoparticles (34 nm, 59 nm, 193 nm, 380 nm) and concentration 1 wt%, frequency 1 MHz.

Figure 4.13 shows the CVP signal amplitude measured for silica nanoparticles suspended in deionized water with a concentration of 1 wt%. The signals are displayed with an amplification factor of 500 kV/A. In order to see how the signals appeared for all different particle sizes, we enlarge (zoom) the CVP signals. For each test we injected the sample into the sample chamber and then, after the test was finished, we used a

plastic pipette to take the sample out and then cleaned everything with deionized water before using the sample chamber for the next test. Each test was repeated three times.

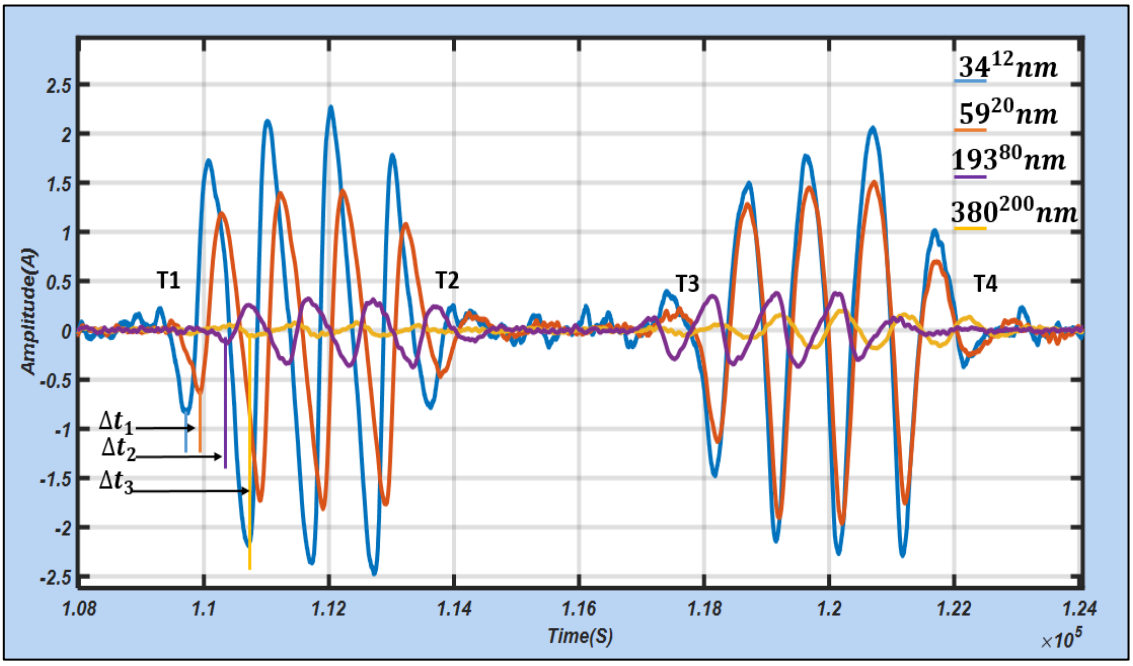

Figure 4.14: Two bursts of CVP signal measured from silica nanoparticles having diameters of 34, 59, 193, and 380 nm, with a concentration 1 wt%, and frequency of 1 MHz.

The time difference between the appearances of each CVP signal peak for each sample was measured at Δt (μs). In order to calculate the phase angle, we require a reference, and at this point we choose one of the CVP signals relative to the other three CVP signals. In order to obtain a clear view of the phase difference between different signals we enlarged (zoomed out) each tail of the signal and this is shown in Figure 4.15. In the silca suspensions the particle with a diameter of 380 nm was used as the reference and in the titanium dioxide suspension the particle with a diameter of 384 nm used as the reference in order to measure the phase difference of the other particles. Both the reference and the samples had the same concentration of 1 wt%. The further literature related to the phase angle can be found in, Divell (2010).

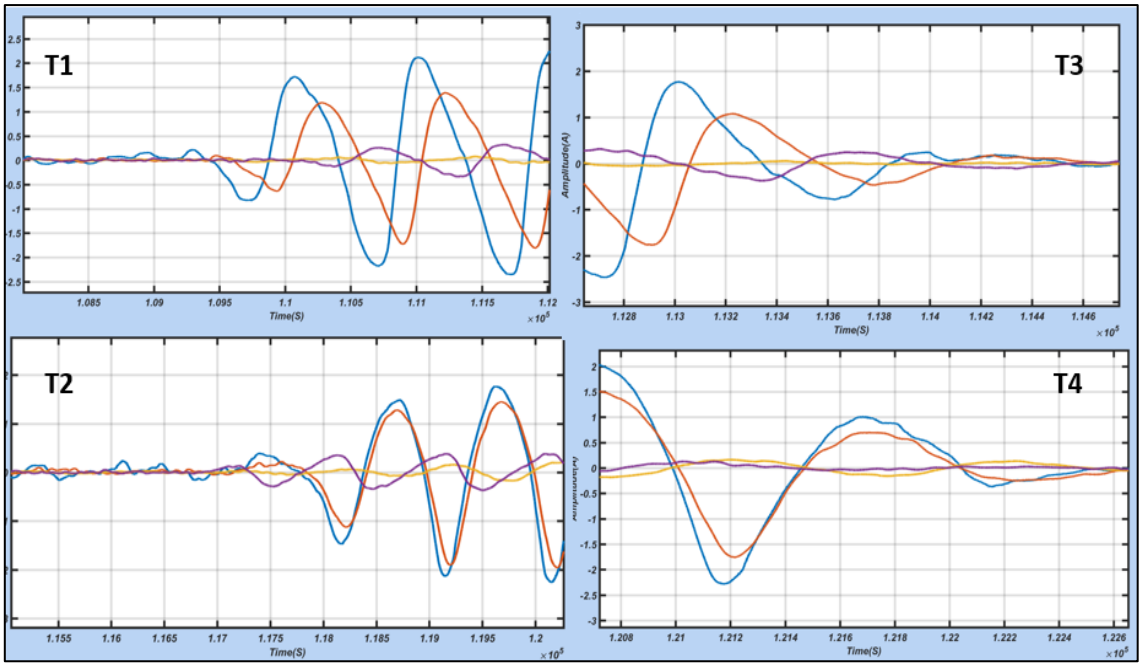

Figure 4.15: Enlarged CVP signal tails for silica nanoparticles.

To calculate the phase angle, we use the following equation.

$$\boldsymbol{\varphi = \frac{kx}{\lambda} = \frac{2\pi\Delta t}{T}} \tag{4.4}$$

Where, $\mathbf{T\ (s) = \frac{1}{f(Hz)} = 1\ \mu s.}$

Table 4. 3 : Particle size as a function of phase angle (silica dioxide)

Particle diameter (nm)	Δt (μs)	Period T(μs)	Concentration wt%	Error %
34	0.06	1	1%	2.3%
59	0.04	1	1%	2.7%
193	0.02	1	1%	3.1%

Table 4.3 shows the measured phase angle for silica nanoparticles suspended in deionized water using Equation 6.4. The relative change of the phase angle of different particle diameters of silica nanoparticles is shown in Figure 4.16.

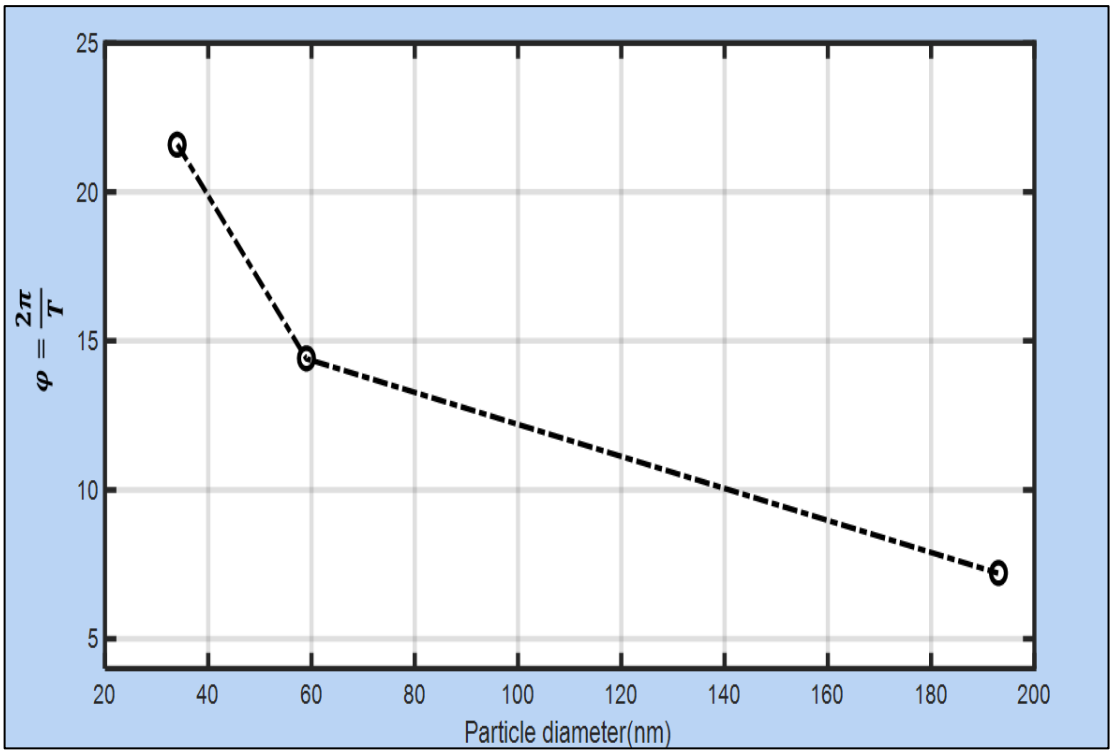

Figure 4.16: Relative changes in phase angle vs particle size with a concentration of 1 wt% for silica nanoparticles.

From Figure 4.16 we can see the phase angle decrease for particles with a larger diameter. This result tells us that when ultrasound pressure is applied to a colloidal suspension, all the particles in the colloid start to vibrate at the same time, but smaller particles accelerate faster than larger particles.

A similar test was carried out for titanium dioxide suspended in deionized water having particle diameters of $51, 185, 285,$ and 394 nm. The PSD, as measured by the Mastersizer, is shown in Figure 4.17. The reason for using two different materials is to further verify whether a similar effect is measured for different samples. The CVP signal was measured for every sample with a frequency of 1 MHz, and concentration of 1 wt%. In both cases the samples were prepared at the same time and measurements taken over several hours on the same day.

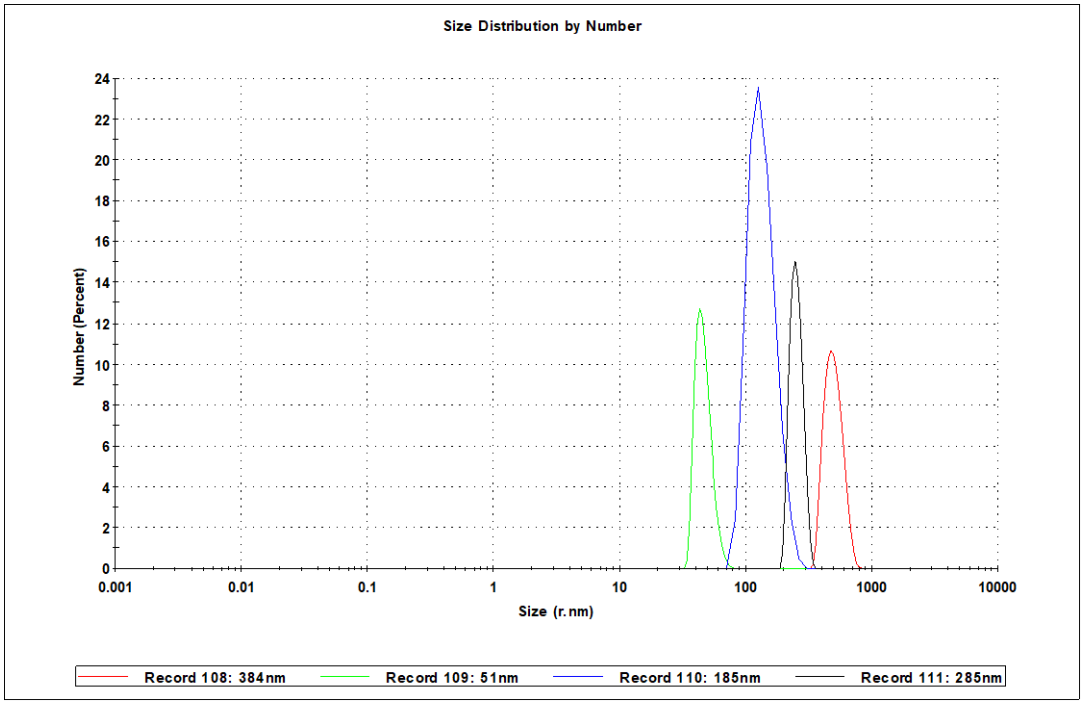

Figure 4.17: Particle size distribution for titanium dioxide nanoparticles suspended in deionized water with a concentration of 1 wt%.

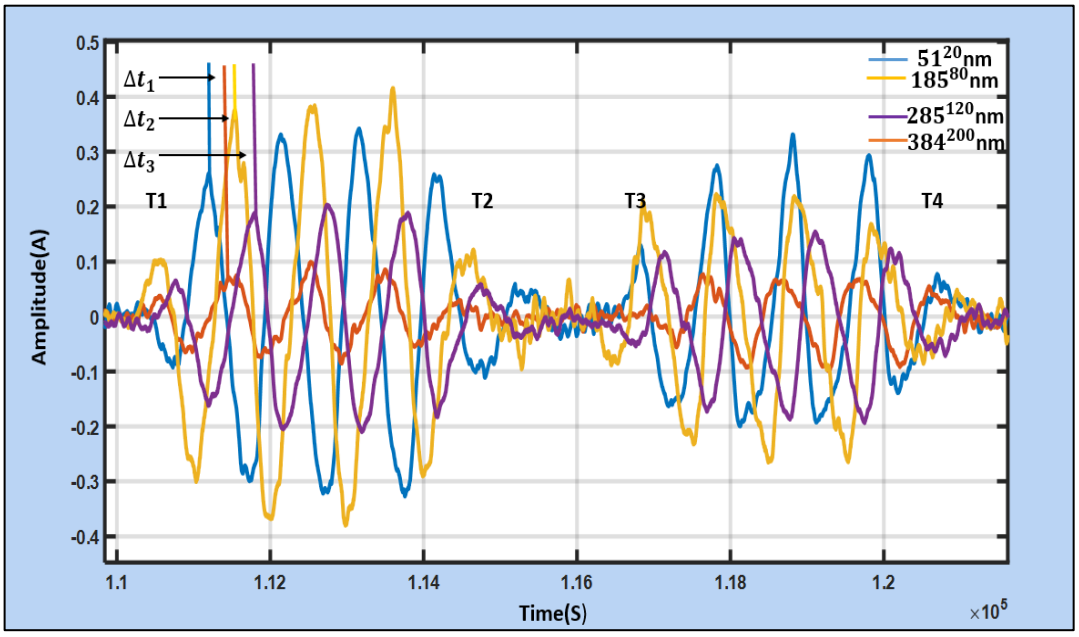

Figure 4.18: Two bursts of CVP signal measured from titanium nanoparticles with a concentration 1 wt%, frequency 1 MHz and diameters of 51, 185, 285, and 384 nm.

Both CVP signals appeared at both sides of the samples. The signals were measured with a frequency of 1MHz. Figure 4.18 shows the CVP signal detected for titanium dioxide nanoparticles suspended in deionized water. In order to obtain a clear view of

the phase difference between different signals we enlarged (zoomed out) each tail of the signal and this is shown in Figure 4.19. From Figure 4.18 the value of the time difference, Δt, is measured with reference to the signal of the titanium dioxide nanoparticle with a particle diameter of 384 nm. The measured data is shown in Table 4.4.

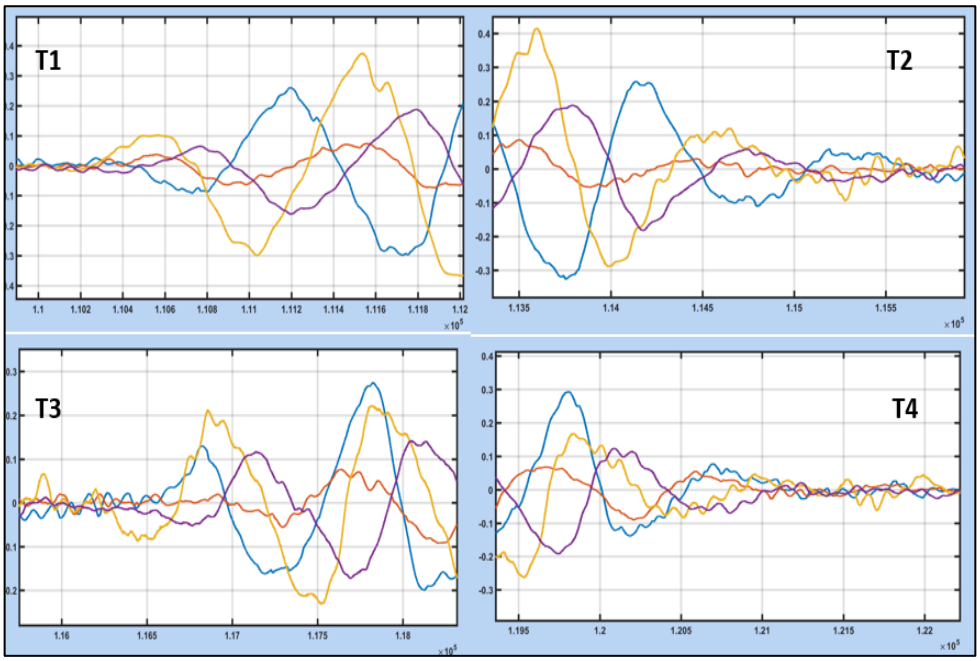

Figure 4.18: Enlarged CVP signal tails for titanium nanoparticles.

Table 4. 4 : Particle size as a function of phase angle (titanium dioxide)

Particle diameter (nm)	Δt (μs)	Period T(μs)	Concentration wt%	Phase angle φ	Error %
51	0.060	1	1%	21.5°	1.3%
185	0.035	1	1%	12.6°	3.7%
285	0.030	1	1%	10.8°	3.8%

The relative change of the phase angle of different particle diameters of titanium dioxide nanoparticles is shown in Figure 4.20.

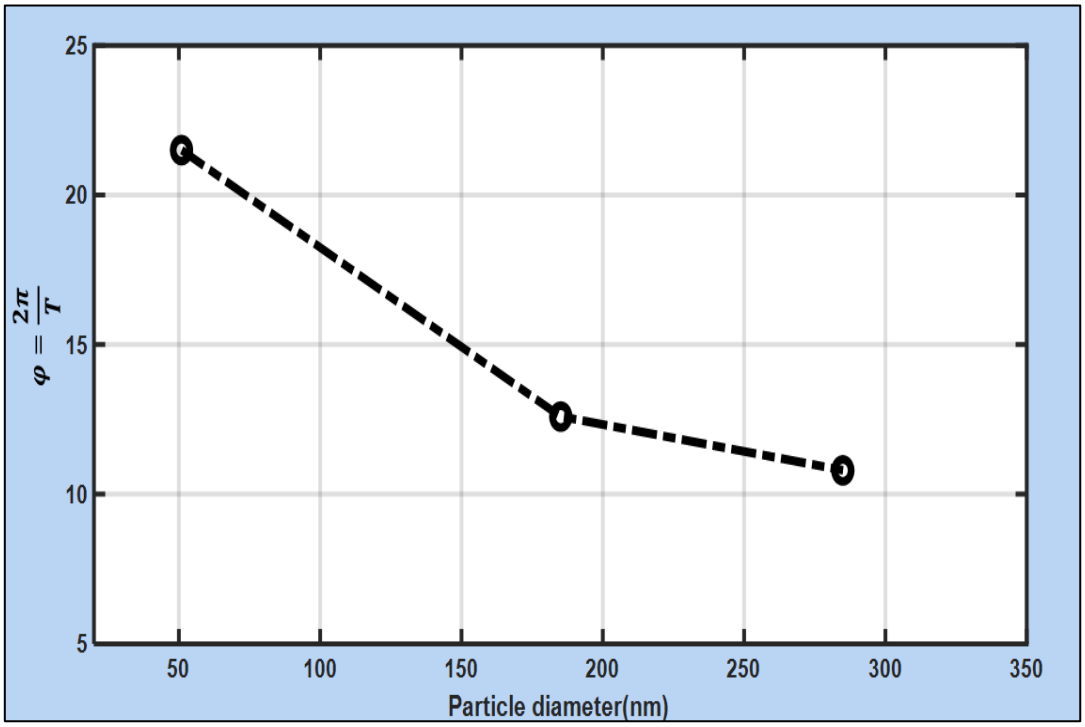

Figure 4.19: Relative changes in phase angle vs particle diameter with a concentration of 1 wt% for titanium dioxide.

From Figure 4.19 we can see the phase angle increases for particles with a smaller diameter and decreases for larger particles. This result is similar to the silica nanoparticles. The results for both silica dioxide and titanium dioxide show that the phase angle has changed inverse proportionally to the particle diameter.

According to this experiment, a smaller particle has also shown a more significant change in phase shift than a larger particle. When the particles start to vibrate in the colloid suspension due to ultrasound pressure, all the particles start to vibrate at the same time but the smaller particles jump and move faster than the larger particles due to their smaller size. This creates a significant phase difference in smaller particles compared to larger particles.

4.5 Summary

In summary, I have presented two different tests relating to nanoparticle size characterizations in colloids. The frequency responses were measured for silica dioxide with different particle diameters. The experimental results show that the frequency response as a function of particle diameter is a useful method for nanoparticle characterization. This method is a good method for PSD as compared to other traditional methods because ultrasound can propagate through concentrated suspensions. In ultrasound technology for PSD measurement no dilution is required. This is capable of measuring different ranges of particle size with a single sensor, and also able to measure a true frequency response from the particles. The second test demonstrated the relationship between particle diameter and phase angle for nanoparticles suspended in colloids. The CVP measurements were taken for two different materials i.e. silica dioxide and titanium dioxide, and the results demonstrated how larger particles and smaller particles vibrate in colloidal suspensions under the effect of ultrasonic pressure. This showed that smaller particles have a significate change in phase angle as compared to larger particles. It also demonstrated that under ultrasound pressure all the particles in a colloidal suspension start to vibrate at the same time but the smaller particles jump and move faster than larger particles.

CHAPTER FIVE: UVP TISSUE-LIKE MODEL

Summary: *This chapter will introduce a new UVP testing phantom (Leeds Standard III). It reports on the progress of the measurement method using electrodes non-intrusively placed outside a mock body made from agar. Ultrasound vibration potential (UVP) signals were received from an agar sample embedded within the mock body containing either ionic or nanoparticular species in good quality. The equivalent circuit diagram for this model will also be presented. Signals were measured from the agar mock body containing multiple layers of silica suspensions. It also reports the technology limitations and further experimental verification.*

5.1Introduction

This Chapter will introduce a new measurement device for ultrasound vibration potential (UVP) imaging. A new testing phantom designed (the Leeds standard III device) for non-intrusive UVP imaging. The progress on this method of measurement, with electrodes non-intrusively set outside a mock body made from agar, can take us a step closer to tissue imaging. This device (Leeds standard II) received signals from an agar sample that was embedded in a mock body containing either ionic or nanoparticle, good quality species, which displays huge potential in providing the physicochemical property of the sample as a corresponding image compared to the conventional ultrasound image. The circuit diagram for this UVP device is also detailed. The signals measured from the mock agar body, containing multiple layers of silica suspensions, are provided in this Chapter. In this research, we used several electronic devices such as: a signal generator, a power amplifier, an ultrasound pulser/receiver, impedance matching, electrode sensors, transducers, and ultrasonic diagnostic machine (DP-6600). Further information and graphic images of these devices are given in more detail. Different samples were used such as, titanium dioxide, silica dioxide, an ionic electrolyte, and agar powder. The details of these materials and the preparation procedure are explained in this Chapter. All apparatus involved in this innovative work will also be discussed in this Chapter. The experiment setup and techniques demonstrating the methodology for this UVP imaging will be discussed along with the results. This Chapter will also explains how UVP signal changes as a function of particles diameter, and also explains

how IVP changes as a function of atomic weight. The last section it will explain the effect of salt and pH on the UVP signal.

5.2Mock Body and Sample of UVP Standard III

To build our new standard device for non-intrusive UVP measurement based on the simulated model presented in (Chapter 3 section 3.4), we required a material that can form a gel with a very low concentrations in order to ignore the boundary between the sample and the body. We wanted to avoid using water to serve the delay line, so we can attach the electrode to the body rather inserted into it. We have made a choice to use material can form a gel that can be easy to build a shape and structure of our device and are able to hold a sample such as liquid within the body. The selected materials are presented in the Table 5.1.

Table 5. 1 : Specification of the selected material for building UVP Leeds standard III device.

Material	Description	Manufacture
Agar	Soluble (80 − 90℃) Cooling solution (40 − 45℃)) Form good strength jell at concentration of 1wt%	Special Ingredients Ltd, Chesterfield, S41 9RN Tel: 01246906247
Gelatin	Soluble (45−60℃) Cooling solution (30 − 35℃)) Form good strength jell at concentration of 9wt%	Healan Ingredient North Newbald York, YO43 4SW Tel: 01430871414
Greens Jell	Soluble (60 − 70℃) Cooling solution (30 − 35℃)) Form good strength jell at concentration of 12.5wt%	Green's Desserts Ltd. Thurcroft, Rotherham, S66 9ER. Tel: 01709700000

We decided to use agar powder to form the gel is because agar can form a good strength gel in low concentrating of 1wt%, and the use of agar gel as a body material simulation for acoustic impedance matching. In particular, we have tested different concentrations such as 1wt%, 2wt%, 3wt%, and we find out that the boundary between the agar body

and the sample can be ignored only when the gel concentration is 1wt% in order to show the significant difference between the UVP and current ultrasound imaging.

The agar powder was purchased from Special Ingredients Ltd. (UK). Agar forms a gel in very low concentrations and becomes soluble between 80–90℃. It produces a firm gel that can be sliced. Agar consists of a mixture of two polysaccharides: agarose and agaropectin, with agarose making up to 70% of the mixture. It is used in plant biology, as an impression material in dentistry, in food applications, and in medicine and molecular biology for the separation of molecules e.g. DNA, (Roberts and Martens, (2016). Agarose has a molecular weight of around 120,000, and the agar mixture has a low melting temperature.

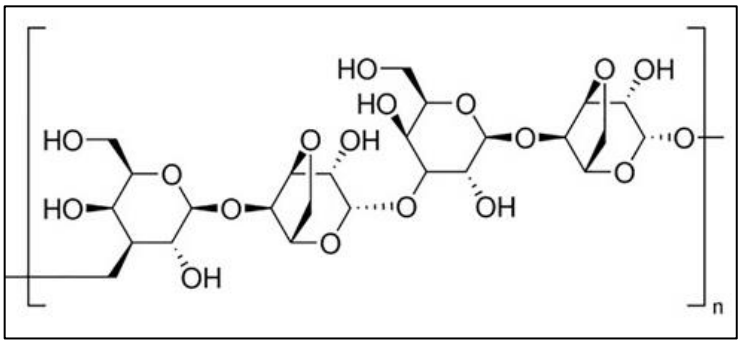

Figure 5. 1: Molecular structure of agarose (Nguyen, 2009).

Gel preparation procedure:

- **a.** 1 wt% agar gel: 500 ml of tested solution was heated to **85**℃ before introducing the agar powder in a large beaker.
- **b.** 5g of agar powder was added to the beaker with a magnetic stirrer inside. The solution was then continually heated for up to 2 hours at a temperature of **80**℃ to remove the air bubbles. The temperature remained stable for up to 30 mins in order to dissolve the agar completely. The suspension was then transferred to a vessel for cooling (to decrease the temperature), achieving a good, firm block of agar.
- **c.** The agar mock body block has dimensions: 82 mm in length, 56 mm in width and 66 mm in depth. Figure 5.3 shows that the mock agar body has a white colour with a sample inside (without specified ions or particles) in the red colour. The sample has a width of 10 mm, length 30 mm and depth of 40 mm. The sample was located 14 mm away from the aluminium sensor and 58 mm away from the transducer face.

d. To avoid a ‘hard interface’ between the sample and the agar tissue, and to make the interface ‘invisible’ with no reflection of the ultrasound, the sample was introduced to the mock body at a temperature of 85℃ and left overnight to cool.

After the agar gel was prepared, it was placed in a vessel to give it the same shape as the device, see Figure 5.2. A cuboid of polypropylene with dimensions: width = 30 mm, height = 40 mm, and length = 10 mm, was placed inside the vessel, in order to make a container to introduce the sample of interest.

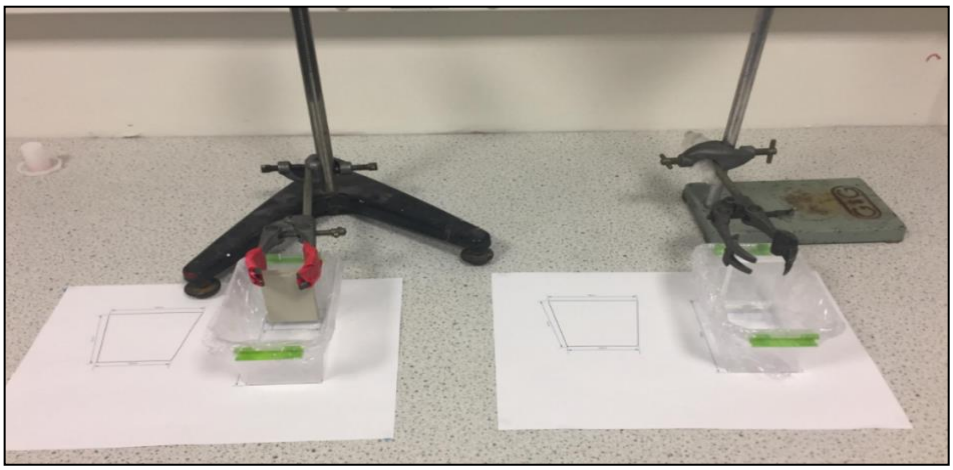

Figure 5. 2: UVP standard III vessel.

The agar gel inside the vessel was left overnight to cool. The agar gel formed inside the vessel and then we gently warmed the outside of the vessel to 40℃ in order for the agar block to be removed smoothly.

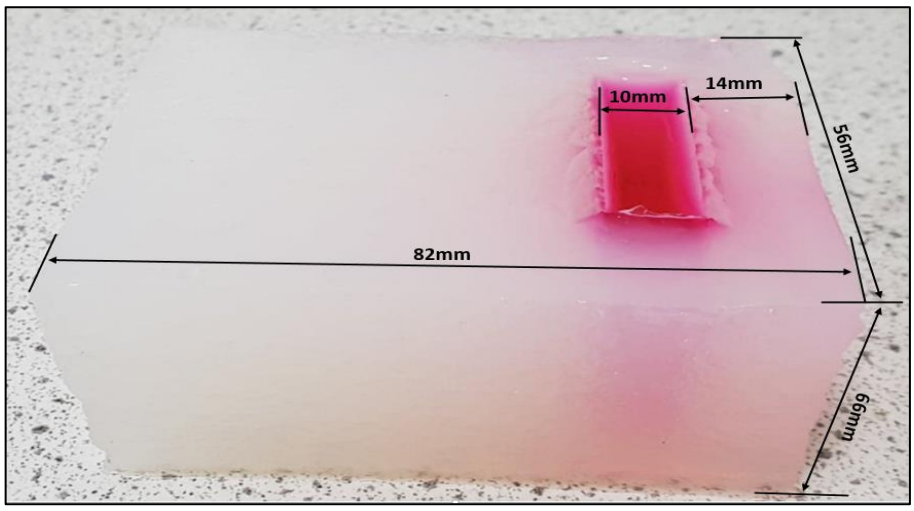

Figure 5. 3: Agar mock body (white colour) with a sample embedded (red colour).

5.3Circuit Model

The UVP signal was generated at two sides of the sample and the equivalent circuit diagram is presented in Figure 5.4. The parallel voltage measurement assumptions applied to the ultrasound wave and the electric field. The ultrasound excitation is characterized as an applied voltage and the sample system (ionic solution or colloidal suspension) is used with external resistance and capacitance which presents an impedance **Z** (bulk impedance of the sample). The applied voltage is characterized as the ultrasound excitation source.

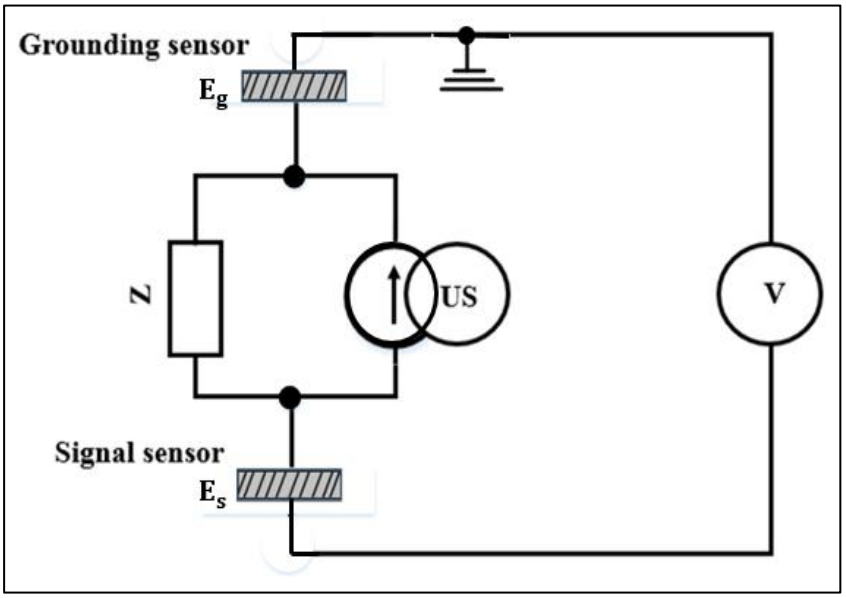

Figure 5. 4: The equivalent circuit diagram of the UVP generation and detection.

Figure 5.4 represents the Leeds standard III circuit model. The voltage is produced by the polarizations due to the presence of ultrasound pressure in colloidal or ionic samples.

5.4UVP Standard III Device

A new UVP measurement device designed as part of my study. This device is a standard for UVP measurement methods. It is made from agar and embedded with a sample of interest. Agar was used in this process because agar forms a gel in very low concentration, and is also an easy to use, cheap product. The process of making the agar gel and forming a cuboid is explained in Section 5.3. Figure 5.5 shows the Leeds standard III device with two electrodes in the shape of a square with dimensions 10 ×

10 mm and made from aluminium foil. These are placed at opposite sides of the mock agar body.

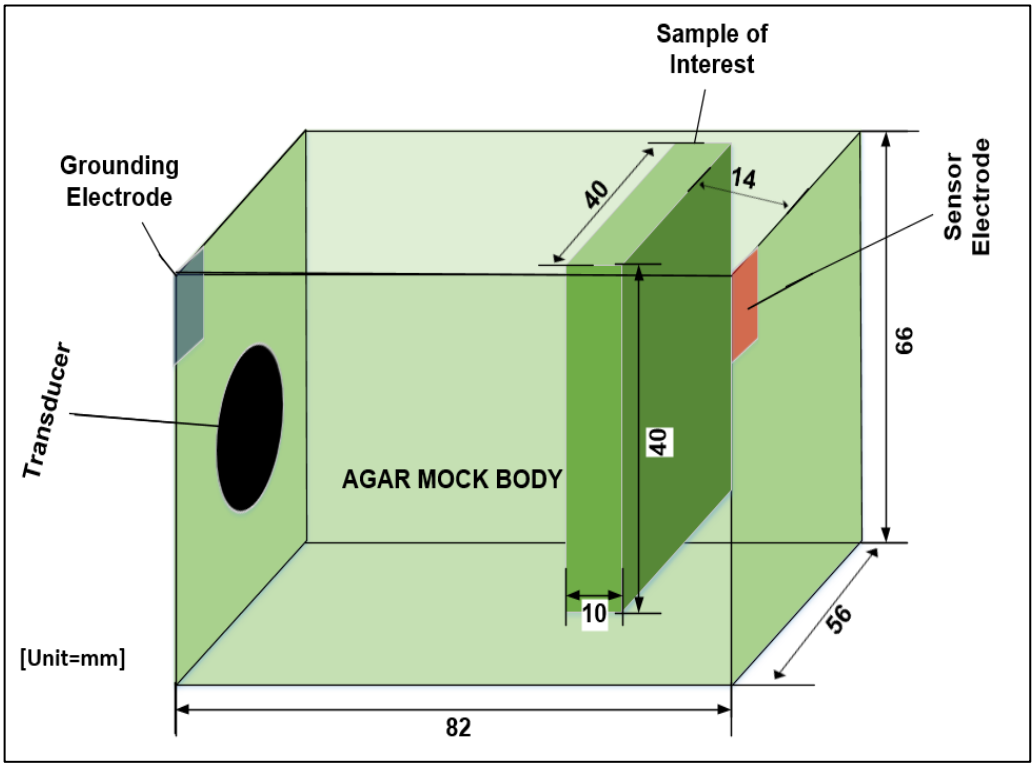

Figure 5. 5: Leeds UVP standard III.

The sample has dimensions 10 × 30 × 40 mm. The sample can be located anywhere within the agar body, but for this experiment we placed the sample at a position 14 mm away from the aluminium sensor, 58 mm away from the transducer face, and 58 mm away from the grounded electrode. The transducer, with a diameter of 25 mm, is attached to the near side of the agar mock body in order to send ultrasound pulses through it. The gap between the transducer and the agar mock body is filled with an ultrasound gel to avoid having air between these two interfaces. The electrodes are non-intrusively placed outside the body. This device enhances the signal quality, can take images of objects with the electrodes placed outside the mock body, and is capable of multilayer imaging. The evidence of imaging a colloidal sample and ionic electrolyte with this device is demonstrated in this Chapter but this model may require further improvement in the sensing method and imaging constructions. This device is suitable for 2D and 3D scanning. The reflection at the far side of the mock body device can be reduced by using ultrasound damping. This device was built with a lower concentration

of 1 wt% to improve the unique feature of UVP imaging. The velocity of the ultrasound in the mock body was taken at 1600 m/s. The only reason we used agar at this stage is because you can make a firm gel with low concentration. This device has advantages over previous UVP standard devices: it is capable of measurement repetition; the sensors are placed outside of the body; there is no interface between the sample and the body; it enhances the signal quality; and it takes us a step closer to tissue imaging.

5.5Sensing System and Mock Tissue Setup

Experiment Setup

The experiment consists of two parts: input and output. The input instruments are the signal generator (Model 33250A manufactured in 2016) set with, $\mathbf{450\ mV_{(pk-pk)}}$, **1 MHz** frequency and six duty cycles, with a burst period of 50 ms, and a duty cycle of 0.01%. The signal generated from the signal generator is sent to the RF amplifier (Model GA-2500A manufactured in 2016) for amplification. The excitation signal is amplified by 40 dB. The output from the RF amplifier is connected to an impedance matching resistor, at $\mathbf{50\ \Omega}$**.** The amplified excitation signal is sent through the agar mock body and the sample via a 1 MHz piezoelectric transducer, with diameter of 25 mm and fixed at the near side of the agar block. This transducer converts the electric signal to a mechanical wave. When the ultrasound wave is applied to the sample, the nanoparticles inside the colloidal suspension start vibrating. This vibration causes the polarization and creates a number of dipoles within the sample. The summing of these dipoles gives an electric potential and this electric potential is measured by both electrodes attached to the mock body of agar.

The output for this experiment consists of two electrodes made from aluminium foil having a square shape with dimensions 10 × 10 mm in order to detect the UVP signal. After the signal is detected by both electrodes it sends the signal to the voltage amplifier (Model 5072PR manufactured in 2015) with an amplification factor of 39 dB. The amplified signal is sent to the digital LeCroy oscilloscope (Model 2GS/s DSO manufactured in 2004) for calibration and data collection.

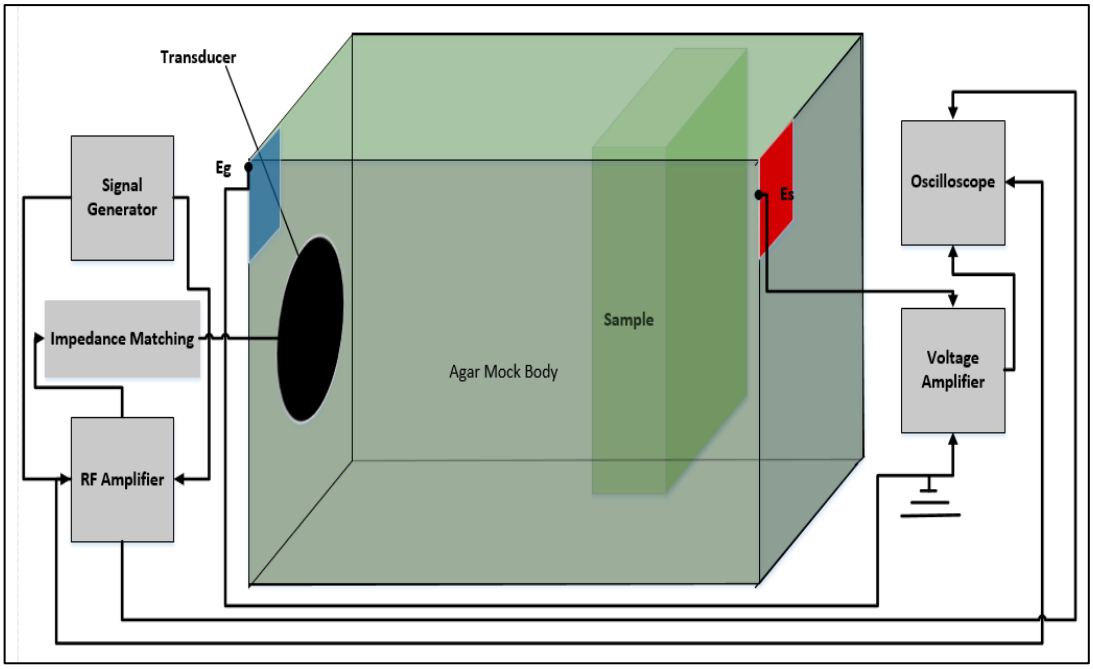

Figure 5. 6: Principle of UVP Imaging

Figure 5.6 represents the experimental setup for UVP imaging using the Leeds standard III device. The measuring and evidence of imaging of the colloidal objects and ionic electrolytes using this model is given in Section 5.5. This experiment involves connecting many electronic devices and I will give a description of each device below.

5.6 Electronics

In this section I give brief details of all the electronic equipment used in the experimental work. All electronic devices are standard and are conversional unit. Each subsection below describes each instrument in detail.

5.6.1 Oscilloscope

The oscilloscope used in this research is manufactured by LeCroy: Wavesurfer 454 with 4 input channels, and a frequency of 500 MHz, 2 GS/s Wavesurfer, (2004). An image of the oscilloscope is shown in Figure 5.7. The oscilloscope demonstrates the graphical behaviour of the electric signal within the given timescale. It performs quantitative measurements, not qualitative. The working principle is that an electron beam shows up as a dot on the screen and the dots depends on the horizontal and vertical deflections

– the vertical axis is driven by the input signal and the horizontal axis is driven by the internal time base (time period).

Figure 5. 7: Oscilloscope.

5.6.2 RF Amplifier

The RF 2500A model was designed to produce a high amplitude radio frequency (RF) which is driven by a continuous wave signal or externally generated RF tone burst. The 5 kW, and 0.3% duty cycle output corresponds to 1440 V peak-to-peak into 50 Ohms. The front panel ten turn potentiometer controls the output level.

Figure 5. 8: RF amplifier.

The total maximum gain is around 60 dB and a signal input of 1 V peak-to-peak is required for maximum output. The instrument is protected against open circuit and short circuit conditions on its output, and also protected against excessive temperature and excessive current by two automatic shutdown circuits, Ritecinc, (2016).

This electronic device has four connections: two input and two output. The input RF is for the voltage in and the input TTL (Transistor-Transistor-Logic) is for the synchronized signal. The two output connections are for monitoring the signal and amplification of the signal.

5.6.3 Signal Generator

The front panel of our signal generator (the 33250A) is straightforward and the numeric keypad can be used to adjust frequency, amplitude, periods, and wave types. This signal generator is manufactured by Agilent technology. The image of the signal generator is shown in Figure 5.9.

Figure 5. 9: Signal generator.

This electronic device is capable of generating different types of signal such as a sine wave, a pulsed wave, a square wave and a chirp signal. This instrument in our research was used to set the sinusoidal waveform with 6 number of cycles and an amplitude of 450 mV with a burst period of 50 ms. The signal can be synchronized for a very low duty cycle of 0.001%. Further details and the specifications can be found on the data sheet for this model Agilent., (2016).

5.6.4 Ultrasonic Pulser/Receiver

The Panametrics 5072PR machine (see Figure 5.10) is a voltage amplifier that can be used as an ultrasound transmitter/receiver, Olympus (2016). It has a variable gain of 0–59 dB and a magnification factor of 1,000. The chosen wave will be sent to the ultrasonic pulser and the response detected by this instrument as an echo wave. It has two modes: Mode 1 pulse-echo, and Mode 2 just a transmitter. This instrument can generate an ultrasound pulsed wave with the desired number of cycles and receive the signal as an echo from the interface testing material. It can be used as a voltage amplifier in order to magnify the detected signal. The Mode 1 operation is based on the pulse-echo method and the reflected signal from the testing material is converted by the transducer to an electrical pulse.

Figure 5. 10: Ultrasound pulser/receiver.

We connect the RF output directly to the transducer and by connecting the output and synchronizing the control the generated waveform can be observed on the oscilloscope. Mode 2 is applied to the UVP setup with the connector, R, and the output can connect to the oscilloscope with the applied gain. This instrument is designed for low-noise receiver response and high-performance pulse control with $\pm 1\,V$ RF output in $50\,\Omega$ load, AV-IQ. (2018).

5.6.5 Current Amplifier

The current amplifier, called a high-speed current amplifier (HCA), gives low noise and high signal quality. It converts a small input current to a high voltage output. This amplifier has a fixed gain of $500\ \mathrm{kV/A}$ and can magnify the ultra-weak signal. The voltage range is $\pm 1\ \mathrm{V}$, and the current range is $\pm 3\ \mu\mathrm{A}$, Components, (2010).

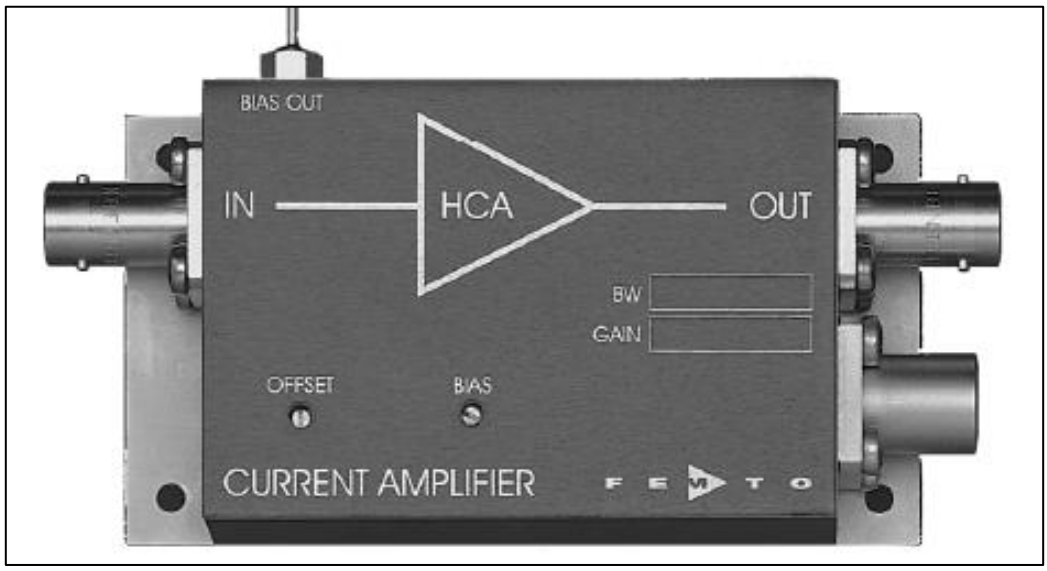

Figure 5. 11: Current amplifier.

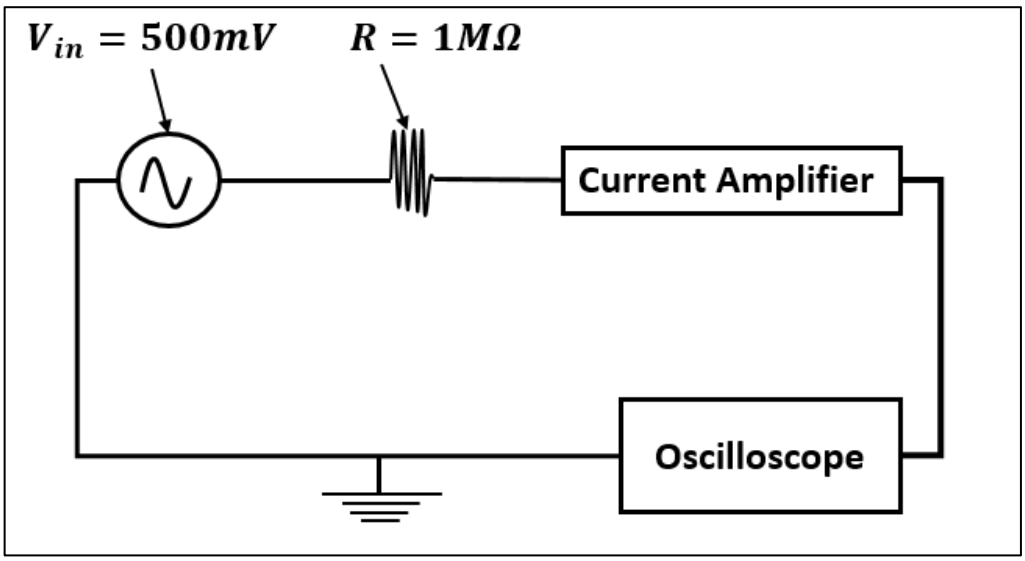

Figure 5. 12: The circuit loop to test the amplifier.

In order to test the amplifier functionality, we connected the amplifier to the power source to 1 MΩ resistor in series and connected to the input of the current amplifier and the output to the oscilloscope as shown in Figure 5.12. This HCA current amplifier is sufficient for the input signal for 500 kV/A. The input signal must not exceed more than ± 1 V in line with the manufacturer's specifications.

$$(output) = (input) \times 500 \times 10^3 \left(\frac{V(volt)}{A(amp)}\right)$$

R is the 1 MΩ resistor connected between the power source and the amplifier input. The circuit diagram in Figure 5.12 is to represent the functionality of the HCA amplifier.

5.6.6 The Piezoelectric Transducer

The ultrasonic transducer converts the mechanical sound wave to an electrical signal and also converts the electrical signal into a mechanical sound wave. Ultrasonic transducers are called *transceivers* because they can transmit and receive the signal. The ultrasound probes are used to apply sound energy to agitate particles in a wide range of lab applications. When the voltage is applied to the sensor, the piezoelectric crystals change shape and size and it makes them oscillate at the same frequency thus producing an ultrasound wave. In our experimental work we used two types of ultrasonic transducer: a piezoelectric transducer with a frequency of 1 MHz, and a curvilinear transducer with a main frequency of 3.5 MHz The piezoelectric transducer was purchased from Olympus NDT Instruments, (2018). The details and description of the curvilinear transducer was given in Section 2.2.2. The crystal diameter of this transducer is 25 mm, and this decreases as a function of frequency. It is an immersion transducer and can placed into liquids. An image of the immersion transducer used in my experiment is shown in Figure 5.13.

Figure 5. 13: Piezoelectric transducer.

5.7 Evidence of Detecting the Physicochemical Properties of an Object Inside a Mock-Tissue Model.

Colloid Vibration Potential (CVP) Signal

The colloidal sample used for the CVP test was silica dioxide (SiO_2) with a particle size of 21 nm and concentration of 1 wt%. The sample was embedded into the agar block at a position 58 mm away from the transducer interface. The colloidal sample has dimensions x = 10, y = 30, and z = 40 mm. The ultrasound pulses travel through the sample and the CVP is signal generated within the sample due to the vibration of the nanoparticles. The generated CVP signal is measured by the external electrodes attached to the agar mock body as shown in Figure 5.6. The signal is amplified by the voltage amplifier with an amplification factor of 39 dB. The electric signal averaged 256 times by the oscilloscope. The zoomed two bursts of CVP signal generated at both sides of the sample are shown in Figure 5.14. The two bursts of CVP signal have a 180° phase shift/angle between them. The original signal was measured at 499 $\mu V_{(pk-pk)}$ for the second pulse, A2, and the original CVP signal was measured at 419 $\mu V_{(pk-pk)}$ for the first pulse, A1, with a frequency of 1 MHz. The CVP signal measuring repeated three times, and the CVP signal shows in the Figure 5.14 below.

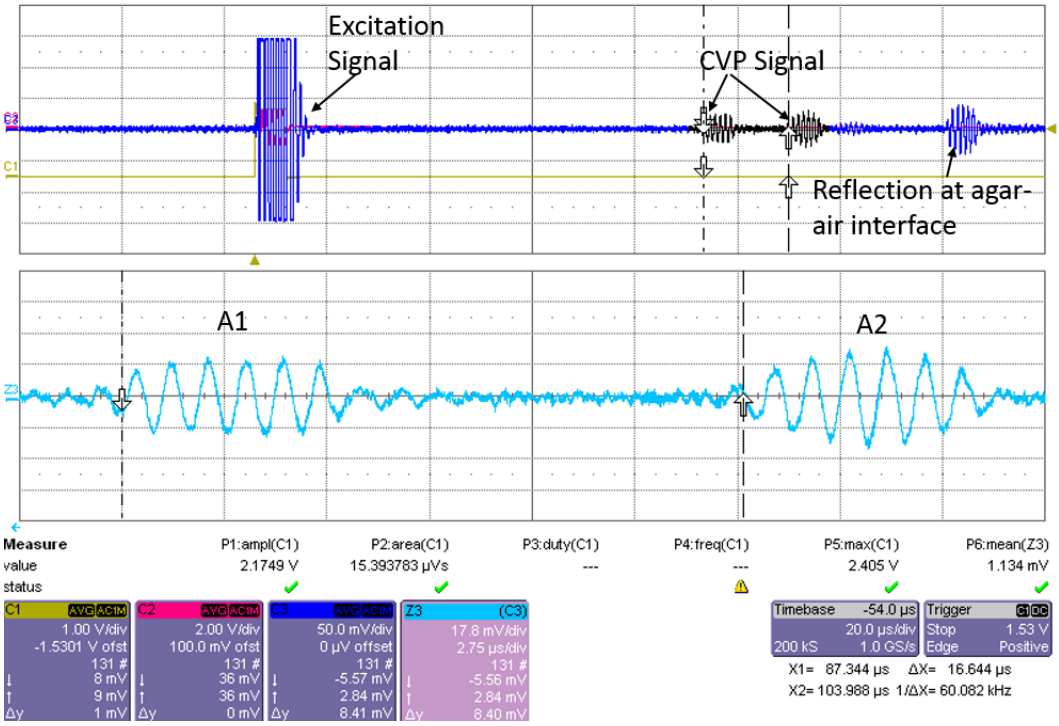

Figure 5. 14: CVP signal with a burst of 6 cycles for silica dioxide with 21 nm size and 1wt% concentration.

In Figure 5.14 the excitation signal is appeared at the left side, and the first burst of the CVP signal appeared at 38.2 µs from the transducer interface-agar interface. Taking the ultrasound speed in agar as 1600 m/s, the distance between the transducer agar-interface, and the entrance into the sample layer given at 61.1 mm. The measured distance between the sample and the transducer interface is 58 mm, and the error is 4.9%. The second CVP signal appeared at the second boundary of the sample at 44.95 µs, giving the distance from the transducer interface to the exit layer of the sample at 71.92 µs. The sample thickness was measured by multiplying the time difference of appearance between the first and the second CVP signal and the ultrasound speed in agar at 10.82 mm. The original thickness was 10 mm, and the error of 8.2% on the sample thickness was made by the diffusion of the sample to the agar mock body. This result gives proof that CVP is measurable with our Leeds standard III UVP device.

The second wave form amplitude is greater than the first wave form due to the difference in separation distance between each boundary of the sample and the sensing electrode location (see Chapter 3 section 3.4, UVPD distribution effect).

Ion Vibration Potential (IVP) Signal

The IVP test were carried out using KCl with a concentration of 1 M/L. The IVP signal was generated within the electrolyte solution and the IVP signal measurement results are presented in Figure 5.15. The two pulses were generated at the entrance and exit of the electrolyte sample. The IVP signal was measure at 27.6 $mV_{(pk-pk)}$ for A2 with the gain factor of 39 dB, and the actual voltage was measured at 309 $\mu V_{(pk-pk)}$. The IVP signal was measured at 14.49 $mV_{(pk-pk)}$ for A1 with the gain factor of 39 dB, and the original signal from the sample for the first pulse, A1, is 162 $\mu V_{(pk-pk)}$. The two bursts of IVP signals appeared in 38.11 µs and 45.02 µs respectively for A1 and A2.

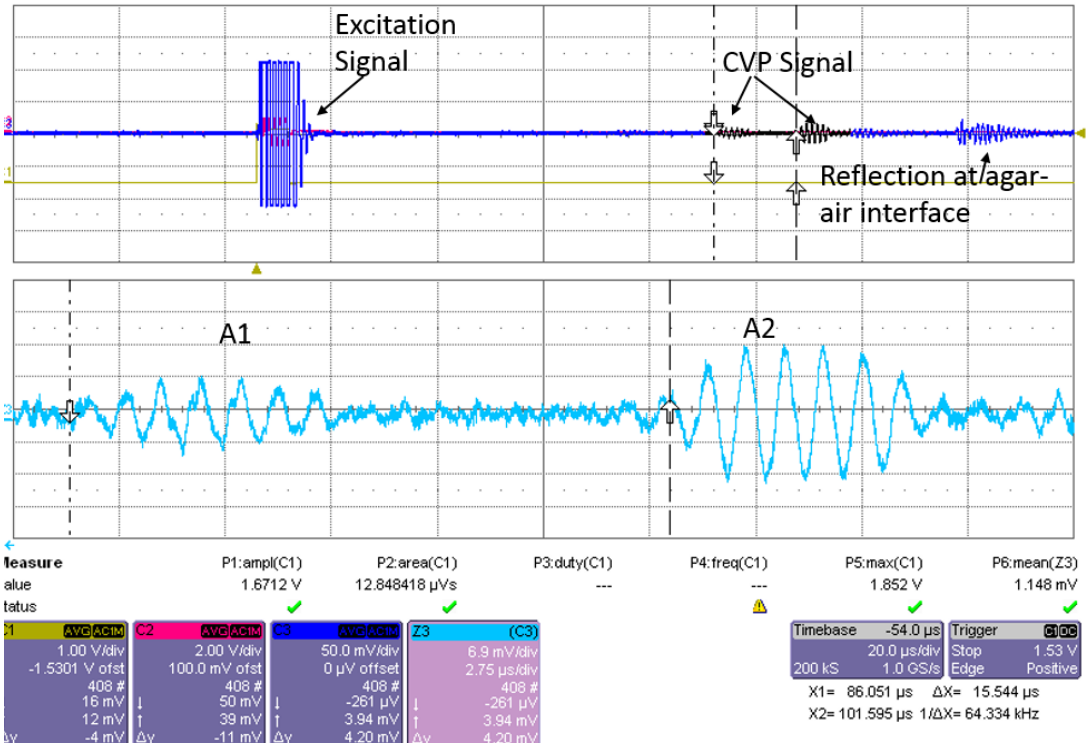

Figure 5. 15: IVP signal with a burst of 6 cycles for KCl with a concentration of 1 M/L.

Figure 5.15 shows that the IVP signal is measurable using the Leeds standard III UVP device. The sample thickness was measured by multiplying the time difference of appearance between the first and the second CVP signal and the ultrasound speed in agar at 11 mm. The % error was found to be 1% due to the diffusion of the electrolyte in to the agar mock body. The two bursts of IVP signal have 180° phase shift/angle

between them. The CVP signal measuring repeated three times and the CVP signal shows in the Figure 5.15. The differences between the CVP signal and the IVP signal is in terms of the amplitude. The CVP signal is larger in colloidal suspension relative to the IVP signal in ionic electrolytes and this is because the particles are large, carry larger ions and have stronger vibrations. The second wave form amplitude is greater than the first wave form due to the difference in separation distance between each boundary of the sample and the sensing electrode location (see Chapter 3 section 3.4, UVPD distribution effect).

5.8 Evidence of Detecting the Physicochemical Properties of Multiple Colloidal Layers within a Mock Tissue Model.

The preparation of the experimental materials and the methods are explained in Section 4.3.3. The agar mock body was set with three samples of silica nanoparticle suspensions with the same particle diameter of 21 nm, and a concentration of 1 wt%. The samples, represented by the green colour, were placed at different positions as shown in the Figure 5.16. Each sample has a dimension of width 10 mm, length 30 mm, and height 40 mm. The first sample was embedded at 14 mm away from the transducer interface or front side. The second sample was placed 36 mm away and the third sample embedded at 58 mm away from the front side interface.

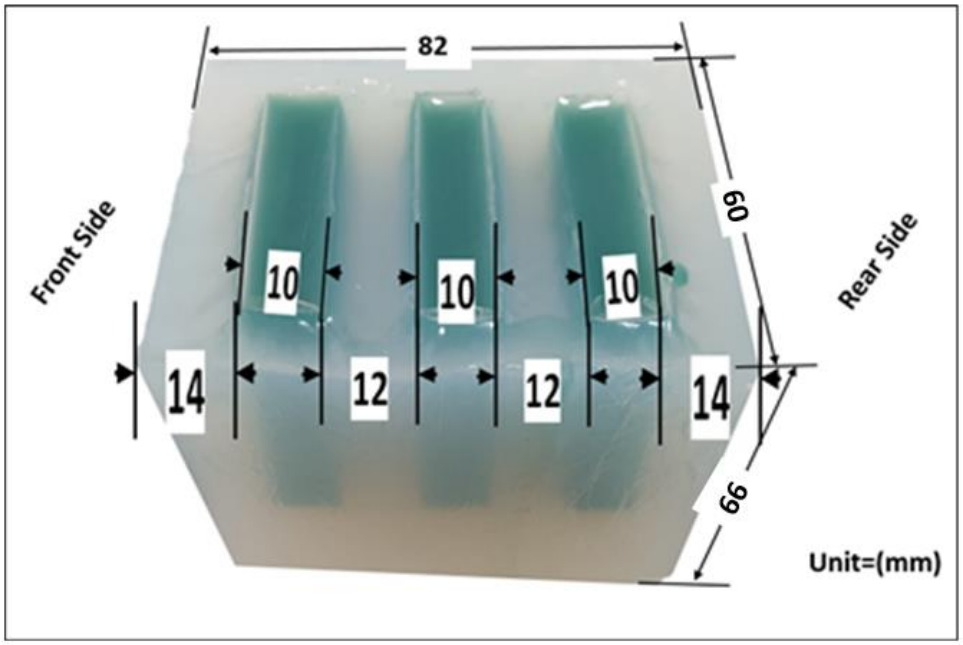

Figure 5. 16: Agar mock body with three sample.

Figure 5.16 shows the image of the mock body embedded with the three samples of silica dioxide suspended in water with a concentration of 1 wt% and particle diameter of 21nm. Two electrodes were placed at the front and rear side of the mock body in parallel in order to detect the voltage difference generated by the samples.

The experimental setup is exactly the same as the diagram connections shown in Figure 5.10. The four periods of ultrasound pulses sent in to the mock body of agar was via a piezoelectric transducer having a frequency of 1 MHz. The electric potential signals were generated within samples, detected by the electrodes and amplified with the voltage amplifier with a gain factor of 39 dB. The amplified signal was displayed on the oscilloscope and the images are shown in Figure 5.17. We send only 4 periods rather than 6 as we used in the previous experiment and this only to separate the signal and for easy measurements, and the CVP signal measurement repeated three times.

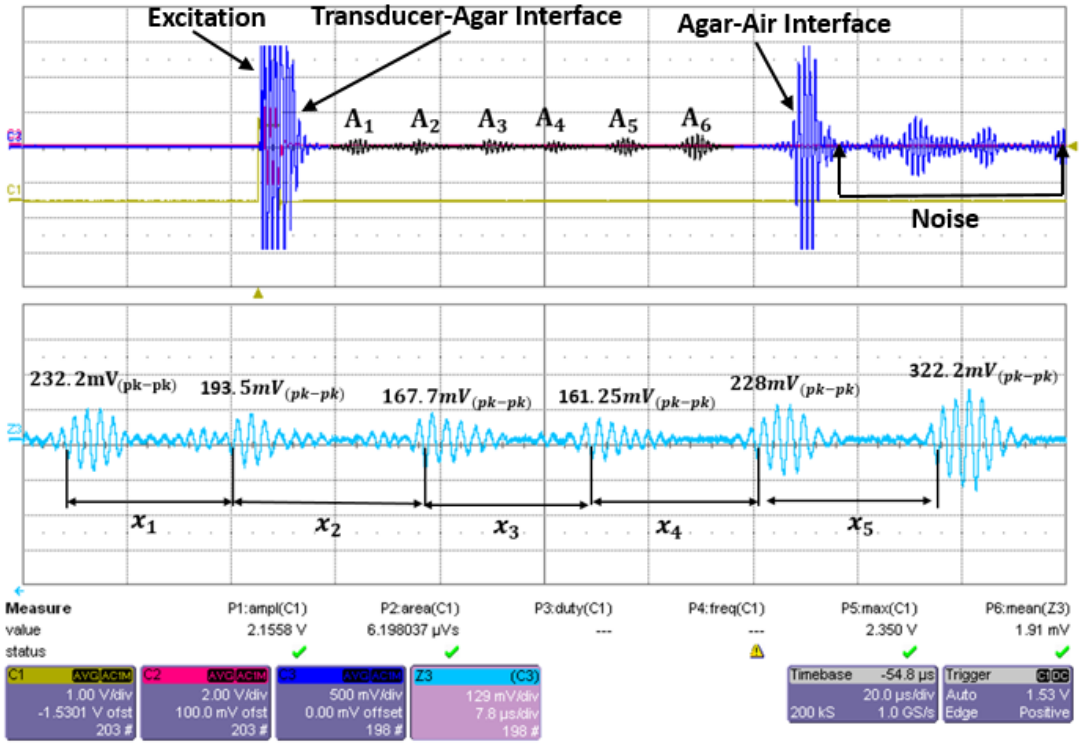

Figure 5. 17: The UVP scan of agar mock body contain three sample layers (SiO_2, 21 nm, 1 wt%) at different positions.

Figure 5.17 shows the six bursts of CVP signal, measured by the two electrodes placed at both side of the agar mock body. The CVP signals generated from each side of the sample with various amplitudes. The signal of the pulse at A6 is larger than A5 and A4,

due to the ultrasound vibration potential distribution effect. The signal amplitude of A1 is also larger than A2 and A3 due to the same effect. The distance between the sample and the electrode sensor has a major effect on the signal amplitude. The measured signal and the measured sample thickness and positions are shown in Table 5.2.

Table 5. 2 : CVP measured for multilayer silica in agar mock body

A_z z = 1, 2, 3, 4, 5, 6	X Setting (z) (mm)	X' Measured (mm)	CVP Gain (39 dB) (mV)	CVP Original (mV)	CVP Normalized (ΔV)
A1	0	0	232.2	2.6	0.58
A2	10	9.96	193.5	2.17	0.26
A3	22	21.82	167.7	1.88	0.05
A4	32	31.80	161.25	1.81	0
A5	44	42.72	228	2.56	0.55
A6	54	53.96	322.2	3.61	1

The transducer also earths itself, therefore, this extra grounding to the near side of A1 causes the difference in signal amplitude of A1, A2, A3 compare to A6 and A5, and A4 respectively. The distance between every two pulses can be calculated by considering the ultrasound arrival times, where the transition time for the electrical signal is ignored. The ultrasound speed in the agar mock body with the concentration of 1 wt% was taken at 1600 m/s, with a temperature of 24℃. The error in the measured distance is caused by the diffusion of the sample into the agar mock body.

The transducer beam diameter also has an effect on the signal amplitude. The electrode size effect is negligible due to the voltage measurement caused by the low input impedance of the measurement device. Figure 5.18 shows the experimental and simulation results of electric potential measurements for the three samples made from silica, SiO_2, with a particle diameter of 21 nm placed at different positions relative to the sensor electrode. The simulation data was presented in Chapter 3, Section 3.4.

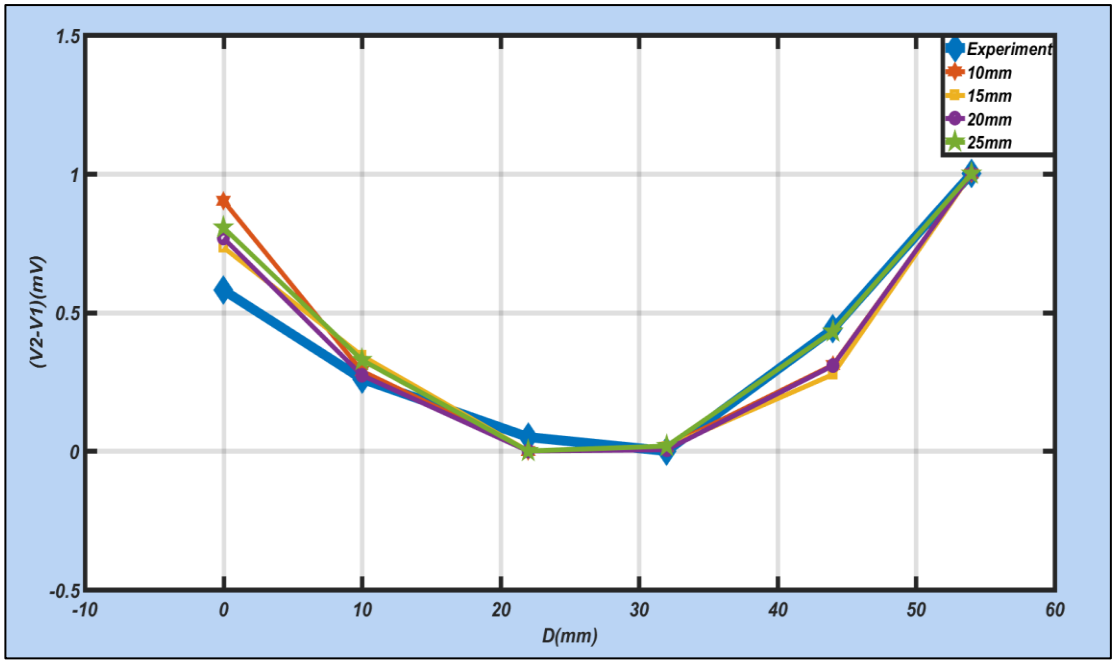

Figure 5. 18: Experimental and simulation UVP signal strength measured based on data from the simulation and experimental measurement of three sample cells across the length (D) of agar body by (E1 $(0.1, 28)$; E2 $(81.9, 28)$.

Figure 5.18 shows the electric potential difference generated in multilayers of colloidal samples embedded in the agar mock body. The potential variation relative to the distance between the electrodes and the source of charge is shown. The electric potential measured for multilayers of colloidal samples experimentally satisfy the theoretical simulation results presented in Chapter 3 Section 3.4. The size of the sample or the larger the source of charge has less effect than a smaller source of charge on the relative distance between the electrode and that source of charge. The electric potential is the potential difference between both electrodes. With an assumption of the ultrasound beam width being the same as the diameter of the ultrasound transducer (in 25 mm), signals from a setup with multiple sample cells are simulated and measured as given in Figure 310. To remove the scale effect of data obtained from the simulation and measurement, both sets of data are normalised. The comparison in Figure 5.18 shows an excellent agreement. The offset appeared at the nearside may be due to the effect of earthing points, where only the grounded metal shell of the transducer is considered in the simulation, however, one of the electrode is actually grounded due to the use of a single input of the oscilloscope. Therefore, the measurements close to the nearside are smaller than those from simulation. This result provides support to our argument for the ultrasound vibration potential distribution (UVPD) model. The transducer beam divergence is ignored due to the length of the near field transducer

which is greater than the length of the mock body. The agar tissue between the sample and the electrode sensor separates the CVP signal from the reflection signal at the far side of the mock body.

5.9 Further Experiments and Verification

To further verify and challenge of our new UVP Leeds standard III device, here we present several other experimental investigations. The experimental works carried out for nanoparticle suspensions such as titanium dioxide, in which the nanoparticles are suspended in deionized water and the suspension process are explained fully in Section 4.2.2. The IVP measurement was carried out for ionic electrolytes and the details are shown in Table 4.1. The experiment connections consist of two parts. In the first part we set the sound wave with a frequency of 1 MHz, amplitude of 450 mV, 6 number of cycles and a burst period of 50 ms. The signal was then sent to an RF amplifier for amplification up to 40dB. The output of the RF amplifier was connected to an impedance matching with a resistance of 50 Ohms. The amplified signal was sent through the device via piezoelectric transducer having frequency of 1 MHz, and crystal diameter of 25 mm. The ultrasound wave travels through the sample and the UVP signal is generated. The detected UVP signal was sent to a current amplifier with a gain factor of 500 kV/A. The amplified signal was then sent to the oscilloscope for calibration and data collection.

5.9.1 Results and Discussion

The experimental setup and connection diagram are same as the Leeds standard III model. In this work for the amplification of UVP signals, we used a current amplifier rather than a voltage amplifier. The generated electric signal was amplified with a gain factor of 500 kV/A. The CVP signal was measured for titanium dioxide and the results are shown in Table 4.5. The generated CVP signals was monitored by the mean peak-to-peak value on the oscilloscope.

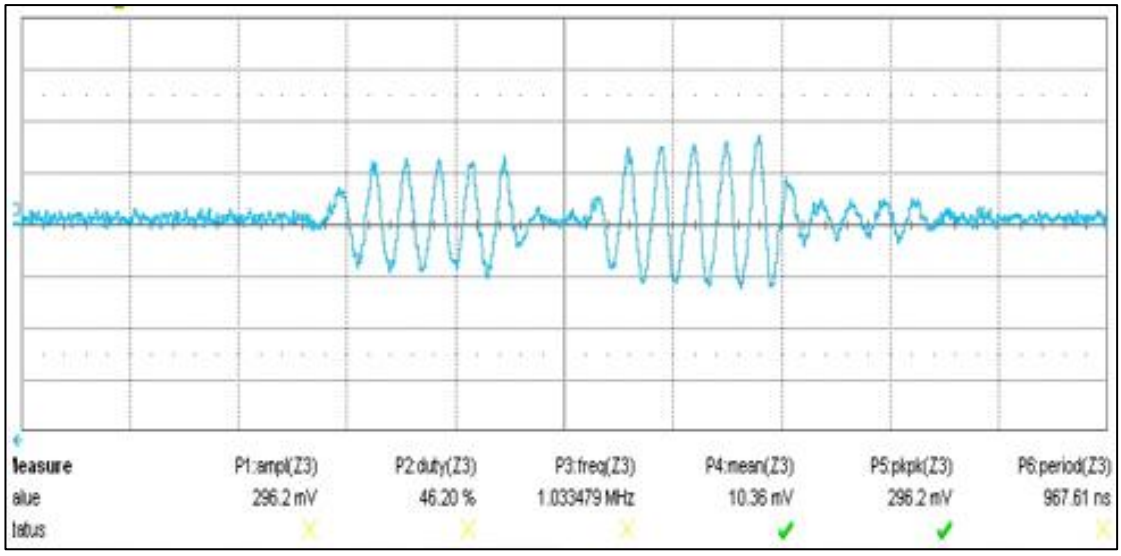

Figure 5. 19 : Six bursts of CVP signal waveform measured for titanium dioxide suspensions (diameter of 21 nm, concentration 1 wt%).

The signals are generated from both sides of the sample. The signal amplitude is measured peak-to-peak. All samples are selected at the same pH value of 7 and the same concentration of 1 wt%. The zeta potential is measured by the Malvern Zetasizer.

Table 5. 3 : CVP signal for titanium dioxide with a concentration of 1 wt%

Sample	PSD Size	Concentration wt%	pH	Zeta Potential (mV)	CVP (mA)	Standard Deviation
TiO_2	12	1	7	-35.7	0.00016	±2.36%
TiO_2	21	1	7	-22.3	0.00036	±3.11%
TiO_2	33	1	7	-4.53	0.0005	±1.35%
TiO_2	45	1	7	-4.20	0.0007	±6.22%
TiO_2	55	1	7	-3.97	0.00135	±4.01%
TiO_2	62	1	7	-17.3	0.00243	±7.15%
TiO_2	85	1	7	-3.21	0.003	±3.31%
TiO_2	113	1	7	-2.49	0.00221	±2.23%
TiO_2	142	1	7	-20.5	0.00108	±5.36%
TiO_2	160	1	7	-31.1	0.00056	±2.44%
TiO_2	177	1	7	-2.33	0.00052	±1.96%
TiO_2	201	1	7	-27.4	0.00047	±2.76%

The data recorded in Table 5.3 is the mean peak-to-peak value of the CVP signal generated from the colloidal suspensions. The placement of the sensor and the cable resistance causes error in this measurement. The possible room noise is another factor of error. The CVP signal was greatest at a particle size of 85 nm.

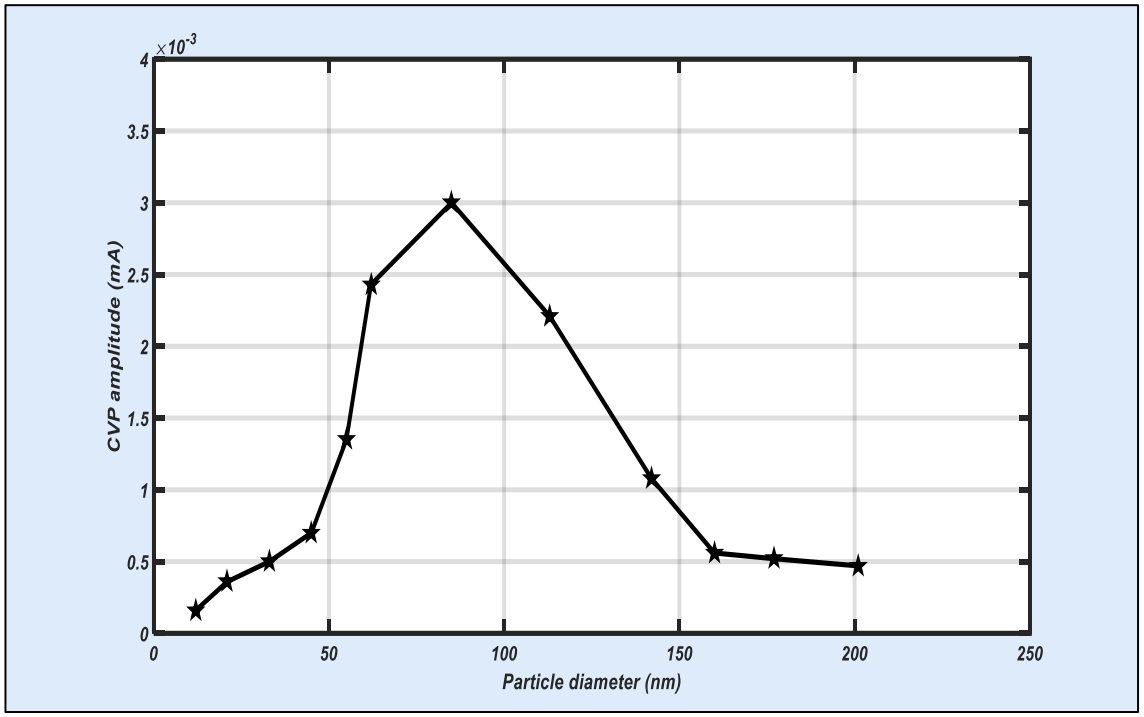

Figure 5. 20: CVP as a function of particle diameter (titanium dioxide, 1 wt %).

Figure 5.20 shows the CVP signal amplitude as a function of Particle diameter. The signal measured for TiO_2 suspension, and the resulting data shown in Table 5.3. The CVP measurement repeated three times for each sample and the average data plotted in Figure 5.20. The standard deviation error bar is shown in Table 5.3.

The reason the signal drops off at a particle size above 85 nm and increases from a particle size of 13 nm to the highest value at 85 nm can be explained by considering the particle surface charge, Ohshima, (2005). We have kept the total sample volume the same for each test and have changed the particle diameter only. When a particle is small enough the signal only becomes zero if the vibration is synchronized. This means that the ions and particles vibrate at the same time with no polarization. The potential increases from suspensions containing 12 nm nanoparticles to suspensions containing nanoparticles with a diameter of 85 nm. At this stage the surface charge plays an important role.

The general surface charge density can be given by:

$$\boldsymbol{\sigma = \frac{q}{A}} \tag{4.8}$$

Where, $\boldsymbol{A}$ is the surface area, $\boldsymbol{q}$ is the net electrical charge, and $\boldsymbol{\sigma}$ is the charge density. The potential given by:

$$\boldsymbol{\Psi = \Psi^{d} \frac{a}{r} e^{-k(r-a)}} \tag{4.9}$$

The relationship between the diffuse layer and stern layer can be given by:

$$\boldsymbol{\sigma = -\varepsilon \epsilon k \Psi (1 + \frac{1}{ka})} \tag{4.10}$$

For the spherical particle, the ratio of the two-parameter Debye-Hückel parameter $\boldsymbol{ka}$ playing a very important role. For the particle with the diameter greater than 85 nm the DL thinner than the particle radius a therefore $\boldsymbol{ka > 1}$.

$$\sigma = -\epsilon \varepsilon k \Psi \tag{4.11}$$

If the particle size smaller than 85 nm, $ka \ll 1$ the DL is thicker than the particle radius, then Equation 4.11 can be given by:

$$\boldsymbol{\sigma = -\frac{\epsilon \varepsilon \Psi}{a}} \tag{4.12}$$

From Equation 4.11 and Equation 4.12 we can say that the surface charge density increases as the size of the particle increases. For particles having a diameter larger than 85 nm, the total sample volume stays the same and the ratio of particle surface area ($4\pi r^2$) to the particle volume ($\frac{4}{3}\pi r^2$) changes and is proportional to $\frac{1}{r}$. If the particle diameter increases, the ratio of particle surface area to its volume decreases and vice versa, for the same concentration. This change suggests the reason why the potential decreases for suspensions containing larger particle diameters. If we have a cuboid and the particle is suspended inside the cuboid, we note that the particle-cubic volume ratio never changes but the surface area to the volume ratio changes inversely with radius.

$$\boldsymbol{V_P = \frac{4}{3}\pi r^3} \tag{4.13}$$

$$\boldsymbol{V_c = (2r)^3} \tag{4.14}$$

$$\frac{V_P}{V_c} = \frac{\pi}{6} \tag{4.15}$$

We can say that the UVP potential for a specific volume (e.g. cube/cubiod) of suspension changes due to the change in the number of particles for the same volumetric concentration. The larger number of charges, the larger the UVP signal.

Further IVP tests were conducted for ionic electrolytes: the IVP signal was measured for ionic electrolytes with different atomic weights. The effect of the IVP signal with atomic weight and valences are explained by, Wang et al., (2013). Table 4.5 gives the IVP signal amplitude of different ionic electrolytes having similar concentrations of 1 M/L.

Table 5. 4 : Mean peak-to-peak signal strength for different ionic electrolytes

Electrolyte	Atomic weight gram/mole	Concentration (M)	IVP (mA)	**Standard Deviation**
NaCl	54.88	1	0.00030	±4.21%
$MgCl_2$	95.211	1	0.00044	±3.31%
$CaCl_2$	110.98	1	0.00059	±6.15%
$RbCl_2$	120.921	1	0.00060	±3.12%
$SrCl_2$	158.53	1	0.00065	±4.71%
$BaCl_2$	208.23	1	0.00085	±2.55%

Table 5.4 shows the IVP signal amplitude and similar results were previously published by Yeager and Zana (1996), with the same experimental work by Mi Wang (2013). It is concluded that the IVP signal increases with increasing atomic weight due to the difference in the mass of cations (see Figure 5.21 for the corresponding graph).

The ions have different masses in the solution and, therefore, may show different accelerations and potentials as the ultrasound pulse passes through the fluid. This potential is measured as IVP. The heavier the metal ion (increasing molecular weight), the larger the IVP signal due to larger charges. Smaller particles have a smaller electron cloud and this smaller cloud creates a weaker electric dipole. The weak electric dipole creates a weaker electric signal.

These ions have the same electron valences with different atomic weights. The size of ions is influenced by the number of electrons, the valence orbitals and the nuclear charge. When an atom loses an electron from its outer shell, it exhibits a positive charge and is called a *cation*. Anions (with a negative charge) are larger than cations.

When an atom loses an electron its size become smaller because it has less electron-electron repulsion and the protons are better able to pull electrons. Atoms with a large number of protons are smaller than atoms with a smaller number of protons. IVP increases with increasing ionic size because the energy level is increased.

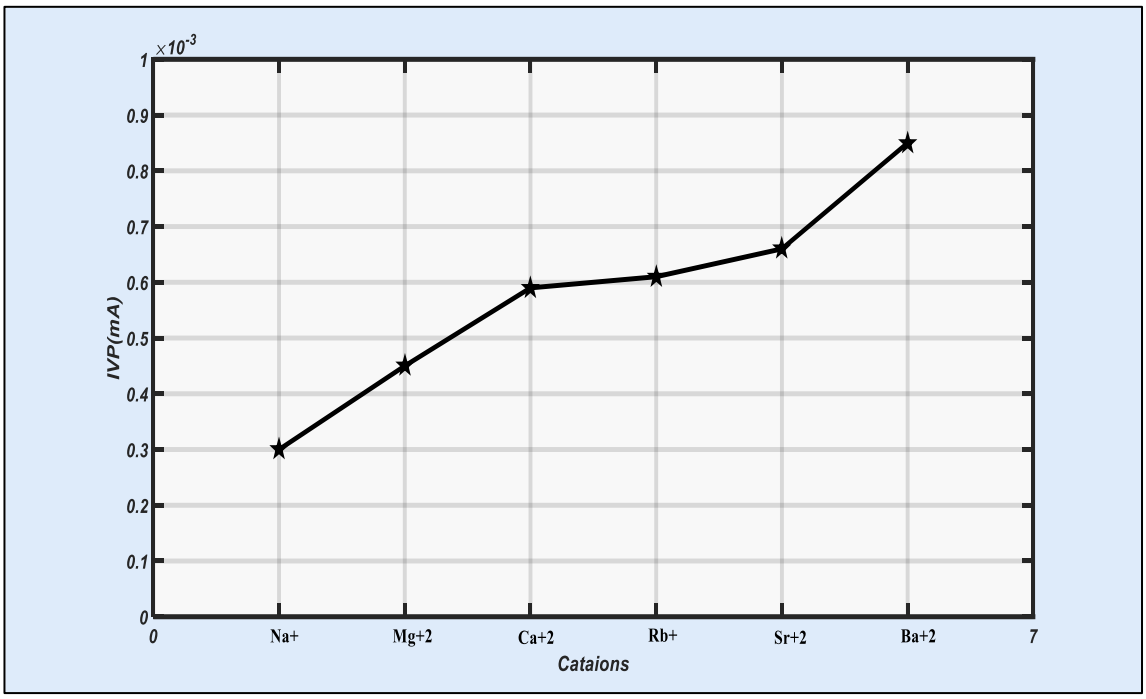

Figure 5. 21: IVP signal amplitude for electrolytes with a concentration of 1 M.

The larger the difference between the cations and anions, the larger the IVP. In this case, we have two ions with different masses and counterions. We know that the mass of an ion is larger than its counterion so that a mass of ions is larger than its parent atoms. When we apply a pressure wave, ions are displaced from their equilibrium position and move apart from their relative parent atoms, and thus the hydrophilic force tries to stop the resulting vibration. In general, the net vibration for heavier ions with their counterions is larger than for lighter ions with their counterions.

5.10 pH and Salt Effects on the IVP Signal

pH is a scale used to specify the basicity and acidity of the aqueous solution, Albert et al., (1989). An acid solution has a pH less than 7 and a basic solution has a pH of more than 7. The pH value can be less than zero for strong acids or greater than fourteen for very strong bases. The conductivity of an electrolyte solution depends on all atoms present in the solution, and the conductivity increases with increasing concentration. When the pH is high, the conductivity increases and the IVP signal decreases, so the stronger the pH, the weaker the IVP.

The surface charge of the particle decreases at low pH values and increases at high pH values. In all cases, there are many effects on both IVP and CVP signal. The CVP signal mostly depends on the vibration term and the sound pressure with a DL charge. Changing the number of ions in the electrolyte changes the electric signal, measured as IVP or CVP. The major effect on the IVP signal is the atomic mass and particle diameter for colloidal suspensions.

5.11 UVP Measuremnt Limitations

This section is to investigate the limitation of UVP measurement across the wide range of 280mm water tank, electrodes placed at the far end of the water tank, and the sample placed inside the water tank at different positions see figure (5.23). It represents the the experimental investigation on the relationship between the UVP signal amplitude and the separation distance (D=mm) between the electrodes and the sample.

Experiment:

The experimental work was carried out using Leeds standard II rig (water tank), instead of using standard III device, this is because making agar gel with such along dimensions having many numbers of sample cells is much more difficult, because the agar gel is soft easy to break out. The rig has a dimensions of $[\text{width} = 280\ \text{mm}, \text{depth} = 7.5\ \text{mm}, \text{height} = 55\ \text{mm}]$ and is filled with tap water having a conductivity of $\sigma = 0.296\ mS/cm$, and teamperature of 24℃. The sample chamber with dimensions of [width=20mm, depth=120mm, length= 50mm] (made with polystrene) sealed with cling film using silicone glue and then filled with an electrolyte sample $BaCl_2$ having a concentration of 1M, see Figure 5.22.

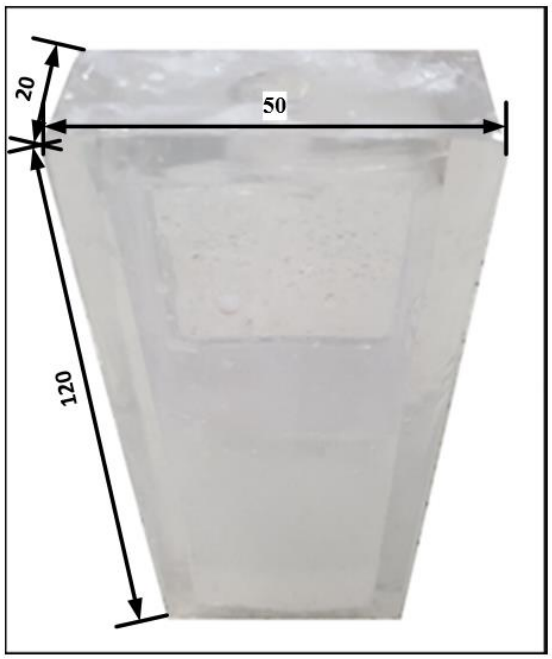

Figure 5. 22: Sample Chamber.

Figure 5.22 shows the sample chamber filed with 50ml of $BaCl_2$ having a concentration of 1M/L. The sample chamber placed at different positions inside the water tank, and then IVP signal measured.

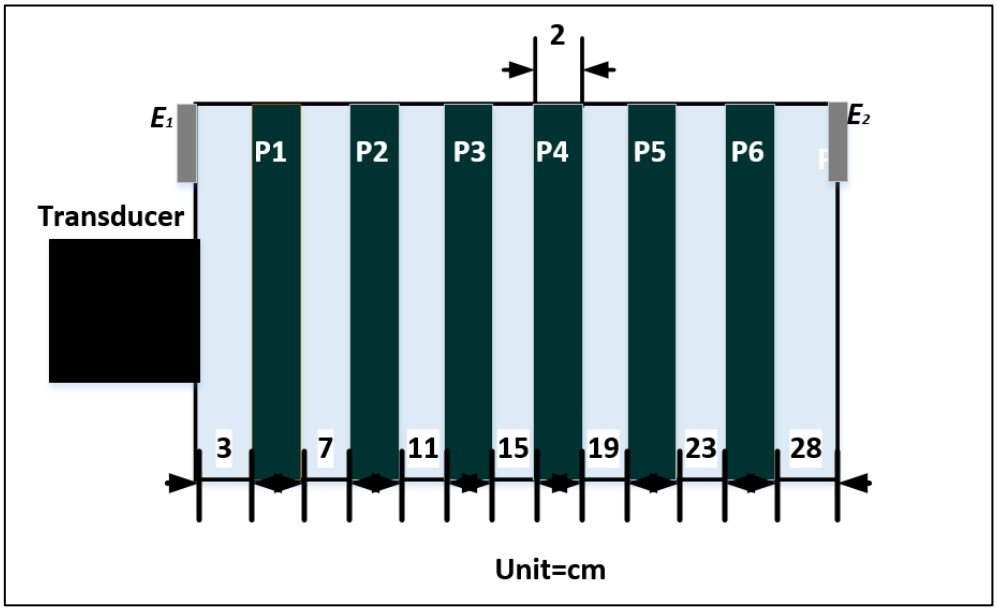

Figure 5. 23: Sample setting positions inside the water tank.

IVP Measurement and Results

The input instruments are the signal generator (Model 33250A manufactured in 2016) set with, $\mathbf{450\ mV_{(pk-pk)}}$, **1 MHz** frequency and six duty cycles, with a burst period of

50 ms, and a duty cycle of **0.01%**. The signal generated from the signal generator is sent to the RF amplifier (Model GA-2500A manufactured in 2016) for amplification. The excitation signal is amplified by **40 dB**. The output from the RF amplifier is connected to an impedance matching resistor, at **50 Ω.** The amplified excitation signal is sent through the water tank and the sample via a **1 MHz** piezoelectric transducer, with diameter of **25 mm** and fixed at the side of the water tank.

The output for this experiment consists of two electrodes made from aluminium foil having a square shape with dimensions **10 × 10 mm** in order to detect the UVP signal. The electrodes placed inside at the near side and rear side of the tank. After the signal is detected by both electrodes it sends the signal to the voltage amplifier (Model 5072PR manufactured in 2015) with an amplification factor of 39 dB. The amplified signal is sent to the digital LeCroy oscilloscope (Model 2GS/s DSO manufactured in 2004) for calibration and data collection. The measurement system shown in figure (5.24).

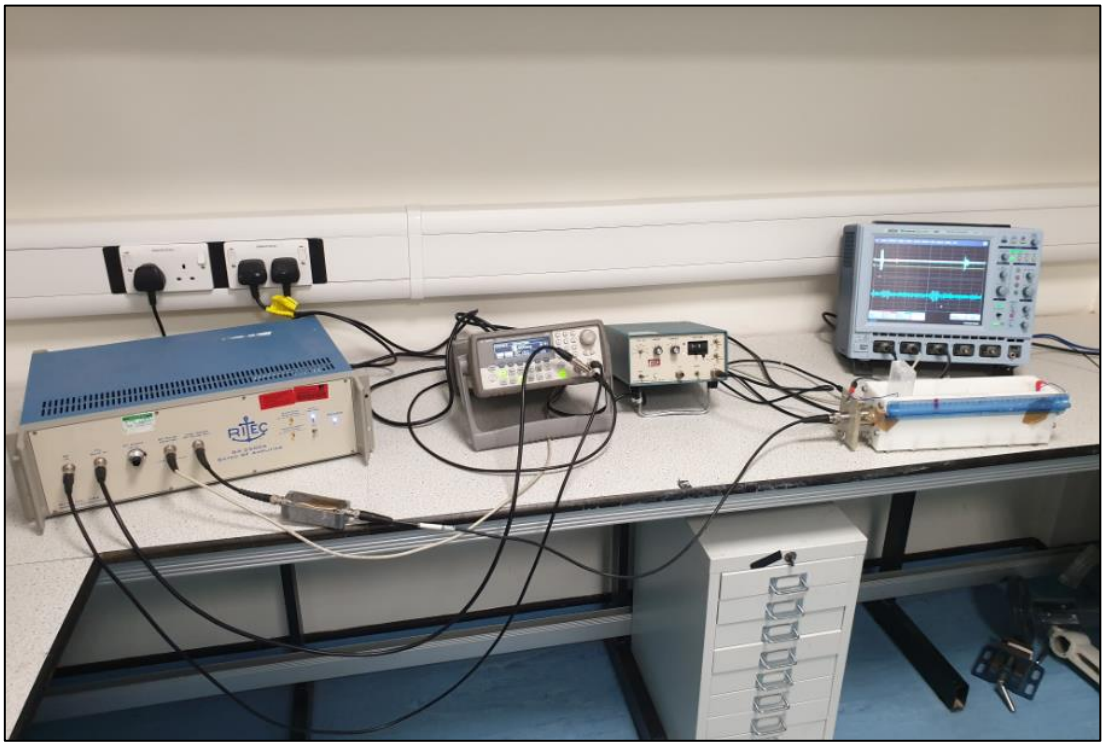

Figure 5. 24: IVP measurement system.

Figure (5.24) shows the IVP measurement system. The IVP signal monitored by the oscilloscope, and shown in figure 4.27. In all figures presented below the amplification of 39dB is applied.

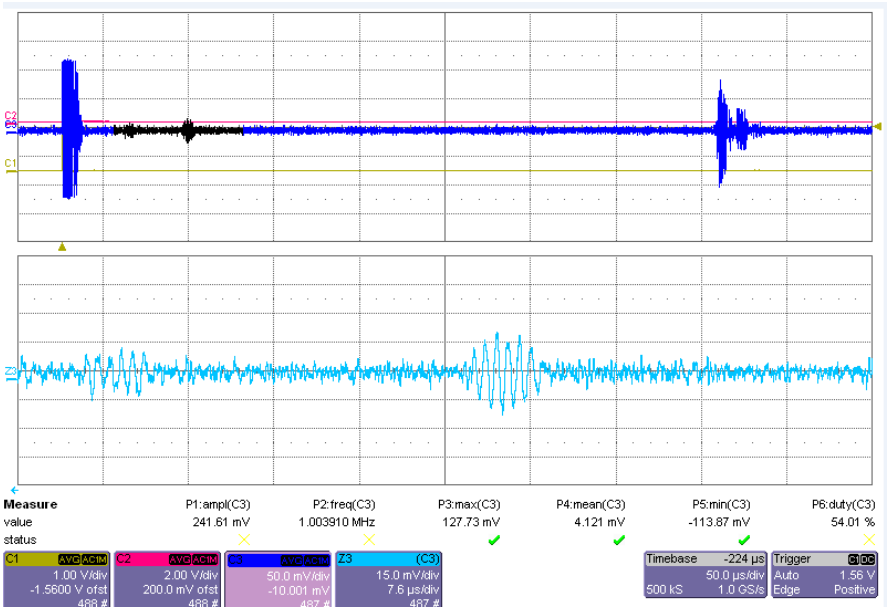

Figure 5. 25: IVP signal measured at Position (1) for $BaCl_2$ at having a concentration 1M/L.

Figure 5.25 shows the IVP signal measured from the $BaCl_2$ solution. The sample placed at 30mm away from the transducer interface (position 1). The two bursts of pulses appeared with 6 cycles. The first pulse cycle of the IVP signal appears at $t_1 = 20\ \mu s$, with amplitude $E_1 = 270 mV_{(pk-pk)}$ by taking the sound speed in the water at 1480 m/s, which gives the distance which gives the distance between the second boundary from the transducer interface at 49.5 mm. between the first boundary of material and the interface between the transducer and sample at $29.6\ mm$. The second IVP signal appears at $t_2 = 33.48\ \mu s$, with amplitude $E_2 = 294.5\ mV_{(pk-pk)}$

The thickness of the sample can be measured by:

$$\boldsymbol{d(m) = C\ (m/s) \times \Delta t\ (s)}$$

Where **d** is the thickness of the sample, **C** is the speed of the ultrasound sound propagation, $\boldsymbol{\Delta t}$ is the time difference between the first signal burst and the second signal burst.

$$d = 1.48 \times 10^6 \left(\frac{mm}{s}\right) \times (33.48 - 20) \times 10^{-6}\ (s) = 19.9\ mm$$

The thickness of the sample was measured at 19.9 mm but the original thickness was 20 mm.

$$Error = \frac{20 - 19.9}{20} \times 100\% = 0.5\%$$

The errors caused by the setting of samples position.

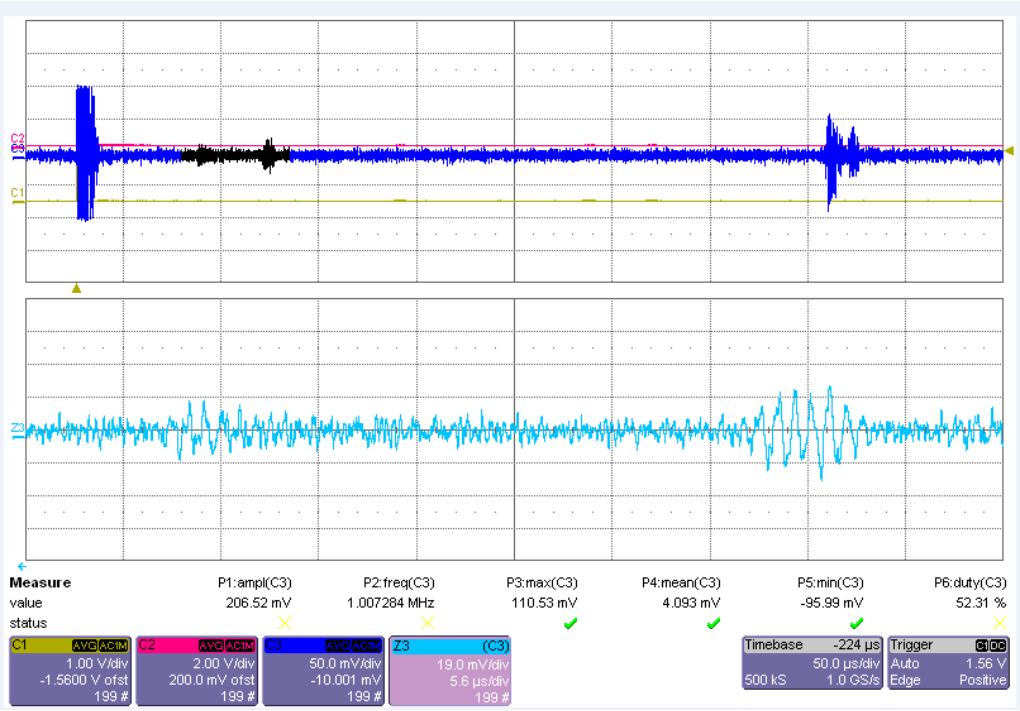

Figure 5. 26: IVP signal measured at Position (2) for $BaCl_2$ at having a concentration 1M/L.

Figure 5.26 shows the IVP signal measured at position (2) from the $BaCl_2$ solution. The two bursts of pulses appeared with 6 cycles. The first pulse cycle of the IVP signal appears at $t_1 = 47.5\ \mu s$, with amplitude $E_1 = 38 mV_{(pk-pk)}$ by taking the sound speed in the water at 1480 m/s, which gives the distance between the first boundary of material and the interface between the transducer and sample at $70.30\ m$m.

The second IVP signal appears at $t_2 = 61.48\ \mu s$, with amplitude $E_2 = 58.9\ mV_{(pk-pk)}$ which gives the distance between the second boundary from the transducer interface at 90.99 mm. The thickness of the sample was measured at 20.69 mm but the original thickness was 20 mm.

$$Error = \frac{20.69 - 20}{20} \times 100\% = 3.4\%$$

The errors caused by the setting of samples position.

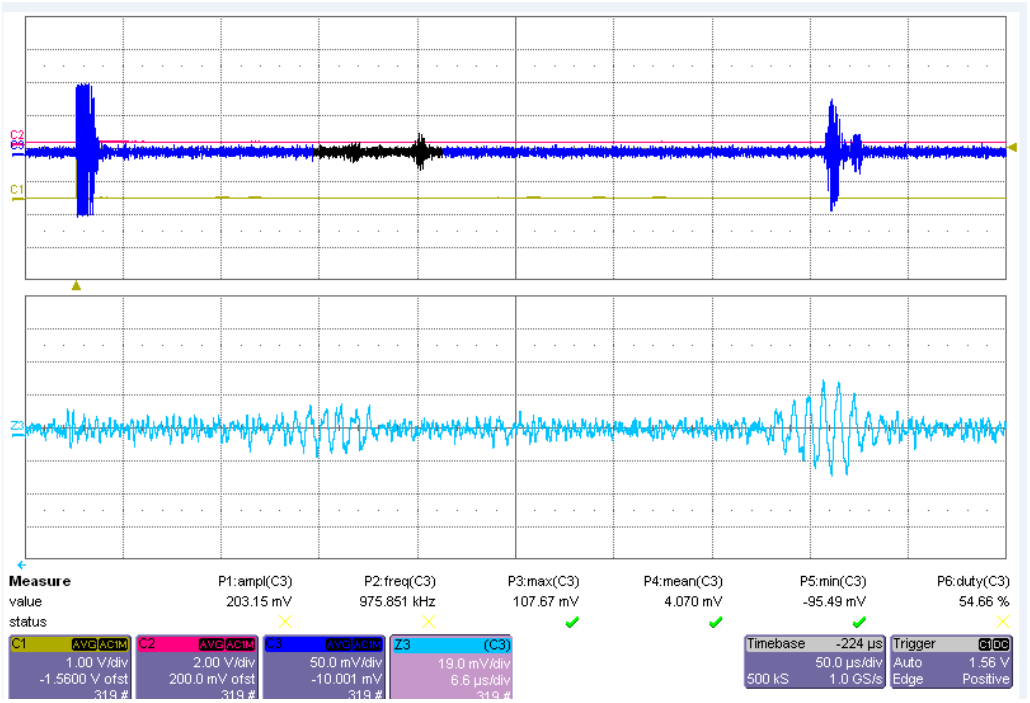

Figure 5. 27: IVP signal measured at Position (3) for $BaCl_2$ having a concentration 1M/L.

Figure 5.27 shows the IVP signal measured at position (3) from the $BaCl_2$solution. The two bursts of pulses appeared with 6 cycles. The first pulse cycle of the IVP signal appears at $t_1 = 74.56\,\mu s$, with amplitude $E_1 = 30.4 mV_{(pk-pk)}$ by taking the sound speed in the water at 1480 m/s, which gives the distance between the first boundary of material and the interface between the transducer and sample at 110.30 mm.

The second IVP signal appears at $t_2 = 87.76\,\mu s$, with amplitude $E_2 = 48.7\,mV_{(pk-pk)}$ which gives the distance between the second boundary from the transducer interface at 129.8 mm. The thickness of the sample was measured at 19.5 mm but the original thickness was 20 mm.

$$Error = \frac{20 - 19.50}{20} \times 100\% = 2.5\%$$

The errors caused by the setting of samples position.

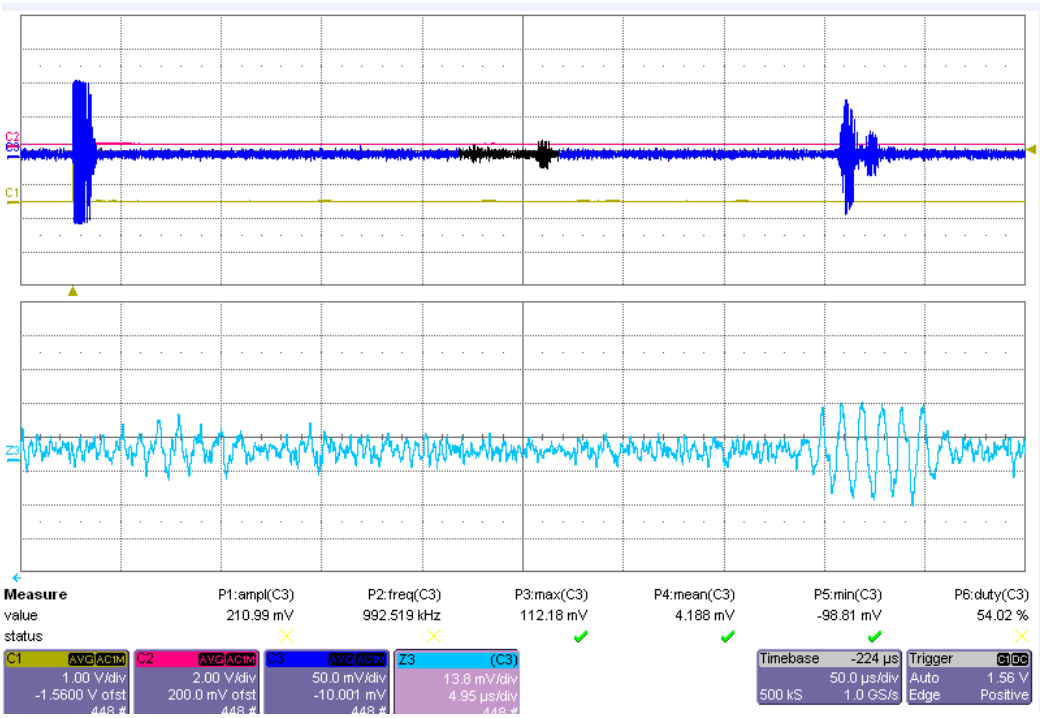

Figure 5. 28: IVP signal measured at Position (4) for $BaCl_2$ having a concentration 1M/L.

Figure 5.28 shows the IVP signal measured at position (4) from the $BaCl_2$solution. The two bursts of pulses appeared with 6 cycles. The first pulse cycle of the IVP signal appears at $t_1 = 100.08\ \mu s$, with amplitude $E_1 = 27.6 mV_{(pk-pk)}$ by taking the sound speed in the water at 1480 m/s, which gives the distance between the first boundary of material and the interface between the transducer and sample at 149.20 mm.

The second IVP signal appears at $t_2 = 114.62\ \mu s$, with amplitude $E_2 = 41.4\ mV_{(pk-pk)}$ which gives the distance between the second boundary from the transducer interface at 169.64 mm. The thickness of the sample was measured at 20.44 mm but the original thickness was 20 mm.

$$Error = \frac{20.44 - 20}{20} \times 100\% = 2.2\%$$

The errors caused by the setting of samples position.

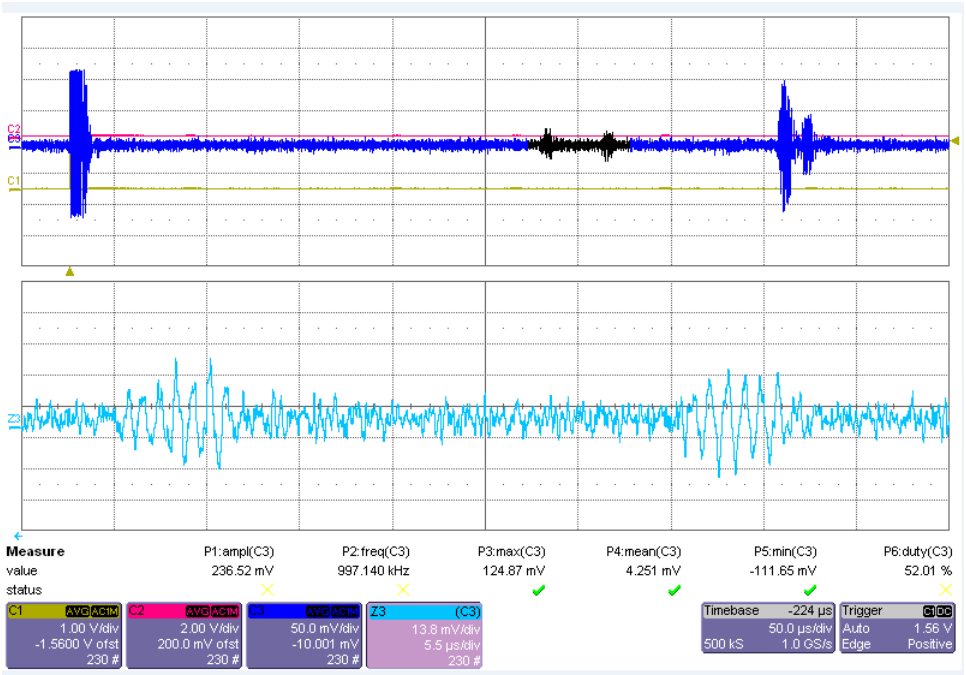

Figure 5. 29: IVP signal measured at Position (5) for $BaCl_2$ having a concentration 1M/L.

Figure 5.29 shows the IVP signal measured from the $BaCl_2$ solution *at* position 5. The two bursts of pulses appeared with 6 cycles. The first pulse cycle of the IVP signal appears at $t_1 = 129.46\ \mu s$, with amplitude $E_1 = 48.3 mV_{(pk-pk)}$ by taking the sound speed in the water at 1480 m/s, which gives the distance between the first boundary of material and the interface between the transducer and sample at $190.16\ m$m.

The second IVP signal appears at $t_2 = 144.3\ \mu s$, with amplitude $E_2 = 69.76\ mV_{(pk-pk)}$ which gives the distance between the second boundary from the transducer interface at 210.35 mm. The thickness of the sample was measured at 20.19 mm but the original thickness was 20 mm.

$$Error = \frac{20.19 - 20}{20} \times 100\% = 0.95\%$$

The errors caused by the setting of samples position.

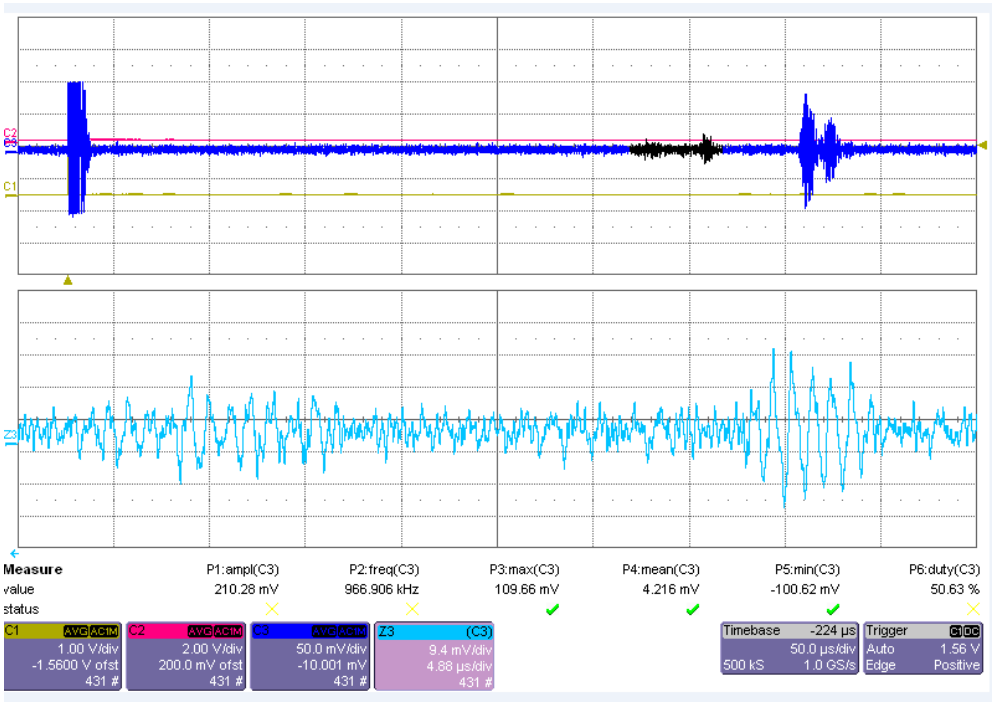

Figure 5. 30: IVP signal measured at Position (6) for $BaCl_2$ having a concentration 1M/L.

Figure 5.30 shows the IVP signal measured at position 6 from the $BaCl_2$ solution. The two bursts of pulses appeared with 6 cycles. The first pulse cycle of the IVP signal appears at $t_1 = 155\ \mu s$, with amplitude $E_1 = 28.2 mV_{(pk-pk)}$ by taking the sound speed in the water at 1480 m/s, which gives the distance between the first boundary of material and the interface between the transducer and sample at $229.40\ m$m.

The second IVP signal appears at $t_2 = 167.42\ \mu s$, with amplitude $E_2 = 54.52\ mV_{(pk-pk)}$ which gives the distance between the second boundary from the transducer interface at 249.20 mm. The thickness of the sample was measured at 19.8 mm but the original thickness was 20 mm.

$$Error = \frac{20 - 19.8}{20} \times 100\% = 1\%$$

The errors caused by the setting of samples position. The distance between the sample and the electrodes has a major effect on the IVP signal amplitude.

Table 5. 5 : The measured IVP signal, sample position, and the setting positions of the sample.

Sample Setting Positions	X Setting (D1) (mm)	X Setting (D2) (mm)	X' Measured (D1) (mm)	X' Measured (D2) (mm)	CVP $(E_2 - E_1)$ Gain (39 dB) (mV)
P1	30	50	29.6	49.5	24.5
P2	70	90	70.3	90.99	20.9
P3	110	130	110.3	129.8	18.3
P4	150	170	147.2	170.6	19.5
P5	190	210	190.16	210.35	21.46
P6	230	250	229.9	249.2	26.32

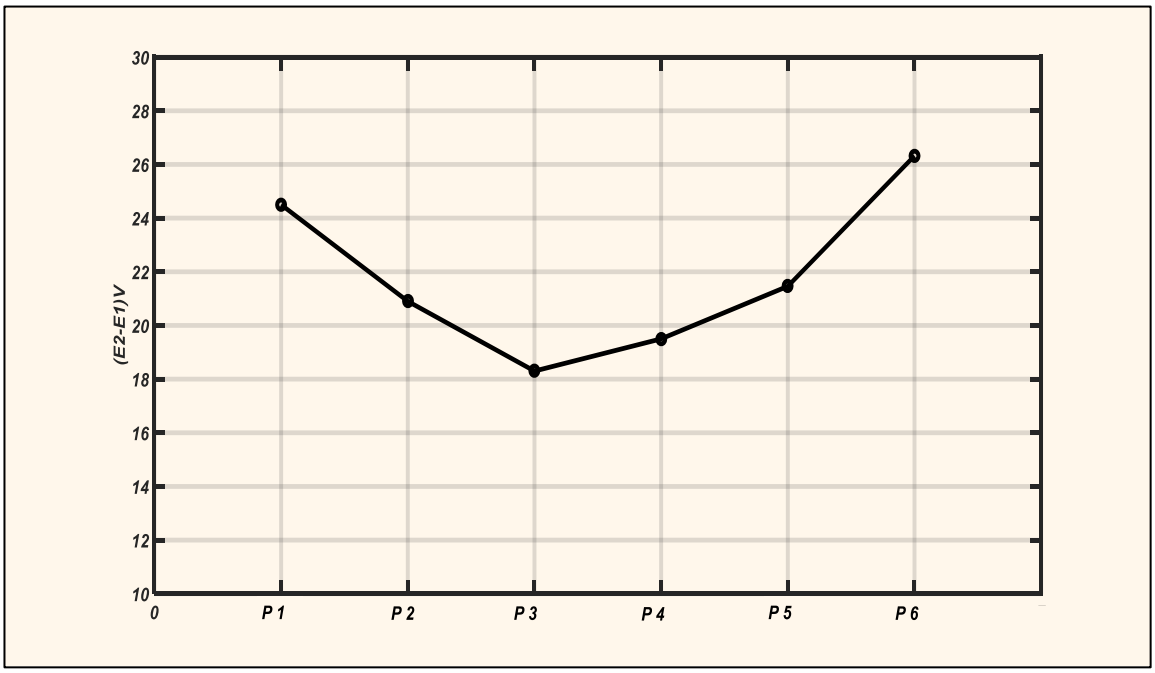

Figure 5. 31: IVP signal amplitude as a function of electrode separations.

Figure 5.31 shows how IVP signal amplitude changes as a function of the separation distance between the two electrodes placed inside of the standard II rig contains a sample located at different positions inside the rig. The IVP signal is measured across the 280mm water tank in length using electrodes placed at the rear and end side of the rig. From the above results, we reveal that the IVP signal is measurable for a sample placed anywhere within the 280mm separation distance between two electrodes.

5.12 Summary

In this Chapter the newly developed UVP model (Leeds standard III device) for UVP imaging have been presented. This device is capable of non-intrusive measurement. It is made from agar, and the electrodes non-intrusively placed outside the mock body. They receive signals from the agar objects containing either ionic or nanoparticular species, thus providing the physicochemical property of the sample as a complementary image to conventional ultrasound imaging. All electronic devices involved in the UVP measurement system has been presented.

The signal was detected for multiple samples inside a mock tissue model. The experimental works were presented in relation to ultrasound UVPD in order to provide information to optimize the UVP device measurements. This work has demonstrated huge potential in developing innovative technology for nanoparticle characterization in engineering and for physicochemical imaging for medicine.

The evidence of detecting different ionic electrolyte by UVP model was presented. This model may require further improvement to the sensing method and imaging constructions. The UVP signal was detected for both ionic electrolytes and colloidal suspensions to verify previous experiments using the newly developed device. Another two factors of salt and pH which can affect the UVP signal are reported. The ultrasound vibration potential measurement technology limitations have presented by measuring the UVP signal using each electrode at 140mm away from the source of charge.

CHAPTER SIX: ULTRASOUND VIBRATION POTENTIAL IMAGING

Summary: *This chapter provides a new method for detecting ultrasound vibration potential (UVP) using a low energy source of excitation. It provides a methodology of colloid vibration potential (CVP) to enhance ultrasound imaging. The signals, data processes and resulting images are presented by combining the two methods of UVP and conventional diagnostic imaging. It presents tissue imaging using three different methods such as CVP, tomography, and conventional ultrasound imaging.*

6.1 Introduction

This chapter represents the experimental investigation of imaging colloidal/ionic objects embedded in a mock agar body. It reports a methodology of UVP imaging using a low energy source of excitation. We address a unique feature of UVP to provide extra information on the objects being imaged. The combination of ultrasound imaging explains the benefits of UVP imaging in comparison to the current ultrasound imaging technique. The result provides physicochemical images of ionic electrolytes and silica nanoparticles, both embedded with a similar concentration into the mock agar body to avoid reflection of the ultrasound wave. The first part of this chapter will demonstrate the unique feature of CVP, by detecting the CVP signal from a colloidal object embedded into agar mock body using the newly devised Leeds standard III model. The 1D imaging of CVP will be compared with 1D and 2D ultrasound imaging. The second part of this chapter will report on the excitation and sensing by utilizing a conventional ultrasound transducer array for signal measurement and decoding, including the signal, data processes, and the resulting images.

The last part of this chapter will investigate whether the CVP signal can be measured from animal tissue with our current instrumentation and its difference from other conventional measurements. This work demonstrates the CVP signal (or one-dimensional imaging), the ultrasound reflection signal and imaging, and electrical tomography imaging on the same tissue. The discovery of a new finding would present specific tissue structures by comparing images of these three modes of tissue

information: specified as being ionic vibration based, ultrasound impedance reflection intensity based, and conductivity distribution based. This work hopes to reveal the feasibility of CVP imaging in future tissue imaging potential.

6.2 Experiment

The experimental work was carried out using a Leeds standard III device. The agar mock body was embedded with silica nanoparticle suspensions, having an average particle diameter of 21 nm. The three methods of imaging using the Leeds standard III device are explained below. Three different imaging tests – 1D CVP, 1D ultrasound, and 1D ultrasound reflection – were carried out for the same samples.

6.2.1 Excitation and Sensing

First, in order to prove that the setup works for the measurement of the CVP signal from the nanoparticle suspension within the agar mock body, we used the Leeds standard III device for UVP imaging. This imaging method consists of two parts: input and output. The input instruments are the signal generator (the Agilent 33250A) set with 450 $mV_{(pk–pk)}$ **1 MHz** frequency and 6 cycles with burst period 50 ms, and a duty cycle of 0.01%. This burst was amplified by a radio frequency (RF) amplifier (GA-2500A, RITEC), for up to 1000 $V_{(pk–pk)}$.

The output from the RF amplifier is connected to an impedance matching resistor **50** Ω and a 1 MHz piezoelectric transducer (Sonatest Ltd), which is fixed at one side of the agar block in order to apply the amplified ultrasound wave into the agar mock body and the sample.

The CVP signal is generated from the colloidal suspension due to the presence of ultrasound pressure inside the sample and this makes the particles and ions vibrate, creating polarization. This polarization creates a number of dipoles and the summing these dipoles is measured as a CVP electric signal by the two electrodes made from aluminium foil and placed non-invasively outside the agar mock body. The detected CVP signal is amplified by an ultrasound pulser/receiver (5072PR.RD.Tech) with a gain factor of 39 dB, and the amplified signal is sent to the digital LeCroy oscilloscope (LT374, Maxim Instruments) for calibration and data collection. The experiment connection diagram for the 1D CVP imaging was shown in Chapter 5, Figure 5.8. The embedded sample dimensions within the agar mock body were: width = 12 mm, length = 30 mm, and depth = 40 mm. The sample and the mock body had similar concentrations

of 1 wt%. The sample was positioned 58 mm away from the transducer interface, and 14 mm away from the sensor electrode. The image of the mock body and the sample are presented in Figure 6.5 in Chapter 5. The CVP signal was measured and displayed on the oscilloscope screen.

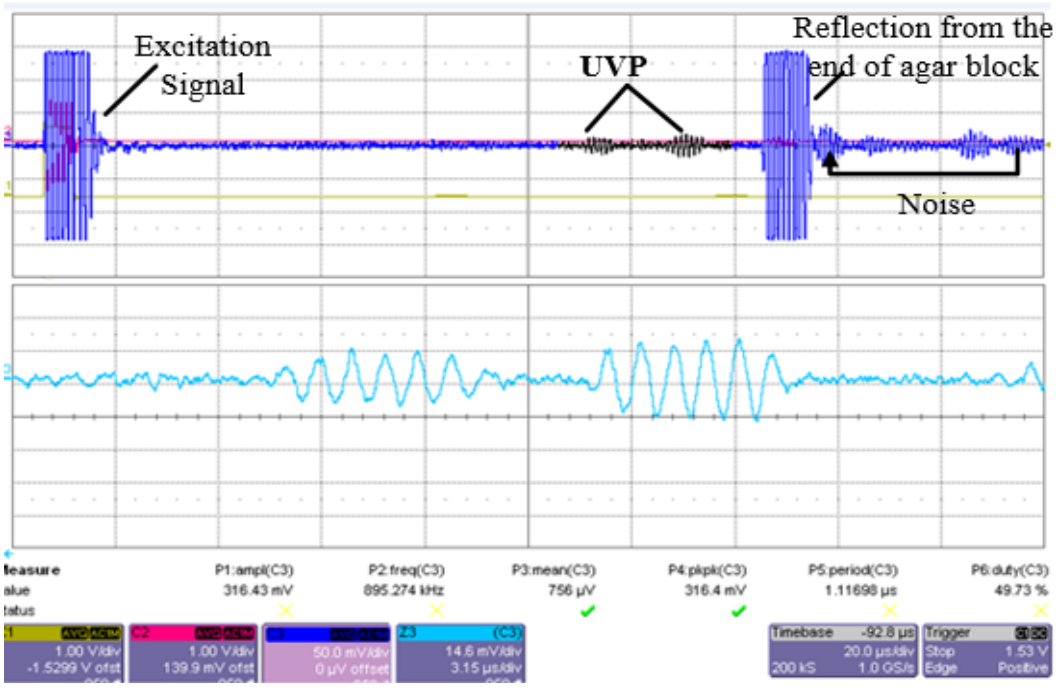

Figure 6.1.: CVP signal for silica dioxide, 21 nm and a concentration of 1 wt%.

Figure 6.1 shows the CVP signal detected from the colloidal suspension of silica dioxide nanoparticles embedded in the agar mock body. The two bursts of pulses appeared with 6 cycles. The first pulse cycle of the CVP signal appears at $t_1 = 37.8\ \mu s$ by taking the sound speed in the agar block at 1600 m/s, which gives the distance between the first boundary of material and the interface between the transducer and agar at 60.48 mm. The second CVP signal appears at $t_2 = 45.6\ \mu s$, which gives a value of the distance between the second boundary from the transducer interface at 72.96 mm.

The thickness of the sample can be measured by Equation 5.1:

$$\boldsymbol{d = C\ (m/s) \times \Delta t\ (s)} \qquad (6.1)$$

Where **d** is the thickness of the sample, **C** is the speed of the ultrasound sound propagation, $\boldsymbol{\Delta t}$ is the time difference between the first signal burst and the second signal burst.

$$d = 1.6 \times 10^{6} \left(\frac{mm}{s}\right) \times 7.875 \times 10^{-6} \, (s) = 12.6 \text{ mm}$$

The thickness of the sample was measured at 12.6 mm but the original thickness was 12 mm. This error is caused by the diffusion.

$$Error = \frac{12 \cdot 6 - 12}{12} \times 100\% = 5\%$$

The error is caused by two major factors: one is the measurement and the second is the diffusion of the sample into the agar mock body. This result shows that CVP is measurable from an agar mock body embedded with a colloidal object. The second imaging test will be the 1D ultrasound reflection detection (URD) and the 2D ultrasound diagnostic imaging using the Mindray DP-6600.

6.3Evaluation of the Unique Feature of UVP

This part of the experiment is to examine the unique feature of UVP imaging. We used a similar agar body containing a colloidal object for this imaging method. The experiment setup and connections for the 1D URD are shown in Figure 6.2. The transducer with 1 MHz frequency was connected to the ultrasound pulser/receiver which allows the pulsed wave to be generated by the transducer and then to receive the reflected signal from the body.

The signal was amplified by 39 dB using the voltage amplifier and then it was sent to the LeCroy oscilloscope, Editor (2004), for calibration. The ultrasound pulses through the agar mock body and the colloidal object. The same ultrasound signal was reflected at the end of the agar mock body at the agar-air interface and was received by the same transducer.

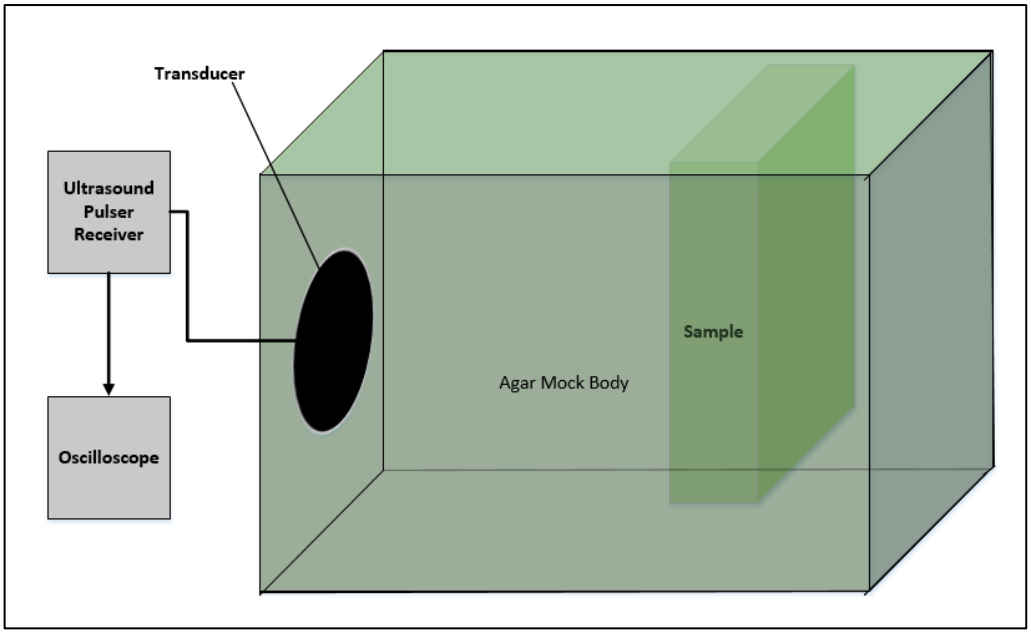

Figure 6.2.: Experiment connection diagram for reflection detection.

Figure 6.2 shows the diagram of the experiment setup and connections for the 1D URD imaging test. The signal was displayed by the oscilloscope screen and this is shown in Figure 6.3.

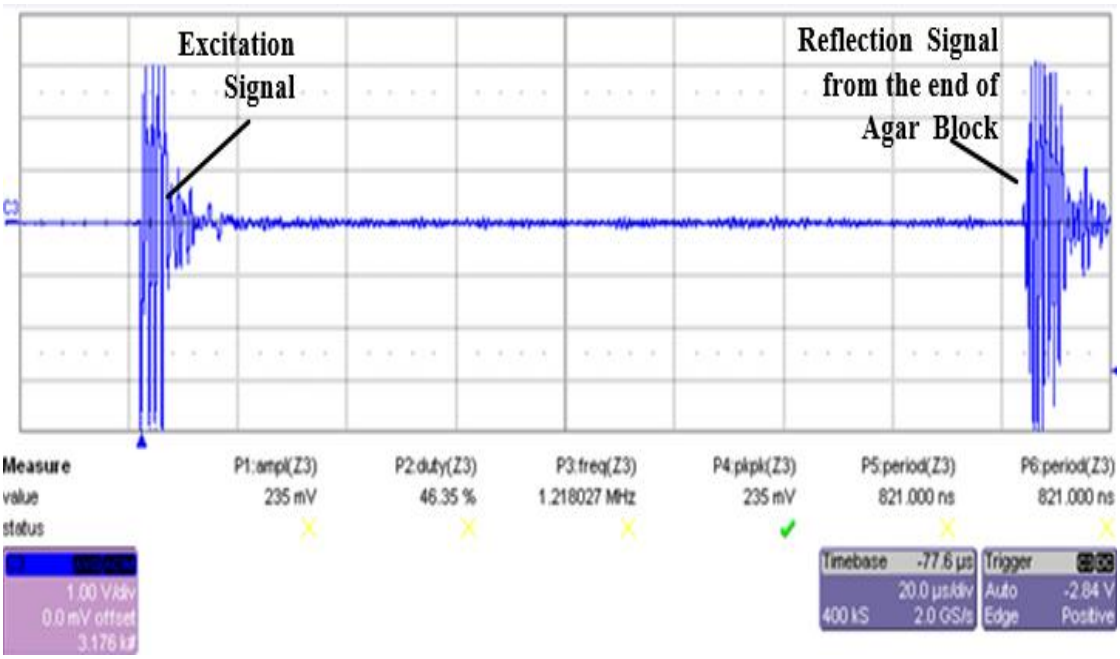

Figure 6.3.: URD signal from the agar mock body.

Figure 6.3 shows that there no reflection signal appeared from the sample. The signal at the left side of Figure 6.3 is the excitation signal and the large signal at the right side is the reflection signal at the end of the agar mock body. There is not any other signal

appearance between the excitation signal and the reflected signal at the agar-air interface.

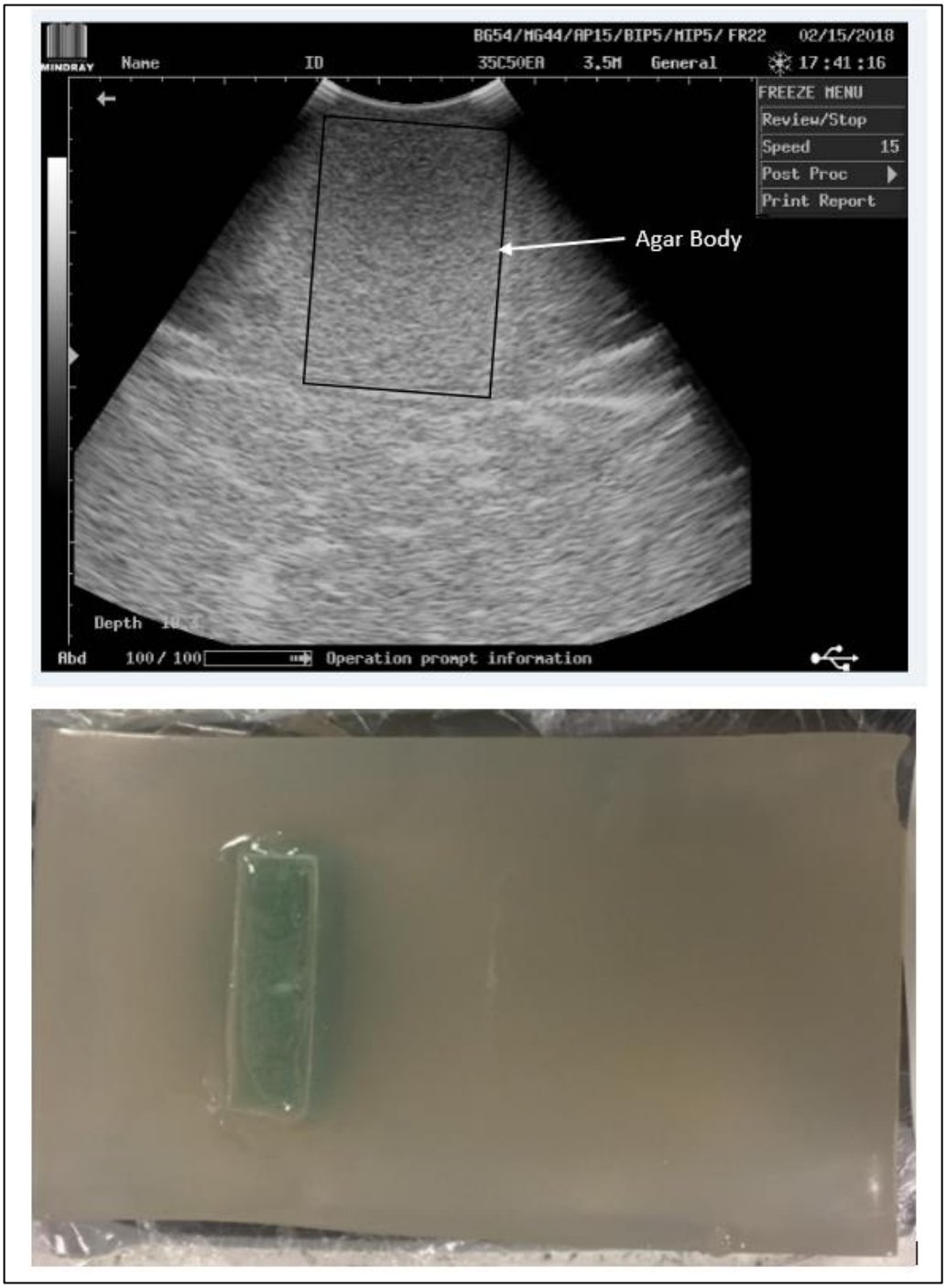

Figure 6.4.: The agar mock body containing a sample (green colour) and the scanned 2D image using a conventional diagnostic machine, the Mindray DP-6600.

Figure 6.4 shows that the sonographic image did not detect the sample which was embedded in the agar mock body, and from Figure 6.1, we can see the signal was detected by our CVP method. The distance between these two signals was measured at 86.24 mm, with an error of 1.2% caused by the measurement and the ultrasound gel thickness placed at the interface between the agar and the transducer. This result provides a unique feature of UVP imaging. Another scan of the agar mock body using a conventional Mindray diagnostic imaging machine and a photographic image of the mock body are shown in Figure 6.4.

We have shown how CVP imaging works for a body containing different material with similar impedance and also the imaging of a similar body using a conventional imaging method. The three imaging results above (for the CVP, URD and ultrasound) clearly show how CVP can enhance ultrasound imaging.

6.4 Signal Feature of the Curvilinear Scanner

We aim to show the capability of UVP method to enhance the ultrasound Imaging. In order for us to measure UVP signal with a commercial ultrasound array, and compared to the current commercial ultrasound imaging, we examine this commercial phased array to measure its scanning feature. The curvilinear transducer (Model 35C50EA) with an average frequency of **3.5 MHz**, was connected to the ultrasound diagnostic imaging machine, the DP-6600 Mindray, (2005), in order to send the ultrasound pulse through the water tank. The extra sensor piezoelectric transducer with a frequency of **5 MHz** used to detect the convex transducer signal was placed at the bottom of the tank, opposite the curvilinear transducer face. The distance between the transmitter (curvilinear transducer) and the receiver (piezoelectric transducer) was**100 mm**, and the curvilinear transducer placed into the water at a depth of **5 mm**. The ultrasound wave with a frequency of 3.5 MHz was sent into the water tank via a curvilinear transducer, and then the signal was detected by the piezoelectric transducer placed at the bottom of the tank opposite the curvilinear probe. The experimental connection diagram is shown in figure 6.5.

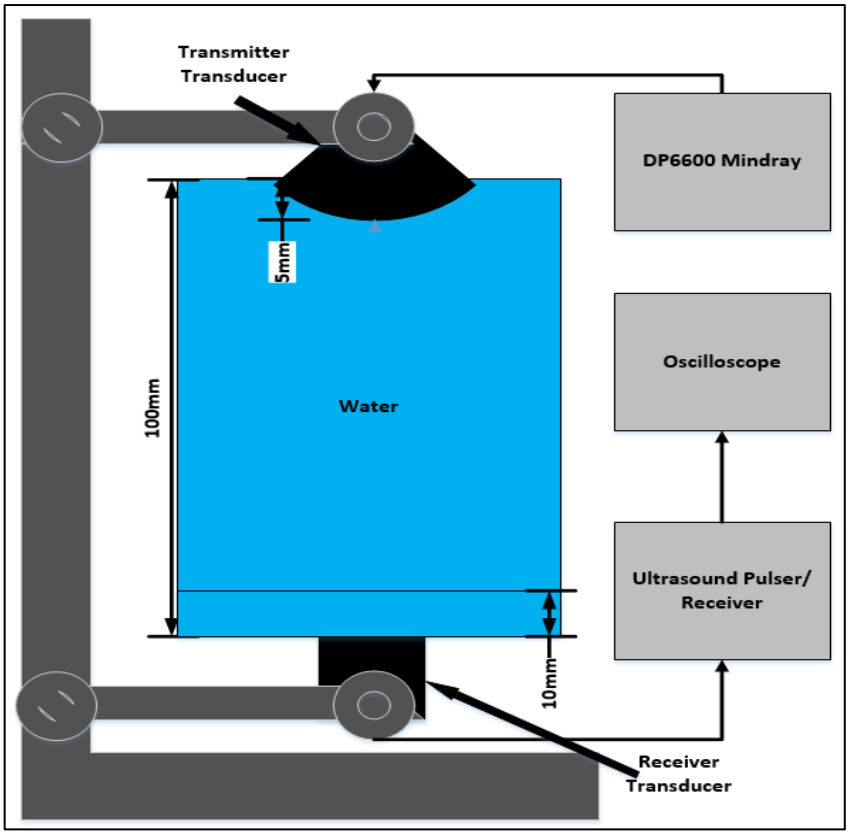

Figure 6.5.: Diagram of experiment setup and connections for DP-6600 signal detection.

The array elements are incrementally switched on and off to generate pulse-echo signals. In a curvilinear transducer, each array element emits one beam at a time, with different angles – more details about this transducer are given in Chapter 2, Section 2.2.2. The curvilinear transducer scans in the $(\boldsymbol{xz})$ plane. The acoustic beams move incrementally by $\Delta\mathbf{x}$ along the direction of the x-axis each time or at each position the pulse-echo beam is created. An elements shifts the beam angle by $\Delta\boldsymbol{\theta}$ and the image in the $\boldsymbol{(xz)}$ plane. The array is situated on a curve with radius $\mathbf{R}$ and line increments ΔS, alongside the curved surface.

$$\Delta \boldsymbol{S} = \boldsymbol{R} \times \Delta \boldsymbol{\theta} \tag{5.2}$$

At any time, one element sends a beam and receives the reflected beam, the next element with an angle difference of $\Delta\boldsymbol{\theta}$ sends a beam and receives echoes.

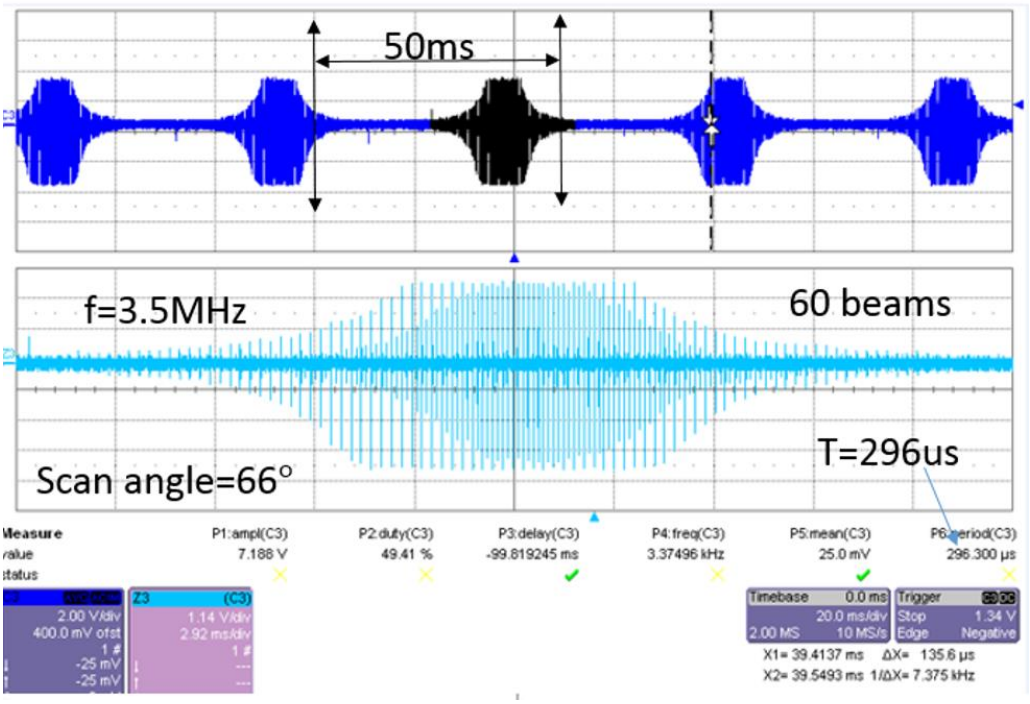

Figure 6.6.: The full scan of the curvilinear transducer signal.

Figure 6.6 shows the full scan of the curvilinear probe. We can see from the figure that the repetition of each scan is at **50 ms**, this means the scan is made at $\frac{\mathbf{20}\boldsymbol{fram}}{\boldsymbol{second}}$. The transducer scans with various angles and the minimum angle we used was $\mathbf{66}°$. The scan was monitored by the oscilloscope and displayed in Figure 6.6. According to our experiment, this transducer produces **66** beams of ultrasound signal. Each ray generates at a time which is different from the other rays. Each element produces a pulse with a perspective of $\Delta\boldsymbol{\theta}$. The measured frequency of this scan was **3.5 MHz**, and this is the mean frequency of this transducer. The pulse repetition period was measured at $\mathbf{296\ \mu s}$.

In Figure 6.6 each line is an excitation signal generated by each element in the transducer. The excitation starts with the component from left to right. The Mindray

diagnostic imaging machine has buttons that can be used to change the transducer scanning angle and frequency.

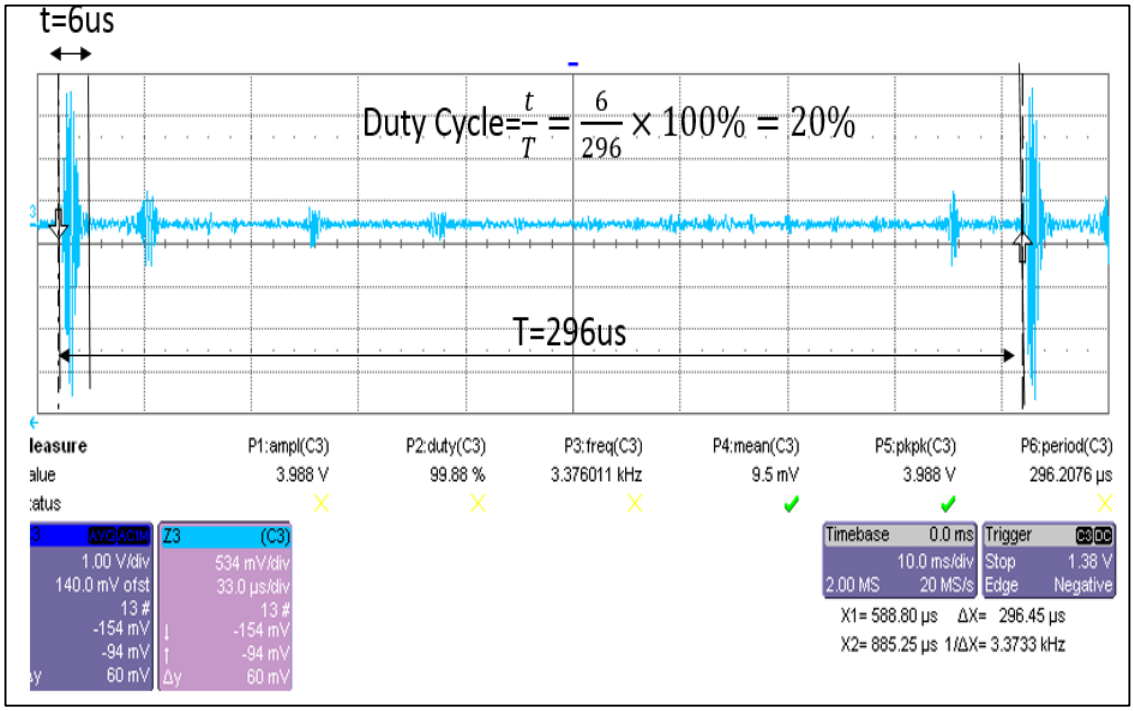

Figure 6.7.Two beams of the curvilinear transducer signal.

Figure 6.7 shows the zoomed image of two beams generated by the curvilinear transducer signal. The transducer scans with various angles and the minimum angle we used was 66°.

The number of beams at each scan we measured from Figure 6.6 is 60 beams.

$$\boldsymbol{Duty\ cycle} = \frac{(\boldsymbol{pulse\ width})}{(\boldsymbol{pulse\ repetition\ period})} \times \mathbf{100\%} \qquad (5.3)$$

$$= \frac{\mathbf{6}}{\mathbf{296}} \times \mathbf{100\%} = \mathbf{20\%}$$

$$\boldsymbol{f(Hz)} = \frac{\mathbf{1}}{\boldsymbol{t}} = \mathbf{3.5 \times 10^{6}\ Hz}$$

$$\boldsymbol{t(s)} = \frac{\mathbf{1}}{\boldsymbol{f}} = \mathbf{296 \times 10^{-6}\ s}$$

6.5Method of CVP Imaging Using Low Excitation Energy

The aim of this test is to examine whether the CVP is measurable using a low power excitation source, and if so, can we use the current conventional imaging system as a source of excitation and measuring the CVP signal using the curvilinear transducer. This experimental work combines ultrasound imaging with CVP imaging and demonstrates that CVP can enhance ultrasound imaging. The agar mock body shown in Figure 6.4 was used to examine the CVP imaging. The input in this experiment comprises the ultrasound diagnostic machine and a curvilinear transducer(the 35C50EA) to generate the ultrasound pulses. The ultrasound pulses were sent through the agar mock body via the curvilinear transducer with a frequency of 3.5 MHz and 60 sound beams. The agar mock body contains a sample of a SiO_2 suspension having a concentration of 1 wt% and particle size of 21nm. The sample has a similar concentration to the agar mock body and the interface between the mock body and the sample was ignored. The distance between the sample and the transducer interface is 58 mm. The sample has dimensions: x = 10 mm, y = 30 mm and z = 40 mm. The output of the experiment consists of two electrodes, the sensor electrode and the grounding electrode, both of which were made from aluminium foil. These electrodes have a square shape with dimension of 10 × 10 mm. Both electrodes were connected to a low input voltage amplifier with an amplification factor of 39 dB. The amplifier output was connected to the oscilloscope. The diagram of the experiment setup and connections for CVP detection using the ultrasound diagnostic machine as a source of excitation is shown in Figure 6.8.

The agar mock body was scanned by the Mindray DP-6600 via a curvilinear transducer with a frequency of 3.5 MHz at a room temperature of 25℃. The CVP signal was generated from the colloidal object due to the vibration of nanoparticles inside the colloidal suspension.

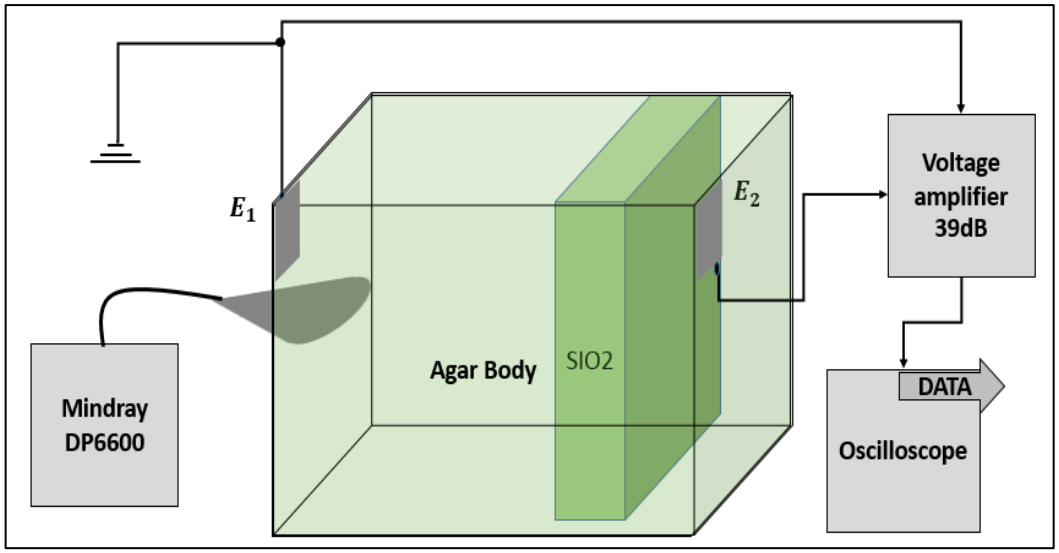

Figure 6.8.: Diagram of CVP imaging using the DP-6600 as an excitation source.

The signal was measured by both electrodes attached to front and rear side of the agar mock body. The measured CVP signal was amplified by the voltage amplifier with an amplification factor of 39 dB. The amplified signal sends to the oscilloscope for calibration and data collection – the data collected by the oscilloscope and the image displayed on oscilloscope screen is shown in Figure 6.9.

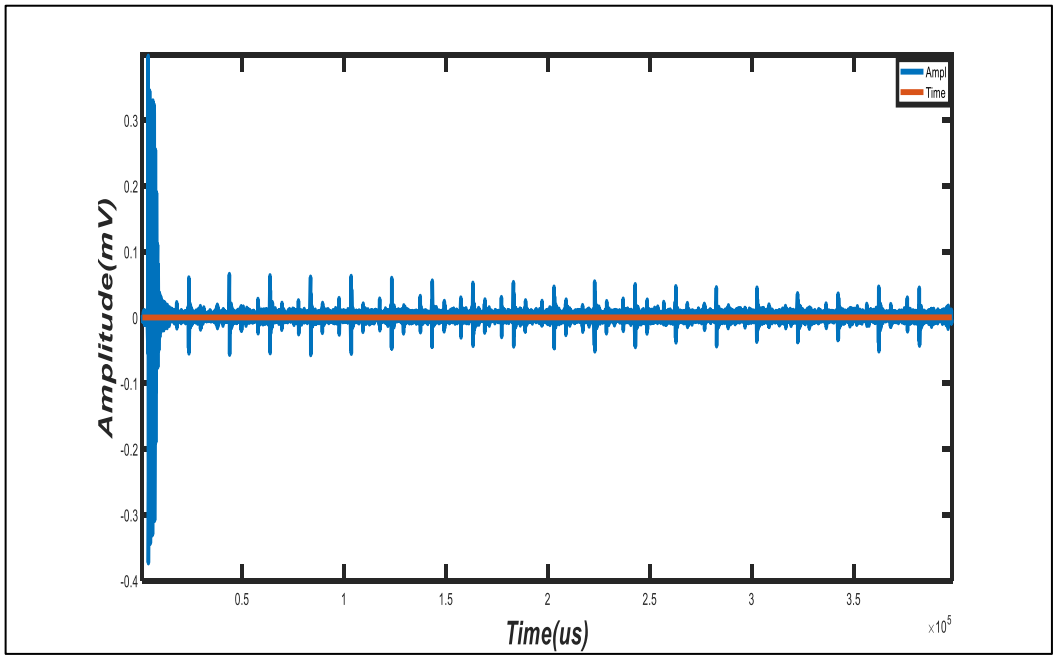

Figure 6.9.: CVP signal for silica, with 21 nm and a 1 wt% concentration.

Figure 6.9 shows the CVP signal detected by both electrodes placed at either side of the agar mock body. The significant excitation signal is shown at the beginning (on the left side of the image), and 38 bursts of the measured CVP signal were followed by the excitation signal. The CVP signal appeared before the significant electric signal at the agar-air interface Reflections signal (RS) signals. The transducer scanned the whole of the agar mock body but the only signals detected were generated by the sample. The sample length was 30 mm, but the agar body length was 56 mm, therefore, not all of the beams generated by the curvilinear transducer were able to go through the sample due to wider scanning angle of the transducer. From Figure 6.9 we can see that for each beam of ultrasound two bursts of CVP appeared. Further explanation of these signals is given in the following section

6.6Data Process and Image Construction

To process the data for image construction, we need to measure the time of appearance of each UVP signal. From Figure 6.10, we can clearly see the 38 bursts of CVP signal measured from the colloidal object.

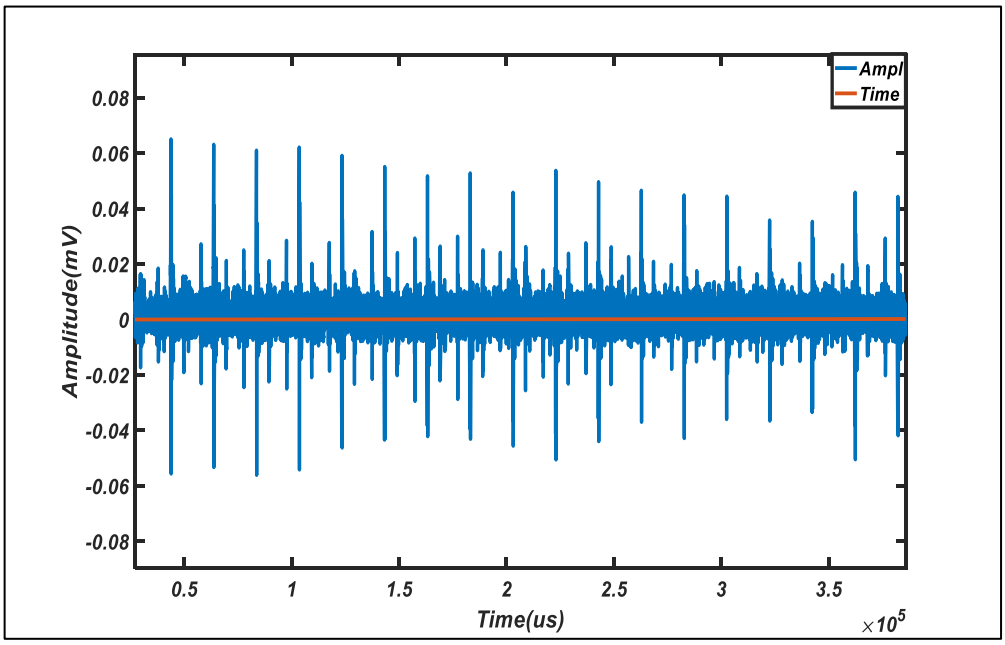

Figure 6.10.: CVP signal for SiO_2.

Figure 6.10 shows 38 bursts of CVP signals appeared at the entrance and exit of the sample and 19 bursts of RS signal appeared at the end of the mock agar body. In the Figure 6.10, the largest amplitude is the reflected signal from the agar-air interface

generated at the end side of the agar mock body. The two pulses of CVP signal appeared and followed a single beam of RS signal. When the ultrasound beam travelled through the agar mock body the first signal appeared at the entry point of the sample, the second pulse of CVP signal appeared at the exit point of the sample, and then the last pulse of RS signal, with high amplitude, appeared at the end of the mock body. Basically, each element in the curvilinear transducer emits one beam at a time and each beam is delayed by time $\boldsymbol{t}$ from the first beam, and each beam is generated at an angle $\boldsymbol{\theta}$. When each beam travels through the sample two bursts of CVP signal are generated by the sample. Each burst of CVP signal is generated at both sides of the sample, therefore, any number of excitation beams go through the sample twice as these number bursts of CVP are generated by the sample.

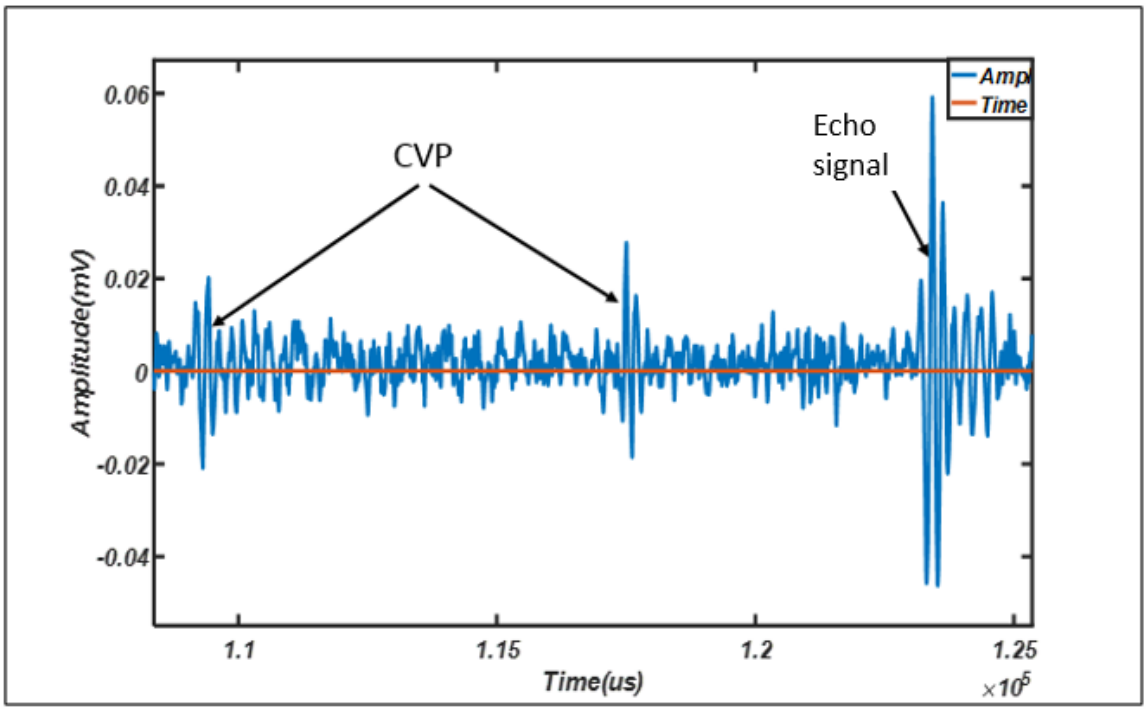

Figure 6.11.: Two bursts of CVP signal for SiO_2 with 1 wt% concentration and particle diameter of 21 nm, with a single beam of echo signal.

Figure 6.11 shows the zoomed image of two bursts of CVP signal detected for SiO_2 with a concentration of 1 wt%, and one burst of the RS signal. In the Figure 6.11 we can see the signal shifted 180° from the entrance to the exit of the sample. The first pulse of UVP detected at the near side of the sample is smaller in amplitude compared to the second pulse of CVP at the far side of the sample. This difference in magnitude is due

to the ultrasound vibration potential distribution (UVPD). The curvilinear transducer scanned 19 beams over the sample width of 30 mm. Each beam has an angle of $\Delta\boldsymbol{\theta}$, and a delay time of $\Delta\boldsymbol{t}$ from each other. The angles are similar for each beam – if we know the angle of one beam, we can calculate the angles of the following beams. The first signal appeared from the entry point of the sample at a time $\boldsymbol{t_1}$ and the second sample appeared from the exit point of the sample at a time $\boldsymbol{t_2}$. If the velocity of the ultrasound (v) in the agar mock body is taken as $1600\ (m/s)$ at a temperature of 25℃, we can measure the thickness of the sample by using Equation 6.1:

The time difference between the appearance of the first burst of CVP signal and the second one is $\Delta\boldsymbol{t}$. From Figure 6.11 we can measure $\boldsymbol{\Delta t}$ at:

$$\boldsymbol{\Delta t = t_2 - t_1 = 7.4\ \mu s}$$

$$\mathbf{d = 1600 \times 10^3 \left(\frac{mm}{s}\right) \times 7.4 \times 10^{-6}\ (s) = 11.8\ mm}$$

The actual thickness of the sample was 10 mm, and the error can be given by:

$$\boldsymbol{Error = \frac{11 \cdot 8 - 10}{10} \times 100\% = 18\%}$$

The error occurred due to the measurement of the sample thickness, and the penetration of the sample in the agar mock body.

The distance between the transducer face and the sample is given at $h = 60$ mm, the length of each side of the sample from the transducer face is b, and the width of the sample $C = 30$ mm, therefore, the scanning angle can be given by:

$$\boldsymbol{\tan(\theta) = \frac{c}{b}} \qquad (6.4)$$

Where: $\boldsymbol{b = \sqrt{\frac{1}{2}c^2 + h^2}}$

$$\boldsymbol{b = \sqrt{450 + 3600} = 63.63\ mm}$$

$$\boldsymbol{\tan(\theta) = \frac{30}{63.63} = 0.5^\circ}$$

We detected 19 CVP beams from the sample and each beam was separated by an angle of $\Delta\theta$. We then used MATLAB software (See Appendix A1) to process the data and construct the image. The code was written to record the time when each burst of CVP

signal appeared. For each beam we have two bursts of CVP signal, measured at t_1 for the first signal burst at the entry point to the sample and the second burst measured at t_2 for the second signal burst. We can use Equation 5.1 to calculate the thickness of the sample **d** (mm). The calculation of the time in which each signal of CVP was measured and the thickness measured between each CVP signal is presented in Table 5.1.

Table 6. 1 : The measurement of CVP signal data, time, thickness, and errors

$t_1(us)$	$t_2(us)$	$\Delta t(us)$	$d(mm)$	$Error\%$
2.95E+04	3.80E+04	8.42E+03	1.35E+01	1.23E-01
4.94E+04	5.75E+04	8.11E+03	1.30E+01	8.13E-02
6.96E+04	7.77E+04	8.11E+03	1.30E+01	8.13E-02
8.95E+04	9.76E+04	8.09E+03	1.29E+01	7.87E-02
1.09E+05	1.18E+05	8.20E+03	1.31E+01	9.33E-02
1.29E+05	1.37E+05	8.20E+03	1.31E+01	9.33E-02
1.49E+05	1.58E+05	8.30E+03	1.33E+01	1.07E-01
1.69E+05	1.77E+05	8.20E+03	1.31E+01	9.33E-02
1.89E+05	1.97E+05	8.20E+03	1.31E+01	9.33E-02
2.09E+05	2.17E+05	8.30E+03	1.33E+01	1.07E-01
2.29E+05	2.37E+05	8.30E+03	1.33E+01	1.07E-01
2.49E+05	2.57E+05	8.20E+03	1.31E+01	9.33E-02
2.69E+05	2.77E+05	8.30E+03	1.33E+01	1.07E-01
2.89E+05	2.97E+05	8.20E+03	1.31E+01	9.33E-02
3.09E+05	3.17E+05	7.80E+03	1.25E+01	4.00E-02
3.28E+05	3.37E+05	8.30E+03	1.33E+01	1.07E-01
3.52E+05	3.57E+05	5.00E+03	8.00E+00	3.33E-01
3.68E+05	3.76E+05	8.10E+03	1.30E+01	8.00E-02
3.88E+05	3.96E+05	8.10E+03	1.30E+01	8.00E-02

The data was first collected by the oscilloscope and downloaded to an excel file. The data transferred to MATLAB to generate the UVP image. The speed of ultrasound selected in agar at 1600m/s, and the UVP starting point at $3us$, and end point $296us$. The fixed threshold selected at 0.008V, with the spanning angle of $0° - 180°$. At each point where the signal appeared the time is measured. We have two different times for each CVP signal: one where the signal appeared at the front side of the sample and another when the signal appeared at other side of the sample.

For every two bursts of CVP signal the time difference between them is measured as Δt. The measured time is multiplied by the sound speed in the agar at 1600 m/s. There is a time difference between each excitation beam, and this gives a separation distance between each pulse at the beginning of the sample and also each pulse at end of the sample. The third reflection signal (RS) signal appeared at the agar-air interface. The image was constructed using MATLAB and is presented in Figure 6.12.

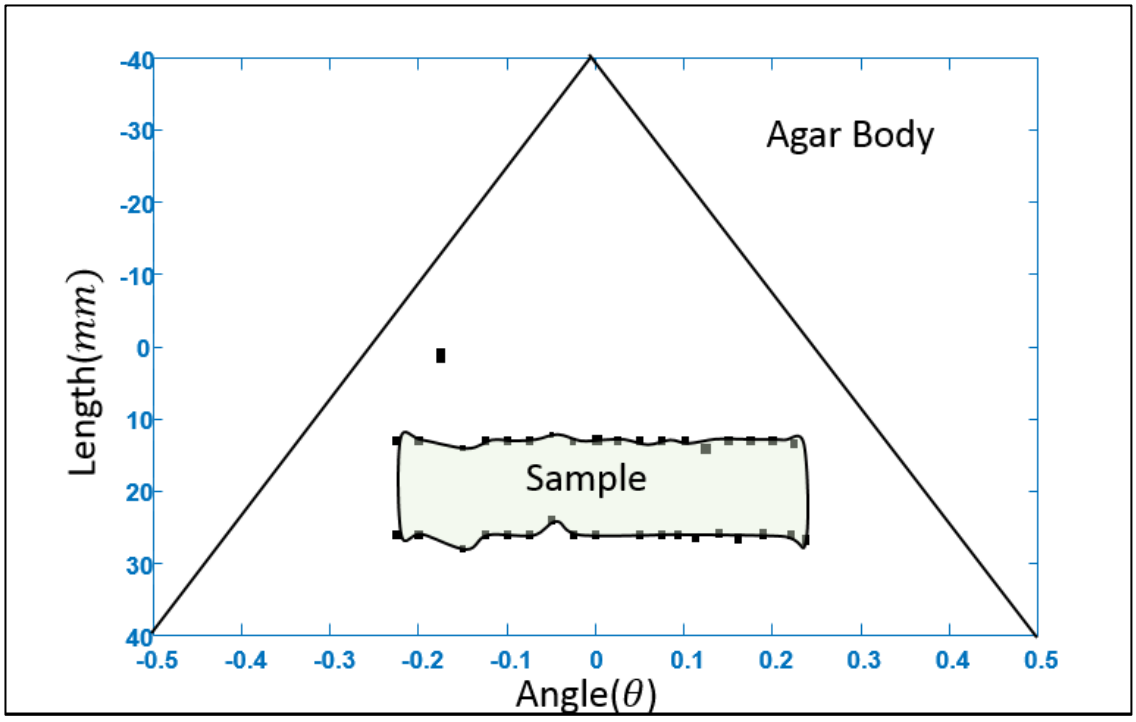

Figure 6.12.: The reconstructed CVP graphic for the agar mock body containing a sample of SiO_2 with a concentration of 1 wt%.

Figure 6.12 is an image generated by the data shown in Table 6.1. Each white dot represents a burst of CVP signal. The first row of white dots represents the signals as they appeared at the entry point of the sound beam into the sample and the second row of white dots represent the CVP bursts as they appeared at the exit point of the sample. This shows that CVP can enhance ultrasound imaging. The distance between the two lines of white dots represents the thickness of the sample. The x-axis is the angle of the scanning by the transducer and the y-axis is the thickness of the sample as measured using Equation 6.1.

6.7 Tissue Imaging

This section investigates whether the CVP signal can be measured from animal tissue using our current instrumentation and highlights its difference over other conventional measurement techniques. This work demonstrates the CVP signal (or one-dimensional imaging), the ultrasound reflection signal and imaging, and the electrical tomography imaging on the same tissues.

The discovery of new finding would present specific tissue structures by comparing images of these three modes of tissue information: specified as being ionic vibration based, ultrasound impedance reflection intensity based, and conductivity distribution-based tissue information. This work hopes to reveal the feasibility of CVP imaging for the potential of tissue imaging.

6.7.1 Experiment

The pork meats were bought from a butcher shop in Leeds Kirkgate Market. The meats prepared for the test were cut into a cuboid shape with dimensions(x, y, z) mm. The meat samples consisted of muscle only (M), muscle with fat (MF), and muscle with fat and skin (MFS), small bone with muscle (SMB), and large bone with muscle (LMB). These samples were kept in a fridge at a temperature of 3℃ for 24 hours before the test. The specific type of tissue (pork tissue) containing sufficient electrolytes (or ionic fluids) and having a difference in physicochemical properties, which might generate a high CVP signal, were preselected for the test.

Table 6. 2 : The description of the samples

Sample Name	Description	Size $(mm)^3$	Animal Product
M	Muscle	$58 \times 25 \times 45$	Pork
MFS	Muscle with fat and skin	$60 \times 38 \times 49$	Pork
MF	Muscle with fat	$55 \times 50 \times 46$	Pork
SMB	Small bone with muscle	$60 \times 30 \times 45$	Pork
LMB	Large bone with muscle	$50 \times 68 \times 62$	Pork

Table 6.2 shows the specific description of the selected samples. The samples were cut with a sharp knife to give a shape that could easily fit into all the vessels to be used for the test.

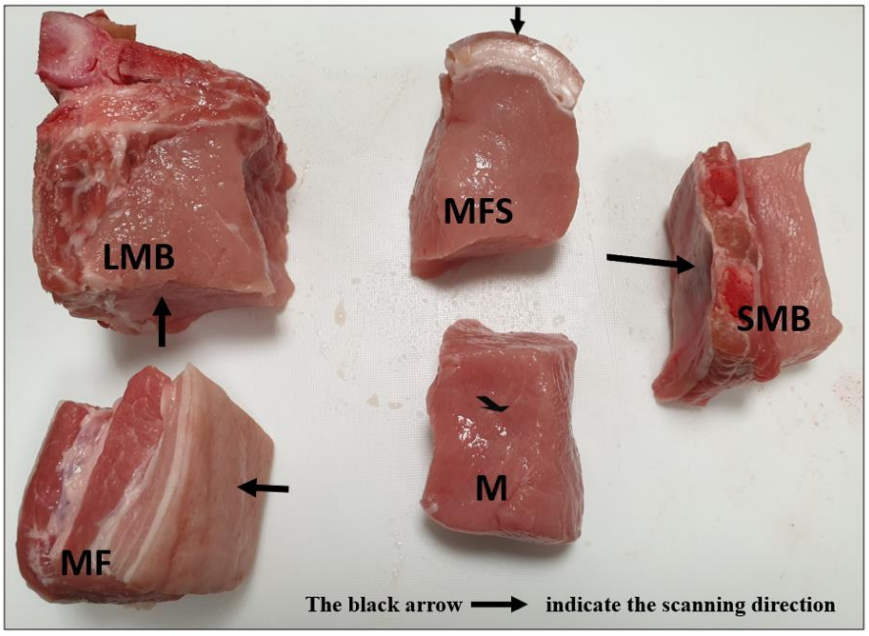

Figure 6.13.: Preselected pork tissue samples.

Figure 5.13 shows the number of tissue samples selected for imaging. After the samples were chosen, the experimental work was conducted immediately. The first imaging test was carried out for the CVP imaging, then the 1D ultrasound reflection signal (URD), then the 2D ultrasound imaging, and then the tomography imaging. We chose the same device (the Leeds standard II) for the CVP, 1D URD, 2D ultrasound imaging, and a vessel with 16 electrodes having a diameter of 14.8 cm used for tomography imaging. The experimental procedure and the measurement details will be explained in the following sections.

6.7.2 Imaging Techniques

6.7.2.1 CVP Imaging

We used the Leeds standard II testing facility for both the CVP imaging and the 1D ultrasound reflection detection (URD) signal and 2D ultrasound imaging. The testing facility consisted of a water tank made from polystyrene with dimensions of width = 57,

height = 80, length = 110 mm. We placed a piece of sponge at one end of the tank to absorb ultrasound energy in order to reduce the signal reflection at the other end of the tank. A piezoelectric transducer with a diameter of **25 mm** and frequency of **1 MHz** was fixed at one side of the water tank. Two electrodes made with aluminium foil and having a square shape and size of **10 × 10 mm**, were placed in opposite positions at the far and near side of the water tank. The CVP testing system is shown in Figure 6.14.

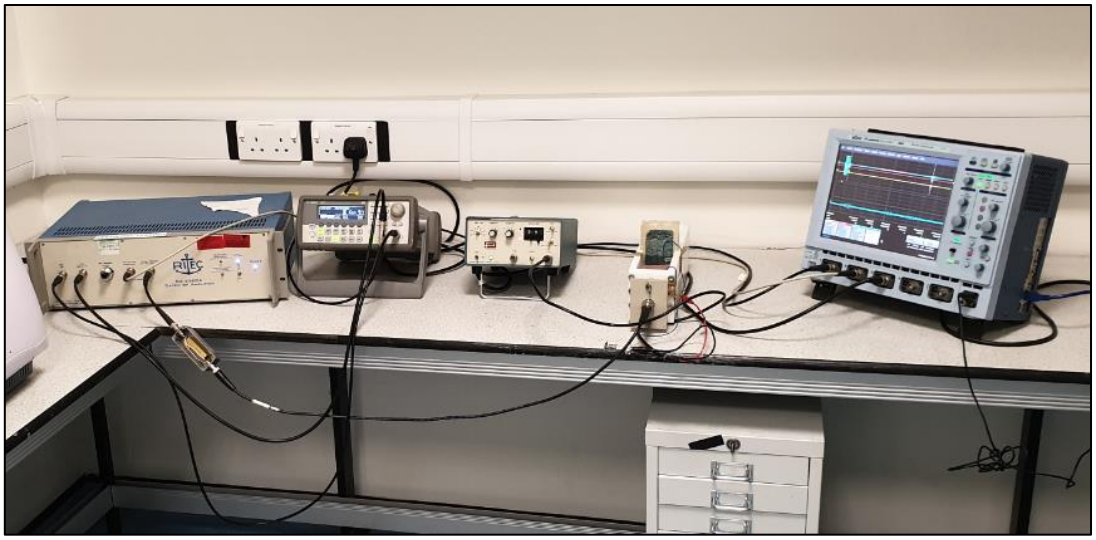

Figure 6.14.The CVP testing system.

The tank was filled with brine having a conductivity of **4.738 mS/cm**. The sample was placed inside the water tank. Four cycles of **1 MHz** signals in a duty of **50 ms (0.5% duty-cycle)** was set in a function generator (the Agilent 33250A) set with **450 mV$_{(pk-pk)}$ 1MH**z frequency and the signal amplified by the RF amplifier (GA-2500A, RITEC), for up to 40dB which operate **5 kW** with a duty cycle of **0.3%.** The output from the RF amplifier was connected to a **50 Ohm** impedance matching resistor. The amplified signal was sent through the water tank and the sample via a piezoelectric transducer. The CVP signal was generated by the sample due to the vibration, and the CVP signal was detected by both electrodes and amplified with a voltage amplifier having a gain factor of **39 dB**. The signal was then calibrated by an oscilloscope.

6.7.2.2 URD Imaging

This test was carried out using a similar water tank to the one used in the CVP imaging. The tank was filled with brine having a conductivity of **4.738 mS/cm**. The sample was

placed inside the water tank. The experiment consisted of two parts: input and output. The input was an ultrasound pulser/receiver (the 5072PR) to produce the ultrasound pulse and receive the reflected signal with an amplitude of up to **300 V(pk–pk),** with **4** cycles and a **1MHz** frequency. The signal was sent through the water tank via a piezoelectric transducer fixed at one side of the tank and having a diameter of **25 mm**, and a frequency of **1MHz**. The reflected signal was measured by the same transducer and amplified by the ultrasound pulser/receiver with a gain factor of **39 dB**. The signal was then measured and displayed on the oscilloscope screen.

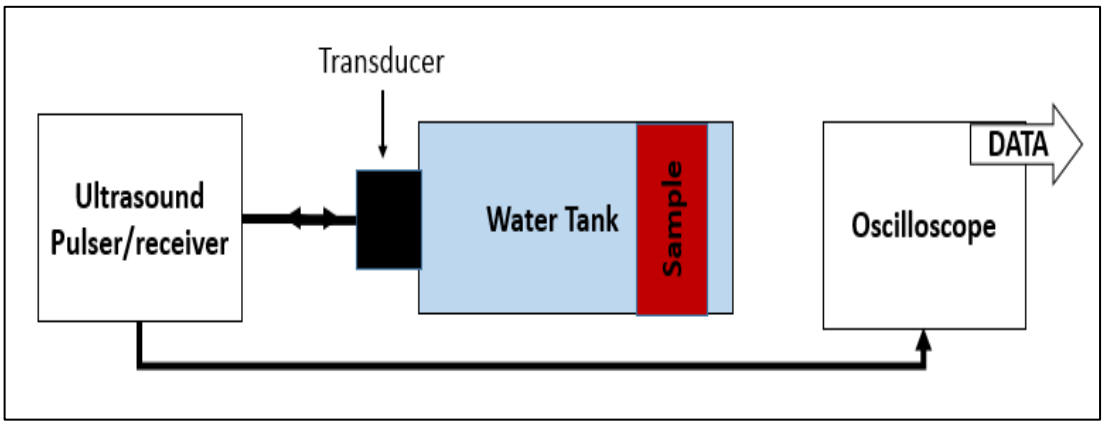

Figure 6.15.The ultrasound reflection testing system.

6.7.2.3 2D Ultrasound Diagnostic Imaging

In this test, the ultrasound diagnostics imaging machine (the Mindray DP-6600), with a curvilinear transducer (the 35C50EA) was used to image the samples. The details of this transducer was explained in Section 6.2.3. The device features black and white images. The system consists of a transducer, a transducer board, a main board, a connection board, a keyboard, a power supply, a monitor, software, and a mechanical structure. This test was carried out using the Leeds standard II water tank similar to CVP imaging tank. The tank was filled with brine having a conductivity of **4.738 mS/cm**. The sample was placed inside the water tank. The curvilinear transducer was set with a **3.5 MHz** frequency and **66** ultrasound beams and then placed at the top of the water tank facing into water. The transducer face was covered with cling film for protection from the water. The image was displayed by the digital diagnostic machine, and save it into the external memory. The dimensions of the water tank were given in Section 6.3.2.1 and the diagram of the experiment system is shown in Figure 6.16.

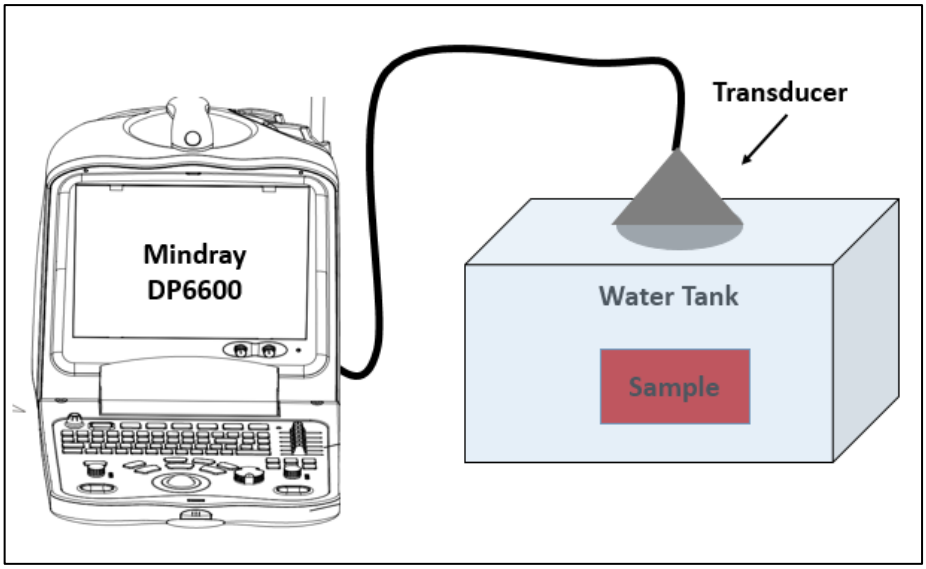

Figure 6.16.The ultrasound imaging testing system.

6.7.2.4 Tomographic Imaging

We have used an electrical resistance tomography method for comparison with the other methods explained above. The system consists of a Perspex vessel with a diameter of **14.8 cm** mounted with **16** ring electrodes and filled with brine water with a conductivity of **4.738 mS/cm**. The adjacent electrode sensing strategy was applied with a **15.07 mA** sinusoidal current at **968 kHz** for the test.

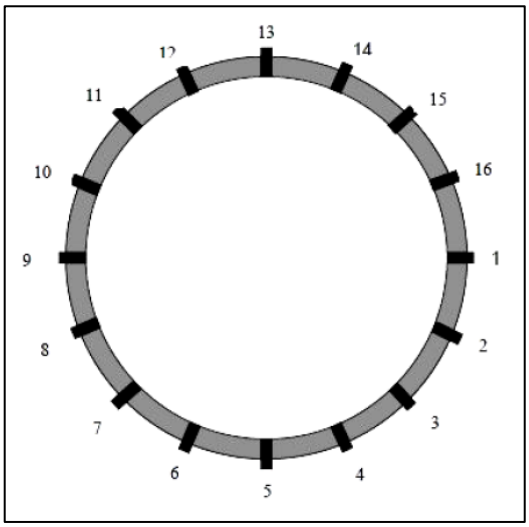

Figure 6.17.: ERT sensor (Faraji,Y., 2013).

Figure 6.17 shows the ring of ERT sensors. In ERT, **16** sensors are spread equally around the edge of the vessel.

Tomography is the process of installing many sensors at the edge of the vessel to be imaged, Yousef, (2013) and taking multiple images. The tomography images reveal the characterization information of the object within the flow. The working principle of electrical resistance tomography (ERT) is to image an object in a vessel, where the conductivity between the dispersed phase and the continuous phase are different.

The sensors are in direct contact with the liquid inside the container and the earthing point is connected to the liquid. A current is applied, and the voltage measured across the cross-section of the pipe. More simply, the current is injected by a pair of electrodes and the voltage measured between all the remaining electrodes. This procedure will continue until a full rotation of the loop is completed. The vessel is filled with water and a reference measurement taken by, Numayer et al., (2011). Then the object is placed inside the pipe – the voltage measurement strategy is assigned by using a data acquisition system (DAS).

We employ the adjacent strategy rather than diagonal or conducting strategy due to the requirement of less hardware and fast image reconstruction. In this strategy, a **15 mA** current was applied and the potential difference measured across all the remaining electrodes until the loop is completed, Deng at al., (2001).

$$\text{Number of voltage measurement} = \frac{\mathrm{n}(\mathrm{n}-3)}{2} = \frac{16(16-3)}{2} \qquad (5.5)$$

The voltage measurements were used to construct the image by the data acquisition system and then the image was constructed by an algorithm. The vessel was filled with brine having a conductivity of **4.738 mS/cm**, and then the sample placed inside the vessel for imaging. This imaging system is shown in Figure 6.18.

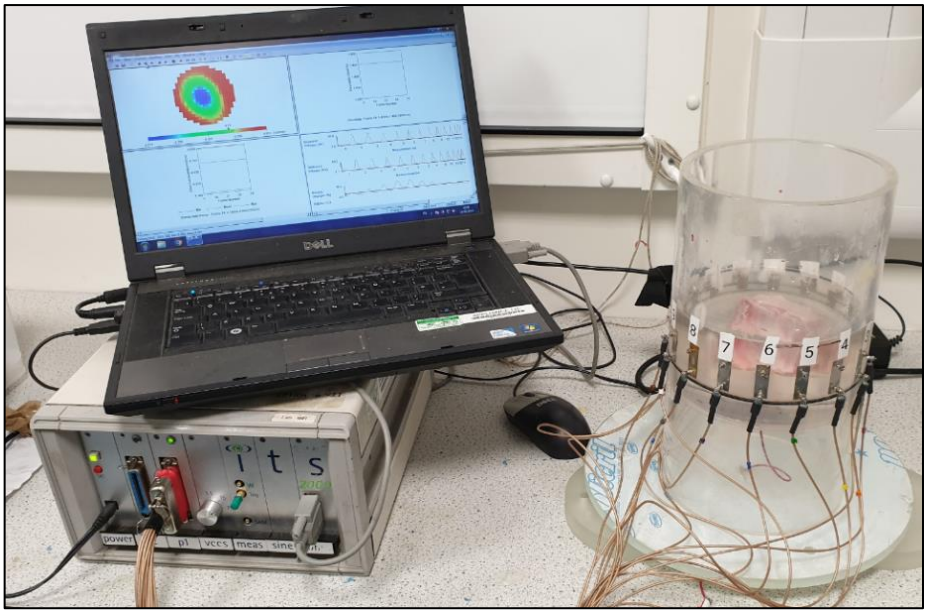

Figure 6.18.: ERT imaging system.

The date was collected by the computer and the image constructed using SCG software.

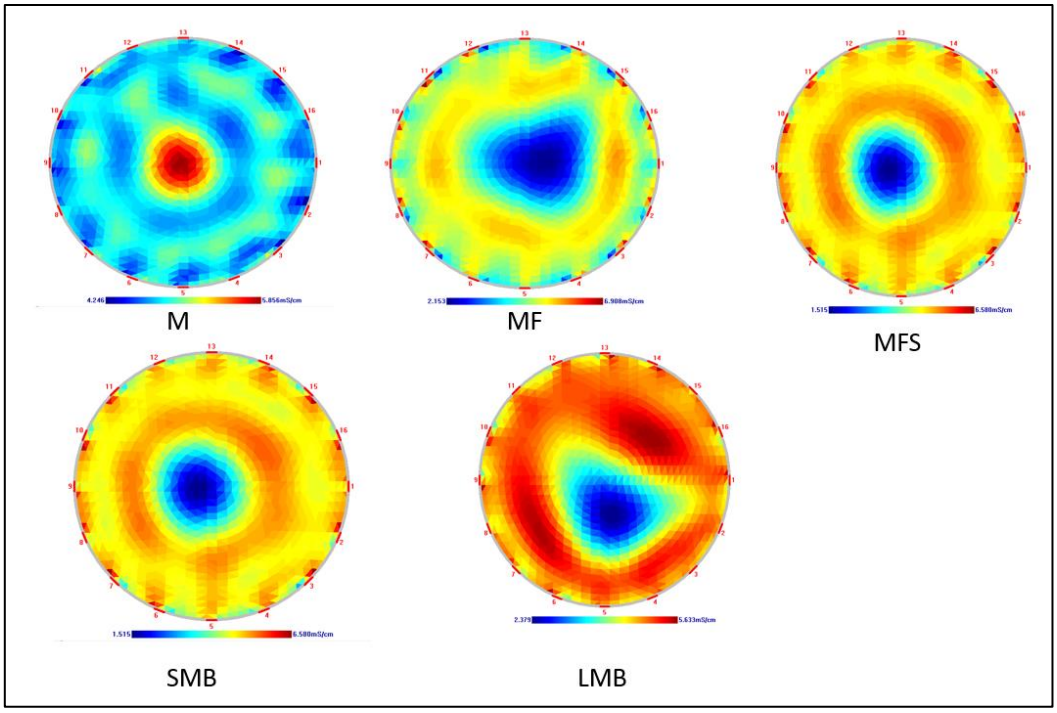

Figure 6.19.: Reconstructed tomography images.

Figure 6.19 shows the constructed image from the samples. The SCG software was used to construct the images. The image (M) is the image of the muscle, (MF) is the image

of muscle with a fat, (MFS) is the image of muscle with fat and skin, (SMB) is the image of small bone with muscle, (LMB) is the image of the large bone with muscle. The ERT imaging system is not as good as CVP imaging and is not able to detect different features within the samples of interest.

6.7.3 Results and Discussion

Test 1: CVP: Sample (M):

A large piece of pork muscle (M) with dimensions $58 \times 25 \times 45$ mm was placed inside the CVP testing device. The CVP signal was generated by the sample and detected by both electrodes. The signal-averaged 256 times, and the detected signal was amplified by the voltage amplifier with a gain factor of 39 dB. The signal was then displayed on the oscilloscope and the result is presented in Figure 6.20.

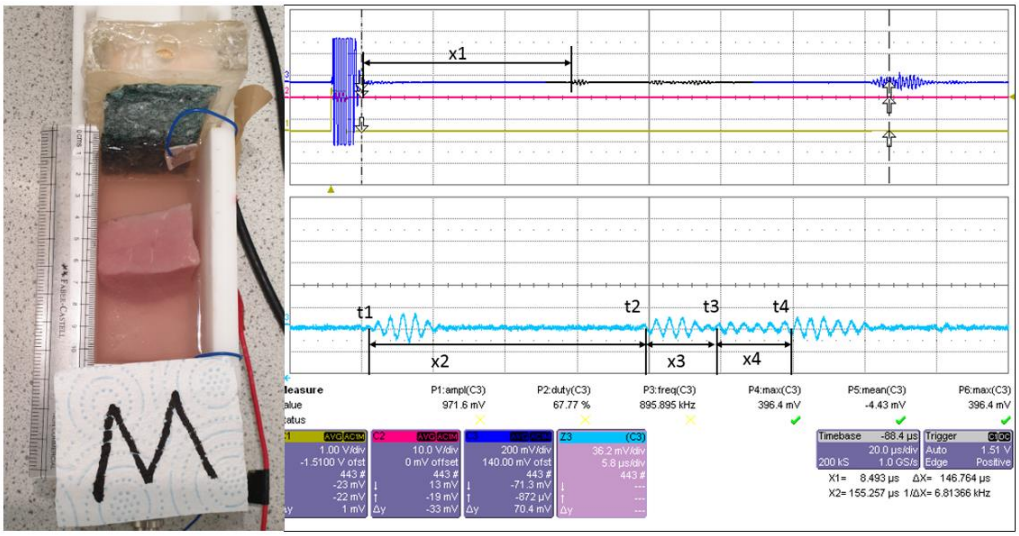

Figure 6.20.: CVP signal for sample (M).

The CVP signals are generated at the water-muscle interface, the muscle-fat interface, the fat-muscle interface, and the muscle-water interface. The thickness of the sample can be measured directly by the following equation:

$$\Delta \boldsymbol{x} = \boldsymbol{v}\left(\frac{\boldsymbol{mm}}{\boldsymbol{us}}\right) \times \boldsymbol{t}\ (\boldsymbol{\mu s})$$

The first pulse cycle of CVP signal appears at $t_1 = 58$ µs by taking the sound speed in water at 1480 m/s, this gives us the distance between the first boundary of the material and the interface between the transducer and water is $x_1 = 42.92$ mm. The second CVP

signal appears at $t_2 = 80$ µs, which gives a value of $x_2 = 11$ (µs) × 1480 $\left(\frac{m}{s}\right)$ = 16.28 mm.

The third CVP signal appears at $t_3 = 85.8$ µs this gives x_3= 2.9 (µs) × 1480 $\left(\frac{m}{s}\right)$ = 4.29 mm.

The fourth and last CVP signals appear at t_4= 91.8 µs and this gives, x_4 = (91.8–85.8) µs × $\frac{1480m}{s}$ = 4.44 mm.

$x_1 = 42.92$ mm, $x_2 = 16.28$ mm, $x_3 = 4.29$ mm, $x_4 = 4.44$ mm

Sample width is $\Delta x = x_2 + x_3 + x_4 = 16.28 + 4.29 + 4.44 = 25.01$ mm

The internal thickness (1): $x_3 = 4.29$ mm

The interior thickness (2): $x_4 = 4.44$ mm

Test 1: URD: Sample (M)

The same sample (M) was left inside the UVP standard II testing device. The transducer was connected to an ultrasound pulser/receiver with a gain factor of 39 dB. The ultrasound pulses were sent through the water tank via a similar transducer (a 1 MHz piezoelectric transducer). The reflected signal was then collected by the same sensor and displayed on the oscilloscope screen. The measured signal is show in Figure 6.21.

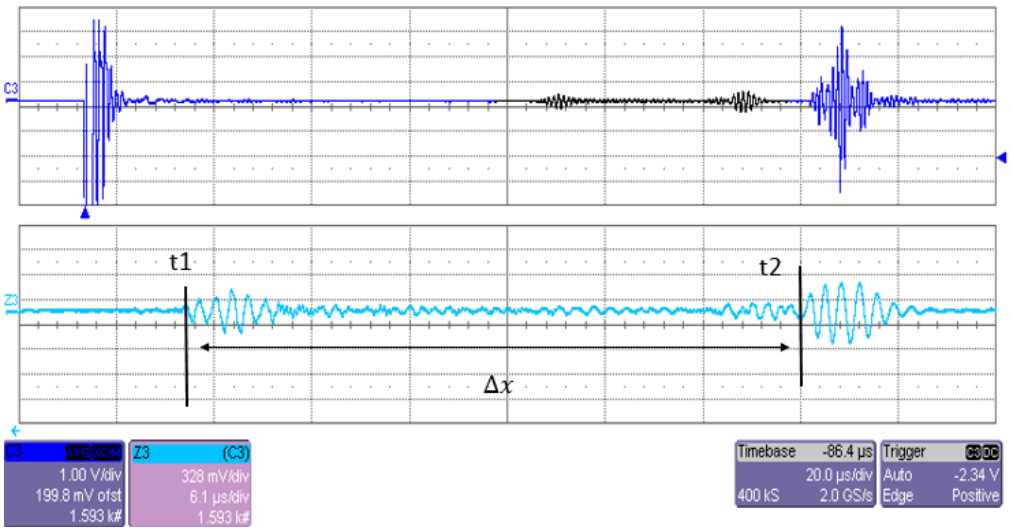

Figure 6.21.Ultrasound reflection detection for sample (M).

Figure 6.21 shows the reflection signal from the sample (M). The first reflected signal appeared at $t_1 = 98.5$ µs, and $t_2 = 134.43$ µs.

$$\Delta x = \frac{1}{2}\Delta t \left(\frac{mm}{us}\right) \times v \left(\frac{mm}{us}\right)$$

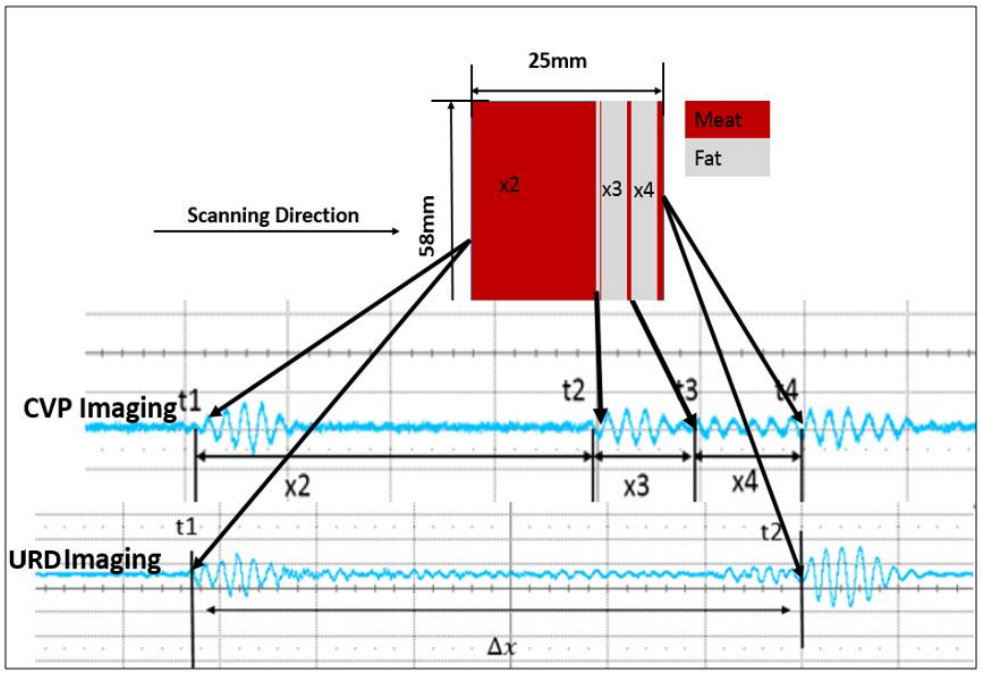

Figure 6.22.CVP and ultrasound imaging.

Figure 6.22 shows the differences between the URD and CVP imaging. The anatomy analyses (visual view) of the specific portion of tissue indicated there was a multilayer of fat inside the muscle after we looked at the sample indicated in Figure 6.22. It is difficult at this stage to indicate the distance between x_3 and x_4 due to the frequency issue. It could be much clear if you use a high frequency e.g. 6 MHz in this stage. From Figure 6.22, we can confidently claim that CVP can image a different ionic features.

Test 1: Diagnostic Imaging (Mindray DP-6600): Sample (M)

The sample (M) was placed inside the water tank of the Leeds standard II device. The sample was positioned in the same way that it was scanned for the previous tests of CVP and ultrasound reflection. The curvilinear transducer was placed at the top of the tank and face down into the water. The image was displayed by the ultrasound diagnostic imaging equipment (the DP-6600). The image is presented in Figure 6.23.

Figure 6.23.Ultrasound diagnostic 2D image of sample M.

All imaging tests were carried out using the same sample (M). Four signals were detected inside the sample (M) using the CVP method, and only two signals appeared using the URD method. The inside of the sample (M) contains two small layers of fat, this feature was detected by the CVP method while the other method was not able to detect this. The sample thickness was measured as $\Delta x = 25.01$ mm in the CVP imaging and $\Delta x = 25.47$ mm in the ultrasound imaging. The layers of fat inside the muscle imaged by CVP were too close to each other. However, in order to enhance the imaging, it is better to use a higher frequency and reduce the number of periods of the wave.

Test 2: CVP: Sample (MF)

A large piece of pork muscle with fat (MF) with dimensions $55 \times 50 \times 46$ (mm) was placed inside the testing rig. The sample was placed 33 mm away from the transducer interface. The eight bursts of CVP signals were generated by the sample (MF) and measured by both electrodes. The signals were amplified by the voltage amplifier with an amplification factor of 39 dB. The measured signal was displayed on the oscilloscope and the image is presented in Figure 6.24.

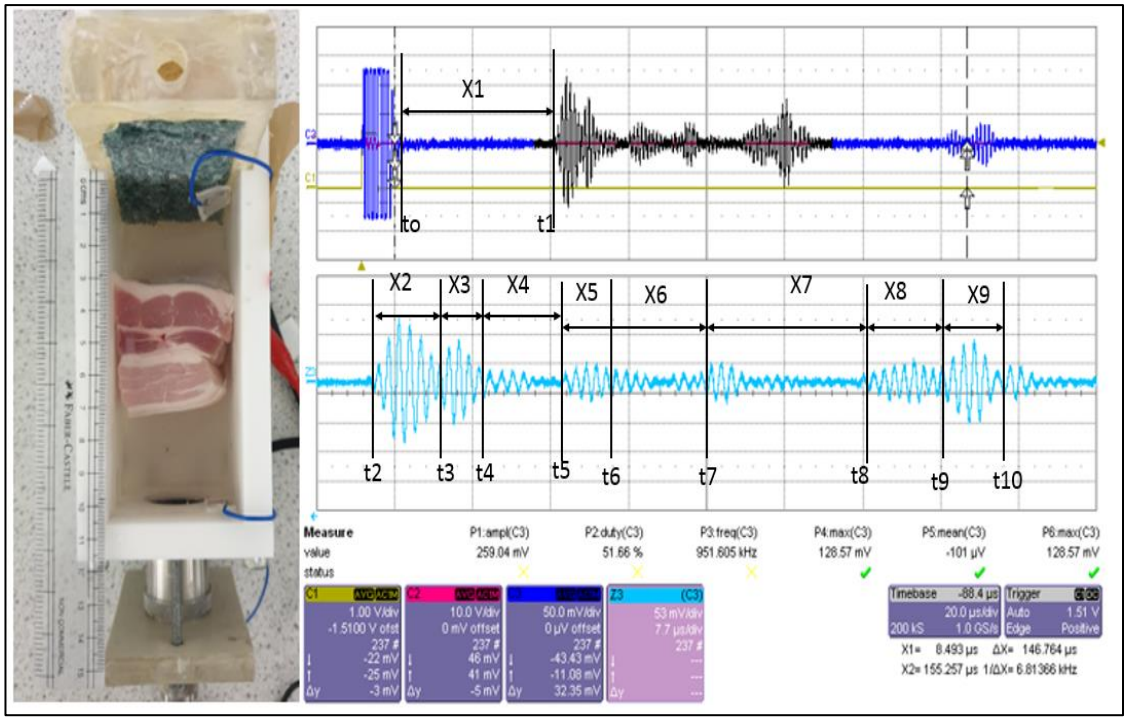

Figure 6.24.: CVP measured from sample (MF).

Figure 6.24 shows the CVP signal measured for the sample (MF). Eight bursts of CVP signal were measured from the sample. From the detected signals, the first burst and the second burst appear to be mixed due to the frequency issue and thickness of the layer, and the fifth and sixth signals are also mixed due to the same problem. This sample contains multilayer fat and muscles. The CVP signals were measured for all the different layers and are shown in Figure 6.24. The thickness of each layer was measured at:

$$x_n = (t_1 - t_0)\ \mu s \times 1480\ (m/s)$$

$x_1 = 32.5$ mm, $x_2 = 5.55$ mm, $x_3 = 2.77$ mm, $x_4 = 5.698$ mm,

$x_5 = 3.988$ mm, $x_6 = 6.837$ mm, $x_7 = 11.396$ mm, $x_8 = 5.698$ mm,

$x_9 = 4.55$ mm

The thickness of the sample measured at $\Delta x = 46.479$ mm. the measured values are x_1 is the distance between the first boundary of the sample and the transducer interface into water. The measured signals are presented in Table 5.3.

Test 2: URD: Sample (MF)

The same sample (MF) was left inside the UVP standard II testing device. The transducer was connected to an ultrasound pulser/receiver with a gain factor of 39 dB. The ultrasound pulses were sent through the water tank via the same transducer (a 1 MHz piezoelectric transducer, 25 mm in diameter). The reflected signal was collected by the same transducer and displayed on the oscilloscope screen. The measured signal is shown in Figure 6.25.

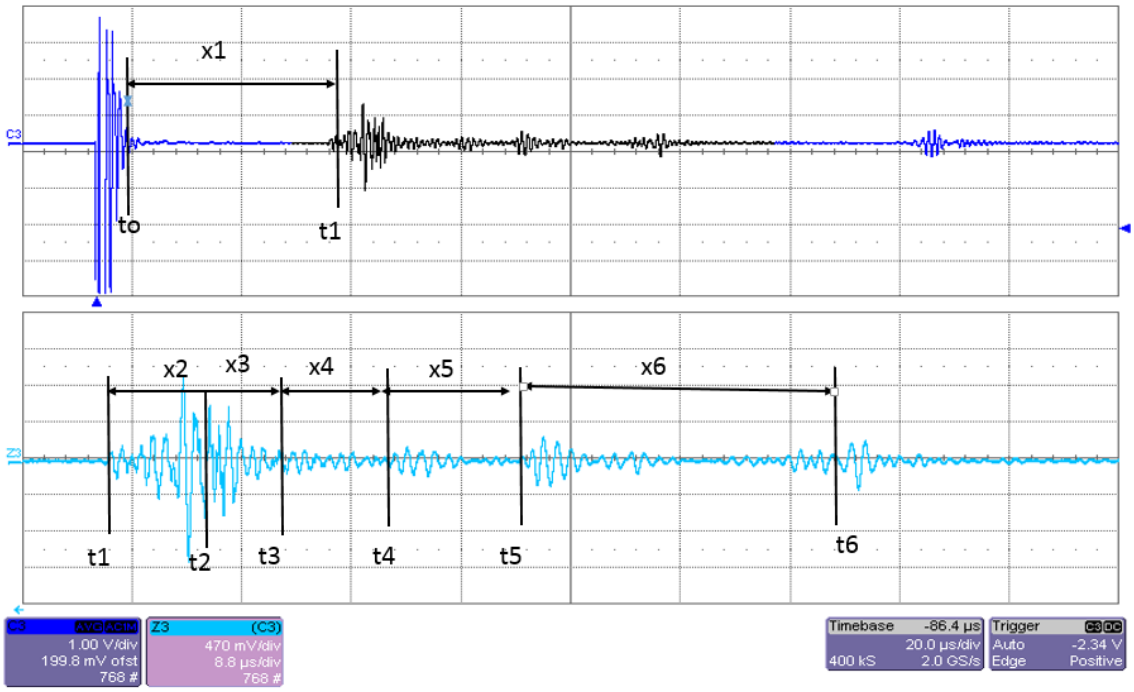

Figure 6.25.: Ultrasound reflection from sample (MF).

Figure 6.25 shows the reflection signal measured for the sample (MF). The thickness of the tissue layer was measured for both CVP and ultrasound and is presented in Table 5.3 below. The sample thickness is measured by:

$$\Delta x = \frac{1}{2}\Delta t\ (\mathrm{mm/\mu s}) \times v\ (\mathrm{mm/\mu s})$$

All the measurements for both CVP and URD imaging are presented in Table 5.3. In the URD measurements, the attenuation is double that of the CVP because the measurement in CVP is taken directly from the sample, whereas in URD, the measurement is made by the reflection from the sample. As can clearly be seen in Figure

6.25, there is a big difference between the amplitude between the first signal the last signal, while in CVP it is less attenuated.

Table 6. 3 : CVP and URD measurement for sample (MF)

x_n	CVP (mm)	URD (mm)
x_1	32.5	28.120
x_2	5.55	5.914
x_3	2.77	3.942
x_4	5.698	5.914
x_5	3.98	9.116
x_6	6.837	18.233
x_7	11.396	……..
x_8	5.698	……..
x_9	4.55	……
Δx	46.479	43.119

Table 6.3 shows the signal measurement for 1D imaging in both the CVP and URD methods for the sample (MF). The signals are detected and measured for *x*7, *x*8, and *x*9 in the CVP method, whereas in URD method, these signals are not detected.

Test 2: Diagnostic Imaging (Mindray DP-6600): Sample (MF)

The sample (MF) was placed inside the water tank of the Leeds standard II devices. The sample was positioned in the same way that it was scanned for the previous tests of CVP and ultrasound reflection. The curvilinear transducer was placed at the top of the tank and face down into the water. The image was displayed by the ultrasound diagnostic imaging equipment (the DP-6600). The image is presented in Figure 6.26.

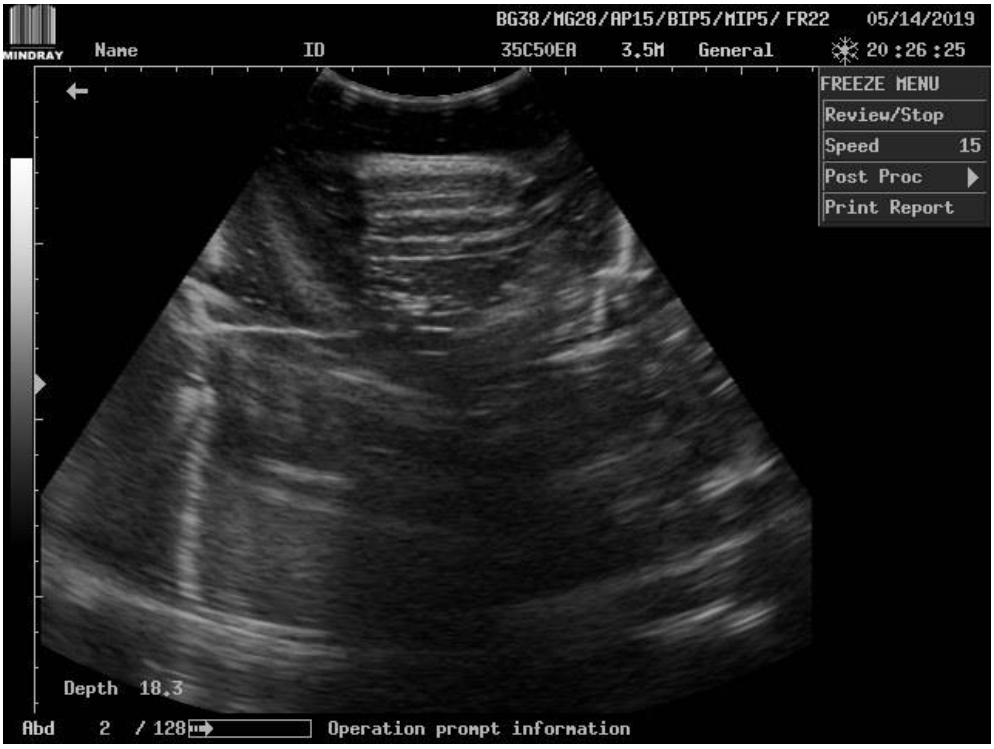

Figure 6.26.: 2D imaging of sample (MF).

Figure 6.26 shows the 2D image of sample (MF), this image shows the layers of fat inside the sample. The results show that the CVP imaging has detected seven out of the eight bursts of CVP signal, whereas the ultrasound imaging can only detect five of the signal bursts. The thickness of the sample was originally 50 mm. The CVP imaging measured this value at 46.479 mm, and the ultrasound measured it at 43.119 mm. In the ultrasound diagnostic 2D image we can see five layers of fat and muscle shown in Figure 6.26. The 2D and URD imaging have not detected any small features between these layers but the CVP imaging has revealed small features between them. The limitation of the current CVP instrumentation makes it difficult to compare CVP with 2D ultrasound imaging but it is easier to compare with 1D URD. In all cases, CVP imaging is able to measure different ionic features and also has less attenuation than URD.

Test 3: CVP: Sample (MFS)

A large piece of pork muscle with fat and skin (MFS) with dimensions $(60 \times 38 \times 49)$ mm was placed inside the testing rig. The sample was placed 15 mm away from the transducer interface. The CVP signal was generated by the sample, detected by both electrodes and then amplified with a voltage amplifier with an

amplification factor of 39 dB. The signal was displayed on the oscilloscope and is presented in Figure 6.27.

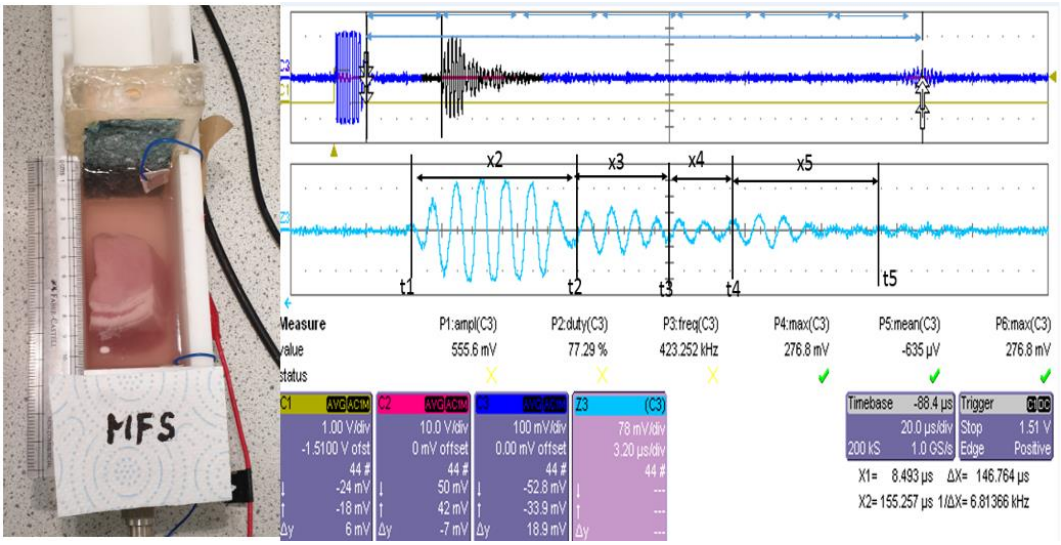

Figure 6.27.CVP signal measured for sample (MFS).

Figure 6.27 shows the CVP signal measured for the sample (MFS). The four bursts of CVP signal were measured with different amplitudes. These measurements are presented in Table 6.4.

Test 3: URD: Sample (MFS)

The same sample (MFS) was left inside the UVP standard II testing device. The transducer was connected to an ultrasound pulser/receiver with a gain factor of 39 dB. The ultrasound pulses were sent through the water tank via a similar transducer (a 1 MHz piezoelectric transducer). The reflected signal was collected by the same transducer and amplified with a voltage amplifier having amplification factor of 39 dB, then the signal was displayed on the oscilloscope screen. The measured URD signal from sample (MFS) is shown in Figure 6.28.

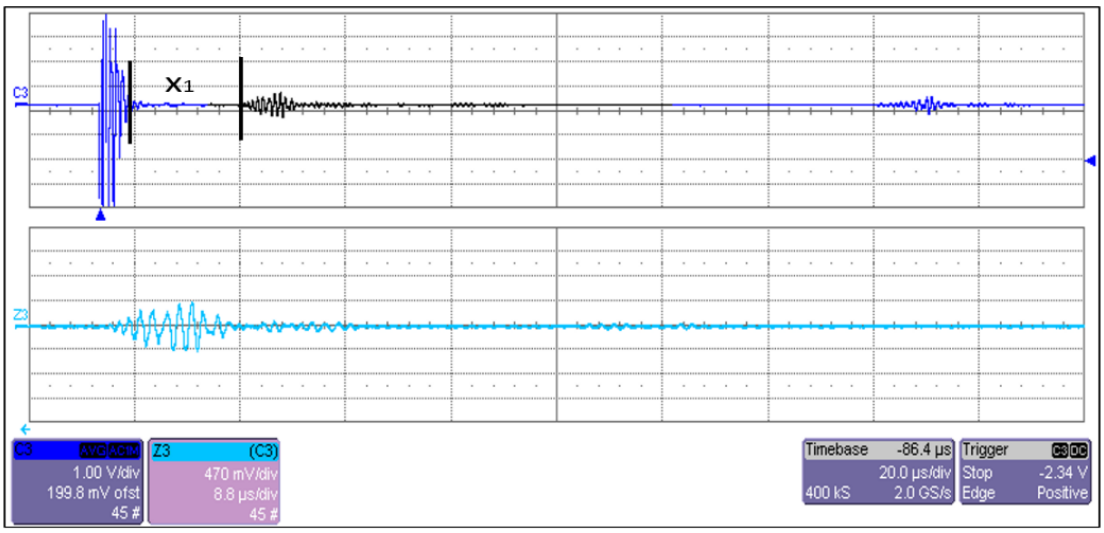

Figure 6.28. URD signal for sample (MFS).

Figure 6.28 shows the URD signal measured for the sample (MFS). A high amplitude of signal is reflected from the skin layer because the skin layer is dried and most of the energy gets reflected. There was no signal reflected from the inside and the end of the sample. The signal measurements for both CVP and URD are presented in Table 6.4.

Table 6. 4 : CVP and URD measurement from sample (MFS)

x_n	CVP (mm)	Ultrasound (mm)
x_1	15.280	14.80
x_2	11.840	…….
x_3	7.104	…….
x_4	4.736	…….
x_5	9.742	…….
x_6	33.422	…….

Due to the structure of the sample (MFS) we were not able to scan 2D ultrasound diagnostic imaging because the sample was too soft to stand up inside the water tank. Only the 1D CVP and the 1D URD imaging is presented for the sample (MFS). From Figure 6.28, we can see the CVP system imaged the skin, fat, and muscle layer of the

sample, while the ultrasound URD system was only able to image the hard skin layer. It is not clear what the sample thickness measurement is due to the structure of the sample shape. The sample was lying in a water tank which makes it difficult for the fixed transducer to scan from side to side, therefore the result did not match our expectations for this sample. The important point is that the CVP measured five bursts of the signal whereas ultrasound reflection was only detected on the skin layer.

Test 4: CVP: Sample (SMB)

A small piece of pork muscle with bones (SMB) having dimensions $\mathbf{60 \times 30 \times 45}$ mm place inside the CVP standard II testing rig. Similar to all the other tests, the signal was generated by the sample and amplified with a voltage amplifier having an amplification factor of 39 dB. The sample was placed 30 mm away from the transducer interface. The measured CVP signal for the sample (SMB) is shown in Figure 6.29

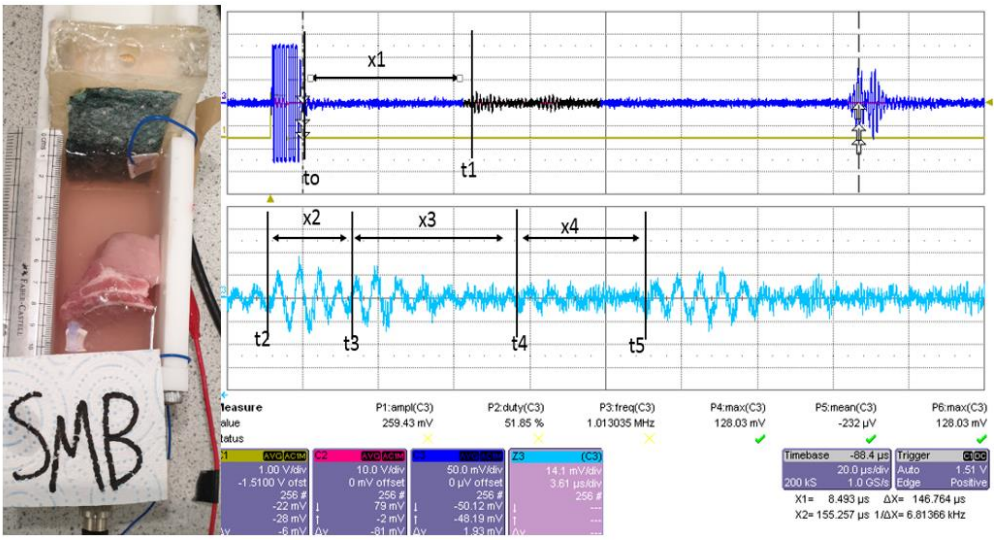

Figure 6.29. CVP signal measured for sample (SMB).

Figure 6.29 shows that four bursts of CVP signal were measured from the sample (SMB). The signals measured within the sample are: x_2 at the first boundary to the sample, x_3 the interface between bone and the muscle, x_4 within the exit from the sample or the muscle-water interface. It is clearly shown from Figure 6.29 that CVP imaging is able to image multilayers of bone and skin from the sample (SMB).

Test 4: URD: Sample (SMB)

The same sample (SMB) was left inside the UVP standard II testing device. The transducer was connected to an ultrasound pulser/receiver with a gain factor of 39 dB. The ultrasound pulses were sent through the water tank via a similar transducer (a 1 MHz piezoelectric transducer).

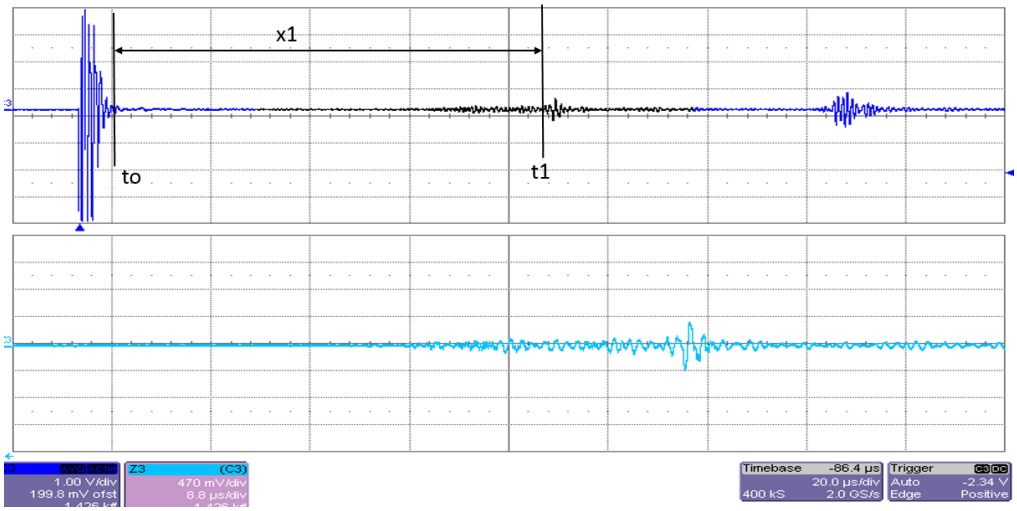

Figure 6.30.: URD signal measured for sample SMB.

In Figure 6.30 the URD signal was measured at 33.31 mm this indicates that a large amount of the signal was reflected from the bone layer. The measured URD and CVP signals for the sample (SMB) are presented in Table 6.5.

Table 6. 5 : CVP and reflection signal from the sample (SMB)

x_n	CVP (mm)	URD (mm)
x_1	29.60	33.31
x_2	6.44	……
x_3	11.754	……
x_4	10.685	……
Δx	28.879	……

The thickness of the sample measured by CVP was 28.879 mm while URD was not able to measure the thickness of the sample due to the larger attenuation of sound energy from the bone structure.

Test 4: Diagnostic Imaging (Mindray DP-6600) :(SMB)

The sample (SMB) was placed inside the water tank of the Leeds standard II device. The sample was positioned in the same way that it was scanned for the previous tests of CVP and ultrasound reflection. The curvilinear transducer was placed at the top of the tank and face down into the water. The image was displayed by the ultrasound diagnostic imaging equipment (the DP-6600). The image is presented in Figure 6.31.

Figure 6.31.: 2D image of sample (SMB).

The 2D image of the sample was scanned by the ultrasound diagnostic imaging (Mindray DP-6600). The image shows the bone in the white colour and the muscles in the darker colour. The image does not show the exact volume of the sample nor the layers inside the sample (SMB), whereas CVP was able to image all the different layers within the sample. In Figure 6.29, we show that the CVP imaging method was able to image the bone, fat, and skin of the sample (SMB), while ultrasound is only able to see the first boundary of the bone structure.

Test 5: CVP: Sample (LMB)

A large piece of pork muscle with the bone (LMB) having dimensions $\mathbf{50} \times \mathbf{68} \times \mathbf{62}(\boldsymbol{mm})$ was place inside the CVP testing rig. The sample was placed 23 mm away from the transducer interface. The ultrasound pulses were sent through the sample via the piezoelectric transducer having 1 MHz frequency and 25 mm in diameter. The CVP signal was generated within the sample and the signal detected by two electrodes placed at the bottom and at the end of the rig. The signal was amplified with an amplification factor of 39 dB and displayed on the oscilloscope. The measured CVP signal is shown in Figure 6.32.

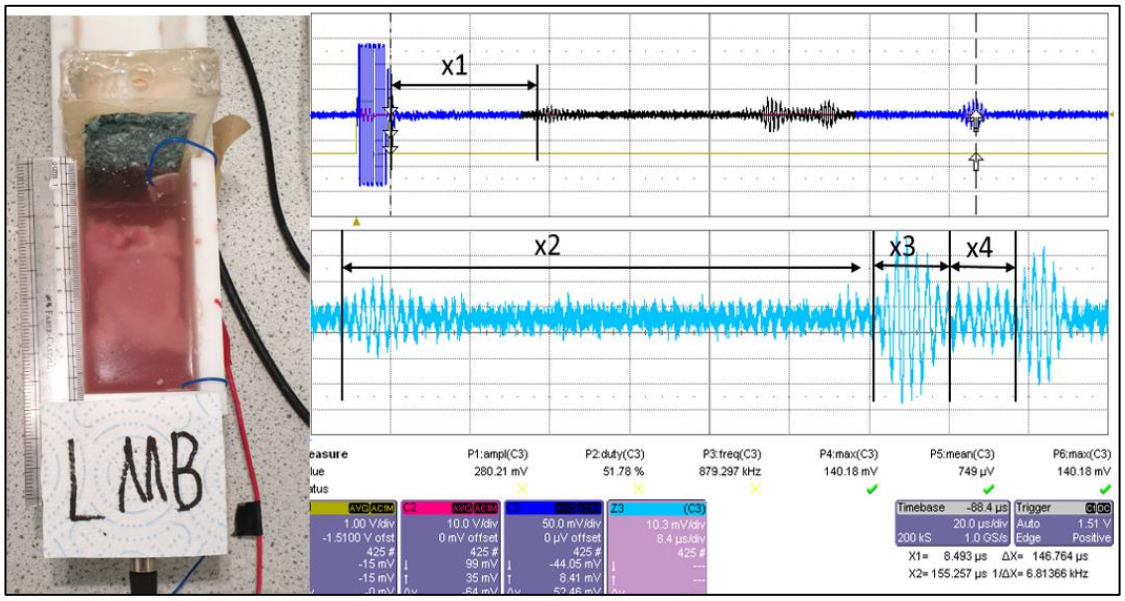

Figure 6.32.CVP signal measured for the sample (LMB).

The CVP signal measured x_1 at the first boundary of the sample, x_2 is the thickness of the muscle from the first boundary to the first boundary of the bone within the sample, x_3 is the structure between the bone layers, and x_4 is muscle tissue beyond the bone and the end side of the sample. The measured CVPs for each layer are presented in Table 5.6.

Test 5: URD: Sample (LMB)

The same sample (LMB) was left inside the UVP standard II testing device. The transducer was connected to an ultrasound pulser/receiver with a gain factor of 39 dB. The ultrasound pulses were sent through the water tank via a similar transducer (a 1MHz piezoelectric transducer). The reflected signal was collected by the same transducer and

amplified with an amplification factor of 39 dB. The URD signal was displayed on the oscilloscope screen, and this is presented in Figure 6.33.

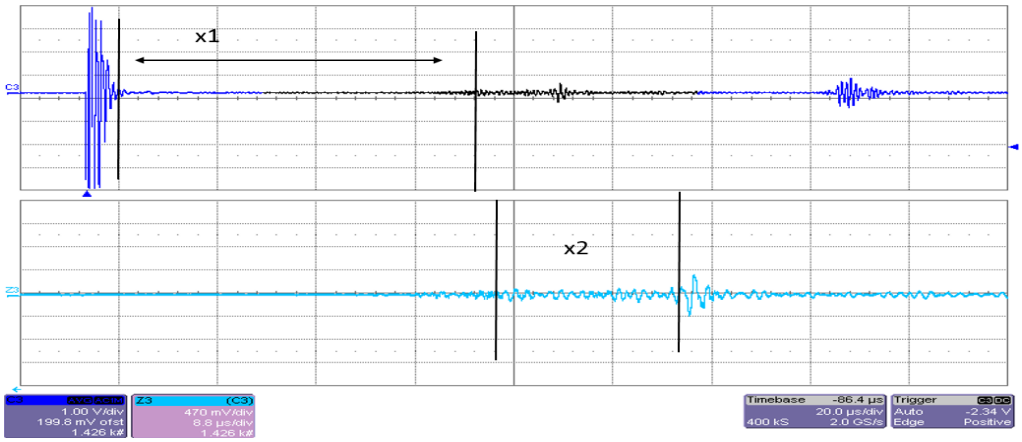

Figure 6.33.URD signal measured from the sample (LMB).

In Figure 6.33 we can see the URD imaging system was only able to detect two signal features. According to the measurements, x_1 is the distance between the first boundary of the bone within the sample and the transducer interface and this distance was measured at x_1= 61.8 mm, this is similar to x_3 in the CVP imaging. The value of x_2 in Figure 6.33 was measured at 13.04 mm and this is similar to x_5 in the CVP imaging.

Table 6. 6 : CVP and URD signal from the sample LMB

x_n	CVP (mm)	URD (mm)
x_1	23.680	61.8
x_2	6.216	13.04
x_3	33.374	……
x_4	8.306	…….
x_5	4.954	……..
Δx	52.85	…….

In both CVP and URD imaging we can see that the CVP can image three different layers such as x_1, x_2, and x_4, whereas the URD was not able to measure any signal within this area of the sample (LMB).

Test 5: Diagnostic Imaging (Mindray DP-6600) :(LMB)

The sample (LMB) was placed inside the water tank of the Leeds standard II rig. The sample was positioned in the same way that it was scanned for the previous tests of CVP and URD. The curvilinear transducer with frequency 3.5 MHz was placed at the top of the tank and face down into the water. The image was displayed by the ultrasound diagnostic imaging equipment (the DP-6600), and this image is presented in Figure 6.34.

Figure 6.34. 2D image of the sample (LMB).

In Figure 6.34, we can see only the big layer of bone, shown with a white colour, and this imaging system is not capable of detecting muscle and other layers beyond the bones.

6.8 Summary

In summary, a method for CVP measurement using a low energy source of excitation have been presented. This method explains that UVP is capable in giving additional information over the current conventional ultrasound imaging technique. We have

demonstrated a combination of ultrasound conventional imaging to UVP imaging. The conventional imaging technique relaying the reflected signal from the material interface makes it difficult to recognize different ion species whereas UVP imaging solves this issue. The UVP signal no longer requires a high voltage source to generate the signal for CVP imaging and provides enough information on the sample of interest. This unique feature of CVP, and the capability of CVP to enhance the ultrasound imaging, are demonstrated with good agreement.

Colloid vibration potential (CVP) refers to the signal generated from the vibration of particles or ions in electrolytes (or tissue), which is a fundamental difference from the conventional URD-based imaging technology. This work has demonstrated the super capability of CVP imaging (or as one-dimensional imaging) over conventional ultrasound imaging. The additional features of CVP revealed the specific physicochemical structures of tissue which conventional ultrasound technique cannot see. The results, with pervious findings, further support the potential of CVP for providing new and/or complementary knowledge for medical diagnosis and research.

CHAPTER SEVEN: CONCLUSION AND FUTURE WORK

7.1 Conclusion

This PhD thesis describes the theoretical and experimental study regarding ultrasound vibration potential (UVP) imaging. A brief history of UVP was theoretically and experimentally reviewed. I have given a clear explanation of the previous work done by both Brown University and the University of Leeds in comparison to my work.

The theoretical work applied to the ultrasound vibration potential distribution (UVPD), in which the problem was solved numerically using COMSOL Multiphysics software, and this also revealed the limitations of the technique. This theoretical model is a good method for future device optimization. Another theoretical model applied to the physicochemical characterizations of nanoparticles in colloidal suspensions. This investigated the frequency response measurement from silica nanoparticles of different diameters and also the phase angle as a function of particle diameter and revealed how large particles and small particles vibrate in colloidal suspensions under ultrasound pressure. The vibration model shows how the colloid vibration potential (CVP) signal was generated due to the vibration of nanoparticles in the colloid. The CVP signal was followed by a tail off of the signal, which we believe is due to the discharging time in the double layer (DL), and this tail confirms that the signal is generated due to the vibration of nanoparticles. The explanation of the total vibration potential (TVP) gives acknowledgement that: in CVP, the signal is dominated by the nanoparticles; the signal increases from a small nanoparticle diameter up to a critical value when the particle diameter reaches 85 nm, in this case the signal increases with increasing particle diameter because the surface charge increases, in the case of when the particle diameter is larger than 85 nm, the CVP signal drops due to a larger surface area. In our understanding the signal will become zero when the particle diameter is small enough, in which case no polarization can be made with ultrasound pressure, or particles and ions have similar acceleration rates, therefore, there will be no polarization and the CVP will be zero. In the case of ion vibration potential (IVP), the signal is dominated by the atomic weight and this is explained briefly by, Khan et al., (2013).

The experimental work was applied to nanoparticles suspended in colloidal suspensions, for example, silica dioxide and titanium dioxide, different ionic electrolytes, and animal tissue i.e. pork tissue. It was applied to the imaging of colloidal objects and could be useful for medical imaging based on UVP methods. Overall a new, innovative experimental technology for UVP measurement signal relative to colloidal samples and ionic electrolytes, has been established and verified during this study. I have designed a new UVP standard device (Leeds standard III) for UVP imaging, where my device is capable of non-intrusive measurement. This work reports the progress on the measurement method with electrodes non-intrusively placed outside a mock body made from agar. This innovative device takes us a huge step further towards UVP imaging in humans. It confirms that the UVP signal is detected outside the sample with electrodes non-intrusively attached to the body. The size of the electrodes does not affect the measured signal. This new UVP device (Leeds standard III) stops the interface between the sample and the body being a problem, whereas previously cling film had to be used in UVP devices to seal the sample.

The signals came from an agar sample that was embedded in the mock body containing either ionic or nanoparticular species in good quality, which shows the potential to provide the physicochemical properties of the sample as a complementary image to conventional ultrasound image. I have presented the equivalent circuit diagram for this model. Signals were measured from the agar mock body containing multiple layers of silica suspensions and this confirmed experimentally that the UVPD signal strength amplitude has a relation to the electrode positions. I presented a methodology to combine conventional ultrasound diagnostic imaging and UVP imaging. This method experimentally explained that UVP can be measured using the current conventional imaging technique as a source of excitation, and it demonstrated the unique feature of CVP. This unique feature shows that CVP imaging system is able to image different ionic recipe within the body, whereas current conventional ultrasound imaging is not able image it. The CVP imaging method is able to provide sufficient information about the sample and this tells us that CVP can enhance ultrasound imaging.

The materials were tested during the experimental works were silica dioxide nanoparticles, titanium dioxide nanoparticles and ionic electrolytes such as potassium chloride, magnesium chloride, calcium chloride, strontium chloride, barium chloride, and radium chloride. All nanoparticles were suspended in deionized water with a

concentration of 1 wt%, and all ionic electrolytes were prepared with a concentration of 1 M. These samples were only tested for theoretical confirmation and verification of the new UVP standard device (Leeds standard III). The animal tissue samples selected from pork were muscle, skin, bone, and fat. The imaging of the animal tissue reveals that CVP is measurable from animal tissue and this enhances ultrasound imaging by detecting features within the sample that current ultrasound imaging has not yet been able to image. This test was carried out using several methods such as (colloid vibration potential imaging) CVPI, ultrasound reflection detection (URD), ultrasound diagnostic imaging, and tomography imaging. In all imaging methods, CVPI shows great advantage over the other methods by proving its unique feature. These measurements gave qualitative agreement to the current theoretical models.

7.2Future work

A. Recommendations to improve the Leeds standard III UVP device:

- Further improvement to the sensing system is recommended since the reflection from the rear side of the device has an effect on the UVP signal. This could be done with materials that can absorb large amounts of ultrasound signal.
- This device is designed for non-intrusive measurement, and to enhance the signal amplitude is to protect the signal from the noise build up from other devices.
- A system with electronic data collection is recommended in order to provide no interference between the collected data and the computer.
- The properties of the transducer are very important, for example, focal point, frequency, and beam divergence, as they help with the signal quality/enhancement.
- I have proved that UVP can be generated with a low excitation voltage, but the signal quality is lower than when using a high excitation voltage. This could be improved by changing the transducer properties and improving the sensing method.
- We could consider placing the electrodes in a better position or perhaps using a coil to measure the UVP signal.
- The novel design method of an excitation signal to derive a high signal and low noise ratio.

B. **The recommendations for the samples:**

- The ionic species and colloidal suspensions can be tested with a minimum concentration of 0.01%, and by using as high a concentration as possible for the frequency response measurement in order to show the technology capability.
- The animal tissue imaging using the Leeds standard III device could be carried out with a minimum sample size and by using different organs, such as a lung. The animal tissue properties may change when they are suspended in the Leeds standard III device, and this has to be carefully considered. One idea is to have a large piece of tissue containing electrolytes, or fat and muscle with abnormal cells. This sample could be scanned directly using a similar method to the Leeds standard III.

C. **Theoretical model suggestions:**

- The UVP methods presented by previous researchers explain the current generation, but a theory for voltage generation measurements is not yet available.
- A theoretical model to explain the limitations of the CVPI technology could be given by considering the smallest object possible that could image.
- Ultrasound vibration potential imaging system CVPI: Currently we use several electrical instruments, and all are connected with external cables. It may be much more conducive if we could build all these instruments into one piece of equipment.

The Bibliography

Agilent., (2016). Function/Arbitrary wave generator. [Online]. Available from www.agilent.com.

Albert, F., Cotton, G., Carlos, A. and Murillo, M.B.,(1980). Advanced Inorganic Chemistry. 4th ed. John Wiley.

Albert,C.Wilkinson., (1989). Advanced Inorganic Chemistry. John Wiley.

Ametek., (2019). Impedance/Gain-phase analyzer. [Online]. Available from: www.ameteki.com

Andrew, C.B. Shoungang, W. and Gerald, J.D., (2004). Imaging based on the ultrasonic vibration potential. . Applied Physics Letters. **85**(22), pp.5466-5468.

Stokes' Law of Viscosity. International Journal of Research in Engineering, Science and Management **2**(2), pp.326-328.

Assadi, A. and Farshi, B., (2011). Size dependent longitudinal and transverse wave propagation in embedded nanotubes with consideration of surface effects Acta Mech. **222**(27), pp.1-13.

AV-IQ., (2018). www.av-iq.com.

Avtar, S.A., (1973). Wave equation and propagation parameter for sound wave propagation in suspensions. . Applied Physics Letters. **44**(11), pp.4863-4867.

Bakeer, J.B., (2005). The history of sonographers. J Ultrasound Med. **24**(1), pp.1-14.

Barisik, M. Atalay, S. Beskok, A. and Qian, S., (2014). Size Dependent Surface Charge Properties of Silica Nanoparticles. The Journal of Physical Chemistry. **118**(4), pp.1836-1842.

Ben, C., (2013). Acoustic for ultrasound imaging. USI Electronotes. pp.4-8.

Beranek, L. and Tim, J.M., (2012). Acoustics: Sound Field and Transducers. First ed. Amsterdam: Elsevier.

Beveridge, A.C. Shoung, S. W and Gusev, V.E., (2004). Vibration Potential Imaging: Theory and Preliminary Results. SPIE **5320**, pp.95-100.

Booth, F. and Enderby, J.A., (1952). On Electrical Effects due to Sound Waves in Colloidal Suspensions. Proceedings of the Physical Society. Section A. **65**(5), pp.321-324.

Bowen, W.R. and Jenner, F., (1996). Dynemic ultrafication model of charged colloidal dispersioin: a wingersize cell approach. SCI. **50**, p1707.

Carbo, R. and Molero , A. C., (2002). Reflection waves by a submerged layer with density sound velocity and attenuation symmetrical gradients. Instituto de Acústica. pp.1-6.

Clarke, S., (1981). The hydrophobic effect: Formation of micelles and biological membranes, 2nd edition (Tanford, Charles). Journal of Chemical Education. **58**(8), pA246.

Colloid-dynemics.com (2019). Colloidal Dynemics Leader in colloid measurement. [Online] Available at: http://colloidal-dynamics.com/ [Accessed 11 Nov. 2019].

Components, l.,(2010). High speed current amplifier. [Online]. Available from: www.lasercomponents.com.

Components, L.,(2017).High-speed current amplifiers for 1 MHz to 400 MHz bandwidth. [Online]. Available from: https://www.lasercomponents.com/uk

Cosgrove, T.,(2010). Chapter 1 An Introduction to Colloids. Bristol: John Wiley & Sons.

Cuong, K.N. Vitalyi, E.G. and Diebold, G. J.,(2013). Vibration potential imaging of spherical objects. Applied Physics Letters. **102**, pp.1-4.

Cuong, K.N.Vitalyi,E.G. and Diebold, G.J.,(2008). Potential distribution from electroacoustic polarization sources. Applied Physics Letters. **93**(18), pp.1-3.

Debye, P.,(1933). A Method for the Determination of the Mass of Electrolytic Ions. Chemical Physics. **1**(1), pp.13-16.

Demer, D.A. and Renfree, J.S.,(2008). Variations in echosounder–transducer performance with water temperature. ICES Journal of Marine Science. **65**(6), pp.1021-1035.

Deng, X., Dong, F., Xu, L.J., Liu, X.P. and Xu, L.A., (2001). The design of dual plane ERT system for cross correlation measurement of bubbly gas's and liquid flow. Measurement Science and Technology. **12**(8), pp.1024-1031.

Divell, M., (2010). Introduction to the physics of waves and sound. Physics and Astronomy. **1**(1), p13.

Dluzhnevskii, G.I., (1970). Interpreting the relationship between the displacement vector D, the electric field E, and the polarization P in an electrostatic field. Springer. **621**(3), pp.713-716.

Dukhin, A.S. and Goetz, P.J., (1996). Acoustic Spectroscopy for Concentrated Polydisperse Colloids with High Density Contrast. Langmuir. **12**(21), pp.4987-4997.

Dukhin, A.S. and Goetz, P.J., (2002). Ultrasound for characterizing colloids : particle sizing, zeta potential, rheology. 1st ed. Amstrdam;Boston: Elsevier Science & Technology.

Dukhin, A.S. and Philip, J.G., (2001). Acoustic and electroacoustic spectroscopy for characterizing concentrated dispersions and emulsions. Advances in Colloid and Interface Science. **92**(1-3), pp.73-132.

Dukhin, A.S., Shilov, V.N., Ohshima, H. and Goetz, P.J., (1999). Electroacoustic Phenomena in Concentrated Dispersions: New Theory and CVI Experiment. Langmuir. **15**(20), pp.6692-6706.

Dukhin.A, S.Goetz.P., (2002). Ultrasound vibration potential for colloid particle and sensing. Elsevier. **First Edition**.

Editor, T., (2004). LeCroy's WaveRunner 6000A Series oscilloscope. [Online]. Available from: Testandmeasurementtips.com

Guang, P. Wang, M. Inaki, H.S. Khanj, J.I. and Valerie, S., (2011). Towardsd a-scan imaging vibration potential measurement. Nuclear Engineering and Design. **241**(6), pp.1994-1997.

Gusev, V., E and Diebold, G. J.,(2004). Imaging with the Ultrasonic Vibration Potential: A Theory for Current Generation. Ultrasound in Med. and Biol. **31**(2), pp.273-278.

Hamilton, T. J. Rose-Petruck, C. and Diebold, G.J., (2004). Acoustically modulated x-ray phase contrast imaging. Physics in Medicine and Biology. **49**(21), pp.4985-4996.

Hans, P.L., (2015). Finite difference methods for vibration analysis, . Department of Informatics University of Oslo. pp.3-31.

Hariharan, S. and Paul, S.P., (2011). Potential adverse ultrasound realated bilogical effects a critical review. Anestheology. **115**(5), pp.1109-1120.

Hermans, J.J., (1938). Charged colloid particles in an ultrasonic field —II. Particles surrounded by a thin double layer. The London, Edinburgh, and Dublin Philosophical Magazine and Journal of Science. **26**(177), pp.674-683.

Hosseini, M. Bramnson, L. Wang, M., (2015). An Experimental Investigation of ionic Vibration Potential Sensing in Electrolytes. Procedia Engineering. **102**, pp.64-71.

Hossein, F. Wang, M., (2019), Modelling and measurement of ultrasound vibration potential distribution in an agar phantom. Journal of Chemical Physics.

Hossein F, Wang M. Colloid Vibration Potential Imaging for Medicine. J Biomed Imag Bioeng. 2019;3(1):114-118.

Hossein, F. and Wang, M. (2020). UVP Distribution and Device for Imaging Physiochemical Property of Nanoparticles or Ionic Species in Colloids - White Rose Research Online. [online] Eprints.whiterose.ac.uk. Available at: http://eprints.whiterose.ac.uk/154575/ [Accessed 4 Feb. 2020].

Hsu, J.P., Lee, E. and Yen, Faraji.Y., (2000). Electrophoreses of contracted spherical particles with a charge-regulated surface. Journal of Chemical Physics, 112(14) pp 6404-6410. **112**(14), pp.6404-6410.

Jens , E.W. Andreas, I.M.Andersen, O.T., (2013). Medical diagnostic ultrasound physical principles and imaging . Bio Engineering, DTU Eleketro. **3**(1), pp.1-21.

John, B., Ernest, Y. and Frank, H., (1947). The application of ultrasound waves to the study of electrolytic solutions I. A modification of Debyes equation for the determination of the masses of electrolyte ions by means of ultrasonic waves. The Journal of Chemical Physics. **15**(8), pp.592-597.

John , G.Lynn, R.L. Zwemer, A.J. Chick, M, A.E., (1942). A new method for the generation and use of focused ultrasound in experimental biology. General Physiology. **26**(2), pp.179-192.

Jrank.D., (2019). How ultrasound wave are generated. www.science.jrank.org. p7075.

Kane, D.Grassi,W.Sturrock, R. Balint, P.V., (2004). A brief history of musculoskeletal ultrasound: ‘From bats and ships to babies and hips’. Rheumatology. **43**(7), pp.931-933.

Khan, J.,(2010). Physics of colloid vibration potential for imaging ionic species and silica Dioxide Nanoparticle systems. P.h.D Thesis, University of Leeds.

Khan, J.I. Wang, M. Schlaberg, H.I. Guan, P., (2013). Effect of ion vibration potential for 1-1 electrolytes. Chemical Physics. **425**(8), pp.14-18.

Kovacs, S.J., (2001). Coulombs Law. Mich.State.Univ. **10/22**, pp.1-20.

Liu, G. Liu, Z., Feng, J. Song, Z. Liu, Z., (2017). Experimental research on the ultrasonic attenuation mechanism of coal. Journal of Geophysics and Engineering. **14**(3), pp.502-512.

Makino, K. and Ohshima, H., (2010). Electrophoretic Mobility of a Colloidal Particle with Constant Surface Charge Density. Langmuir. **26**(23), pp.18016-18019.

Mann, R.W., (1997). Electrical process topography. Measurement and Control. p208.

Marlow, B., J and Fairhurst, D., (1988). Colloid vibration potential and the electrokinetic characterization of concentrated colloids. Langmuir. **4**(3), pp.611-626.

Marlow, B.J. and Fairhurst, D.,(1987). Colloid Vibration Potential and the Electromagnetic Characterization of Concentrated Colloids. American Chemistry Society. **4**, pp.611-626.

Minding, R.D.,(1971). High frequency vibrations of piezoelectric crystall plates. International Journal of Solid and Structures. **8**(7), pp.895-906.

Mindray, S.,(2007). Mindray DP-6600 Ultrasound Machine For Sale From IDD. [Online]. Available from: https://mindrayamerica.com/mindray-medical-equipment/mindray-dp-6600-ultrasound-machine/

Mortimer , A., J., (1982). Physical characteristic of ultrasound. In:Repacholi M,H,(eds) Essential of medical ultrasound. Medical Methods Press.

Murat, B.A., (2014). Size dependent surface charge property of silica Nanoparticles. The Journal of Physical Chemistry. pp.1836-1842.

NDK., (2019). Basic prnciple of medical ultrasonic probes. [Online]. Available from: https://www.ndk.com/en/sensor/ultrasonic/basic02.html

NDT., (2017). Attenuation of sound waves. [Online]. Available from: https://www.nde-ed.org/EducationResources/CommunityCollege/Ultrasonics/Physics/attenuation.htm

Neumayer, M. Steiner, G. Watzening, H.Z., (2011). Spatial resolution analysis for real-time application in electrical capacitance tomography. Nuclear Engineering Design. **241**(6), pp.1988-1993.

Nguyen, C., K., (2009). Ultrasound Vibration Potential Imaging:Theory and Experiments. P.hD thesis, Brown University.

Nguyen., C.K. 2009. Ultrasonic Vibration Potential Imaging: Theory and Experiment. Brown University,Ph.D Thesis., pp.87-107.

NTD.,(2019).Transducer.[Online].Available from: https://sonatest.com/products/transducers

O'Brien, R.W., (1987). Electro-acoustic effects in a dilute suspension of spherical particles. Journal of Fluid Mechanics. **190**, pp.71-86.

O'Brien, R.W., (2006). A method for the calculation of the effective transport properties of suspensions of interacting particles. Journal of Fluid Mechanics. **91**(1), pp.17-39.

Ohshima, H., (2005). Electrophoresis of a colloid particle in a salt-free medium. Chemical Engineering Science. **61**(7), pp.2104-2107.

Ohshima, H., (2009). Theory of electrostatics and electrokinetics of soft particles. Science and Technology of Advanced Materials. **10**(6), p063001.

Ohshimaa, H. and Dukhin, A.S., (1999). Colloid vibration potential in a suspension of soft particles. . Journal of Colloid and Interface Science. **212**(2), pp.449-452.

Olympus, N., (2006). Ultrasonic Transducers and Technical Notes. [Online]. Available from: https://mbi-ctac.sites.medinfo.ufl.edu/files/2017/02/ultrasound-basics.pdf

Olympus., N., (2016). Telab.vuse.vanderbilt.edu. [Online]. Available from: http://telab.vuse.vanderbilt.edu/docs/specs/Olympus-5072PR.pdf

NTD., (2018). [Online]. Available from: www.olympus-ims.com

Paul, H., (1998). Fourier transform and the Fast Fourier Transform (FFT) Algorithm. Computer Graphics. **2**, pp.1-13.

RITEC., (2018). http://www.ritecinc.com/pdfs/ga2500specs.pdf. [Online].

Ritecinc.,(2016)High power pulse amplifier, Model GA-2500A. [Online]. Available from: www.ritecinc.com

Tadros, T., (1982). Zeta potential in colloid science. Principles and application. Colloids and Surfaces, 5(1), pp.79-80.

Cootney, R. (2001). Ultrasound Imaging: Principles and Applications in Rodent Research. ILAR Journal, 42(3), pp.233-247. Roberts, J.J. and Martens, P., (2016). Engineering biosynthetic encapsulation system. Bio Polymer for Medical Applications., pp.205-239.

Schlaberg, H., Wang, M., Guan, P. and Khan, J. (2011). Ultrasound Vibration Potential measurement techniques for imaging. Nuclear Engineering and Design, 241(6), pp.1981-1987.

Mindray.com.(2016). Mindray.[online] Available at: https://www.mindray.com/en/Index.html [Accessed 6 Nov. 2018].

Specialingredients.co.uk. (2018). Modernist Cuisine - Ultratex, Flavour Drops - Molecular Gastronomy. [online] Available at: https://www.specialingredients.co.uk [Accessed 6 Jul. 2018].

Stephane, P. (2016). Characterization of coated optical fibers by Fourier-domain optical coherence tomography. NYC, Ph.D Thesis.

Stetefeld, J., McKenna, S.A. & Patel, T.R. Biophys Rev (2016) 8: 409.

Behrens, S. and Borkovec, M. (1999). Electric double layer interaction of ionizable surfaces: Charge regulation for arbitrary potentials. The Journal of Chemical Physics, 111(1), pp.382-385.

Vincent, B. (2013). Tharwat Tadros. Advances in Colloid and Interface Science, 137(2), pp.144-149.

Tomas, L. S. (2004). Diagnostic Ultrasound Imaging: Inside Out (Second Edition). Ultrasound in Medicine & Biology, 41(2), p.622.

Szabo, T. and Lewin, P. (2013). Ultrasound Transducer Selection in Clinical Imaging Practice. Journal of Ultrasound in Medicine, 32(4), pp.573-582.

Shah, V. and Balasubramaniam, K. (1996). Effect of viscosity on ultrasound wave reflection from a solid/liquid interface. Ultrasonics, 34(8), pp.817-824.

Gusev, V. and Diebold, G. (2005). Imaging with the ultrasonic vibration potential: A theory for current generation. Ultrasound in Medicine & Biology, 31(2), pp.273-278.

Wang, M. Bramson, L and Khan, J. I. (2013). Methods of colloid the ultrasonic vibration Imaging for caracterisation of nano-particle suspension. Nano Tech, (3), pp.16-19.

Wang, S., Beveridge, A., Li, S., Diebold, G. and Nguyen, C. (2006). Frequency domain vibration potential imaging: Objects with symmetry in one dimension. Applied Physics Letters, 89(24), p.243902.

Gusev, V. and Diebold, G. (2005). Imaging with the ultrasonic vibration potential: A theory for current generation. Ultrasound in Medicine & Biology, 31(2), pp.273-278.

Imperial.ac.uk,(2019),[online]Available:at; ttps://www.imperial.ac.uk/media/imperial-college/ /7293026.PDF [Accessed 6 Nov. 2015].

Wells, P. N., (1988). Ultrasound Imaging. Biomedical Engineering, 10(6), pp.548-554.

Yanlin, Z., (2012). Methods for Electrical Impedance Spectroscopy and Tomograpghy Characterizing Particles in Suspension and Crystallization Precess. Ph.D Thesis, University of Leeds.

Yousef , F., (2013). Measurement and visualisation of slurry flow using electrical resistance tomography. Ph.D Thesis, University of Leeds.

Yuncheng, L., Nidal, H., Paul, L. and Victor, S., (2007). Interaction forces between colloidal particles and liquid. Colloid and Interface Science. **134**(135), pp.156-166.

Zana, R. and Yeager, E., (1967). Ultrasonic vibration potentials and their use in the determination of ionic partial molal volumes. The Journal of Physical Chemistry. **71**(3), pp.521-536.

List of My Publications

Hossein F, Wang M. 2019. UVP Distribution and Device for Imaging Physiochemical Property of Nanoparticles or Ionic Species in Colloids. Proceedings of the 7th UK-China International Particle Technology Forum VII Proceedings of the 7th UK - China International Particle Technology Forum University of Edinburgh (28 July 2019): University of Edinburgh VII, pp. 35-36.

Hossein F, Wang M. Colloid Vibration Potential Imaging for Medicine. J Biomed Imag Bioeng. 2019;3(1):114-118.

Hossein F, Wang M. Modelling and measurement of ultrasound vibration potential distribution in an agar phantom. J of Chem Phys.(2019).

Hossein F, Wang M. An Experimental Method of Measuring particle characteristics Using Ultrasound Vibration Potential.(2020).

Hossein F, Wang M. Electroacoustic Spectroscopy Measurements for Characterizing Concentrated Nanoparticles in Colloid.(2020)

APPENDIX A: MATLAB CODE CVPI

```
%%%%%%%%%%%%%%%%%%%%%%%%%%%%%%%%%%%% UVP imaging
%%%%%%%%%%%%%%%%%%%%%%%%%%%%%%%%%%%%
uvpfile = 'F:\Backup\D-driver\Projects\UVP\data\07032018\UVP.xlsx';
%uvpfile = 'D:\Projects\UVP\data\07032018\UVP.csv';
 uvpVel = 1600; % m/s
uvpStartPoint = 3e-6; % second
uvpEndPoint = 2.961e-4; % second
 uvpThreshold = 0.008;
 uvpTimeOfFly = 0.08; % m
 uvpNumOfBeams = 30;
uvpSpanAngle = 33; % degree
PI = 3.14159265;
 uvpPeriod = 10e-6; % sec
 uvpAvgWindow = 50;
 startAngle = 180 - ((180-uvpNumOfBeams)/2);
angleIncre = double(uvpSpanAngle)/double(uvpNumOfBeams -1);
 % init figure handle
uvpImage = subplot(1,2,2);
cla(uvpImage);
set(uvpImage, 'YDir', 'reverse' )
set(uvpImage, 'color', 'black' );
hold(uvpImage, 'on');
halfRadian = double((uvpSpanAngle/2+1))*PI/180;
x=uvpTimeOfFly*tan(halfRadian);
drawLine([0 0], [x uvpTimeOfFly], uvpImage);
drawLine([0 0], [-x uvpTimeOfFly], uvpImage);
maxDist = uvpTimeOfFly/cos(halfRadian);
 [time ampl] = readAllData(uvpfile, uvpStartPoint, uvpEndPoint);
uvpSigInterval = 1e-8;
uvpSigPeriodNumPoints = int32(uvpPeriod/uvpSigInterval);

% find receiver positions
receiverPos = zeros(uvpNumOfBeams+1, 1);
for i = 1 : uvpNumOfBeams + 1
    if i == 1
        tempstart = 1;
        tempend = findPosition(uvpPeriod/2.0, time);
    else
        tempstarttime = time(receiverPos(i-1)) + 0.5*uvpPeriod;
        tempstart = findPosition(tempstarttime, time);
        tempend = findPosition(tempstarttime+ uvpPeriod, time);
    end

    if tempend > length(time)
        tempend = length(time);
    end
    %plot(time(tempstart), ampl(tempend), 'marker','x');
    [peakAmpl, peakPos] = max(ampl( (tempstart):(tempend) ));
    receiverPos(i) = tempstart + peakPos;
    %plot(time(receiverPos(i)), ampl(receiverPos(i)), 'marker','o');
end
% receiverPos(end) = length(time);

% find UVP signals bewteen 2 successive receivers
for i = 1 : uvpNumOfBeams
```

```
    [up, lo] = envelope(ampl(receiverPos(i):receiverPos(i+1)),
uvpAvgWindow, 'peak');
    [objPeaks, objPeaksIndex] = findpeaks(up);
    for k = 1: size(objPeaks,1)
        if objPeaks(k) >= uvpThreshold
            dist = double(uvpVel)*double(time(receiverPos(i) +
objPeaksIndex(k)) - time(receiverPos(i)));
            if abs(dist) > maxDist
                continue;
            end

            x = dist*cos(double(startAngle - double(i-
1)*angleIncre)*PI/180.0);
            y = dist*sin(double(startAngle - double(i-
1)*angleIncre)*PI/180.0);
            disp(['dist= ', num2str(dist), ', x=', num2str(x), ', y=',
num2str(y), ', angle: ', num2str(double(startAngle - (i-1)*angleIncre))]);
            plot(uvpImage, x, y, 'MarkerFaceColor',[1 1
1],'MarkerEdgeColor',[1 1 1],'Marker','o',...
                'LineStyle','none','MarkerSize', 2);
        end
    end
end
```

APPENDIX B :MATLAB CODE FFT

```
close all;
clear all;

filename = 'F7_10.5_00000.csv'; %name of files except numbers3
M=csvread(filename,1,0);
signal = M(:,2:1);
raws=length(signal(:,1));
time=1:raws;

% figure;
% plot(time(0.000164:0.00011309, 1), data(0.0000164:0.000011309,2));
%%%%%%%%%%%%%%%%%%%%%%%%%%%%%%%%%%%%%%%%%%%%%%%%%%%%%%%%%%%%%%%%%%%%%%%%%%%%
%%%%%
 for n = 1
    plot(time,signal(:,1));

     N = length(signal);
%      T = max(M(:,1));
   T=0.00015
    Fs = N/T;
%      wo = 300/(Fs/2);  %      bw = wo/35;
%      [b,a] = butter(3, wo, 'high'); %filter coeff to remove 50 Hz noise
%      filtsignal = filter(b, a, signal); %filter signal

    %% Calculate fft
    Y = fft(signal(:,1));
    P2 = abs(Y/N);
    P1 = P2(1:N/2+1);
    P1(2:end-1) = 2*P1(2:end-1);
    f = Fs*(0:(N/2))/N;

    freqdata(:,n) = P1;
end

figure;
plot(f, P1);
%% Smooth data
freq = f(1, 622:3549)';


% for n = 1:filenum
    smoothdata = smooth(P1(622:3549,1), 10);
% end
```

APPINDIX C: UVPD SIMULATION

2D simulation

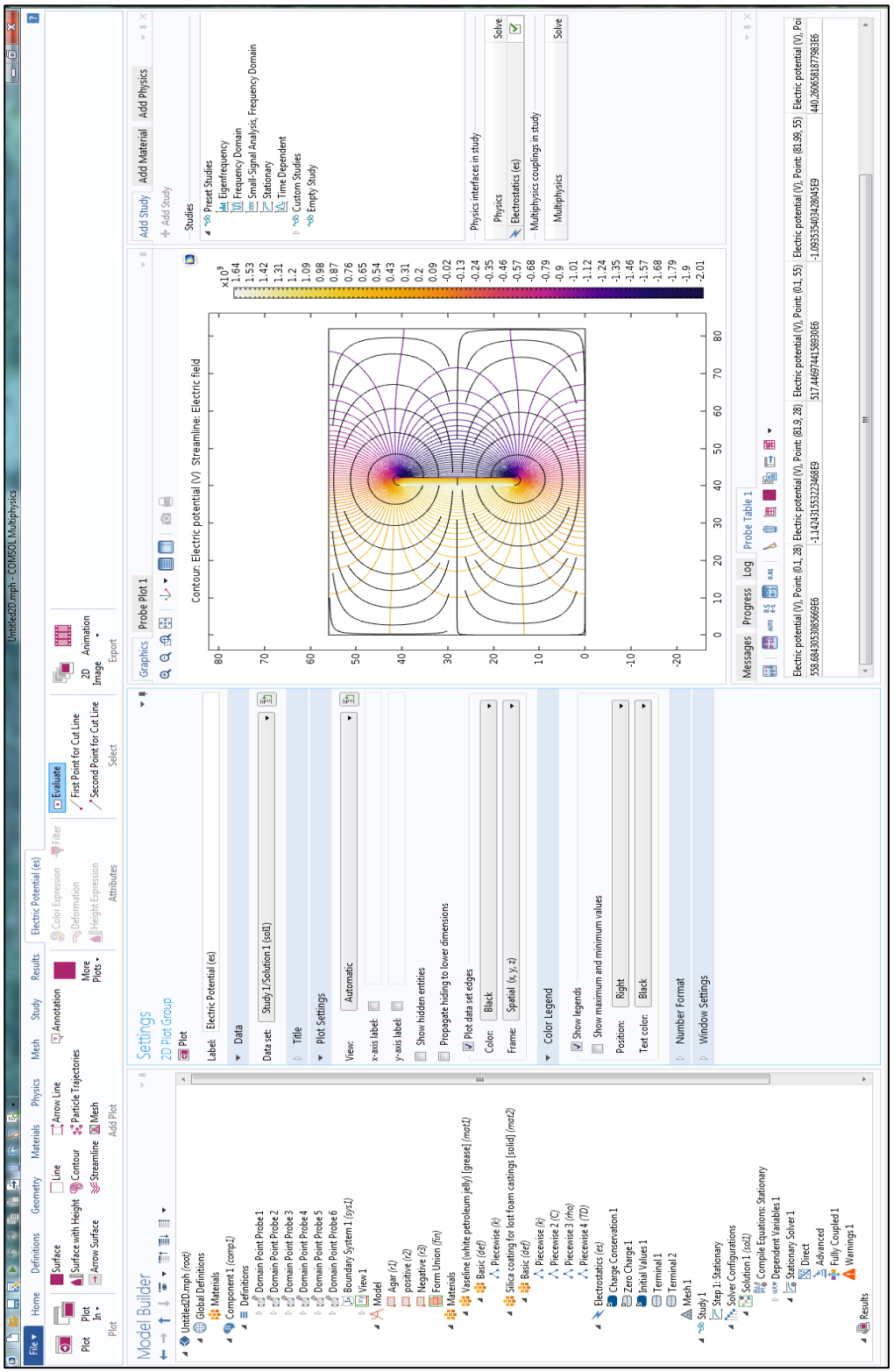

3D Simulation

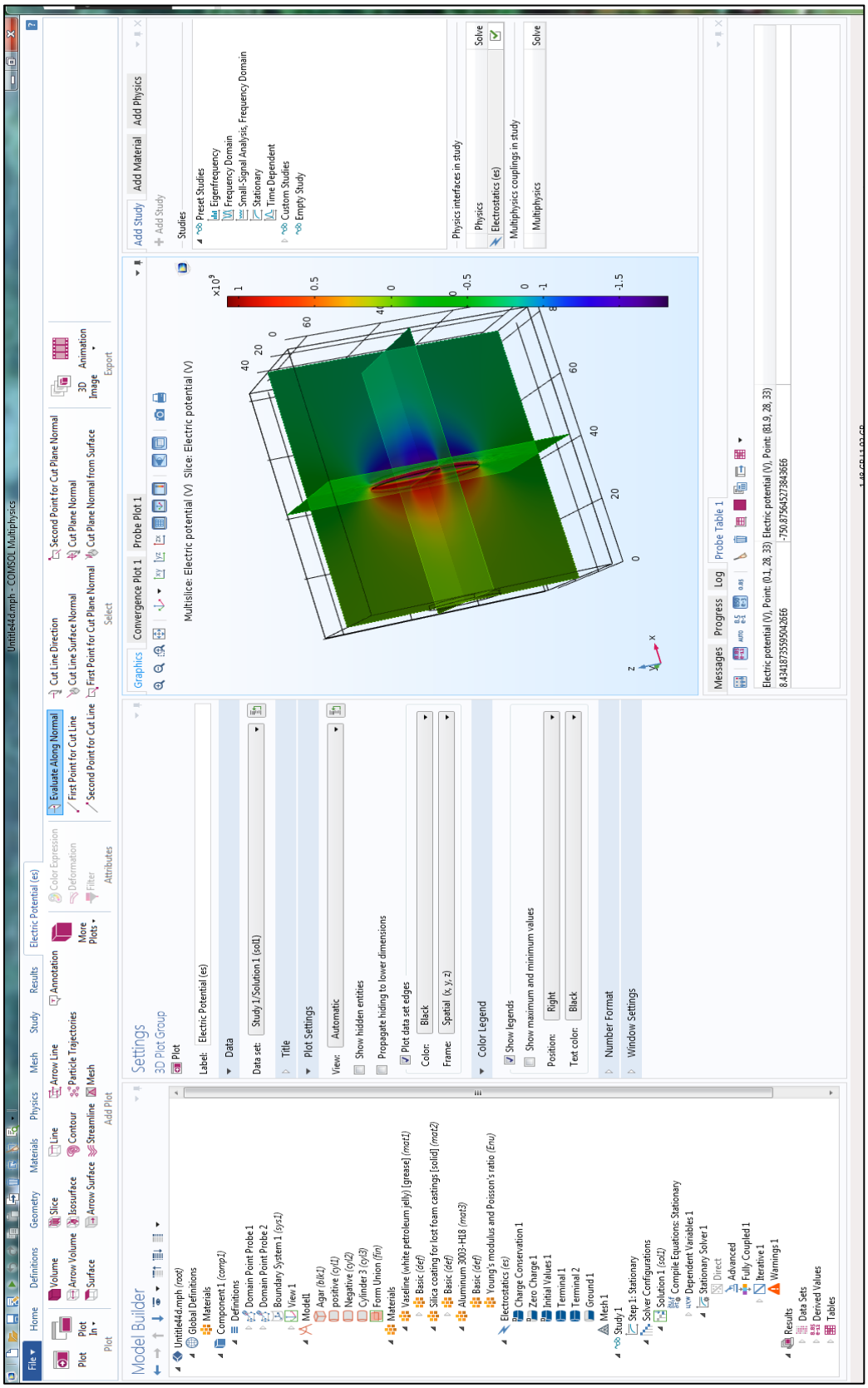

APPENDIX D: TRANSDUCER SPECIFICATIONS.

Sonatest, planar transducer;

TRANSDUCER CERTIFICATE

SONATEST - Sound Solutions -

Date stamp

– 5 APR 2006

SLIM1-25

Type of probe	Immersion Probe
Serial number	614/01
Frequency ± 10% (MHz)	1
Crystal shape	Circular
Crystal size (mm)	25
Crystal material	Lead Metaniobate
Probe dimensions (mm)	Ø35x35
Probe weight (g)	205
Connector type	UHF
Connector position	Top
Focal type	N/A

Signal Waveform

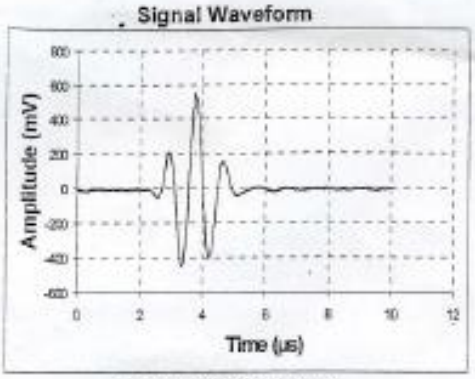

Frequency Spectrum

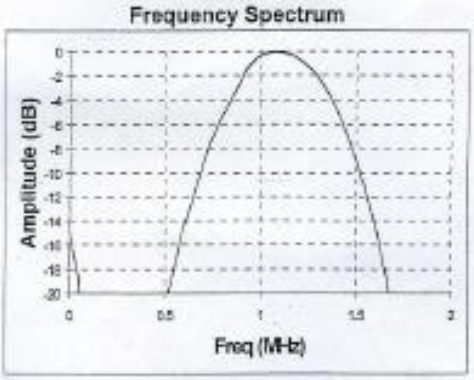

Test Results

Peak frequency	1.07 MHz	Pulse duration	2.33 µs	-6dB upper	1.43 MHz
Centre frequency	1.05 MHz	Peak to peak voltage	996.8 mV	-6dB lower	0.78 MHz
Near field length	111.1 mm			Bandwidth	0.66 MHz

Test Conditions

Instrument used	Masterscan 330
Pulse width	500 ns
Pulse impedance	50 Ohms
Inspector name	David Waller

Dickens Road, Old Wolverton, Milton Keynes, MK12 5QQ, England.
Registered in England No. 1981000

INVESTOR IN PEOPLE

APPENDIX E: AGAR POWDER SPECIFICATION

JUST INGREDIENTS

JUST INGREDIENTS TRADE

Agar Agar Powder - Product Specification

ALLERGEN STATEMENT

JustIngredients Limited supplies a range of products that are internationally sourced from approved suppliers. Information is gathered from all suppliers to enhance knowledge of the product and supplier handling procedures.

The following products which are or may contain allergens are regularly handled by JustIngredients Limited and their approved suppliers. Handling procedures are in place to reduce the likelihood of allergens being present, but we cannot guarantee our ingredients are totally free of traces in the products supplied. If in doubt, please email technical@justingredients.co.uk.

- Cereals containing gluten (wheat, rye, barley, oats, spelt, kamut and their hybrid strains)
- Peanuts
- Soybeans
- Nuts
- Celery
- Mustard
- Milk and dairy products
- Sesame seeds
- Products containing sulphur dioxide and sulphites at concentrations of more than 10mg/kg or 10mg/litre expressed as sulphur dioxide.

ADDITIONAL INFORMATION	
Key: ✓ Indicates that the product has the relevant certification and certificates	
Vegetarian	✓
Vegan	✓
Organic	
Kosher Suitable	✓

Storage & shelf life	
Shelf Life	Typical shelf life is 2 years.
Storage	Store in cool dry conditions away from direct sunlight
Labelling	Product name, Weight. Batch/lot code. Best before date. Allergen information as applicable

HEALTH & SAFETY

A non-hazardous product if used under normal circumstances. Buyers of our products are aware that if our products are used for food use, goods must be cooked thoroughly before use/consumption. If you are unsure of the suitability of our product for your specific use, you should not use and seek further information from our technical team technical@justingredients.co.uk

[i] SMART software is an impedance measurement software that allows you to control the Solarton instrumentation and display the measurement results.